



**HAL**  
open science

# Direct numerical simulation of complex Representative Volume Elements (RVEs): Generation, Resolution and Homogenization

Karim Hitti

► **To cite this version:**

Karim Hitti. Direct numerical simulation of complex Representative Volume Elements (RVEs): Generation, Resolution and Homogenization. Materials. École Nationale Supérieure des Mines de Paris, 2011. English. NNT : 2011ENMP0054 . pastel-00667428

**HAL Id: pastel-00667428**

**<https://pastel.hal.science/pastel-00667428>**

Submitted on 7 Feb 2012

**HAL** is a multi-disciplinary open access archive for the deposit and dissemination of scientific research documents, whether they are published or not. The documents may come from teaching and research institutions in France or abroad, or from public or private research centers.

L'archive ouverte pluridisciplinaire **HAL**, est destinée au dépôt et à la diffusion de documents scientifiques de niveau recherche, publiés ou non, émanant des établissements d'enseignement et de recherche français ou étrangers, des laboratoires publics ou privés.

Ecole doctorale n° 364 : Sciences Fondamentales et Appliquées

## **Doctorat ParisTech**

### **T H È S E**

pour obtenir le grade de docteur délivré par

**l'École nationale supérieure des mines de Paris**

**Spécialité “ Mécanique Numérique”**

*présentée et soutenue publiquement par*

**M. Karim HITTI**

le 07 décembre 2011

**Direct numerical simulation of complex Representative**

**Volume Elements (RVEs): Generation, Resolution and Homogenization**

~ ~ ~

**Simulation numérique de Volumes Élémentaires Représentatifs (VERs) complexes :  
Génération, Résolution et Homogénéisation**

Directeur de thèse : **Thierry COUPEZ**

Co-encadrement de la thèse : **Marc BERNACKI**

#### **Jury**

**Pr. Nabil NASSIF**, American University of Beirut

**Pr. Houman BOROUCI**, LASMIS, Université de Technologie de Troyes

**Pr. Olivier MILLET**, LEPTIAB, Université La Rochelle

**Pr. Patrice LAURE**, Laboratoire J. A. Dieudonné, Université de Nice

**Pr. Thierry COUPEZ**, CEMEF, MINES ParisTech, Sophia Antipolis

**Dr. Marc BERNACKI**, CEMEF, MINES ParisTech, Sophia Antipolis

Président

Rapporteur

Rapporteur

Examineur

Directeur de thèse

Co-encadrant de thèse



**...إلى أبي و أمّي**



## Acknowledgements

First of all, I would like to convey my deepest gratitude to my advisor Marc Bernacki. I had a real chance of working with him and I am very grateful for his help and support. I appreciate all his contributions, ideas, and remarks. He also had a big influence on all my written and oral communications. I would like also to thank Thierry Coupez, the director of my Ph.D., for recruiting me and giving me the opportunity to achieve this work and also for his brightful and fruitful ideas. It is important to mention Luisa Silva and Patrice Laure as well. I thank them for guiding me through some important phases of this thesis.

I want to thank Stephanie as well who stood by me during my the final Ph.D. year and encouraged and supported me. My appreciation goes to Elie Hachem who gave the first opportunity to come to CEMEF as an intern and helped me during all my stay in France.

I would like to express my gratitude for all my friends in CEMEF, Pamela, Nadine, Esteban, Ala, Ana-Laura, Greg Fidel, Jeff, Vu-thu, Christophe, Emile, Larbi, Greg Puaux...

I can not forget my brothers and friends outside CEMEF who supported me and gave me good advice during these three years, Ramzi, Toni, Mazen, Assad, Eddy, Georges, Nadim, Joe and Carine.

A special "thanks" goes to the Ladies of CEMEF who make the working environment joyful, Marie-Françoise, Sylvie, Françoise, Geneviève, Florence, Carole, Murielle and the librarians Brigitte and Sylvie. I would like to thank also all the staff at CEMEF, Group EII and special mention to the directors: Jean-Loup Chenot and Yvan Chastel.

I am very grateful to Patrick Coels for his advices, motivation, help and for the fruitful conversations we had.

Thank you God for giving me the power and strength to complete this work.

To my parents I dedicate my thesis.



# Contents

<b>1</b>	<b>General introduction</b>	<b>1</b>
1.1	Virtual Microstructures . . . . .	2
1.2	Objectives and a brief literature review . . . . .	2
1.2.1	Applications . . . . .	7
1.2.1.1	Foam compression . . . . .	8
1.2.1.2	Permeability computation . . . . .	10
1.3	The framework of this thesis . . . . .	11
1.4	Layout of this thesis . . . . .	12
1.5	Résumé français . . . . .	13
<b>2</b>	<b>Microstructure Generation</b>	<b>15</b>
2.1	Introduction . . . . .	16
2.2	Sphere packing . . . . .	17
2.2.1	Dynamic techniques . . . . .	18
2.2.2	Constructive techniques . . . . .	19
2.2.3	The method used . . . . .	22
2.2.3.1	Scheme of the algorithm . . . . .	23
2.2.3.2	Detailed analysis of the algorithm . . . . .	26
2.2.4	Some results . . . . .	32
2.2.5	The Powder Optimization Algorithm (POA) . . . . .	34
2.2.5.1	The three-dimensional POA . . . . .	35
2.3	Polyhedral microstructures . . . . .	51
2.3.1	Laguerre tessellations . . . . .	52
2.3.2	The Grain Optimization Algorithm (GOA) . . . . .	55
2.4	Extension to other microstructures . . . . .	56
2.4.1	Semi-solid granular structures . . . . .	56
2.4.2	Foams . . . . .	57
2.4.3	Disordered fiber arrays . . . . .	61
2.5	Conclusion . . . . .	63
2.6	Résumé français . . . . .	65

<b>3</b>	<b>Statistical microstructure modelling</b>	<b>69</b>
3.1	Introduction . . . . .	70
3.2	Modelling applications: Comparison with existing methods . . . . .	70
3.2.1	Powder RVE modelling . . . . .	71
3.2.2	Equiaxial polycrystal RVE modelling . . . . .	74
3.2.3	3D RVEs modelling . . . . .	77
3.3	Modelling applications: Experimental examples . . . . .	81
3.3.1	Powder RVE modelling . . . . .	82
3.3.2	Equiaxial polycrystal RVE modelling . . . . .	85
3.4	Conclusion . . . . .	87
3.5	Résumé français . . . . .	89
<b>4</b>	<b>Level-Set Approach and Meshing Adaptation</b>	<b>93</b>
4.1	Introduction . . . . .	94
4.2	The Level-Set approach . . . . .	95
4.2.1	Voronoi tessellations . . . . .	95
4.2.2	The Delaunay triangulation . . . . .	96
4.2.2.1	Comparison of numerical costs . . . . .	100
4.2.3	Cell spreading . . . . .	102
4.2.4	Spherical particles . . . . .	102
4.2.5	Laguerre tessellations and Open-cell foams . . . . .	102
4.2.5.1	The weighted Delaunay triangulation . . . . .	103
4.2.5.2	Laguerre tessellations . . . . .	105
4.2.5.3	Three-dimensional open-cell foams . . . . .	105
4.3	Meshing adaptation . . . . .	105
4.4	Conclusion . . . . .	111
4.5	Résumé français . . . . .	112
<b>5</b>	<b>Finite element calculations</b>	<b>117</b>
5.1	Introduction . . . . .	119
5.2	Elastic foam compression . . . . .	121
5.2.1	Governing equations . . . . .	121
5.2.2	Numerical approach . . . . .	124
5.2.3	The finite element formulation . . . . .	125
5.2.3.1	Classical mixed formulation . . . . .	126
5.2.3.2	Stable mixed formulation . . . . .	127
5.2.3.3	Matrix formulation . . . . .	129
5.2.4	Simulations and discussions . . . . .	130
5.2.4.1	The RVE's size . . . . .	130
5.2.4.2	The effect of the air . . . . .	131
5.2.4.3	The effect of varying cell irregularity . . . . .	133
5.2.4.4	Compression of a three-dimensional closed-cell foam . . . . .	137
5.3	Permeability computation of disordered fiber arrays . . . . .	138

5.3.1	Governing equations . . . . .	138
5.3.2	Numerical approach . . . . .	142
5.3.3	The FE formulation . . . . .	142
5.3.4	The RVE . . . . .	143
5.3.4.1	Ripley's $K_r$ . . . . .	144
5.3.5	Permeability computation . . . . .	144
5.3.5.1	Computation of the transverse permeability tensor . . . . .	145
5.3.5.2	Computation of longitudinal permeability . . . . .	147
5.3.6	Numerical Results . . . . .	147
5.3.6.1	The RVE's size . . . . .	147
5.3.6.2	Isotropic properties . . . . .	148
5.3.6.3	The effect of $\sigma$ on $\mathcal{K}$ . . . . .	148
5.4	Conclusion . . . . .	151
5.5	Résumé français . . . . .	153
<b>6</b>	<b>General conclusion and perspectives</b>	<b>159</b>
	<b>References</b>	<b>163</b>



# List of Figures

1.1	The different length scales . . . . .	3
1.2	A 2D polycrystal generated using the LSM with anisotropic remeshing at the cells' interfaces . . . . .	7
1.3	(a) A Voronoï honeycomb, (b) a closed-cell foam and (c) an open-cell foam . . . . .	9
2.1	(a) A hexagonal lattice and (b) the cubic close packing arrangement . . . . .	17
2.2	A 2D illustration of the “isotropic compression” method . . . . .	18
2.3	The “particle expansion” method in 2D . . . . .	19
2.4	The steps of the “collective rearrangement” method in 2D . . . . .	19
2.5	Illustration of the “sequential inhibition” method . . . . .	20
2.6	Illustration of the triangulation method . . . . .	20
2.7	Illustration of the method proposed in [105] . . . . .	21
2.8	Illustration of the classical “dropping and rolling” method [23] . . . . .	21
2.9	Illustration of the “Advancing-front Method” . . . . .	22
2.10	Mono-sized generated discs in a unit square by the IPM. 2789 discs of radius 0.01 are generated. The density is equal to 0.876 . . . . .	23
2.11	(a) The validity control in the IPM and (b) the first three levels in the filling process . . . . .	25
2.12	A 2D illustration of the IPM: creation of the initial front (upper left), the beginning of the filling process (upper right) and the convergence towards the center of the domain (lower figures) . . . . .	27
2.13	A 3D illustration of the IPM: the first step of the creation of the initial front (upper left), the face filling process which is the 2D IPM (upper right and lower left) and the domain filling (lower right) . . . . .	28
2.14	Example of a global initial front in 3D [38] . . . . .	29
2.15	(a) 150 discs with a density of 0.76 and radii chosen by $U[0.02; 0.06]$ and (b) 1951 spheres with a density of 0.475 and radii chosen by $U[0.02; 0.06]$ . . . . .	32
2.16	(a) 9703 discs with a density of 0.79 and (b) comparison between the density function obtained and the one of $N(\mu, \sigma^2)$ . . . . .	33
2.17	(a) 1034 discs with a density of 0.8 and (b) comparison between the wanted and obtained probabilities . . . . .	34
2.18	The flow chart of the classical dropping and rolling algorithms [22,23,40] . . . . .	35

2.19	The dropping phase in the 3D POA: (a) the search for $c_2$ and (b) the dropping of $c_1$ . . . . .	37
2.20	The rolling phase 1.1 in the 3D POA: (a) the search for spheres intersecting the torus and (b) the case where $\varphi = 0$ . . . . .	39
2.21	Searching for possible solutions of the Eqs.(2.20) to (2.22) with regards to the condition $\varphi' \in [0, \varphi]$ in the rolling phase 1.2 in the 3D POA: (a) no solutions exist, (b) only one solution exists and (c) two solution exist . . .	40
2.22	The rolling phase 1.2 in the 3D POA: the new position of $c_1$ tangent to $c_2$ and $c_3$ . . . . .	41
2.23	After the rolling steps 3 or 4, a case where the sphere of center $c_1$ intersecting the face $X = Xmax$ . . . . .	42
2.24	(a) The sphere of center $c_1$ is returned to a face-touching position and (b) the construction of the fictitious sphere of center $c_3^f$ . . . . .	43
2.25	The rolling phase 1.2 in the 3D POA: the new position of $c_1$ tangent to $c_2$ and $c_3$ . . . . .	44
2.26	The rolling phase 2.1 in the 3D POA: (a) going back to step 1 and (b) the sphere of center $c_4$ is found . . . . .	45
2.27	Checking the stability of the sphere of center $c_1$ . . . . .	48
2.28	A case where $P_{c_1} \in \Omega_{23}$ . . . . .	49
2.29	Illustration of the two-dimensional POA for a disc of center $c_i$ : (a) dropping, (b) rolling and (c) unstable position . . . . .	50
2.30	Effects of the POA on mono-disperse discs: (a) before applying the POA and (b) after applying the POA. . . . .	51
2.31	Effects of the POA on poly-disperse discs: (a) before applying the POA and (b) after applying the POA . . . . .	52
2.32	Effects of the POA on poly-disperse spheres: (a) before applying the POA, (b) a cut in the domain showing the inner filling before applying the POA, (c) after applying the POA and (d) a cut in the domain showing the inner filling after applying the POA . . . . .	53
2.33	A Voronoï diagram in the two-dimensional space $\mathbb{R}^2$ . . . . .	54
2.34	(a) A Voronoï diagram obtained in Mathematica and (b) a 3D Voronoï diagram with 200 Voronoï sites . . . . .	54
2.35	Generated spherical particles and the corresponding Laguerre tessellations: (a) the 2D case and (b) the 3D case . . . . .	55
2.36	Illustration of GOA.3: (a) a case where the displacement on the position of the barycenter is not responsible of overlapping so, this position is validated and (b) this displacement caused overlapping with another particle of the graph, hence, a linear displacement from the barycenter toward the initial position is realized step by step until a non-overlapping configuration is obtained. . . . .	57
2.37	A zoom on an equiaxial polyhedric RVE illustrating the effects of the GOA: (a) before applying the GOA and (b) after applying the GOA. . . . .	58

2.38	Spread Voronoï cells modelling a biphasic granular structure in a unit cube with $\epsilon_{min} = 0.02$ and $\epsilon_{max} = 0.05$ [23] . . . . .	59
2.39	Two spread cell with a channel size equal to $\epsilon_i + \epsilon_j$ . . . . .	60
2.40	(a) A regular Voronoï honeycomb with relative density 0.075 and (b) a Voronoï honeycomb with a regularity degree of 0.5 and a relative density of 0.125 . . . . .	61
2.41	A three-dimensional closed-cell foam with a regularity degree of 0.5 and a relative density of 0.2 . . . . .	61
2.42	The unidirectional disordered fibers at their microscopic scale . . . . .	62
2.43	Three equally spaced discs of radius $R$ and their equilateral disposition . .	63
2.44	Fiber distributions generated by our method in a $10 \times 10$ square: (a) 6130 fibers with $\phi = 0.51$ and $\sigma = 0.06R$ , (b) 6111 fibers with $\phi = 0.51$ and $\sigma = 0.12R$ , (c) 3678 fibers with $\phi = 0.7$ and $\sigma = 0.03R$ and (d) 3634 fibers with $\phi = 0.7$ and $\sigma = 0.4R$ . . . . .	64
2.45	A comparison between the wanted and obtained distributions of the inter-fiber distances $\delta_i$ of the fiber array represented in Figure 2.44b . . . . .	65
3.1	(a) The probability density functions obtained in each domain of the first test case compared with the density function of $U[6 \times 10^{-2}, 4.2 \times 10^{-1}]$ and (b) the obtained frequencies compared with the wanted ones for the second test case in $H_0$ . . . . .	73
3.2	The probability density functions obtained in each domain of the third test case compared with the density function of $N(\mu_p, \sigma_p^2)$ . . . . .	74
3.3	(a) The powder RVE obtained using the POA in $U_4$ made of 53805 discs and (b) a zoom at the center of the microstructure . . . . .	75
3.4	(a) The powder RVE obtained without using the POA in $G_2$ and (b) the same powder RVE when the POA is applied . . . . .	76
3.5	The probability density functions obtained without optimization, using the GOA and using the LS method in each domain compared with the density function of $N(\mu_G, \sigma_G^2)$ . . . . .	78
3.6	4810 equiaxial grains generated in $G_1$ using the GOA . . . . .	79
3.7	The obtained size distributions in the 3D powder modelling case . . . . .	79
3.8	2031 spheres in a unit cube modelling a 3D powder RVE: (a) the whole domain before applying the POA, (b) a cut in the domain showing the inner filling before applying the POA, (c) the whole domain after applying the POA and (d) a cut in the domain showing the inner filling after applying the POA . . . . .	80
3.9	The obtained size distributions in the 3D equiaxial grain modelling case . .	81
3.10	A 3D equiaxial grain RVE containing 1748 grains and generated using the GOA . . . . .	82
3.11	The frequencies obtained in $S_0$ , $S_1$ and $S_2$ for each generation method compared with the experimental frequencies . . . . .	83

3.12	(a) The powder RVE obtained using the IPM without the POA in $S_0$ , (b) the same powder RVE when the POA is applied and (c) the powder RVE obtained using the dropping and rolling technique . . . . .	84
3.13	7777 spheres in $E_0$ , generated using the IPM, modelling a 3D powder RVE: (a) the whole domain before applying the POA, (b) a cut at middle of the domain showing the inner filling before applying the POA, (c) the whole domain after applying the POA and (d) a cut at middle of the domain showing the inner filling after applying the POA . . . . .	86
3.14	9495 spheres in $E_1$ , generated using the dropping and rolling technique, modelling a 3D powder RVE: (a) the whole domain and (b) a cut at middle of the domain showing the inner filling . . . . .	87
3.15	A microscopic illustration of a stainless steel 304L with grain joints drawn in white lines . . . . .	87
3.16	The frequencies obtained in all the domains compared with the experimental frequencies in the 2D case . . . . .	88
3.17	An equiaxial polycrystal RVE containing 3680 grains obtained using the GOA in $S_3$ . . . . .	89
4.1	The level-set function of a square domain. The interface of the square is in black . . . . .	96
4.2	Four level-set functions defining four Voronoï cells. The Voronoï nuclei are the white dots and the cells' interfaces are in black . . . . .	97
4.3	The $\phi_{glob}(x)$ function corresponding to 4 Voronoï cells . . . . .	97
4.4	The $\phi_{glob}(x)$ function corresponding to 300 Voronoï cells [17]. FE mesh in white . . . . .	98
4.5	The Delaunay triangulation (full lines) and the corresponding Voronoï tessellation (dashed lines) [51] . . . . .	98
4.6	The <i>supertriangle</i> containing all the nuclei . . . . .	99
4.7	$P$ is the red point: (a) The cavity of $P$ and (b) the ball of $P$ . . . . .	100
4.8	FE mesh (red), Delaunay triangulation (white), the nucleus $S_i$ (black), its graph (white points) and the global level-set function defining the Voronoï tessellation . . . . .	101
4.9	(a) The global level-set function $\phi_{glob}(x)$ defining a 3D semi-solid granular structure with a solid fraction of 0.9 generated using the LTM and the cell spreading technique and (b) the global interface of a 3D closed-cell foam given by the iso-zero of $\phi_{glob}(x)$ . . . . .	103
4.10	(a) The global level-set function $\phi_{glob}(x)$ defining 243 discs and (b) the global interface of the discs given by the iso-zero of $\phi_{glob}(x)$ . . . . .	104
4.11	(a) The global level-set function $\phi_{glob}(x)$ defining 306 Laguerre cells and (b) the global interface of the cells given by the iso-zero of $\phi_{glob}(x)$ (in blue) and the weighted Delaunay triangulation (in red) . . . . .	104
4.12	Representation of an open-cell foam in 2D where intersections between the Laguerre cell generating discs were forced . . . . .	106

4.13	A three-dimensional foam . . . . .	107
4.14	(a) Anisotropic meshing adaptation for an equiaxial polycrystal and (b) zoom at a triple junction . . . . .	109
4.15	(a) A 2000 equiaxial polycrystal RVE made of Laguerre cells, described using five level-set functions (one color per level-set function) and (b) a zoom illustrating anisotropic meshing at the interfaces of the Laguerre cells . . . . .	112
4.16	(a) A powder RVE made of 554 discs obtained by the POA described by five level-set functions thanks to the graph coloration algorithm (one color per level-set function) and (b) the finite element mesh in a zoom of the microstructure . . . . .	113
4.17	(a) A poly-dispersed powder RVE made of 585 spheres, described using eight level-set functions and (b) a zoom on 2 cutting planes illustrating meshing at the interfaces of the spherical particles . . . . .	114
4.18	(a) A 3D tetrakaidecahedral foam microstructure made of 250 cells, generated using the LTM and described by eight level-set functions and (b) the mesh on three orthogonal cross sections . . . . .	115
5.1	Mixing the air's viscosity $\eta_f$ with $\mu\Delta t$ . . . . .	126
5.2	The MINI-element $P1 + /P1$ . . . . .	128
5.3	Elementary volumes extracted from an irregular Voronoï honeycomb containing 198 cells in order to determine the size of the RVE . . . . .	131
5.4	The influence of the number of cells in the honeycomb elementary volumes on the reduced stress/strain predictions . . . . .	132
5.5	(a) The initial regular Voronoï honeycomb made of 135 cells and (b) the same honeycomb after 25% deformation . . . . .	132
5.6	(a) The reduced stress/strain curve of the regular Voronoï honeycomb and (b) the mass variation of the whole structure (solid and air) . . . . .	133
5.7	(a) The elastic solid skeleton of a regular Voronoï honeycomb in its stable position, (b) a zoom at a triple junction showing the nonexistence of mesh elements inside the cells and (c) the same honeycomb after 20% deformation . . . . .	134
5.8	(a) The velocity of the solid skeleton at 20% deformation and (b) the pressure of the solid skeleton at 20% deformation . . . . .	135
5.9	Comparison between the response of a solid skeleton with air inside the honeycomb's cells and without air . . . . .	136
5.10	The influence of cell irregularity on the reduced stress/strain predictions . . . . .	136
5.11	(a) The Voronoï honeycomb with $\gamma = 0.7$ in its undeformed state and the anisotropic meshing at the interfaces (b) after 25% of biaxial compression . . . . .	137
5.12	The velocity's norm of the Voronoï honeycomb with $\gamma = 0.7$ after 25% of biaxial compression . . . . .	138
5.13	(a) The iso-zero of the level-set function defining a three-dimensional closed-cell foam made of 107 cells with a cell irregularity of 0.5 and a relative density of 0.1 at its initial state with the anisotropic remeshing and (b) the same foam after 30% deformation . . . . .	139

5.14	(a) The velocity's norm at 30% deformation of the closed-cell foam shown at the foam's interface and (b) the pressure at 30% deformation also shown at the foam's interface . . . . .	140
5.15	(a) The reduced stress/strain curve of the irregular closed-cell foam and (b) the variation of its mass . . . . .	141
5.16	(a) $\eta(\alpha)$ defined on the whole computational domain using a mixture law and (b) anisotropic remeshing at the solid-fluid interface . . . . .	142
5.17	The $L(r)$ functions of the fiber distributions described in Figure 2.44 . . . . .	145
5.18	Elementary volumes extracted from a $10 \times 10$ microstructure in order to determine the size of the RVE . . . . .	149
5.19	The size effect on $\langle K \rangle / R^2$ . The fiber distributions were generated with $\sigma = 0.06R$ and $\phi = 0.51$ . The error bars represent the standard deviations $\pm \sigma_p$ . . . . .	150
5.20	The size effect on the porosity . . . . .	151
5.21	The averaged permeability components at different values of $\sigma$ : (a) $\phi = 0.51$ , (b) $\phi = 0.7$ and (c) $\phi = 0.9$ . . . . .	152
5.22	Flow paths for boundary conditions 2 across unidirectional fiber array: (a) $\phi = 0.7$ , $\sigma = 0.03R$ and (b) $\phi = 0.7$ , $\sigma = 0.4R$ . . . . .	153
5.23	Contours of fluid velocity for longitudinal flows across unidirectional fiber array: (a) $\phi = 0.7$ , $\sigma = 0.03R$ and (b) $\phi = 0.7$ , $\sigma = 0.4R$ . . . . .	154
5.24	The effect of averaged standard deviation of the inter-fiber spacing on the normalized averaged transverse (a) and longitudinal (b) permeability. Also shown are permeability values for hexagonal arrays [80] . . . . .	155

# Chapter 1

## General introduction

### Contents

---

<b>1.1</b>	<b>Virtual Microstructures . . . . .</b>	<b>2</b>
<b>1.2</b>	<b>Objectives and a brief literature review . . . . .</b>	<b>2</b>
1.2.1	Applications . . . . .	7
1.2.1.1	Foam compression . . . . .	8
1.2.1.2	Permeability computation . . . . .	10
<b>1.3</b>	<b>The framework of this thesis . . . . .</b>	<b>11</b>
<b>1.4</b>	<b>Layout of this thesis . . . . .</b>	<b>12</b>
<b>1.5</b>	<b>Résumé français . . . . .</b>	<b>13</b>

---

## 1.1 Virtual Microstructures

The mechanics of heterogeneous materials concentrated for a long time on the notion of global behavior by estimating their properties in a macroscopic way. But, the influence of microstructural heterogeneities on material processing is an issue of prime importance [1], which explains the need to generate a digital material, statistically equivalent to the considered microstructure, and to connect this digital description to a specific computational method such as the Finite Element Method (FEM) [2, 3]. Thanks to the considerable progress accomplished in the techniques of multi-scale modelling, the increase of the means of calculation, and the evolution of the experimental techniques, we can have access to the local information, or microscopic, and model it. Despite this progress in the last decade [4, 5], consistent analysis of real-world large-scale engineering structures by multi-scale techniques are still far from being executed routinely. The first cause of such a situation is simply the cost of analysis: even on large parallel networks, the size of the problem remains to be limited to selected structural parts [6]. The second important restriction is the intrinsic randomness of materials' microstructures, typically observed on all relevant length scales. The high cost of a fully coupled micro-macro simulation can be significantly reduced when restricting the attention to a fully uncoupled analysis. In this context, the response of a Representative Volume Element (RVE) when it is subject to a given loading path is of the main interest.

The RVE represents the mesoscopic scale which is the intermediate scale between the microscopic and macroscopic scales (see Figure 1.1). The RVE has to be big enough to statistically represent the material, which means, to include a sample of all microstructural heterogeneities which appear in one heterogeneous material (grains, porosity, fibers, inclusions, etc) and it has to be rather small so that variations of macroscopic fields would be negligible. Boundary conditions are also important to characterize an RVE subject to a loading path. Periodic boundary conditions are used [7], when the RVE is constructed or considered as periodic. In other cases, most precisely when the RVE's size is determined by studying the variations of a certain physical property in function of the size of different volume elements, symmetrical boundary conditions [8] can be used.

## 1.2 Objectives and a brief literature review

Generally, the generation of microstructures or RVEs and the mechanical applications performed on these microstructures are two independent topics. Usually, when the construction or generation phase is advanced, it is concentrated on one type of microstructure and no mechanical testings are performed. Inversly, when mechanical testings are performed, the generation step is briefly described or only cited.

A main objective of this thesis is to propose a formalism in order to generate statistical virtual microstructures and to connect easily this virtual description to Finite Element (FE) computations. It will be impossible to give an exhaustive list of concerned applications but recurrent types of microstructures in the literature are polyhedric and

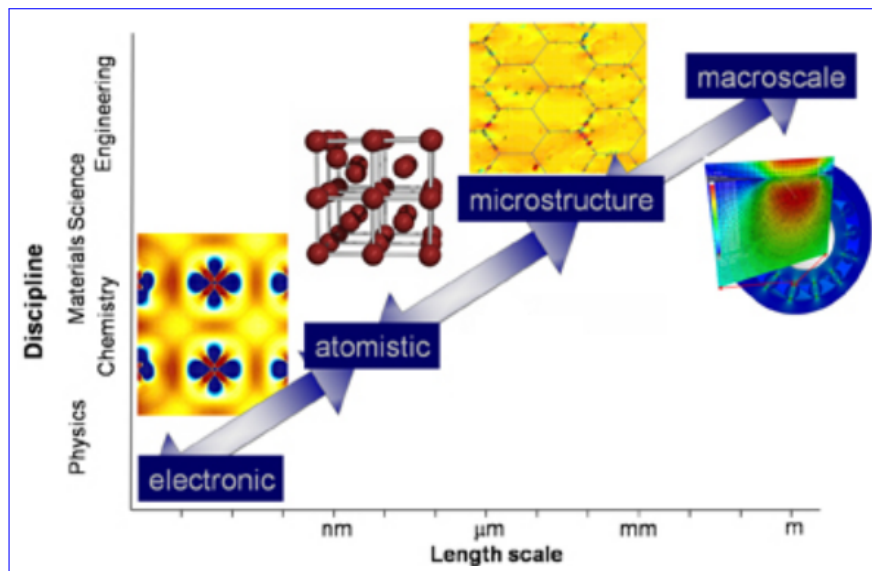


Figure 1.1: The different length scales

spherical arrangements. For example, Voronoï cells are currently used to model foams [7, 9, 10, 11, 12, 13], polycrystals [14, 15, 16], granular semi-solids [17, 18, 19], etc; whereas, spherical packings are currently used to generate suspensions [8, 20, 21], powder RVEs [22, 23], granular assemblies [24, 25], etc.

As it will be detailed later, two particular applications at the mesoscopic scale are studied in the proposed formalism: the numerical modelling of foam deformation and the permeability computation inside a unidirectional fiber material. However it is important to underline that, in term of statistical generation of RVEs, the methodology proposed and the builder developed in CimLib [26] during this Ph.D. thesis are used in CEMEF for other microstructures such as polycrystal [27, 28], high density sphere packing [29, 30] or granular semi-solid [17].

Two independent microstructure generators already exist in CimLib [26], the FE C++ library used and developed in this work. The first generates suspensions of solid particles [31]. It was used for modelling composite materials (matrix + spherical particles and/or fibers) with a simple size distribution for the spherical particles and fibers with a precise length and diameter. Although the application performed on the microstructure of this generator required only moderated particle densities, high densities were not achievable. Moreover, complex size distribution laws for the solid particles were not implemented in this generator. The second generator was used for modelling metallurgical grains using Voronoï tessellations [14]. A first limitation of this builder, similar to one of the first, is the impossibility of imposing a cell size distribution which is a global weakness of the classical Voronoï Tessellation Method (VTM). A second weak point is its limitation to a moderated number of cells especially in 3D.

Numerous generation methods and algorithms exist in the literature. We begin by shedding light on the ones using cell generating methods modelling polyhedral microstructures.

Zhu and coworkers used the VTM to model Voronoï honeycombs (or two-dimensional foams) [7, 12] and open-cell foams [11, 13] with different irregularity degrees and relative densities (see section 2.4.2). They studied the effect of cell irregularity on the high strain compression and on the elastic properties and found that, for both kinds of foams, a more irregular foam has a higher tangential modulus at low strain but supports a lower compressive stress at higher strain when compared with a more regular one (hexagonal in 2D and tetrakaidecahedral in 3D), and the more irregular the random foams, the larger will be their effective Young's modulus and shear modulus, and the smaller will be their bulk modulus. Also the VTM is used in the works of Li et al. to model two-dimensional cellular solids [32] and open-cell foams [9] in order to study the effects of cell shape and cell wall thickness variations on the elastic properties of foams. Distortions in regular foams were used to model irregular cell shapes and random thicknesses were given to each cell wall to model its thickness variation. Their simulations indicated that the Young's and shear moduli increase as cell shapes become more irregular, but decrease as cell wall thickness gets less uniform. Roberts and Garboczi [10, 33] used Voronoï tessellations of seeds positioned in a body-centered cubic lattice to generate the tetrakaidecahedral model for closed-cell foams and deleted cell faces to get open-cell foams.

Voronoï tessellations were also used to generate polycrystalline aggregates to model primary recrystallization [15] and to simulate the plastic deformation of these aggregates [16]. The same method coupled with a set of cell boundary shifts was used to generate an equiaxed semi-solid granular structure in order to compute its permeability [17]. In these works, level-set functions were used to define the Voronoï cells and efficient anisotropic mesh adaptation was performed to properly describe the considered microstructures.

Benabbou et al. [25, 34] used the Laguerre tessellation method (LTM) which is similar to the VTM but with an imposed cell size distribution to model granular structures. In their work, spheres were used as a basis for approaching the cell size distribution and a specific sphere packing method (detailed later in this manuscript) was used to respect the size distributions. In this context, it is important to underline, that the principal difficulty of LTM is common to the close packing of spheres: to respect a given statistical size of spheres with the highest possible density.

Rollett et al. [35, 36] generated virtual 3D polycrystals. Their methodology is linked to real microstructures through the collection of statistical distributions of grain size and shape in 2D. These distributions are extrapolated to 3D, and then used to bound a synthetic microstructure generation process. In these studies, a distribution of ellipsoids is used to represent grains in the polycrystalline microstructure. The ellipsoids' centers are then used as nucleation sites to fill space through continuous nucleation and growth of the grains on a regular grid of voxels. Here as well, object packing (i.e. ellipsoid packing) was used for generating the grains.

Object packing methods were, and still are, an active research field. In the works of Bagi [24, 37], two-dimensional sphere packing methods were developed in order to model

granular structures. Benabbou et al. [25, 34, 38] modified Bagi's *advancing front method* [24] and extended it to a three-dimensional sphere packing method called the *Inwards Packing Method (IPM)* in the goal of modelling granular structures as well. They have also performed the transition between spheres and Laguerre cells as another way of modelling polyhedral structures. Both of the above-cited authors' microstructures respected a given size distribution law and obtained a high sphere packing density especially in 2D. The densities obtained in 3D by the IPM can be considered as averaged ranging from 0.47 to 0.5. The computational cost, in 2D, of the IPM was compared to Bagi's dropping method [37] and to a gravitational deposition method [39] and was found to be much faster.

A three-dimensional dropping and rolling technique was used in [22, 23, 40] in order to model powder-based structures and rocks' pore space. The packing densities obtained were high and well above the ones of Benabbou's method but this packing algorithm lacked of speed. Although no computational times were reported, the recursive phases of dropping and rolling, where tiny steps are considered in order to achieve the sphere's final position, prove the slowness of this algorithm.

Disc packing coupled with a Monte Carlo procedure [1] is used by Chen and Papanthasiou [8, 20] to generate unidirectional disordered fiber arrays governed by the choice of the porosity and the minimum allowable inter-fiber distance. They studied the effect of the mean nearest inter-fiber spacing on both the transverse and longitudinal permeabilities. They found that the latter decreases on all porosity levels and the former increases on porosity levels ranging from 0.45 to 0.7 and decreases above these levels when mean nearest inter-fiber spacing increases.

Moving away from spherical particles, Donev et al. [41] achieved the highest density in equal ellipsoidal packing which they referred to as crystal packing. They have reached a density of 0.7707 where a unit cell consisting of several ellipsoids with at least two inequivalent orientations is periodically replicated on a lattice to fill Euclidean space. Their density is higher than the densest packing of spheres in the three-dimensional Euclidean space which is approximately 0.74048, realized by the face-centered cubic (fcc) lattice packing.

Non-intersecting elliptical and ellipsoidal particles are used in the works of Wang and coworkers [42, 43] to model 2D and 3D granular assemblies. Each ellipsoidal particle is approximated by the revolution of an ellipse, formed by four connected arcs and the domain to be filled with particles can be a polygon of any shape.

A packing algorithm for three-dimensional non-overlapping polyhedrons was developed by Lee et al. [44]. Their method allowed them to efficiently detect particle-particle and particle-container wall overlappings and was validated by a system shaking process where the particles sink to the bottom of the container. Most recently, Jin et al. [45] developed a probability-based contact algorithm for polyhedral particles in order to model realistic granular particles and their algorithm was validated by simulating the Hopper experiment [46].

Another important objective of this work is to connect easily the microstructures obtained by our generator to FE computations to perform specific mechanical applications.

Calculations on the generated statistical RVEs, made of cells or particles, can be performed by various methods. The Discrete Element Method (DEM), for example, is used usually when spherical particles are in question because it requires only a local model of the contact behavior between particles. It was used to simulate powder compaction [47] and polymer foam compression [48] where cells are considered as a collection of spherical particles. The Meshed Discrete Element Method (MDEM), where the particles in the DEM are meshed, was used for simulating compaction of granular packings [49, 50].

Furthermore, the modelling of contact behavior is a simplification to realistic cases and it can be much more complicated when more complex microstructures are modelled such as Laguerre/Voronoi cells, hence it is better to use the Finite Element Method (FEM) which is more expensive in computational times but more precise and more realistic. In this case, the transition between the generation of a statistical RVE and finite element calculations performed in this RVE is not straightforward as the interfaces of the microstructure should be represented in the FE mesh. Classical approaches consist in describing the interfaces of the different parts of the RVE thanks to nodes of the FE mesh. The different interfaces are so given explicitly by a set of nodes of the mesh. Most precisely, surface meshes of the interfaces are generally built and subsequent volume mesh conform to the interfaces' surface meshes is generated. In [34, 38], and in a 2D context, the discretization of the boundary and the generation of a mesh of the points of the discretized boundary are firstly performed. Then, a combined advancing front-Delaunay approach [51] is used to generate the meshes. In the 3D context, the boundary is considered as a 2D surface and a surface mesh is built at first then a volume mesh is constructed. In these cases, the mesh generation is a long procedure combining steps of discretization, mesh construction and quality improvement. This method can be very costly for structures having a large number of grains especially in 3D. In [36, 52], a mesh was constructed for a 3D grain-based microstructure. Firstly, a Voronoi tessellation is constructed by taking the centroids of the grains and additional points as the only seed points. Then, an initial mesh is generated by triangulating each face of each Voronoi cell. After triangulating each face, each corner of a triangle is connected to the seed point that generated the Voronoi cell to which the face belongs. This method necessitates the construction of a Voronoi tessellation included inside the microstructure's grains and involves complex quality improvement techniques. Another important discussion concerns meshing adaptation which can be necessary to describe correctly the RVE considered and so for several reasons. First of all, purely geometric consideration concerning the RVE's characteristics can lead to perform meshing adaptation at the interfaces of the cells. Indeed, for example, in a monolithic context, a foam made of less than 1% of solid or a granular semi-solid made of less than 1% of liquid described by spreading Voronoi cells undermines the necessity to work with very fine meshes at the cells' interfaces and with a coarsest mesh size in the cells' bulk to avoid prohibitive calculation times. Second, mesh refinement at cells' interfaces could be also prescribed to take into account discontinuities of physical properties in monolithic resolution contexts or to describe contact conditions in multi-domain resolution contexts.

Given these facts, the Level-Set Method (LSM) appears clearly as an interesting recent alternative tool to describe RVEs in an FE mesh and to adapt the FE mesh to the RVE's

constituents. The LSM was initially presented by Osher and Sethian [53] and later on detailed by Sethian [54]. The principle of the method is to represent implicitly an interface by the zero level of a distance function, called the level-set function which is defined as a field on the FE mesh. Other than representing the microstructure, the level-set functions are used for mixing laws [55], mesh adaptation [15, 16, 17] and simulating the transport of an interface. The use of level-set functions to model equiaxial polycrystals made of Voronoï cells was introduced by Bernacki [15, 56] and later on used to model 3D polycrystalline aggregates [16] and semi-solid granular structure [17]. This approach was applied successfully for the generation of 2D or 3D polycrystals and for meshing adaptation at the grains interfaces (see Figure 1.2). Further on it was, extended to the generation of Laguerre cells [57] and foams [58]. Also, the level-set approach was used to define spherical particles modelling suspensions [21], unidirectional fiber arrays [59] and powders [30, 57].

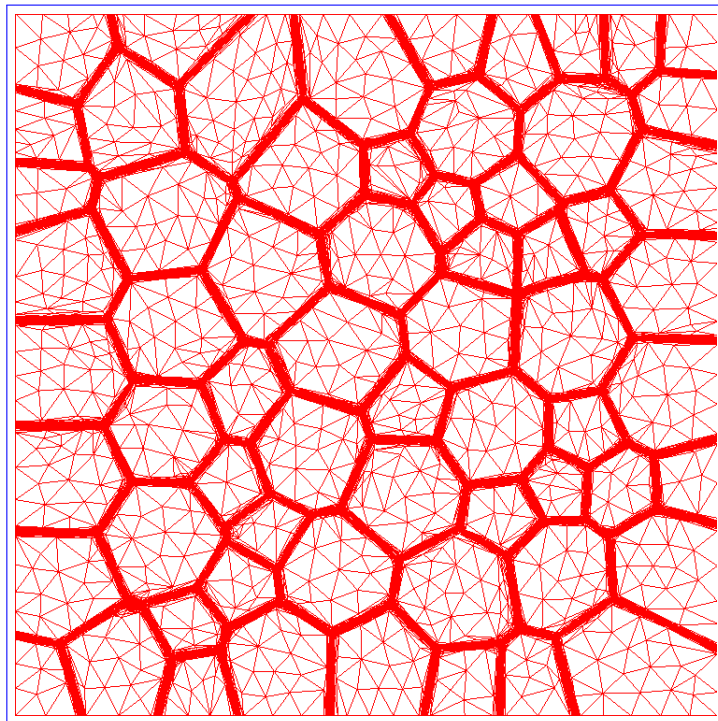


*Figure 1.2: A 2D polycrystal generated using the LSM with anisotropic remeshing at the cells' interfaces*

### 1.2.1 Applications

Several applications have been already performed using the microstructure generated by our statistical virtual RVE builder. The permeability of an equiaxed semi-solid granular structure, generated using the VTM coupled with cell spreading, was computed [17]. The

primary recrystallization of a polycrystal with a specific cell size distribution, obtained using the Laguerre tessellation method [28], and the compaction of a powder with a specific granulometry, obtained using our spherical particles packing algorithms [29, 30], were performed.

To cover a wide range of the mechanical applications which can be performed on our virtual microstructures, we were interested in foam compression as an application on a cell-based microstructure and in permeability computation of 2D disordered fibrous media as an application on a particle-based microstructure.

### 1.2.1.1 Foam compression

Foams are present in our everyday life under diverse forms and functions. They serve, for example, in the manufacturing of mattresses, car bumpers, in the heat or phonic insulation, etc (an extensive review may be found in [60]). Two-dimensional foams, also referred to as Voronoï honeycombs, can appear under regular (square or hexagonal) and irregular shapes. Three-dimensional foams, which are either closed-cell or open-cell, also appear under regular (cubic or tetradecehedrale) and irregular forms (see Figure 1.3).

Analytical or numerical calculations have been performed on idealized microstructures constructed from a repeating unit cell. Structural mechanics have been applied to open cell foams schematized either by a regular tetrahedral arrangement of beams [61, 62] or by a regular arrangement of tetrakaidecahedral cells [63, 64]. In the case of closed cell structures, finite element calculations on tetrakaidecahedral unit cell have also been derived [65]. All these approaches lead to similar scaling laws for modulus or strength. They give quite fair estimations of modulus and strength though discrepancies are observed with experimental values. These discrepancies are attributed by the authors to the difference between the ideal geometry assumed in the models and the actual perturbed architecture observed in the materials. Thus, different kinds of imperfections or defects have also been introduced to try to explain the experimental discrepancies. The strut cross-sectional area variations for example were accounted for in [9] and the cell wall thickness in [32]. Distortions in cell shapes have been introduced as well through more or less perturbed Voronoï tessellations [7, 11, 12, 13]. In these cases the cell walls were considered as beam elements and the presence of the air inside the foam's cells was never taken into account though its presence may affect the foam's behavior.

In order to simulate biaxial compression of a foam modelled by Voronoï cells, a uniform velocity is imposed on the upper and lower boundaries of the computational domain, composed of triangles (tetrahedrons in 3D). By taking the presence of air inside the foam's cells, which are bounded by the elastic solid skeleton, into consideration a Fluid Structure Interaction (FSI) problem occurs between a compressible elastic solid and a compressible fluid. Using this approach, we will be able to understand the effect of the air on the compression of an elastic foam.

Most of the commercial software packages solve FSI problems using an Arbitrary Lagrangian Eulerian (ALE) formulation [66, 67]. The solid domain is treated with a Lagrangian formulation. The nodes belonging to the interface between the solid and

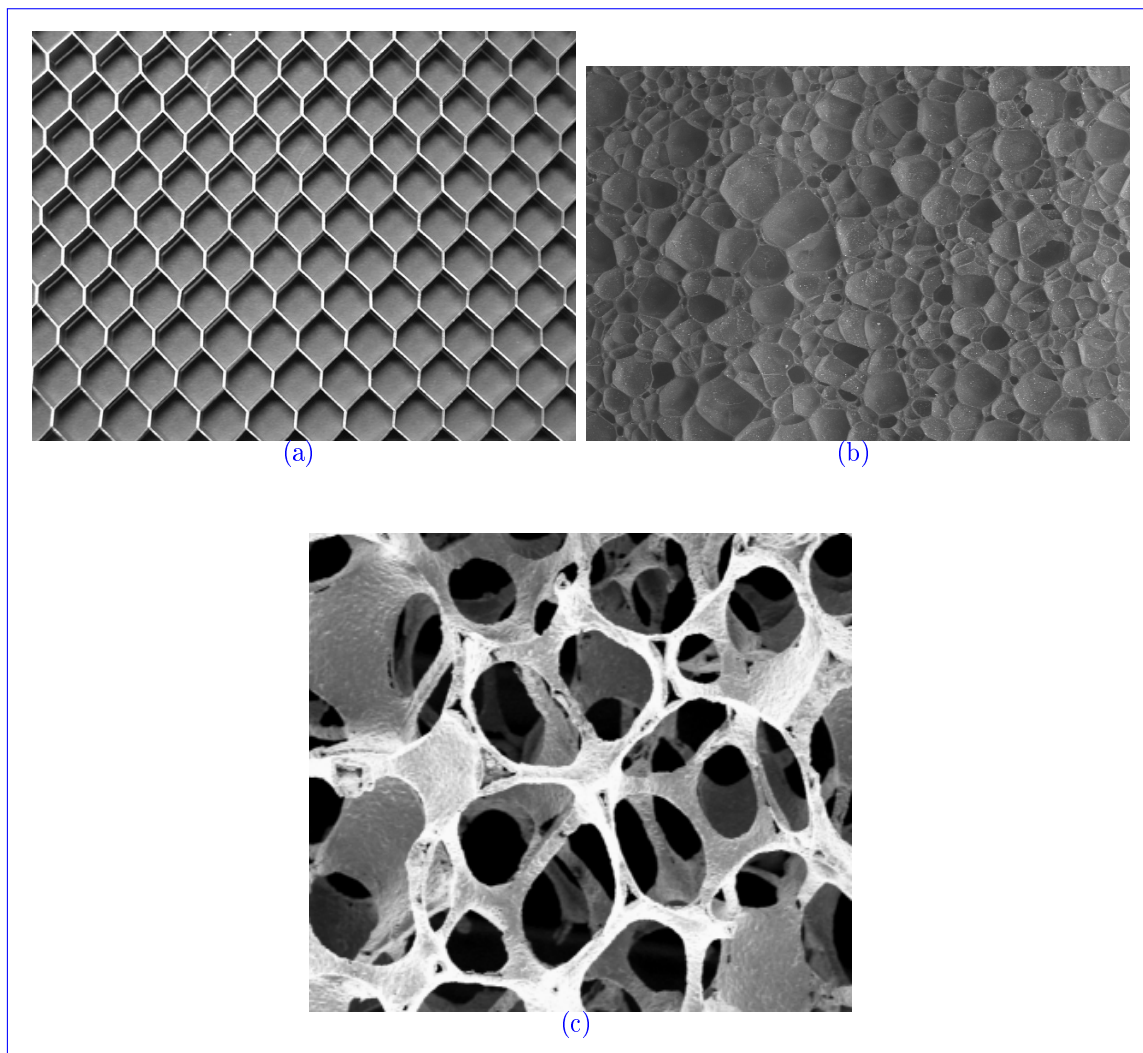


Figure 1.3: (a) A Voronoï honeycomb, (b) a closed-cell foam and (c) an open-cell foam

the fluid are moved with the solid. The displacement of the nodes in the fluid domain do not depend on the fluid's motion, but only ensures the continuity between the fluid and the solid domain, and a good mesh quality. ALE methods are robust and accurate, and do not need any extra degrees of freedom. However, important problems arise if the deformations, displacements and rotations of the solid becomes very important [68, 69, 70]. Partitioned approaches, which allow the use of a specific solver for each domain, recently gained popularity. The difficulty remains in transferring the information between the codes. The coupling between the two phases can be enforced using different schemes: weakly or strongly coupled version [71, 72, 73]. This approach is accurate and quite efficient but present an inherent instability depending on the ratio of the densities and the geometry of the domain [74]. As a result, the numerical cost increases drastically and coupling algorithms may not converge. For 3D problems, such difficulties become even

more severe. Monolithic approaches have been proposed to overcome these drawbacks. The whole domain, composed by the fluid and solid phases, is considered as a single one and meshed by a single grid. The continuity at the interface is then obtained naturally and there is no need to enforce it, as it was the case in partitioned methods. If the multi-mesh approaches permit the use of classical fluid and solid solvers, monolithic approaches impose the use of an appropriated unique constitutive equation describing both the fluid and the solid domain. Interface tracking, between the two different domains, can be completed by the Immersed Boundary Method (IBM) [75] where the interface is convected in a Lagrangian framework or by the Immersed Volume Method (IVM) based on the level-set approach, mixing laws and on mesh adaptation [55].

For solving our FSI problem, a monolithic formulation is used. Such strategy gives rise to an extra stress tensor in the Navier-Stokes equations, which are solved by a mixed FEM with a P1+/P1 interpolation, coming from the presence of the structure in the fluid [76]. We used a Lagrangian framework in order to simulate foam compression. In this case, each node remains in coincidence with the same phase throughout the whole deformation process. In particular, the nodes located at the interface of the solid skeleton remains on its boundary during the whole simulation and hence, tracking a moving interface does not present major difficulties.

### 1.2.1.2 Permeability computation

Injection processes are used for manufacturing complex materials with fiber reinforcements. Numerical simulations at the macroscopic scale are based on the resolution of Darcy's law [77, 78] to predict flow front progression, filling time and injection pressure and to improve the design of tools and molds.

In the case of ordered fiber arrays, several analytical relations have been established to predict the permeability of fibrous media [79, 80, 81, 82, 83]. All of these studies consider simple geometries, such as square or triangular packing of unidirectional arrays of cylinders and the analytical relations are only a function of the porosity. By considering some hypothesis, different authors provide analytical solutions of the Stokes equations to obtain the permeability. These different laws give a valid solution for different fiber volume fractions. In what concerns numerical predictions, several studies had been done at the microscopic and mesoscopic scales through the finite element or finite volume methods [80, 81, 84, 85]. In these studies, fibers or yarns are considered as impermeable solids. Then, only the fluid domain is meshed and no-slip boundary conditions are imposed on solid boundaries. Velocity and pressure fields are computed on the fluid domain and permeability of the volume is then obtained by a homogenization method.

In the case of disordered fiber arrays which represent real fiber performs, the use of porosity alone cannot define their permeability. Other microstructural parameters should be taken into account. Chen and Papathanasiou [8, 20] studied the effect of the mean nearest inter-fiber spacing on both the transverse and longitudinal permeabilities. In other words, they studied the effect of the degree of disorder on the permeability.

In order to compute the permeability of the fibrous arrays, we used a mixed FEM with

an immersed domain approach to represent the porous material at its microscopic scale. Therefore the Stokes equations are solved in the whole domain (including solid part) using a penalization method. Homogenization techniques, mainly volume averaging [86], are used to obtain Darcy's equation and hence, the permeability could be computed.

The permeability is a tensor for anisotropic porous media, like fibrous media for example. In the case of unidirectional fiber packings, if the  $z$  axis of the coordinate system is taken in the same direction that the axis of fibers, the permeability tensor can be then written as follows:

$$\mathcal{K} = \begin{pmatrix} K_{\perp} & 0 \\ 0 & K_{\parallel} \end{pmatrix} \quad (1.1)$$

with  $K_{\perp}$  the transverse permeability tensor and  $K_{\parallel}$  the longitudinal permeability (i.e. along the fiber axis).

### 1.3 The framework of this thesis

This thesis was conducted as part of the project *μcim* supported by Consortium *Rem3D*<sup>®</sup> which gathers the following partners:

- **Arkema** ([www.arkema.com](http://www.arkema.com)) : petro-chemical, polymer furnisher
- **Dow Chemicals** ([www.dow.com](http://www.dow.com)) : polymer producer
- **Rhodia** ([www.rhodia.com](http://www.rhodia.com)) : speciality chemicals producer
- **Schneider Electric** ([www.schneider.fr](http://www.schneider.fr)) : electrical parts distribution, plastic equipment
- **SNECMA Propulsion Solide** ([www.snecma.fr](http://www.snecma.fr)) : aeronautic equipment
- **Transvalor** ([www.transvalor.fr](http://www.transvalor.fr)) : industrialization and commercialization of material forming software

All the developments and calculations in this thesis were done in CimLib [26] an FE C++ library developed in CEMEF ([www.cemef.mines-paristech.fr](http://www.cemef.mines-paristech.fr)) by group CIM (Calculs Intensifs en mise en forme des Matériaux) under the direction of T.Coupez. CimLib is the base for different numerical applications developed at CEMEF, in collaboration with other research teams and industrial partners. This scientific library represents an Object Oriented Program and a fully parallel code, written in C++, and gathers the numerical developments of the group (Ph.D. students, researchers, associate professors, etc). It aims at providing a set of components that can be organized to build numerical softwares, such as REM3D, XIMEX, Forge3 and THOST. It also has the capability of performing mesh adaptation by calculating metrics which are in turn send to MTC, a topological mesher-remesher interfaced in CimLib and developed by T.Coupez [87]. MTC is based on local mesh topology optimizations and works for all meshing applications, from adaptive remeshing to mesh generation, using a minimal volume principle.

## 1.4 Layout of this thesis

After this first introductory chapter, the manuscript is organized as follows. The second chapter constitutes the core of our statistical virtual microstructure builder where we first detail the sphere packing method used in our developments, which is based on an advancing-front method and called "Inwards Packing Method" (IPM), and a void optimization algorithm adapted to powder modelling and based on the dropping and rolling technique is introduced. This chapter deals as well with polyhedral microstructure generation where we explain the construction of Voronoï and Laguerre tessellations along with the introduction of an optimization algorithm adapted to equiaxial polyhedral RVE modelling. Furthermore, the extension of these methods for generating semi-solid granular structures, foams and unidirectional disordered fiber arrays is explained. In the third chapter, statistical modelling applications are performed in order to prove the efficiency of our algorithms in 2D and 3D. The fourth chapter details the use of the LSM for immersing the different RVEs in a FE mesh and performing mesh adaptation. We begin by explaining the use of level-set functions to define Voronoï cells and the impact of the introduction of the Delaunay triangulation to the method introduced in [15, 56] which optimizes the computation times. Afterwards, the extension of this method to the generation of Laguerre tessellations and spread cells is explained and the construction of a level-set function defining three-dimensional open-cell foams is detailed. Furthermore in this chapter, we propose a strategy based on graph coloration in order to decrease the number of requisite level-set functions used in meshing adaptation. The fifth chapter is dedicated to the mechanical applications performed on the microstructures generated by our virtual microstructure builder. We deal with the compression of elastic foams and with permeability computations of unidirectional disordered fiber arrays. Finally, the sixth chapter is the general conclusion of this work.

The work in this thesis has contributed to the following written communications:

- K. Hitti, P. Laure, T. Coupez, L. Silva, and M. Bernacki, Fast generation of complex statistical Representative Elementary Volumes (REVs) in a finite element context, submitted to *Journal of Computational Physics*.
- K. Hitti, L. Silva, M. Bernacki, and P. Laure, Permeability computation on a Representative Volume Element (RVE) of unidirectional disordered fiber arrays, submitted to *Computational Materials Science*.

and the following oral communications:

- K. Hitti, T. Coupez, L. Silva, and M. Bernacki, Generation of cellular Representative Volume Elements (RVEs) in a finite element (FE) context - application to foam compression, In *20ème Congrès Français de Mécanique, 28 August - 2 September 2011, Besançon, France, 2011*.

- K. Hitti, P. Laure, T. Coupez, L. Silva, and M. Bernacki, Generation of statistical Representative Elementary Volumes (REVs) in a finite element context - application to powder metallurgy. In *Powder Seminar, 2 February 2011, Sophia Antipolis, France*, 2011.
- K. Hitti, P. Laure, T. Coupez, L. Silva, and M. Bernacki, Fast Generation of complexes REV. In *IV European Conference on Computational Mechanics, 16-21 May, Paris, France*, 2010.

## 1.5 Résumé français

Ce chapitre constitue l'introduction de cette thèse effectuée au Centre de Mise en Forme des matériaux (CEMEF). Premièrement, la notion de volume élémentaire représentatif (VER) a été introduite. Deuxièmement, une brève étude bibliographique sur les différentes méthodes de génération de VER et sur les applications traditionnellement liées à la génération de ces microstructures virtuelles a été réalisée. Ensuite, le générateur de microstructures virtuelles statistiques développé dans le cadre de travail de thèse, couplé à une approche level-set et une technique d'adaptation de maillage, a été introduit. Ce générateur, adapté à la fois aux cellules polyédriques et aux particules sphériques, peut ainsi répondre à la création de nombreux types de microstructures. Le développement de ce générateur et son implémentation dans la librairie C++ CimLib ont été les premiers objectifs de ce travail. Si de nombreuses applications sur VERs réalisées au Cemef s'appuient aujourd'hui sur le générateur développé, les applications sur VERs auxquelles nous nous sommes intéressées dans le cadre de ce travail de thèse sont introduites dans le cinquième chapitre. La première application concerne la compression de mousses élastiques et la deuxième le calcul de perméabilité dans des milieux fibreux. En ce qui concerne la compression de mousses, l'air présent dans les cellules donne naissance à un problème d'interaction fluide structure entre un fluide compressible et un solide élastique compressible. Ce problème est gouverné par les équations de Navier-Stokes comportant un terme d'extra-contrainte au second membre qui s'explique par la présence d'une structure solide dans un fluide. Concernant le calcul de perméabilité, les équations de Stokes gouvernent l'écoulement dans le milieu fibreux et la loi de Darcy, obtenue en moyennant les équations de Stokes, permet de calculer la perméabilité du milieu. Finalement, l'organisation de ce manuscrit de thèse a été détaillée et les contributions liées à ces travaux de thèse ont été énumérées.



# Chapter 2

## Microstructure Generation

### Contents

---

<b>2.1</b>	<b>Introduction</b>	<b>16</b>
<b>2.2</b>	<b>Sphere packing</b>	<b>17</b>
2.2.1	Dynamic techniques	18
2.2.2	Constructive techniques	19
2.2.3	The method used	22
2.2.3.1	Scheme of the algorithm	23
2.2.3.2	Detailed analysis of the algorithm	26
2.2.4	Some results	32
2.2.5	The Powder Optimization Algorithm (POA)	34
2.2.5.1	The three-dimensional POA	35
<b>2.3</b>	<b>Polyhedral microstructures</b>	<b>51</b>
2.3.1	Laguerre tessellations	52
2.3.2	The Grain Optimization Algorithm (GOA)	55
<b>2.4</b>	<b>Extension to other microstructures</b>	<b>56</b>
2.4.1	Semi-solid granular structures	56
2.4.2	Foams	57
2.4.3	Disordered fiber arrays	61
<b>2.5</b>	<b>Conclusion</b>	<b>63</b>
<b>2.6</b>	<b>Résumé français</b>	<b>65</b>

---

## 2.1 Introduction

As one of our goals is the creation of a multi-physical virtual microstructure builder which can simultaneously generate spherical particles and cells, the Inwards Packing Method and the Laguerre/Voronoi tessellation method are used for several reasons, that we detail in this chapter.

On one hand, spherical particles can be used to model granular structures [25, 88], particle suspensions [89], fibrous media [8, 20, 90], porous media [91], powders [92], etc. In our study, we are going to concentrate on generating spherical particles that are densely packed and respect a specific size distribution law. By performing an additional step on the sphere packing method, disordered fiber arrays can be modelled as well. Since the distribution of spherical particles serves as a basis for constructing equiaxial cells thanks to the Laguerre method, the geometrical modelling of a cellular RVE can be considered as a classical sphere-packing problem. However, for the both kinds of microstructure considered, powders and polyhedrals, the spherical particles should be densely packed to be realistic in the case of powder RVEs and to optimize the size difference between them and the resulting Laguerre cells for equiaxial cell RVEs. Hence, a sphere packing method that generates high sphere densities and respects a size distribution law should be used.

On the other hand, the Voronoi tessellation method (VTM) is a geometric method that partitions a space of dimension  $d$  into space-filling, convex polyhedra or cells. Owing to its resemblance, in geometric and statistical appearance, to many cellular structures and stochastic patterns appearing in nature, Voronoi tessellations have found many applications over the past years in a wide range of fields, including biology [93], zoology [94], metallurgy [3, 15] and foam modelling [7, 13]. But the VTM presents some limitations towards cell size distributions since the location of the nuclei is the only way to define the Voronoi tessellations without control on the cells characteristics. To overcome this difficulty, Laguerre tessellations [95, 96] were developed. A Laguerre diagram corresponds to a Voronoi diagram where the location of the cells faces is constrained by a given non-intersecting spherical packing.

Furthermore, an optimization method used to eliminate any local decorrelation between the size of the spherical particles and the size of the corresponding Laguerre cells is introduced. This method, which is a variant of the so-called "Laplacian Smoothing" (LS) algorithm [38] and detailed in section 2.3.2, is dedicated to equiaxial cellular modelling and referred to as "Grain Optimization Algorithm" (GOA).

This chapter is divided into three major parts. The first part considers sphere packing. We will begin by presenting a general overview of existing methods to fill a domain with particles detailing the dynamic and constructive techniques. Afterwards, the Inwards Packing Method, used in this work, is analyzed by detailing all the steps of its algorithm and some results are shown. Finally, since this method has the disadvantage of generating local voids, an optimization technique based on dropping and rolling is introduced. The second part considers polyhedral microstructure generation where we detail the VTM and the LTM. Also the GOA, which is the method used to eliminate any local decorrelation between the size of the spherical particles and the size of the corresponding Laguerre cells,

is introduced. The third part explains the extension of our methods to generate semi-solid granular structures, foams and disordered fiber arrays.

## 2.2 Sphere packing

As mentioned in the introduction of this chapter, the geometrical modelling of powders or equiaxial grains is similar to the sphere (disc) packing problem. This topic generally concerns the mathematical study of disjoint spheres (discs) which fill a given domain. A typical sphere (disc) packing problem is to determine the repartition of the particles which maximizes the density in the domain. This density depends mainly on the particle size distribution and on their repartition in the domain to fill. Theoretically, it is not possible to predefine the maximal density if the distribution is heterogeneous.

On the other hand, in the two dimensional Euclidean space Carl Friedrich Gauss proved that the regular arrangement of discs with the highest density is the hexagonal packing arrangement, in which the centers of the discs are arranged in a hexagonal lattice, and each disc is surrounded by 6 other discs (see Figure 2.1.a). The density of this arrangement is  $\frac{\pi}{2\sqrt{3}} \simeq 0.9069$ . In 1940 Hungarian mathematician László Fejes Tóth proved that the hexagonal lattice is the densest of all possible disc packing, both regular and irregular. In the three dimensional Euclidean space Johannes Kepler had conjectured, in 1611, that the maximum possible density for both regular and irregular arrangements corresponds to the cubic close packing arrangement (see Figure 2.1.b) with a maximal density of  $\frac{\pi}{\sqrt{18}} \simeq 0.74048$ . This was demonstrated by Hales and Ferguson in 1998 [97, 98] following the approach suggested by László Fejes Tóth.

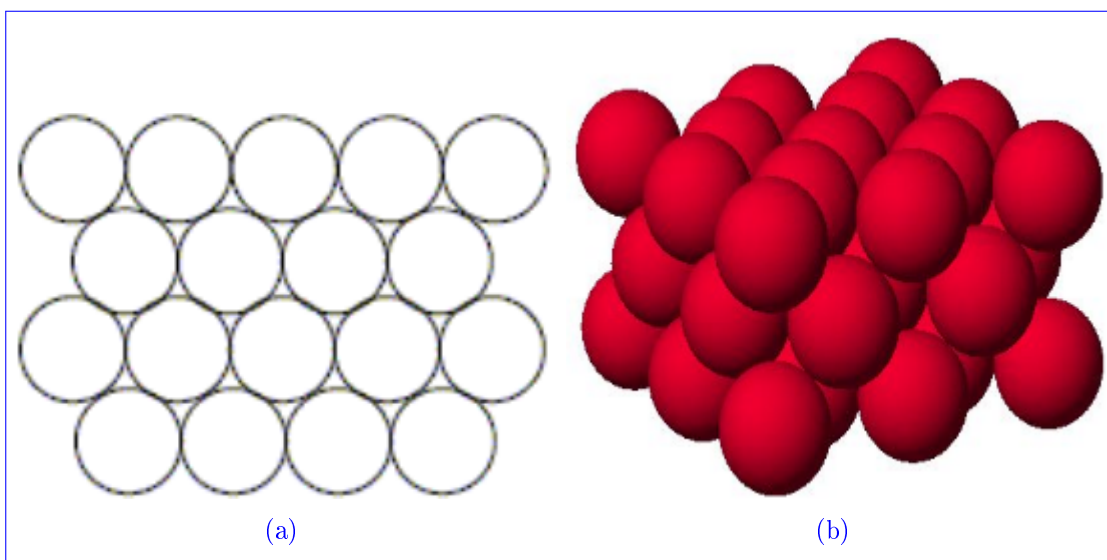


*Figure 2.1: (a) A hexagonal lattice and (b) the cubic close packing arrangement*

Note that the maximal density value in 3D, given above, concerns regular arrangements only (especially when the number of particles tends to infinity). For irregular

arrangements of equal spheres in 3D, the highest density traditionally reported is about 0.64, which corresponds to the random close packing configuration [99]. In practice, the efficiency of a filling algorithm to generate structures with high densities, in the general case where the particles have different sizes, is measured by considering it in the particular case of monosized particles, such that the density of the generated structure can be compared with the values 0.64 in 3D and 0.9069 in 2D.

The following two sections present a brief overview of some existing approaches to fill a domain with particles in two and three dimensions. These methods can generally be classified into two major families: dynamic techniques and constructive techniques.

### 2.2.1 Dynamic techniques

The dynamic methods are based on the motion and/or the resizing of the particles. The movements of these particles can be calculated either by purely geometric models or by dynamic models, where each particle has one or more physical properties allowing it to find an equilibrium position depending on its interactions with the other particles. Usually, the dynamic methods are very expensive in terms of computing times, because the position and/or the size of each particle are modified during the whole filling process.

A first technique, called “isotropic compression”, consists in iteratively moving the particles, by compressing the domain in an isotropic manner [100]. Most precisely, it consists in creating a virtual domain (much bigger than the real one) where the particles are put. At first, these particles have a large space between them. Then, the borders of this domain converge in an isotropic way to the real domain while controlling the intersections between the particles. This method is time consuming because the particles are moved continuously and the domain’s size changes at each step. And also high densities can not be obtained because particles are put randomly in the domain without finding their optimal position. Figure 2.2 illustrates the steps of this method in a two dimensional case.

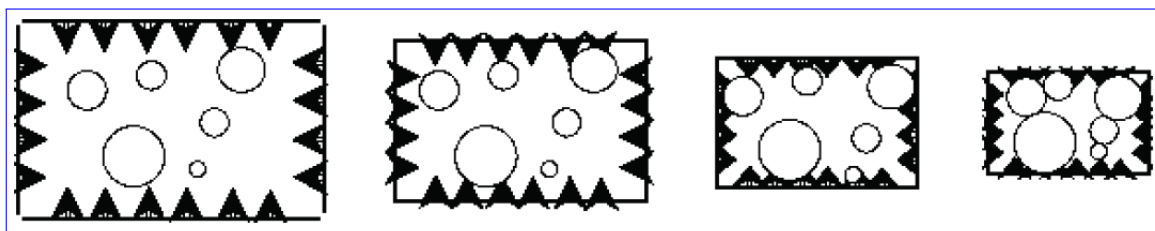


*Figure 2.2: A 2D illustration of the “isotropic compression” method*

A second technique could be considered as the opposite of the first. It is called “particle expansion” [101]. In fact, instead of changing the size of the domain, the size of the particles is modified. First a wanted number of particles is put in the domain with radii smaller than the ones wanted. Then, the size of these particles are increased progressively till the wanted density is obtained (see Figure 2.3). This method does not reach high

densities because of the un-optimal initial positioning of the particles. Furthermore, following a specific size distribution is not straightforward.

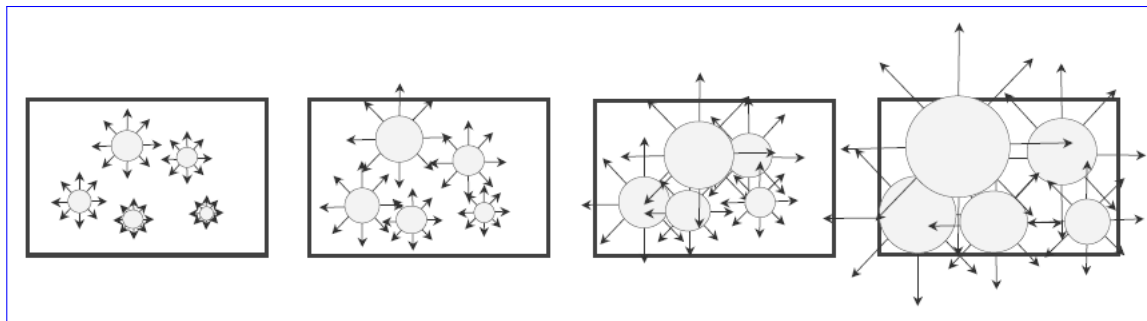


*Figure 2.3: The “particle expansion” method in 2D*

A third technique, called “collective rearrangement” [92] consists on randomly generating the wanted particles inside the domain. To this point, intersections between particles is permitted. Then these particles are moved and/or shrunk to eliminate the intersections. This method was used to create suspensions of particles (spherical and/or fibrous) in 2D and 3D [31]. Figure 2.4 illustrates this method in a two dimensional case. This method needs a considerable calculation time because the size of the particles is modified throughout the process and intersections between particles may persist if a size distribution is imposed.

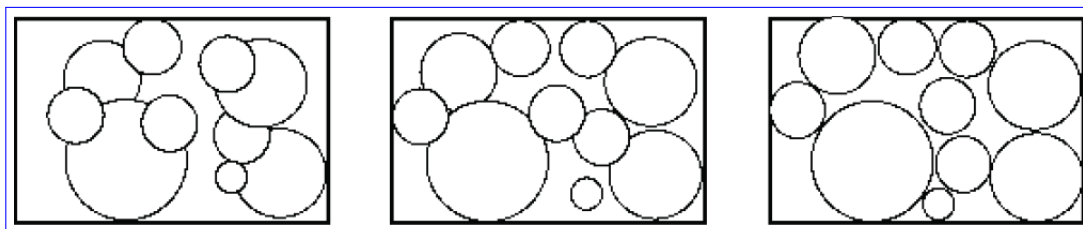


*Figure 2.4: The steps of the “collective rearrangement” method in 2D*

### 2.2.2 Constructive techniques

In the constructive techniques, the calculations are purely geometric, and the position and often the size of each particle are kept throughout the filling process. Hence, these methods are relatively fast and tend to respect size distribution laws. In many contexts, the constructive techniques may be considered as an advantageous alternative solution compared with the dynamic ones.

A first constructive technique is the “sequential inhibition” [102]. The radii of the particles are chosen according to a size distribution law, then the positions are proposed

randomly. When a new particle intersects an existing one, its position is rejected and another position is proposed maintaining the same radius (see Figure 2.5). This method was used in this manuscript to generate the spherical particles shown in figure 4.11 of section 4.2.5.1. It is very easy to implement, but its “trial and error” character makes it unusable for achieving moderate and high packing densities.

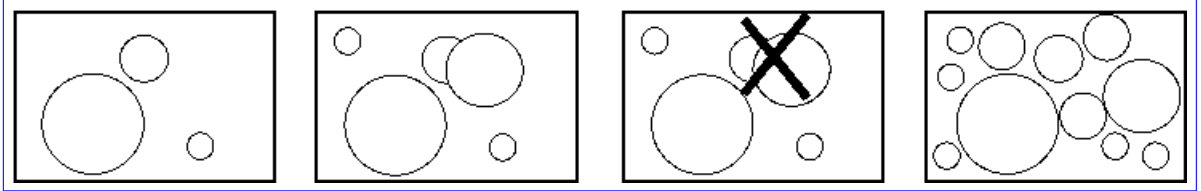


*Figure 2.5: Illustration of the “sequential inhibition” method*

A second technique [103] is a triangulation based approach. First, a triangulation based on the elements’ quality is built. Second, the incircles (inspheres) of the triangles (tetrahedra) of this triangulation are deduced. Third, spherical particles are added on the vertices of the triangulation to increase the density (see Figure 2.6). This method needs pre-constructions, generates low densities and does not respect complex size distributions.

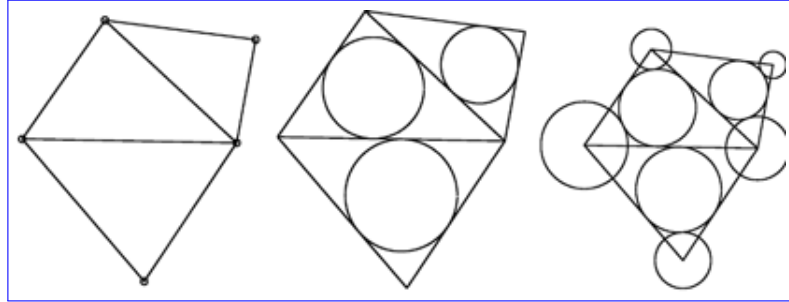


*Figure 2.6: Illustration of the triangulation method*

A third technique is the one proposed in [104, 105] where the filling process starts by randomly generating the desired number of particles (initially the size of each particle is 0) and then calculating the size of each particle (see Figure 2.7) either as half of the distance from its center to the center of its closest particle [105] or progressively enlarging each particle until it comes in contact with another particle [104]. These methods are easy to implement but they are not capable of following distribution laws nor in obtaining high packing densities.

A fourth technique, uses the concept of “dropping and rolling” [22, 23, 40] where each particle is dropped till it reaches another particle or the bottom of the domain. Then it is rolled till it is in contact with a third particle. The “rolling” is a recursive process until an equilibrium state is obtained (see Figure 2.8). This method is time consuming since small

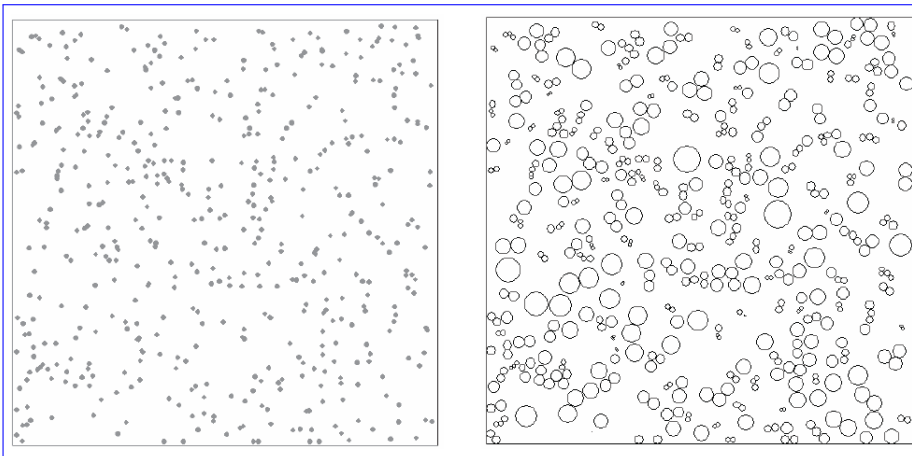


Figure 2.7: Illustration of the method proposed in [105]

dropping and rolling steps are used to reach the stable position but has the capability of respecting complex distribution laws and can reach high densities in 2D and 3D. A new variant of the classical “dropping and rolling” method will be detailed in section 2.2.5 as it is going to be used in our developments.

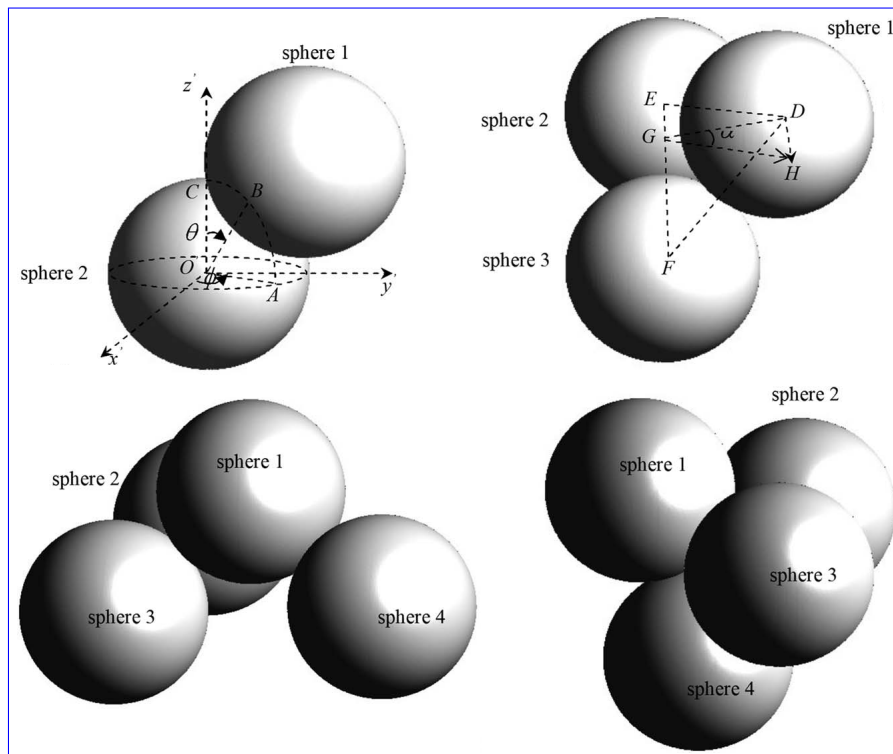
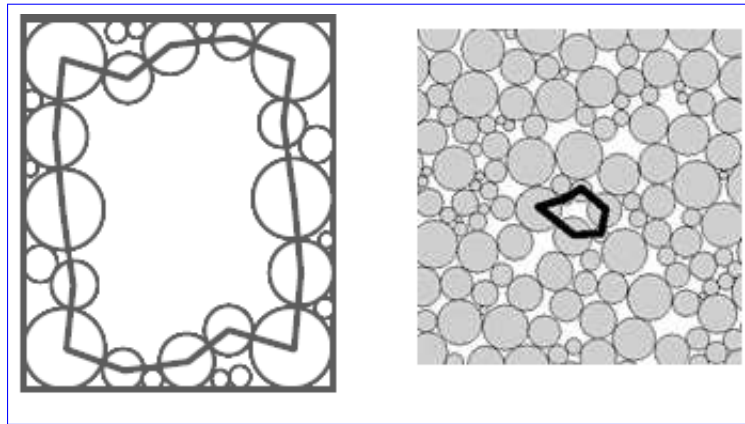


Figure 2.8: Illustration of the classical “dropping and rolling” method [23]

### 2.2.3 The method used

A detailed analysis of the classical methods cited above reveals that they present certain limitations. Some of them are fast and very easy to implement like the “sequential inhibition” [102] or the methods used in [104, 105] but they generate low packing densities and/or do not to respect a size distribution law. Others need pre-conditioning [101], pre-constructions [103] or require a considerable calculation time [31, 92].

As one of our goals is the creation of a multi-physical microstructure builder which generates spherical particles and polyhedra with high sphere packing densities and with respect of size distribution laws, we were interested by more complex constructive techniques such as one advancing-front method (AFM) (see Figure 2.9), the so-called “Inwards Packing Method” (IPM). This method consists in constructing a first initial front tangent to the domain boundary then progressively moving this front towards the center of the domain while filling it. It was introduced by Bagi [24] in 2D, modified and extended to 3D, by Benabbou [25, 34] and used as the sphere packing method of this work.



*Figure 2.9: Illustration of the “Advancing-front Method”*

This method is relatively fast, easy to implement and generates high densities especially in 2D. But, in 3D, it is limited to moderated densities (about 0.5) when it comes to generating poly-disperse spheres. And, based on an advancing-front approach, traditionally used in mesh generation, the spherical particles generated by this method present heterogeneities for the local density (voids can be seen, especially when mono-sized discs are generated, see Figure 2.10). This weakness is a general trend of advancing front methods and can lead to local sphere density heterogeneities and unrealistic particle positioning when modelling powder RVEs for example. Furthermore, it can affect the modelling of equiaxial polyhedral structures since the size of a polyhedral is approached by the size of spherical particle included within and these local voids would enhance the difference between the sizes of these geometries.

In the following sections, we present a detailed algorithm of this method in 2D and 3D and we introduce a technique to optimize the local voids encountered using the IPM.

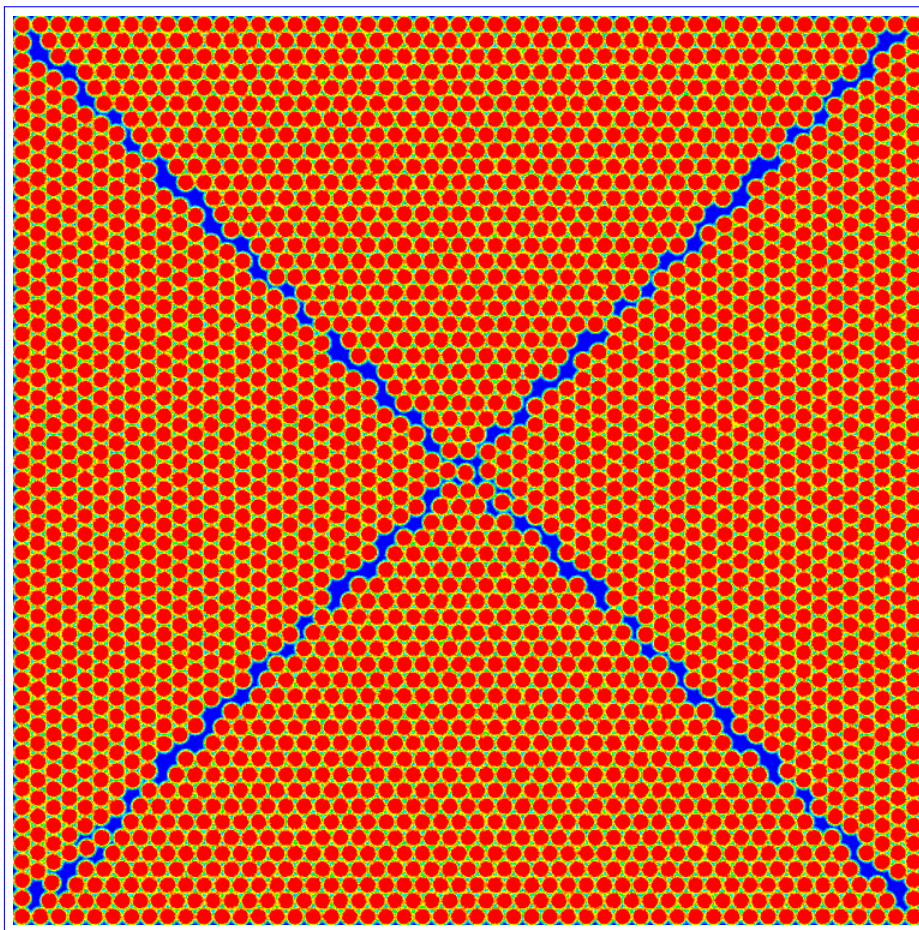


*Figure 2.10: Mono-sized generated discs in a unit square by the IPM. 2789 discs of radius 0.01 are generated. The density is equal to 0.876*

### 2.2.3.1 Scheme of the algorithm

We remind here that our aim is not to construct a triangulation of a certain domain using an advancing-front approach, but to generate spherical particles in a rectangular domain that follow a specific size distribution law. So, the advancing-front approach is only used to propose the positions of the new particles (discs or spheres). For this reason, we are not going to deal with the advancing-front approach in the context of mesh generation and we send the reader to [51] for more details.

In an analogy between the meshing advancing-front approach and the sphere packing algorithm of Benabbou [34], a node of the mesh becomes the center of a particle in the geometrical modelling. The size of these particles are defined using the specified size distribution law.

There are front elements and mesh elements. The front elements (segments in 2D and triangles in 3D) are entities of dimension  $d - 1$ , where  $d$  is the dimension of the considered

space (2 or 3). The mesh elements (triangles in 2D and tetrahedra in 3D) are entities of dimension  $d$ . Since the goal is not to generate a mesh, we are not concerned with the mesh elements themselves. In this method, the idea is to use the advancing-front approach, which allows us to propose the positions of the new particles using the front elements. Note that intersections between front elements are not controlled and they may occur in this case. Only intersections between particles are controlled and not allowed. In the algorithm written and detailed in [38, 25, 34], a localization grid made of squares (cubes in 3D) is used to control the validity of a new particle. Actually, when the position of a new particle is proposed, the square (cube) containing its center is localized and intersection tests are carried out with the particles whose centers are contained in the same square (cube) and in its 8 nearest neighboring squares (26 neighboring cubes). As the validity of a new particle is not obtained by a global comparison with all the existing particles, this method reduces the computing time. But since a smaller number of microstructural heterogeneities (particles or cells) than the ones generated in [25, 34, 38] can be immersed in the FE mesh and used for the mechanical applications (which is the main objective of this work), this technique was not implemented in CimLib. More precisely, in the context of this work, the sphere packing itself is sequential and the volume immersion is parallel hence a study of the computational time for the whole process will be performed in chapter 4 for a reasonable number of particles/cells.

In the case of the IPM, a front element is a segment (triangle) connecting the centers of two discs (three spheres). A disc (sphere) is the association of a center position and a radius defined according to a size distribution law. The position of each disc (sphere) is determined using an element of the front in such a way as to maximize the local density with the discs (spheres) of this front element. The position of a new particle (sphere or disc) is valid if this particle does not overlap the existing particles and if it is completely contained in the domain (see Figure 2.11a). To make this advancing-front method convergent, the front level concept was introduced [34]. Indeed, the level of a front is defined by the level of its first active element. The level of an element is defined by the sum of the levels of its particles (spheres or discs). The particles level ranges from 0 (the level of the initial front particles) to a level  $n$  corresponding to the level of the last front particles (see Figure 2.11b). The level of a new particle (detailed in section 2.2.3.2) is a function of the levels of the particles of the front element used to insert this new particle. For the convergence of the method, the following two conditions must be satisfied: (a) a new particle's level is at least equal to the minimum of the levels of the particles of the front element used to insert this new particle, and (b) the filling using the elements of a front with a level  $l$  is initiated only when the fronts with levels less than  $l$  are completely saturated.

The algorithm of the IPM [34] can be described by the following items:

**IPM.1** Create an initial front defined by a chain of tangent discs.

**IPM.2** While the front still contains active elements, do:

- (a) Generate a random radius according to the size distribution law.

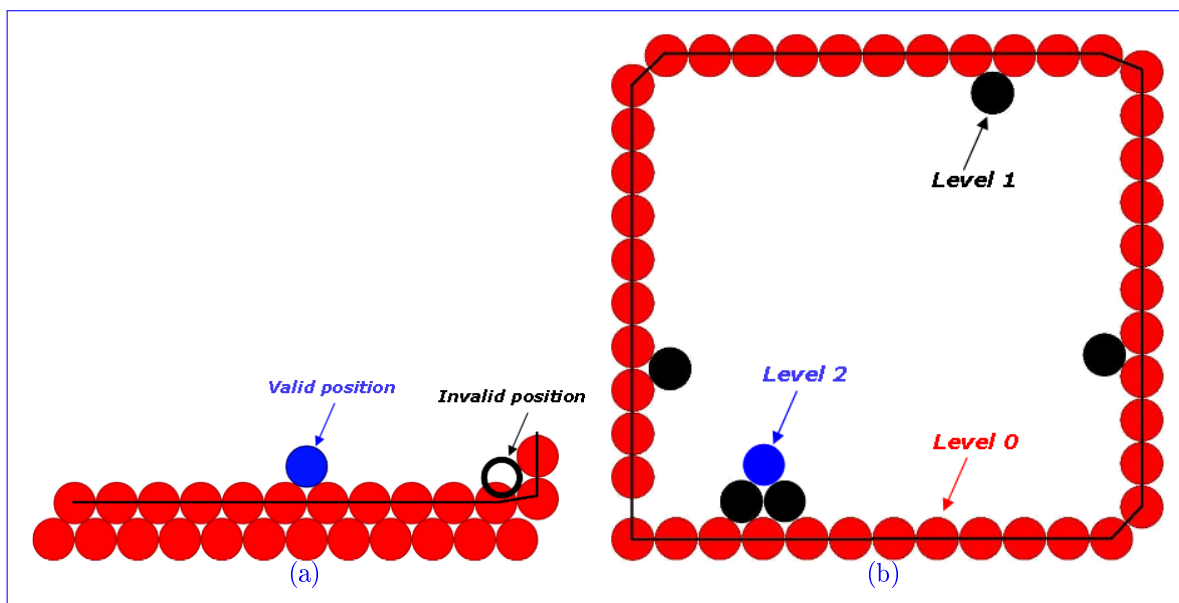


Figure 2.11: (a) The validity control in the IPM and (b) the first three levels in the filling process

- (b) Determine the level  $l$  of the front which is equal to the level of its first active element.
- (c) For the front of level  $l$ , do:
- i. Select an active element  $e$  if its level  $l_e \leq l$
  - ii. Define the position of  $P_{new}$ : tangent to the particles of  $e$ .
  - iii. Control the validity of  $P_{new}$ : no intersections with the existing particles.
  - iv. If  $P_{new}$  is valid:
    - Delete  $e$ .
    - Connect  $P_{new}$  to the particles of  $e$ . This connection will create new front elements (two in 2D and three in 3D) with a level at least equal to  $l_e$ .
    - Go to (a).
  - v. If  $P_{new}$  is not valid:
    - If there are active elements not yet tested to generate  $P_{new}$ , with a level less than or equal to  $l$  then select the first of these elements and go to ii.
    - If all the active elements with a level less than or equal to  $l$  have been tested to place  $P_{new}$  without success, then:
      - Deactivate the first active element  $e_f$  in the front (with level  $l$ ).
      - Determine the existing particle which maximizes the local density with the particles of  $e_f$ .
      - For each set  $s$  containing  $d - 1$  particles of  $e_f$ , where  $d$  is the space dimension, do: connect the determined particle to the particles of  $s$  if they

are not already connected and if the level of the resulting new front element is greater than  $l$  in the 3D case (in the 2D case it can be less than or equal to  $l$ ). Go to (b).

(d) End do.

End while.

In the first step, an initial front is created by connecting the particles, which are placed on the interior side of the domain boundary. Then, the filling is made by an inwards spreading of the front. Figures 2.12 and 2.13 show illustrations of the IPM in a polydisperse 2D and a polydisperse 3D case respectively.

### 2.2.3.2 Detailed analysis of the algorithm

**Creation of the initial front:** The first step is the creation of an initial front made up of a set of particles tangent to each other and to the domain's boundary. In the 2D case, each disc of the initial front is in contact with the domain boundary as well as with two other discs of this front. These discs are placed anticlockwise so that the segments of the initial front, where each segment connects the centers of two consecutive discs, are oriented with a normal vector directed toward the interior of the domain. We begin by placing the first disc at the bottom left corner of the domain with coordinates equal to the chosen radius. Then, depending on our position in the domain, the coordinates of a new disc are calculated in function of the previous one. For example, we want to place a new disc with radius  $R_{new}$  at the bottom of the domain. Its coordinates will be defined as:

$$\begin{cases} x_{new} = x_{previous} + 2\sqrt{R_{previous} \cdot R_{new}} \\ y_{new} = R_{new} \end{cases} \quad (2.1)$$

This new position will be accepted if and only if  $x_{new} + R_{new} \leq x_{max}$  with  $x_{max}$  the x-upper boundary of the (x,y)-rectangular domain (see upper-left image of Figure 2.12).

In the 3D case, the initial front is a set of triangles, where the vertices of each triangle are the centers of three spheres tangent to the planes of the domain's boundary. To generate these triangles, and then the initial front in the 3D case, two steps are needed. Firstly, an initial front of each plane of the domain's boundary is constructed similarly to the 2D case. The initial front is then a set of oriented segments, where each segment connects the centers of two consecutive spheres tangent to 2 or 3 planes of the domain's boundary and to each other (see upper-left image of Figure 2.13).

Secondly, to construct the global initial front which is a set of triangles, the 2D filling process is applied to each plane of the domain's boundary. Indeed, the filling of a plane in 3D is similar to the filling of a rectangular domain in 2D, with the particularity that the center of each particle is not in the plane, but to a distance equal to its radius. So, the local initial front of each plane which is a set of segments is used to apply the 2D filling process and hence constructing the global initial front (see Figure 2.14).

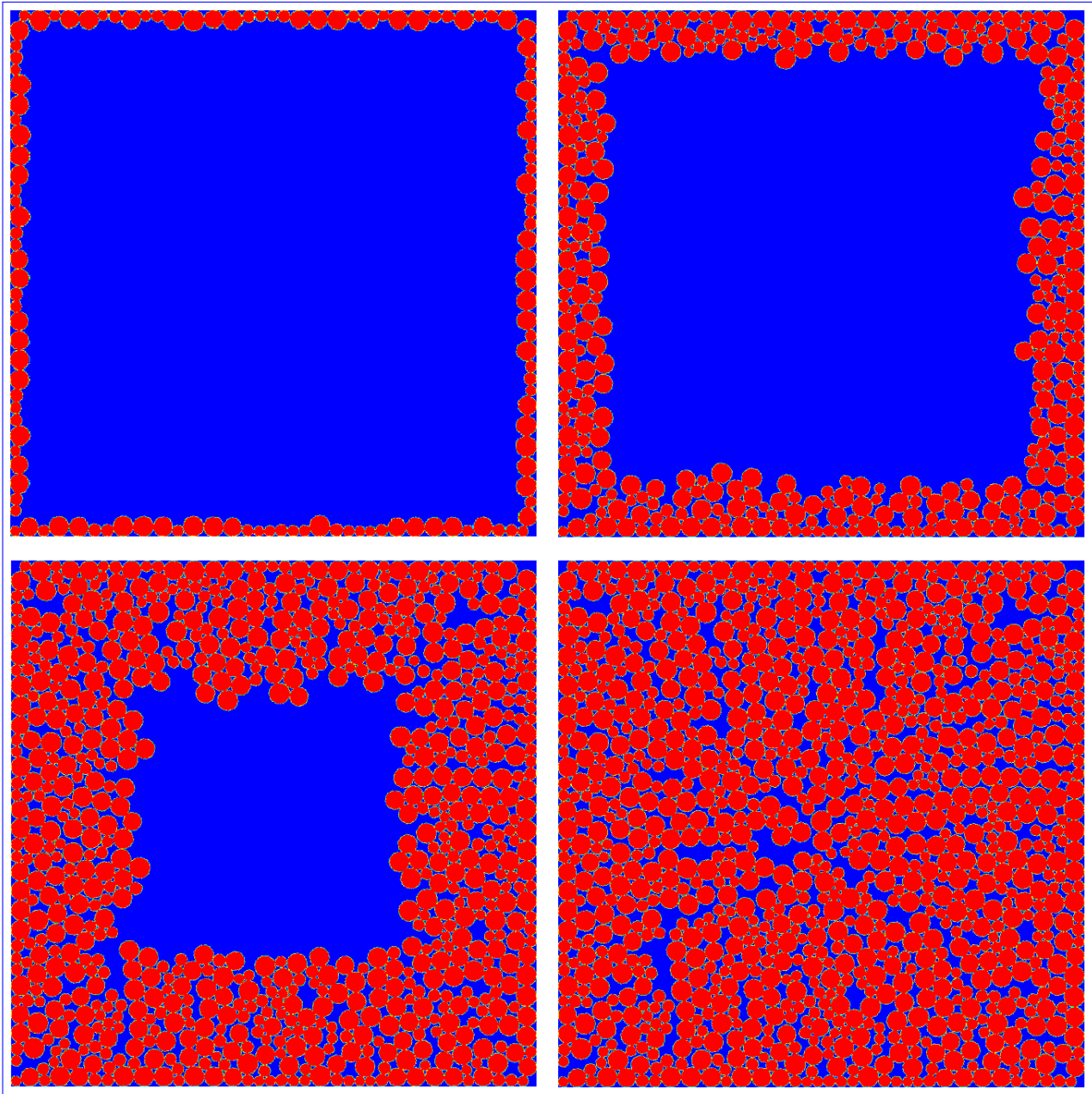


*Figure 2.12: A 2D illustration of the IPM: creation of the initial front (upper left), the beginning of the filling process (upper right) and the convergence towards the center of the domain (lower figures)*

**Radii generation:** Each new generated particle must have a radius randomly chosen according to the specified size distribution law.

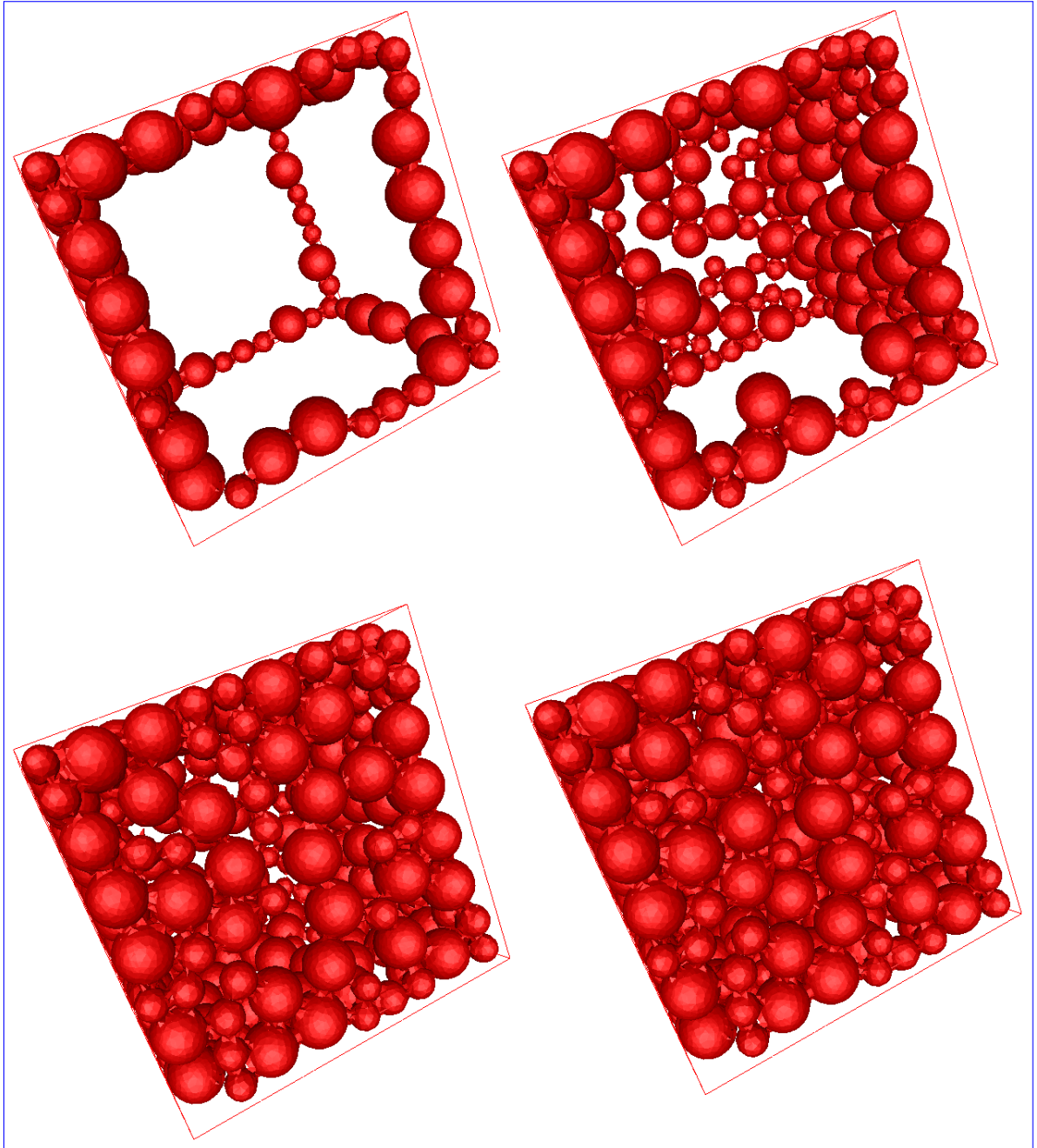


*Figure 2.13: A 3D illustration of the IPM: the first step of the creation of the initial front (upper left), the face filling process which is the 2D IPM (upper right and lower left) and the domain filling (lower right)*

**Selection of a front element:** An element (triangle in 3D and segment in 2D) can be selected only if it is active and its level is less than or equal to the level of the current front. An element is said to be active if it has not been deleted from the front, either

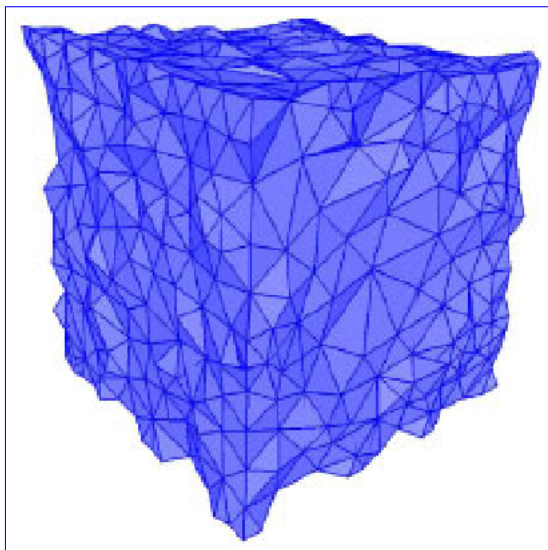


Figure 2.14: Example of a global initial front in 3D [38]

because it has been used to insert a new particle or because it has been the first active element of a front in the case where no element of this front could insert the new particle. The level of an element is the sum of the levels of its particles and the level of the front is determined by its first active element. For efficiency, a third constraint is taken into account to select an active element in the current front. Indeed, let  $R$  be the chosen radius. An active element whose level is less than or equal to the level of the current front is selected only if it has not been tested, with failure, to place a particle with a radius less than or equal to  $R$  (otherwise, this element obviously cannot place this new particle). Thus, each element in the front is then associated with a radius  $R_e$  initiated by the value  $R_{max}$  (the greatest radius in the size distribution) and decreased as this element is tested to place particles with different radii.

**Calculation of a new particle's position:** For the calculation of a new particle's position, we used the same methods in [25] where the calculations in 2D and 3D were distinguished. In both cases, the new particle will be tangent to the particles of the selected front element, two discs in 2D and three spheres in 3D. In the 2D case, let  $e = (P_i, P_j)$  be the selected front element, a segment formed by the two discs with centers  $P_i$  and  $P_j$  with radii  $R_i$  and  $R_j$ , respectively. Let  $R$  be the radius of the new particle to be generated and let  $\vec{e}_n = (0, 0, 1)$  be the normal vector of the domain. A local basis  $B = (P_i, \vec{u}, \vec{v})$  centered in  $P_i$ , is constructed with:

$$\vec{u} = \frac{\overrightarrow{P_i P_j}}{\|\overrightarrow{P_i P_j}\|} \quad \text{and} \quad \vec{v} = \vec{e}_n \wedge \vec{u}, \quad (2.2)$$

with  $\|\overrightarrow{P_i P_j}\|$  the Euclidian norm of  $\overrightarrow{P_i P_j}$  and  $\wedge$  the cross product. In the new basis  $B$ , the

coordinates  $(u, v)$  of the new particle are:

$$\begin{cases} u = \frac{\|\overrightarrow{P_i P_j}\|}{2} + \frac{(R_i - R_j)(R_i + R_j + 2R)}{2\|\overrightarrow{P_i P_j}\|}, & v = \sqrt{(R_i + R)^2 - u^2} \quad \text{if } \|\overrightarrow{P_i P_j}\| \leq R_i + R_j + 2R \\ u = R_i + \frac{\|\overrightarrow{P_i P_j}\| - R_i - R_j}{2}, & v = 0 \quad \text{if } \|\overrightarrow{P_i P_j}\| > R_i + R_j + 2R \end{cases} \quad (2.3)$$

In the 3D case, let  $T = (P_i, P_j, P_k)$  be the selected front element, a triangle formed by the three spheres with centers  $P_i, P_j$  and  $P_k$  and radii  $R_i, R_j$  and  $R_k$  respectively and let  $R$  be the radius of the new particle to be generated. First, a local basis  $B = (P_i, \vec{u}, \vec{v}, \vec{w})$ , centered in  $P_i$  is constructed, where:

$$\vec{w} = \frac{\overrightarrow{P_i P_j} \times \overrightarrow{P_i P_k}}{\|\overrightarrow{P_i P_j} \times \overrightarrow{P_i P_k}\|}, \quad \vec{u} = \frac{\overrightarrow{P_i P_j}}{\|\overrightarrow{P_i P_j}\|} \quad \text{and} \quad \vec{v} = \vec{w} \wedge \vec{u}, \quad (2.4)$$

The coordinates  $(u, v)$  of the new particle, in the plane of the triangle  $T$ , are calculated using the system:

$$\begin{cases} 2uu_j = (R_i - R_j)(R_i + R_j + 2R) + u_j^2 \\ 2uu_k + 2v.v_k = (R_i - R_k)(R_i + R_k + 2R) + u_k^2 + v_k^2 \end{cases} \quad (2.5)$$

where  $u_j = \overrightarrow{P_i P_j} \cdot \vec{u}$ ,  $u_k = \overrightarrow{P_i P_k} \cdot \vec{u}$  and  $v_k = \overrightarrow{P_i P_k} \cdot \vec{v}$ . Hence, the coordinate  $w$  of the new particle is given by:

$$w = \sqrt{(R_i + R)^2 - u^2 - v^2} \quad \text{if } (R_i + R)^2 \geq u^2 + v^2. \quad (2.6)$$

In the case where  $(R_i + R)^2 < u^2 + v^2$ , the new particle is not placed using the selected front element and there are two possible configurations:

- If there are still some active elements, which have not been tested yet to place the new particle, then the first of these elements is selected and the algorithm resumes.
- If all the elements of the current front have been tested to place the new particle, without succeeding, then the selected front element is necessarily the first active element in the current front. In this case, among the three segments  $(P_i, P_j)$ ,  $(P_i, P_k)$  and  $(P_k, P_j)$ , the segment  $(P_1, P_2)$  maximizing the quantity  $\|\overrightarrow{P_1 P_2}\| - R_1 - R_2$ , where  $R_1$  and  $R_2$  are the radii of  $P_1$  and  $P_2$  respectively, is selected. Then the new particle is placed using the selected segment  $(P_1, P_2)$ . Indeed, a new local basis  $B = (P_1, \vec{u}, \vec{v}, \vec{e}_n)$  is built, where:

$$\vec{u} = \frac{\overrightarrow{P_1 P_2}}{\|\overrightarrow{P_1 P_2}\|}, \quad \vec{e}_n = \vec{v} \quad \text{and} \quad \vec{v} = \vec{e}_n \wedge \vec{u}. \quad (2.7)$$

Then the coordinates  $(u, v, w)$  of the new particle, in the new local basis, are:

$$\begin{cases} u = \frac{\|\overrightarrow{P_1 P_2}\|}{2} + \frac{(R_1 - R_2)(R_1 + R_2 + 2R)}{2\|\overrightarrow{P_1 P_2}\|}, & v = \sqrt{(R_1 + R)^2 - u^2}, \\ w = 0 & \text{if } \|\overrightarrow{P_1 P_2}\| \leq R_1 + R_2 + 2R \\ u = R_1 + R, \quad v = 0, \quad w = 0 & \text{if } \|\overrightarrow{P_1 P_2}\| > R_1 + R_2 + 2R \end{cases} \quad (2.8)$$

**The validity control:** To be accepted, the new particle must not overlap any of the existing particles. Thus, the control of the validity of the new particle is realized by checking its possible intersections with the existing particles. Two cases exist.

First case: the new particle is valid. This case corresponds to the situation where the new particle does not intersect any of the existing particles. In this case, a level is assigned to the new particle, the front element used to place it is deleted and new front elements are created. The level  $l_p$  of the new particle  $P$  is calculated by

$$l_p = \min_i(l_i) + \max(1, \max_i(l_i) - \min_i(l_i)), \quad (2.9)$$

where  $l_i$  are the levels of the particles of the front element used to place the new particle  $P$ . The elements of the initial front are made up of particles with level 0 and are oriented so that the filling remains directed inwards to the domain. To maintain this orientation, the front elements are written using a certain convention. Indeed, if the used front element is written  $(P_1, P_2)$  (respectively  $(P_1, P_2, P_3)$  in 3D) then the two (three) new front elements are written  $(P_1, P)$  and  $(P, P_2)$  (respectively  $(P, P_1, P_2)$ ,  $(P, P_2, P_3)$  and  $(P, P_3, P_1)$ ).

Second case: the new particle is rejected. In this case, there are two situations. The first situation is when there are active elements in the front with levels less than or equal to the level of the current front, associated with radii greater than the new particle radius. In this situation, the first of these elements is selected and the algorithm resumes. The second situation is when the active elements of the front are either with levels greater than the level of the current front or/and associated with radii less than or equal to the new particle radius. In this situation, all the existing particles which are in conflict with the new particle, when the first active element in the current front is used to place this new particle, are detected. Among these conflicting particles  $P_k$ , the particle  $P_e$ , which maximizes the local density with the particles of the first active element in the current front is selected. To maximize the local density with the first active element particles, the selected particle must minimize the function  $\sum_i [d(P_i, P_k) - R_k - R_i]$ , where  $d$  is the Euclidean distance between  $P_i$  and  $P_k$ ,  $P_i$  are the centers of the particles (with radii  $R_i$ ) of the first active element in the current front and  $P_k$  is the center of a conflicting particle with radius  $R_k$ . Then, the first active element  $e_f$  with level  $l_f$  is deleted from the front and new elements are possibly created. Indeed, let  $s$  be a subset of  $e_f$  containing  $n - 1$  particles of  $e_f$ , where  $n$  is the number of  $e_f$  particles (three in 3D and two in 2D). For each subset  $s$ , we check if the particle  $P_e$  is already connected with its particles. If the particle  $P_e$  is not connected with the particles of  $s$  then a new front element is created by connecting  $P_e$  to the particle of  $s$  with a condition that its level is greater than  $l_f$  in the 3D case. The level  $l$  of this new front element is calculated by  $l = l_e + \sum_i l_i$ , where  $l_e$  is

the level of  $P_e$  and  $l_i$  are the levels of the particles of  $s$ . The condition  $l > l_f$ , in the 3D case, is crucial for the convergence of the algorithm [34].

### 2.2.4 Some results

Figure 2.15 shows discs and spheres generated by the IPM in a unit square and a unit cube respectively with radii chosen according to the uniform distribution law  $U[0.02; 0.06]$ .

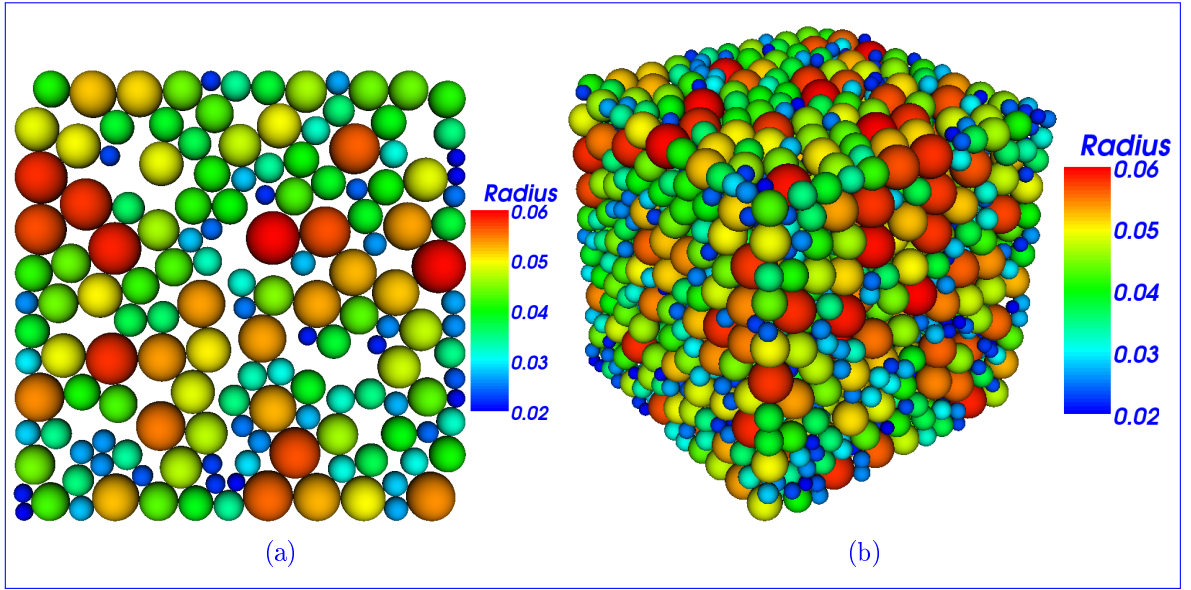


Figure 2.15: (a) 150 discs with a density of 0.76 and radii chosen by  $U[0.02; 0.06]$  and (b) 1951 spheres with a density of 0.475 and radii chosen by  $U[0.02; 0.06]$

Furthermore, the Box-Muller algorithm [106] is used to generate random numbers following a normal (the lognormal is implied) distribution law. Figure 2.16a shows discs generated by the IPM in a  $4 \times 4$  square with radii chosen using a Gaussian distribution law with mean  $\mu = 0.04$  and standard deviation  $\sigma = 0.01$  and Figure 2.16b illustrates a comparison between the density function obtained and the density function of  $N(\mu, \sigma^2)$ . To avoid unphysical results or large disc surface dispersal, a cut-off of 0.075 for disc radius was chosen.

Figure 2.17 illustrates discs generated by the IPM in a unit square with radii chosen by a histogram distribution law and a comparison between the probabilities wanted and obtained.

It is noticed from figures 2.16b and 2.17b that we are close to the exact solution but we do not coincide with it. This is due to the fact that the advancing front method privileges the generation of small particles when bigger ones are not generated. A study of convergence will be performed in the next chapter. Furthermore, Figures 2.15a, 2.16a and 2.17a show the obvious existence of local voids in the packings generating by the IPM. A solution for this weakness is proposed in the following section.

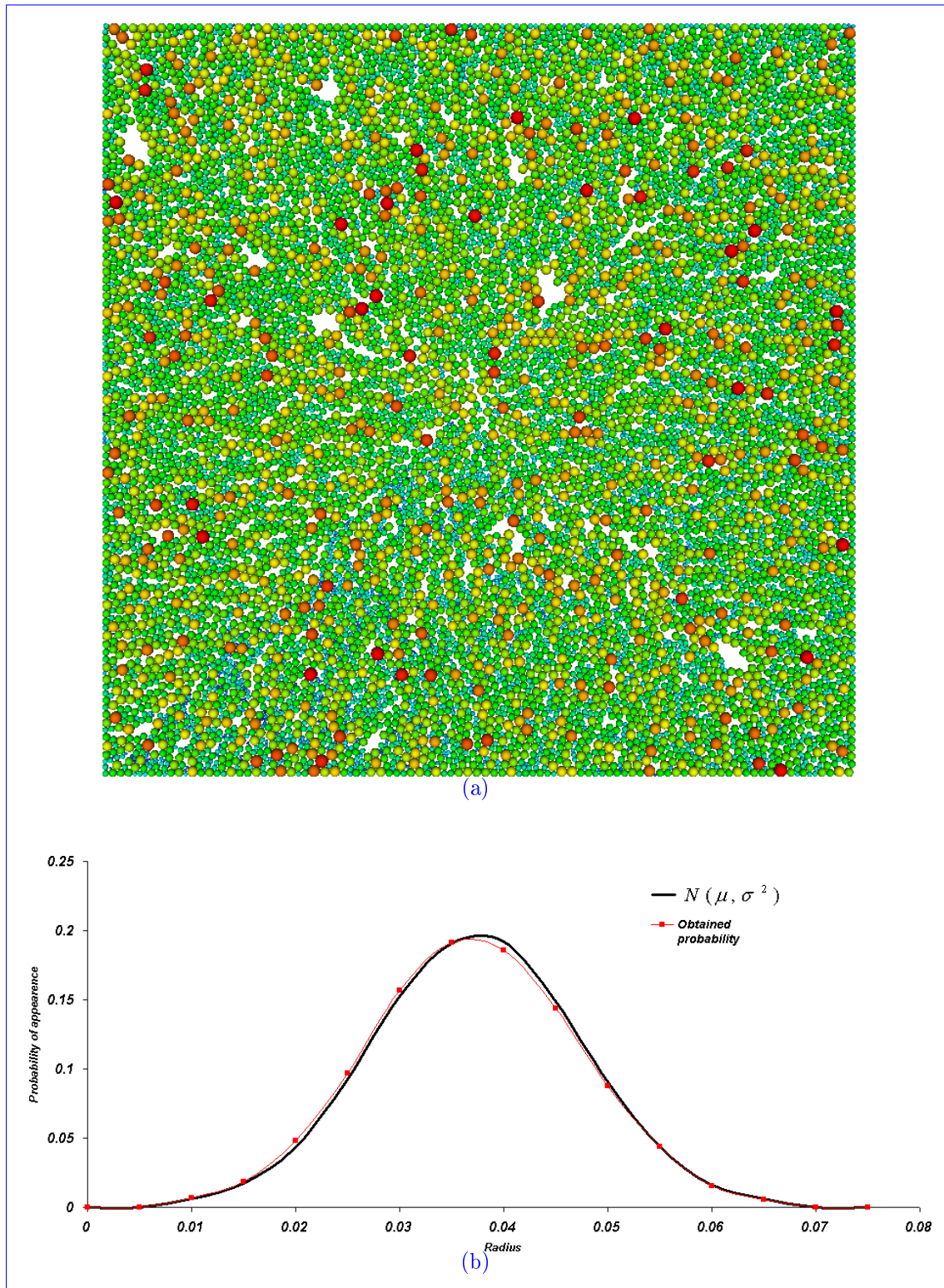


Figure 2.16: (a) 9703 discs with a density of 0.79 and (b) comparison between the density function obtained and the one of  $N(\mu, \sigma^2)$

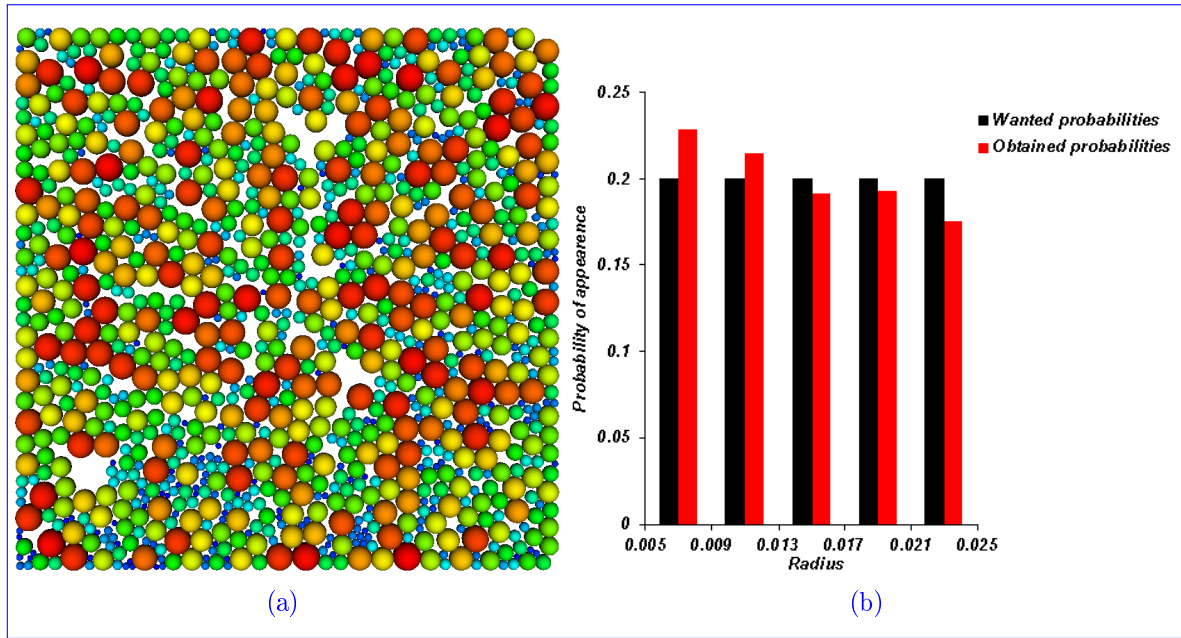


Figure 2.17: (a) 1034 discs with a density of 0.8 and (b) comparison between the wanted and obtained probabilities

### 2.2.5 The Powder Optimization Algorithm (POA)

As we have seen earlier in this chapter, the sphere packing generated by the IPM respects a given statistical size distribution and also reaches high densities. However, the resulting sphere packing can present heterogeneities for the local density (voids can be seen (see Figures 2.15a, 2.16a and 2.17a), especially when mono-sized discs are generated, as in Figure 2.10). Hence, the use of this method without any void optimization technique can not model realistic sphere packings in the sense that no stability conditions are imposed on the spheres. To overcome this weakness, a void optimization technique was developed. It is adapted to powder RVEs and based on the idea of enriching the IPM by a variant of the classical dropping and rolling method [22, 23, 40]. Further on, this technique is referred to as "Powder Optimization Algorithm" (POA). The POA has for goals the elimination of the voids created by the IPM and also the displacement of the un-physically positioned particles that are in suspension while conserving the advantages of the IPM (high global density and respect of the imposed size distribution). The advantage of our POA is that, unlike other dropping and rolling algorithms [22, 23, 40], we do not use tiny dropping or rolling steps in order to reach the desired positions but these positions are calculated analytically by mathematical and geometrical equations. Furthermore, our POA does not generate spherical particles, it displaces the un-physically positioned particles generated by the IPM. The procedure is detailed for 3D configurations and briefly described afterwards in a 2D context.

### 2.2.5.1 The three-dimensional POA

Figure 2.18 illustrates the flow chart of the classical dropping and rolling algorithms [22, 23, 40]. The basic idea is that each newly generated sphere would be firstly dropped till hitting another preexisting sphere or the floor. Afterwards, it is rolled till it is in contact with another sphere or the floor. Then, it is rolled on the two touched spheres till achieving a third hit with another sphere or the floor. Finally, the stability of the sphere is checked to see weather the rolling must continue or a new sphere can be generated. We notice from Figure 2.18 that tiny steps are used to displace the sphere. This way of performing the dropping and rolling can be very time consuming especially when small particles are used because the step size must less than the radius of the smallest particles. In the following, we explain our dropping and rolling techniques where the desired positions are calculated analytically.

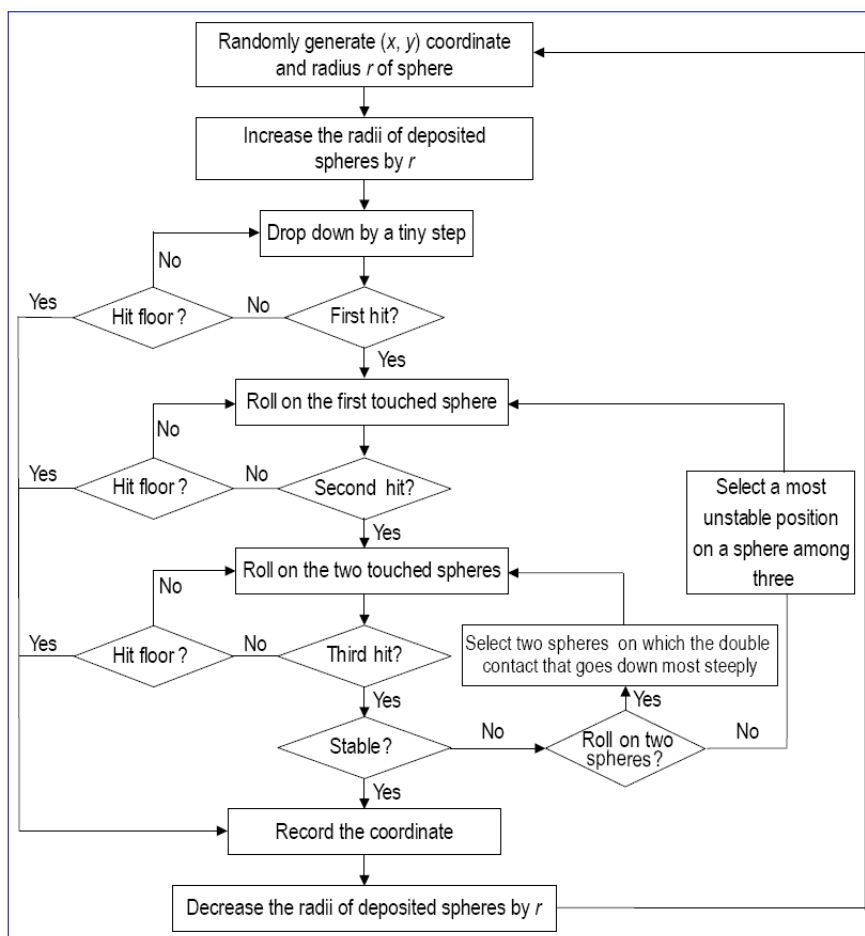


Figure 2.18: The flow chart of the classical dropping and rolling algorithms [22,23,40]

At first, the IPM is performed according to the imposed radius distribution and the sphere packing obtained, called SP, is sorted according to the dropping and rolling direc-

tion, from minimum to maximum. This direction will be denoted  $z$ . Then for all spheres  $S_i$ , of center  $c_i$  and radius  $r_i$ , the following algorithm is performed:

**1. Dropping:** In what follows, the superscripts 0, 1, 2 and 3 designate the initial, first, second and third position of  $c_i$  respectively. The sphere in question in its initial position is denoted  $S_1^0 = S(c_1^0, r_1)$  of center  $c_1^0(x_1^0, y_1^0, z_1^0)$  and radius  $r_1$ . If  $z_1^0 - r_1 = 0$ , the sphere is already at the bottom of the domain and its position is final. If not, let

$$E_0 = \{S(c(x, y, z), r) \in SP \setminus \{S_1^0\} / z < z_1^0 \quad \text{and} \quad (x_1^0 - x)^2 + (y_1^0 - y)^2 < (r_1 + r)^2\}. \quad (2.10)$$

Then we search for a  $S_2 \in E_0$  minimizing the function (see Figure 2.19a)

$$f_0(S) = \left( z_1^0 - z - \sqrt{(r_1 + r)^2 - ((x_1^0 - x)^2 + (y_1^0 - y)^2)} \right). \quad (2.11)$$

If  $S_2$  does not exist, it means that there is no spheres underneath the sphere  $S_1^0$  and its final position will be  $S_1^{final} = S(c_1^1(x_1^0, y_1^0, r_1), r_1)$ . Else, the position of  $c_1^0$  is updated by writing (see Figure 2.19b):

$$\begin{cases} z_1^1 = z_2 + \sqrt{(r_1 + r_2)^2 - ((x_1^0 - x_2)^2 + (y_1^0 - y_2)^2)} \\ y_1^1 = y_1^0 \\ x_1^1 = x_1^0 \\ S_1^1 = S(c_1^1(x_1^1, y_1^1, z_1^1), r_1) \end{cases} \quad (2.12)$$

Then, SP is updated.

**2. Determining  $\theta$  and  $\varphi$ :** The position of  $c_1^1$  can be written with the conventions of Figure 2.19b:

$$\begin{cases} x_1^1 = x_2 + (r_1 + r_2)\cos\varphi\cos\theta \\ y_1^1 = y_2 + (r_1 + r_2)\cos\varphi\sin\theta \\ z_1^1 = z_2 + (r_1 + r_2)\sin\varphi \end{cases} \quad (2.13)$$

With  $\theta \in [0, \Pi[$  and  $\varphi \in ]0, \Pi/2[$

Hence, by using the positive sign of  $\cos\varphi$  and system (2.13), we have:

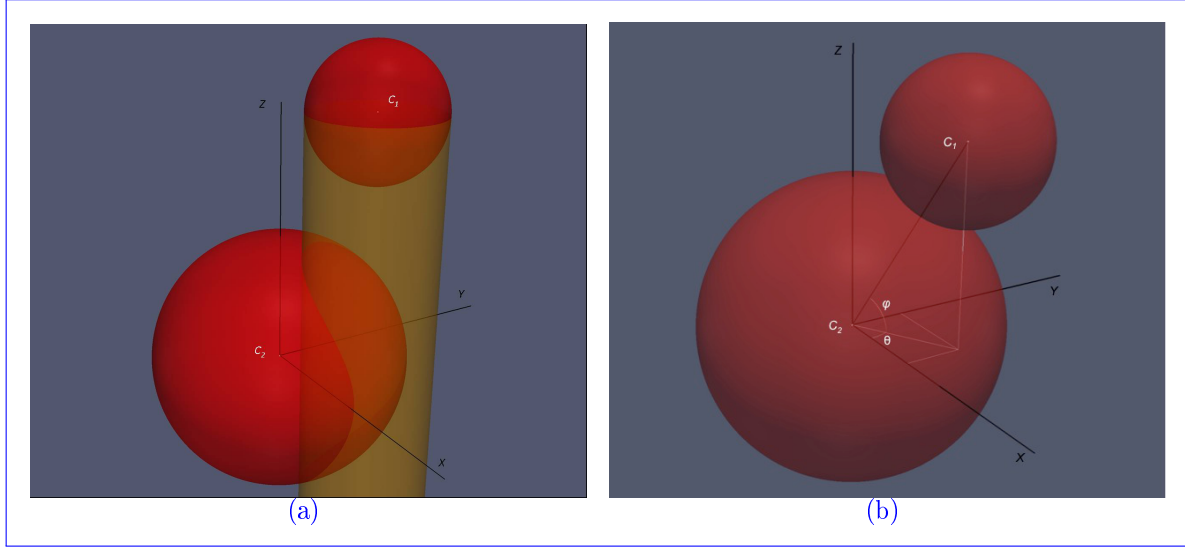


Figure 2.19: The dropping phase in the 3D POA: (a) the search for  $c_2$  and (b) the dropping of  $c_1$

$$\left\{ \begin{array}{l} \cos\varphi = \frac{\sqrt{(x_1^1 - x_2)^2 + (y_1^1 - y_2)^2}}{r_1 + r_2} \\ \sin\varphi = \frac{z_1^1 - z_2}{r_1 + r_2} \\ \cos\theta = \frac{x_1^1 - x_2}{\sqrt{(x_1^1 - x_2)^2 + (y_1^1 - y_2)^2}} \\ \sin\theta = \frac{y_1^1 - y_2}{\sqrt{(x_1^1 - x_2)^2 + (y_1^1 - y_2)^2}} \end{array} \right. \quad (2.14)$$

In the particular case where the sphere of center  $c_1^1$  is directly over the sphere of center  $c_2$  which leads to having  $\sqrt{(x_1^1 - x_2)^2 + (y_1^1 - y_2)^2} = 0$ , and undermines the non-uniqueness, the following strategy is adopted: if the sphere of center  $c_1^1$  is not tangent to any of the domain's faces,  $\theta$  is taken as null. In the other case,  $\theta$  is given particular values such that the rotation will be towards the interior of the domain to avoid intersecting the faces.

Furthermore, we denote  $B_0 = (\vec{u}_0, \vec{v}_0, \vec{w}_0)$  (see Figure 2.20a) the new working basis obtained by the rotation of angle  $\theta$  and axis  $z$  of the canonic basis  $(\vec{i}, \vec{j}, \vec{k})$ . We denote  $M_0$  the transformation matrix:

$$M_0 = \begin{pmatrix} \cos\theta & -\sin\theta & 0 \\ \sin\theta & \cos\theta & 0 \\ 0 & 0 & 1 \end{pmatrix} \quad (2.15)$$

The first rolling step is performed by updating the position of  $c_1^1$  by modifying the value of  $\varphi$  in the new basis.

**3. Rolling Phase 1.1:** First of all, we search for the spheres intersecting the fictitious sphere of center  $c_2$  and radius  $r_2 + 2r_1$ . So let  $E_1 = \{S(c, r) \in SP \setminus \{S_1^1, S_2\} / c_2c < r_2 + 2r_1 + r\}$ . If  $E_1 \neq \emptyset$ , for all the spheres  $S \in E_1$ , we search for the ones intersecting the fictitious torus of axis  $\overrightarrow{c_2c_1^1}$ , small radius  $r_1$  and big radius  $r_1 + r_2$  (see Figure 2.20a). The coordinates of  $c$  in the new basis  $B_0$ ,  $(\tilde{x}, \tilde{y}, \tilde{z})$ , are given by:

$$\overrightarrow{c_2c} = M_0^{-1} \overrightarrow{c_2\tilde{c}} \quad (2.16)$$

and its signed distance to the torus (with the convention of positive inside and negative outside),  $dist$ , is given by:

$$\begin{cases} d_1 = \sqrt{\tilde{x}^2 + \tilde{z}^2} - (r_1 + r_2) \\ d_2 = \sqrt{d_1^2 + \tilde{y}^2} \\ dist = r_1 - d_2 \end{cases} \quad (2.17)$$

Let  $E_2 = \{S \in E_1 / dist + r > 0\}$ . If  $E_1 = \emptyset$  or  $E_2 = \emptyset$ ,  $S_1^1$  is displaced until reaching the plane of equation  $z = z_2$  as described in Figure 2.20a. Most precisely, the new coordinates of  $c_1^1$  are obtained by taking  $\varphi = 0$  in Eqs.(2.13):

$$\begin{cases} x_1^2 = x_2 + (r_1 + r_2)\cos\theta \\ y_1^2 = y_2 + (r_1 + r_2)\sin\theta \\ z_1^2 = z_2 \\ S_1^2 = S(c_1^2(x_1^2, y_1^2, z_1^2), r_1) \end{cases} \quad (2.18)$$

Under the condition that this new position does not intersect one the domain's faces (see step 5), we go back to step 1 of our algorithm (see Figure 2.20b) with  $S_1^0 = S_1^2$  and SP is updated. If  $E_2 \neq \emptyset$ , we go to the next rolling phase.

**4. Rolling Phase 1.2:** In this phase, we search for a sphere  $S_3(c(x, y, z), r) \in E_2$  having the maximal  $\varphi'$  verifying:

$$\begin{cases} \varphi' \in [0, \varphi] \\ x_1^2 = x_2 + (r_1 + r_2)\cos\varphi'\cos\theta \\ y_1^2 = y_2 + (r_1 + r_2)\cos\varphi'\sin\theta \\ z_1^2 = z_2 + (r_1 + r_2)\sin\varphi' \\ c_1^2c = r_1 + r \end{cases} \quad (2.19)$$

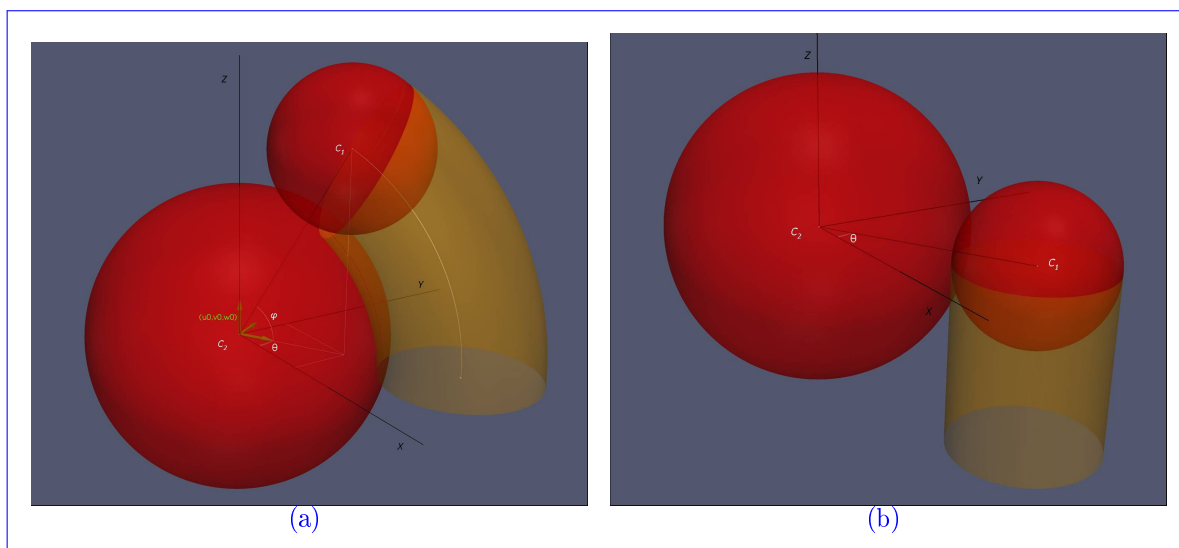


Figure 2.20: The rolling phase 1.1 in the 3D POA: (a) the search for spheres intersecting the torus and (b) the case where  $\varphi = 0$

By letting  $T = \cos\varphi'$ , the solutions in  $T$  of this system are the roots of the second order polynomial:

$$\begin{cases} (K_1^2 + K_2^2)T^2 - 2K_1K_3T + K_3^2 - K_2^2 \\ K_2(K_3 - K_1T) \geq 0 \end{cases} \quad (2.20)$$

where:

$$\begin{cases} K_1 = 2(W_x \cos\theta + W_y \sin\theta) \\ K_2 = 2W_z \\ K_3 = W_x^2 + W_y^2 + W_z^2 + 1 - W^2 \end{cases} \quad (2.21)$$

and

$$\begin{cases} W_x = \frac{x-x_2}{r_1+r_2} \\ W_y = \frac{y-y_2}{r_1+r_2} \\ W_z = \frac{z-z_2}{r_1+r_2} \\ W = \frac{r_1+r}{r_1+r_2} \end{cases} \quad (2.22)$$

We will denote  $sol_S$  the intersecting solution of the Eqs.(2.20) to (2.22). These equations can admit 0,1 or 2 solutions. Figure 2.21a illustrates the first case where  $E_2 \neq \emptyset$  but where

the position of  $c_3$  is incompatible with the condition  $\varphi' \in [0, \varphi]$  and so  $sol_S = \emptyset$ . Figure 2.21b illustrates the second case where only one solution  $T_1$  is possible in agreement with the condition  $\varphi' \in [0, \varphi]$  and hence,  $sol_S = \{T_1\}$ . Finally, Figure 2.21c illustrates the third case where two solutions  $T_1$  and  $T_2$  are possible. In this case, only the upper position is conserved and so  $sol_S = \min\{T_1, T_2\}$ .

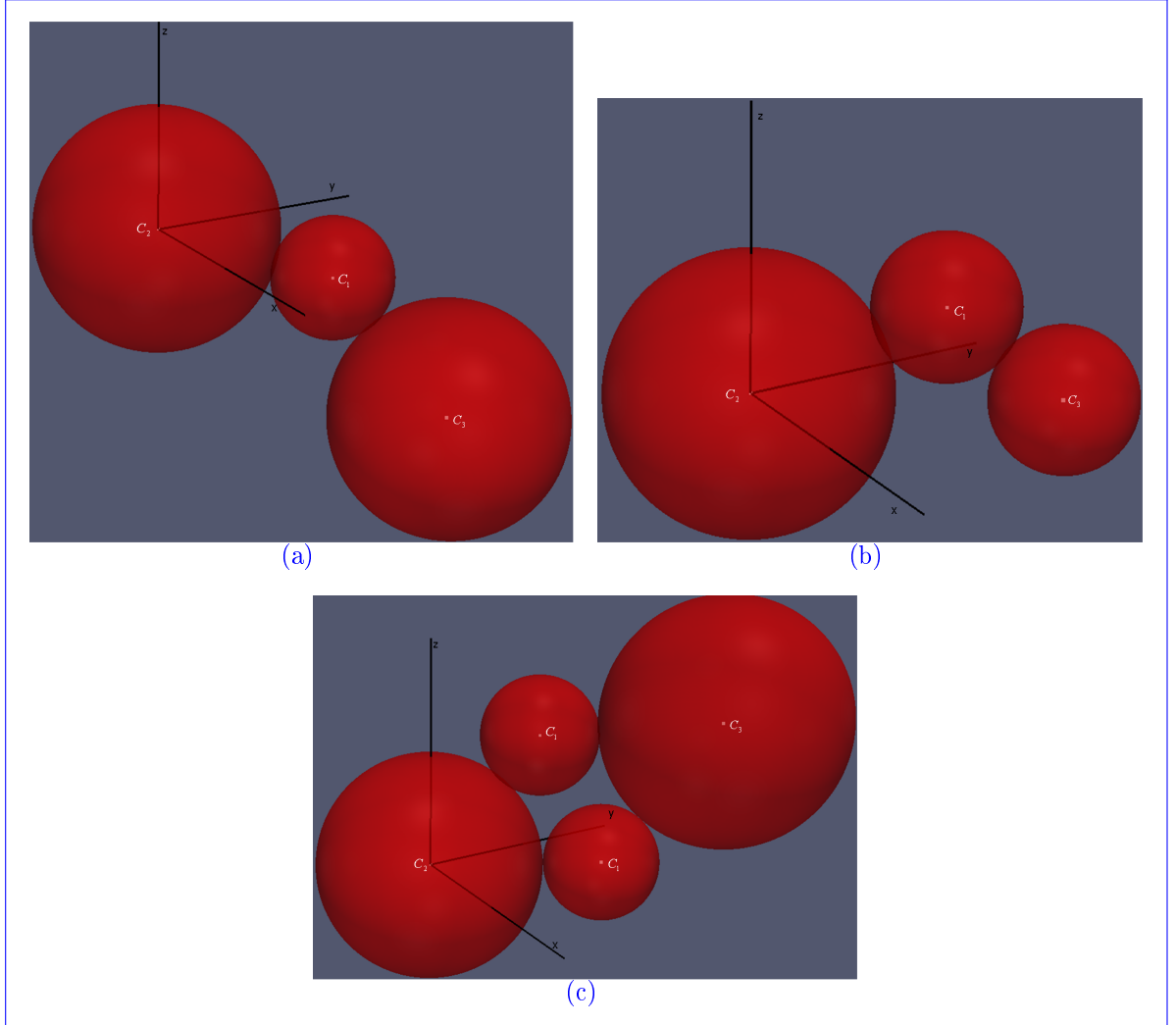


*Figure 2.21: Searching for possible solutions of the Eqs.(2.20) to (2.22) with regards to the condition  $\varphi' \in [0, \varphi]$  in the rolling phase 1.2 in the 3D POA: (a) no solutions exist, (b) only one solution exists and (c) two solution exist*

Moreover, let  $E_3 = \{S \in E_2 / sol_S \neq \emptyset\}$ . If  $E_3 = \emptyset$ , the coordinates of  $c_1^1$  are updated by system (2.18) and we go back to step 1. Else, we search for  $S_3 \in E_3$  such that  $sol_{S_3} = \min_{S \in E_3}(sol_S)$  and the coordinates of  $c_1^1$  are updated by (see Figure 2.22):

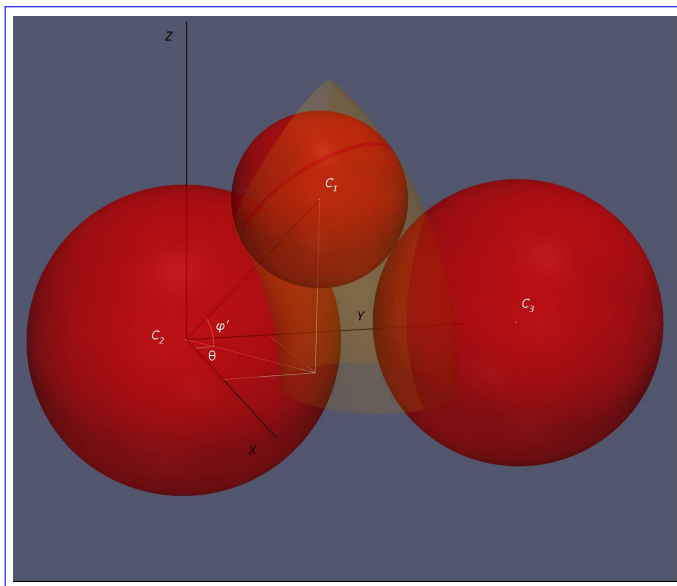


Figure 2.22: The rolling phase 1.2 in the 3D POA: the new position of  $c_1$  tangent to  $c_2$  and  $c_3$

$$\left\{ \begin{array}{l} \varphi' = \arccos(sol_{S_3}) \\ x_1^2 = x_2 + (r_1 + r_2)sol_{S_3}\cos\theta \\ y_1^2 = y_2 + (r_1 + r_2)sol_{S_3}\sin\theta \\ z_1^2 = z_2 + (r_1 + r_2)\sqrt{1 - sol_{S_3}^2} \\ S_1^2 = S(c_1^2(x_1^2, y_1^2, z_1^2), r_1) \end{array} \right. \quad (2.23)$$

And SP is updated.

**5. Checking for face intersection 1:** After steps 3 and 4 of the algorithm, we need to check if the sphere in its new position intersects one of the domain's faces. We first check if the sphere intersects the face  $Z = Zmin$  then we check for intersections with the other faces. If the sphere intersects only  $Z = Zmin$ , it is put in a face-touching position and this position becomes final and SP is updated. In the other cases, the rolling continues after putting the sphere in a face-touching position. In the case illustrated by Figure 2.23, the sphere intersects the face  $X = Xmax$ .

Hence, it should be put in a face-touching position only. This is done by modifying  $\varphi'$  as follows:

$$x_1^2 = x_2 + (r_1 + r_2)\cos\varphi'\cos\theta = Xmax - r_1, \quad (2.24)$$

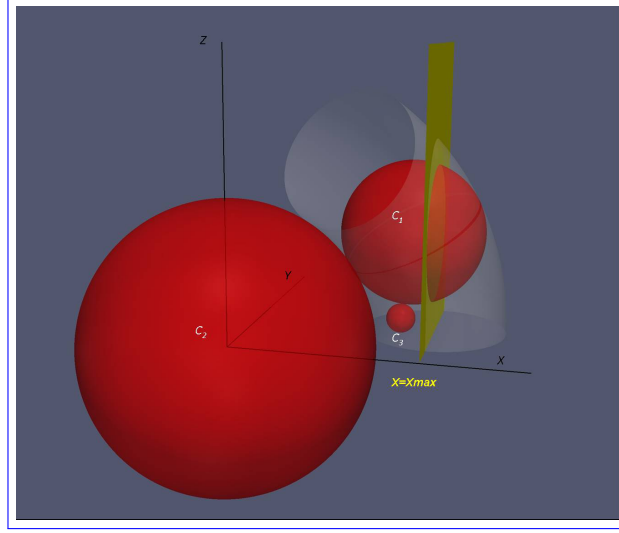


Figure 2.23: After the rolling steps 3 or 4, a case where the sphere of center  $c_1$  intersecting the face  $X = Xmax$

which gives that

$$\varphi' = \arccos \left( \frac{Xmax - x_2 - r_1}{(r_1 + r_2)\cos\theta} \right). \quad (2.25)$$

Afterwards, the coordinates of  $c_1^2$  are modified by writing (see Figure 2.24a):

$$\begin{cases} x_1^2 = Xmax - r_1 \\ y_1^2 = y_2 + (r_1 + r_2)\cos\varphi'\sin\theta \\ z_1^2 = z_2 + (r_1 + r_2)\sin\varphi' \end{cases} \quad (2.26)$$

In order to continue the rolling process, a fictitious sphere  $S_3(c_3^f, r_3^f)$ , symmetric of  $S_2$  with regard to the plane  $X = x_1^2$ , is created (see Figure 2.24b). Furthermore, the intersections with the other faces should be checked as well except for  $Z = Zmax$  because all the spheres are dropped and intersecting this plane is not possible. For a better understanding in what follows, a possible fictitious sphere  $S_3^f(c_3^f, r_3^f)$  will be also denoted as a regular sphere  $S_3(c_3, r_3)$ . Finally, and once again, if this treatment is realized,  $S_1^2$  and SP are updated.

**6. Constructing the new local coordinate system:** Knowing the centers  $c_1^2$ ,  $c_2$  and  $c_3$  (which can be the one of a fictitious sphere), a new coordinate system  $(\Omega, B_1 = (\vec{u}_1, \vec{v}_1, \vec{w}_1))$  is considered with  $\Omega$  the orthogonal projection of  $c_1^2$  on  $[c_2, c_3]$  (see Figure 2.25).  $(\vec{u}_1, \vec{v}_1, \vec{w}_1)$  are given by:

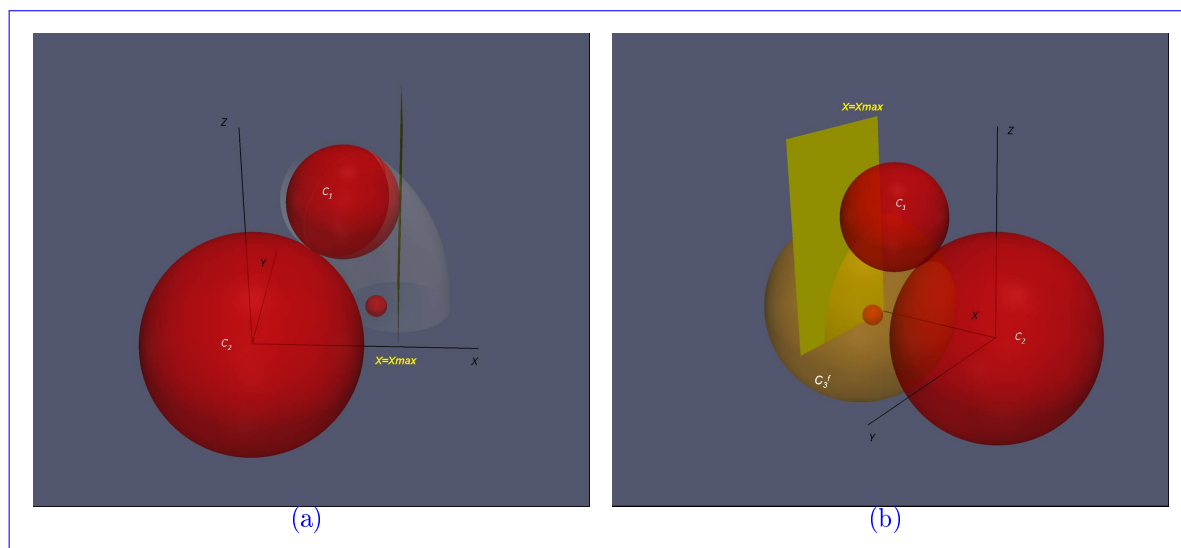


Figure 2.24: (a) The sphere of center  $c_1$  is returned to a face-touching position and (b) the construction of the fictitious sphere of center  $c_3^f$

$$\begin{cases} \vec{u}_1 = \frac{\vec{c_2c_3}}{\|\vec{c_2c_3}\|} \\ \vec{v}_1 = (0, 0, 1) + \alpha\vec{u}_1 \\ \vec{v}_1 \cdot \vec{u}_1 = 0 \\ \vec{w}_1 = \vec{u}_1 \times \vec{v}_1 \end{cases} \quad (2.27)$$

The position of  $\Omega$  is given by the equation:

$$\vec{c_2\Omega} = \vec{c_2c_3} \frac{\vec{c_2c_1} \cdot \vec{c_2c_3}}{\|\vec{c_2c_3}\|^2}, \quad (2.28)$$

The coordinates of  $c_1^2$  in the new coordinate system are:

$$\begin{cases} 0 \\ \Omega c_1^2 \cdot \cos\beta \\ \Omega c_1^2 \cdot \sin\beta \end{cases} \quad (2.29)$$

And the transformation matrix between the canonic system and the new system is written:

$$M_1 = \begin{pmatrix} x_{\vec{u}_1} & x_{\vec{v}_1} & x_{\vec{w}_1} \\ y_{\vec{u}_1} & y_{\vec{v}_1} & y_{\vec{w}_1} \\ z_{\vec{u}_1} & z_{\vec{v}_1} & z_{\vec{w}_1} \end{pmatrix}. \quad (2.30)$$

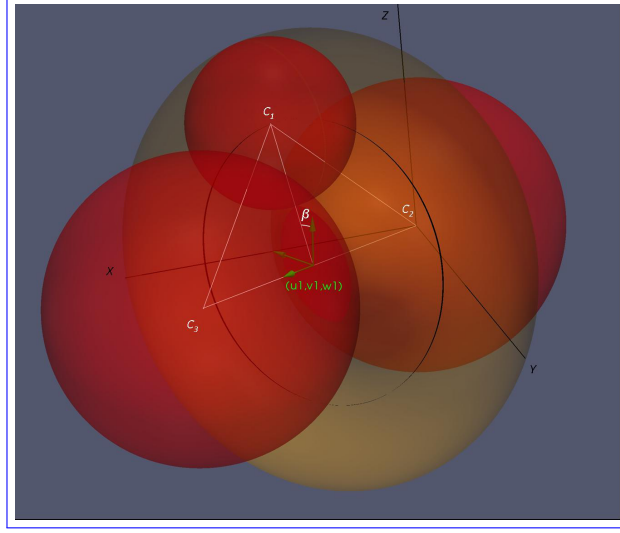


Figure 2.25: The rolling phase 1.2 in the 3D POA: the new position of  $c_1$  tangent to  $c_2$  and  $c_3$

**7. Rolling Phase 2.1:** The procedure here is similar to step 3, we first search for the spheres intersecting the fictitious sphere of center  $\Omega$  and radius  $r_1 + \Omega c_1^2$ . So let  $E_4 = \{S(c, r) \in SP \setminus \{S_1^1, S_2, S_3\} / \Omega c < r_1 + \Omega c_1^2 + r\}$ . If  $E_4 \neq \emptyset$ , for all the spheres  $S(c(x, y, z), r) \in E_4$ , we search for the ones intersecting the fictitious torus of axis  $\overrightarrow{c_2 c_3}$ , center  $\Omega$ , small radius  $r_1$  and big radius  $\Omega c_1^2$  (see Figure 2.25). The coordinates of  $c$  in the new basis,  $(\tilde{x}, \tilde{y}, \tilde{z})$ , are given by:

$$\overrightarrow{\tilde{\Omega}c} = M_1^{-1} \overrightarrow{\Omega c} \quad (2.31)$$

and its signed distance to the torus (with the convention of positive inside and negative outside),  $dist$ , is given by:

$$\begin{cases} d_1 = \sqrt{\tilde{y}^2 + \tilde{z}^2} - \Omega c_1^2 \\ d_2 = \sqrt{d_1^2 + \tilde{x}^2} \\ dist = r_1 - d_2 \end{cases} \quad (2.32)$$

Let  $E_5 = \{S \in E_4 / dist + r > 0\}$ . If  $E_4 = \emptyset$  or  $E_5 = \emptyset$ , the coordinates of  $c_1^2$  are updated as follows (see Figure 2.26a):

$$\begin{cases} x_1^3 = x_\Omega - \Omega c_1^2 \cdot x_{\vec{v}_1} \\ y_1^3 = y_\Omega - \Omega c_1^2 \cdot y_{\vec{v}_1} \\ z_1^3 = z_\Omega - \Omega c_1^2 \cdot z_{\vec{v}_1} \\ S_1^3 = S(c_1^3(x_1^3, y_1^3, z_1^3), r_1) \end{cases} \quad (2.33)$$

And SP is updated. If  $z_1^3 \leq \min(z_2, z_3)$ , we go back to step 1 with  $S_1^0 = S_1^3$ . Else if  $z_3 < z_1^3$ , we go back to step 2 by replacing  $S_2$  by  $S_3$ . If  $E_5 \neq \emptyset$ , we go to the next rolling phase.

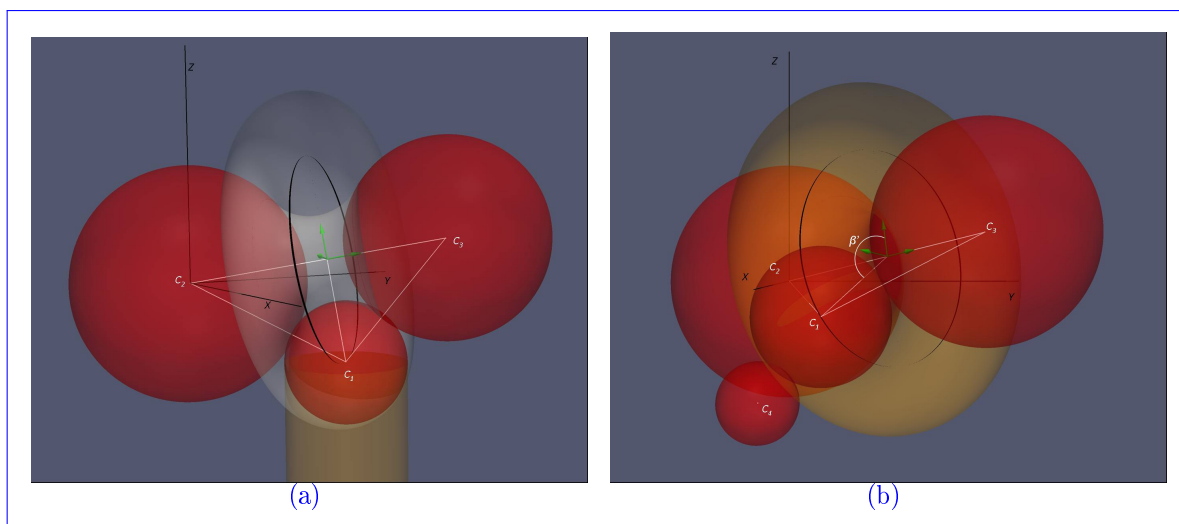


Figure 2.26: The rolling phase 2.1 in the 3D POA: (a) going back to step 1 and (b) the sphere of center  $c_4$  is found

**8. Rolling Phase 2.2:** First,  $\beta$  needs to be calculated. The coordinates of  $c_1^2$  in the coordinate system of center  $\Omega$ , denoted  $(a, b, c)$ , are given by:

$$\overrightarrow{\Omega c_1^2} = M_1^{-1} \overrightarrow{\Omega c_1^2} = \begin{pmatrix} a \\ b \\ c \end{pmatrix}. \quad (2.34)$$

Hence, by combining this equation with Eq.(2.29),  $\beta = \arccos(\frac{b}{\Omega c_1}) \cdot \text{sign}(c)$ . Then, we need to search for a sphere of  $E_5$  having a maximal  $\beta'$  verifying:

$$\left\{ \begin{array}{l} \beta' \in \begin{cases} [\beta, \pi] & \text{if } \beta \geq 0 \\ [-\pi, \beta] & \text{if } \beta < 0 \end{cases} \\ x_1^3 = 0 \\ y_1^3 = \Omega c_1^2 \cdot \cos \beta' \\ z_1^3 = \Omega c_1^2 \cdot \sin \beta' \\ c_1^2 c = r_1 + r \end{array} \right. \quad (2.35)$$

By letting  $T = \cos \beta'$ , the solutions in  $T$  of this system are the roots of the second order polynomial:

$$\left\{ \begin{array}{l} (K_1^2 + K_2^2)T^2 - 2K_1K_3T + K_3^2 - K_2^2 \\ K_2(K_3 - K_1T) \geq 0 \end{array} \right. \quad (2.36)$$

where:

$$\left\{ \begin{array}{l} K_1 = \tilde{y} \\ K_2 = \begin{cases} \tilde{z} & \text{if } \beta \geq 0 \\ -\tilde{z} & \text{if } \beta < 0 \end{cases} \\ K_3 = \frac{\tilde{x}^2 + \tilde{y}^2 + \tilde{z}^2 + (\Omega c_1^2)^2 - (r_1 + r)^2}{2\Omega c_1^2} \end{array} \right. \quad (2.37)$$

We will denote  $sol_S$  the intersecting solution of the Eqs.(2.36) to (2.37). These equations can admit 0,1 or 2 solutions, denoted  $T_1$  and  $T_2$ , similarly to step 4. In the case where two solutions are possible, the upper positions is conserved and so  $sol_S = \max(T_1, T_2)$ . Let  $E_6 = \{S \in E_5 / sol_S \neq \emptyset\}$ . Then, we search for  $S_4 \in E_6$  such that  $sol_{S_4} = \max_{S \in E_6}(sol_S)$  and the coordinates of  $c_1^2$  are updated by:

$$\left\{ \begin{array}{l} \beta' = \begin{cases} \arccos(sol_{S_4}) & \text{if } \beta \geq 0 \\ -\arccos(sol_{S_4}) & \text{if } \beta < 0 \end{cases} \\ \tilde{x}_1^3 = 0 \\ \tilde{y}_1^3 = \Omega c_1^2 \cdot \cos \beta' \\ \tilde{z}_1^3 = \Omega c_1^2 \cdot \sin \beta' \end{array} \right. \quad (2.38)$$

Finally, the coordinates of  $c_1^3$  in the standard basis are given by (see Figure 2.26b):

$$\overrightarrow{\Omega c_1^3} = M_1 \overrightarrow{\Omega c_1^3}, \quad (2.39)$$

and,  $S_1^3 = S(c_1^3(x_1^3, y_1^3, z_1^3), r_1)$  and SP is updated.

**9. Checking for face intersection 2:** After the steps 7 or 8, we need to check again for intersections with the domain's faces. This step of the algorithm is similar to step 5 but without the creation of a fictitious sphere and by considering the face-touching position of the sphere as final. In case of intersection, the sphere  $S_1^3$  is put in a face-touching position by modifying  $\beta'$ . First we should write the coordinates of  $c_1^3$  in the standard basis. Since its coordinates in the new basis of center  $\Omega$  are  $(0, \Omega c_1^3 \cdot \cos\beta', \Omega c_1^3 \cdot \sin\beta')$ , they are written in the standard basis as:

$$\begin{cases} x_1^3 = x_\Omega + \Omega c_1^3(x_{\vec{v}_1} \cos\beta' + x_{\vec{w}_1} \sin\beta') \\ y_1^3 = y_\Omega + \Omega c_1^3(y_{\vec{v}_1} \cos\beta' + y_{\vec{w}_1} \sin\beta') \\ z_1^3 = z_\Omega + \Omega c_1^3(z_{\vec{v}_1} \cos\beta' + z_{\vec{w}_1} \sin\beta') \end{cases} \quad (2.40)$$

By taking the same example as in step 5 where the sphere intersects the face  $X = Xmax$ , we obtain:

$$x_1^3 = x_\Omega + \Omega c_1^3(x_{\vec{v}_1} \cos\beta' + x_{\vec{w}_1} \sin\beta') = Xmax - r_1. \quad (2.41)$$

As in step 8, the values of  $\beta'$  are obtained by solving the system given by Eq.(2.36) but with:

$$\begin{cases} K_1 = x_{\vec{v}_1} \\ K_2 = \begin{cases} x_{\vec{w}_1} & \text{if } \beta \geq 0 \\ -x_{\vec{w}_1} & \text{if } \beta < 0 \end{cases} \\ K_3 = \frac{Xmax - r_1 - x_\Omega}{\Omega c_1^3} \end{cases} \quad (2.42)$$

Afterwards, the coordinates of  $c_1^3$  given in system (2.40) are modified using Eq.(2.41) and the new value of  $\beta'$  and the sphere is then in its final face-touching position,  $S_1^{final} = S(c_1^3, r_1)$  and SP is updated. Also, the intersections with the other faces should be checked as well except for  $Z = Zmax$  because all the sphere are dropped and intersecting this plane is not possible.

**10. Testing the stability:** In order to check the stability of the sphere  $S_1$ , we perform the classical test [23] used with the classical dropping and rolling algorithm. Figure 2.27 shows the orthogonal projections,  $P_{c_1^3}$ ,  $P_{c_2}$ ,  $P_{c_3}$  and  $P_{c_4}$ , of  $c_1^3$ ,  $c_2$ ,  $c_3$  and  $c_4$  respectively on the plane  $z = z_0$  ( $z_0$  can be chosen randomly).

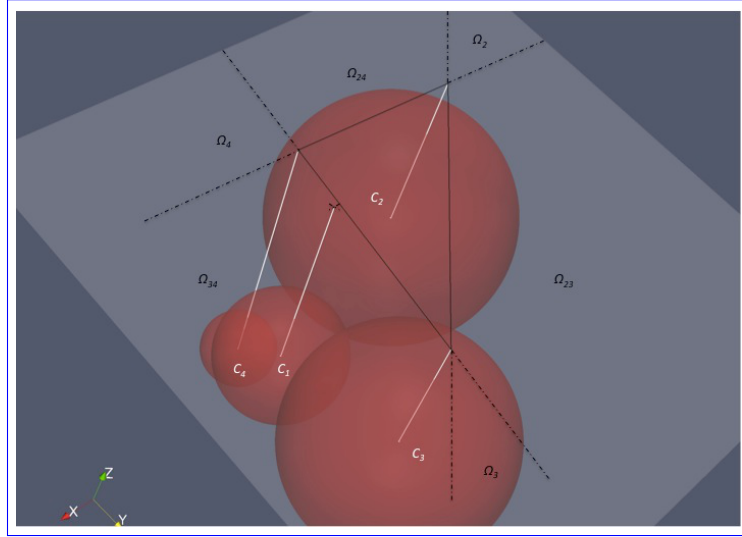


Figure 2.27: Checking the stability of the sphere of center  $c_1$

The stability of the sphere  $S_1^3$  is given by the position of  $P_{c_1^3}$ . If it is contained inside the triangle  $P_{c_2}P_{c_3}P_{c_4}$ , the sphere is stable. In this configuration,  $S_1^3$  becomes the final position of the sphere and SP is updated. If  $P_{c_1^3} \in \Omega_{ij}$ , we go back to step 6 with  $\{S_2, S_3\} = \{S_i, S_j\}$ . If  $P_{c_1^3} \in \Omega_i$ , we go back to step 2 with  $S_2 = S_i$ .

In order to determine if  $P_{c_1^3}$  is positioned at the same the side of the line  $(P_{c_2}P_{c_3})$  as  $P_{c_4}$  for example, we calculate the following variables:

$$\begin{cases} \vec{u}_{23} = M \cdot \overrightarrow{P_{c_2}P_{c_3}} \\ a_{23} = \vec{u}_{23} \cdot \overrightarrow{P_{c_2}P_{c_4}} \\ b_{23} = \vec{u}_{23} \cdot \overrightarrow{P_{c_2}P_{c_1^3}} \end{cases} \quad (2.43)$$

where  $M$  is a matrix given by:

$$M = \begin{pmatrix} 0 & 1 & 0 \\ -1 & 0 & 0 \\ 0 & 0 & 1 \end{pmatrix} \quad (2.44)$$

If  $a_{23} \cdot b_{23} \geq 0$ ,  $P_{c_1^3}$  and  $P_{c_4}$  are on the same side. If not, they are on opposite sides. This calculation is performed to find the position of  $P_{c_1^3}$  with regard to  $(P_{c_2}P_{c_4})$  and  $(P_{c_3}P_{c_4})$  as well. It is interesting to underline that this efficient and classical stability test for all the dropping and rolling algorithms can lead to particular cases where the convergence is not certain and that this difficulty was never discussed in the literature. Indeed, let us consider the case where  $P_{c_1^3} \in \Omega_2$  or  $P_{c_1^3} \in \Omega_{23}$ . In these configurations, realizing again the dropping and rolling procedure can lead to an unchange in the determination of  $S_2$ ,  $S_3$  and  $S_4$  and so be synonymous to an infinite loop. In the context of the proposed

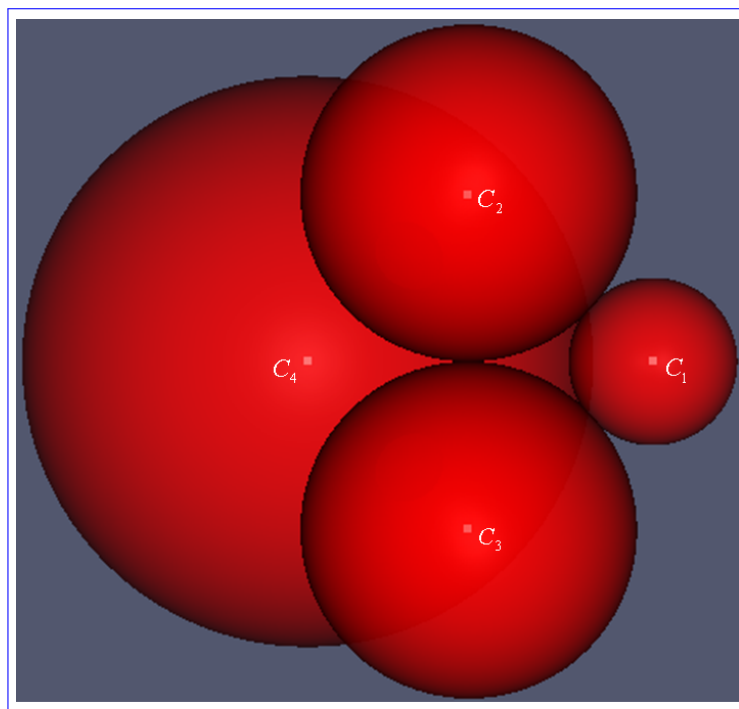


Figure 2.28: A case where  $P_{c_3} \in \Omega_{23}$

algorithm, thanks to the choice of the  $\varphi'$ -interval in (2.19) and of the  $\beta'$ -interval in (2.35), the situation  $P_{c_3} \in \Omega_2$  can never occur. However, in rare particular configurations, our algorithm can lead to  $P_{c_3} \in \Omega_{23}$  and to an infinite loop when the dropping and rolling procedure is performed again. Figure 2.28 illustrates one of these cases.

A simple solution to overcome this difficulty is then to modify the  $\beta'$ -interval in (2.35) by:

$$\beta' \in \begin{cases} [-\pi, \beta] & \text{if } \beta \geq 0 \\ [\beta, \pi] & \text{if } \beta < 0 \end{cases} \quad (2.45)$$

In the two-dimensional case, the POA consists at first in sorting the discs, according to the dropping and rolling direction denoted  $y$ , from minimum to maximum. Then, each disc of center  $c_i$  is dropped using the dropping step of the algorithm (see Figure 2.29a). Afterwards, it is rolled till reaching a third disc of center  $c_k$ . The rolling step is performed using a similar version of steps 3 and 4 but only with the use of one angle which is  $\varphi$  (see Figure 2.29b). If the disc is not stable, which is equivalent to verifying  $P_{y^\perp}(\overrightarrow{c_i c_j}) \cdot P_{y^\perp}(\overrightarrow{c_i c_k}) > 0$ , where  $P_{y^\perp}$  corresponds to the projection operator on the  $y^\perp$  space, it continues its rolling phase until reaching a stable position (see Figure 2.29c).

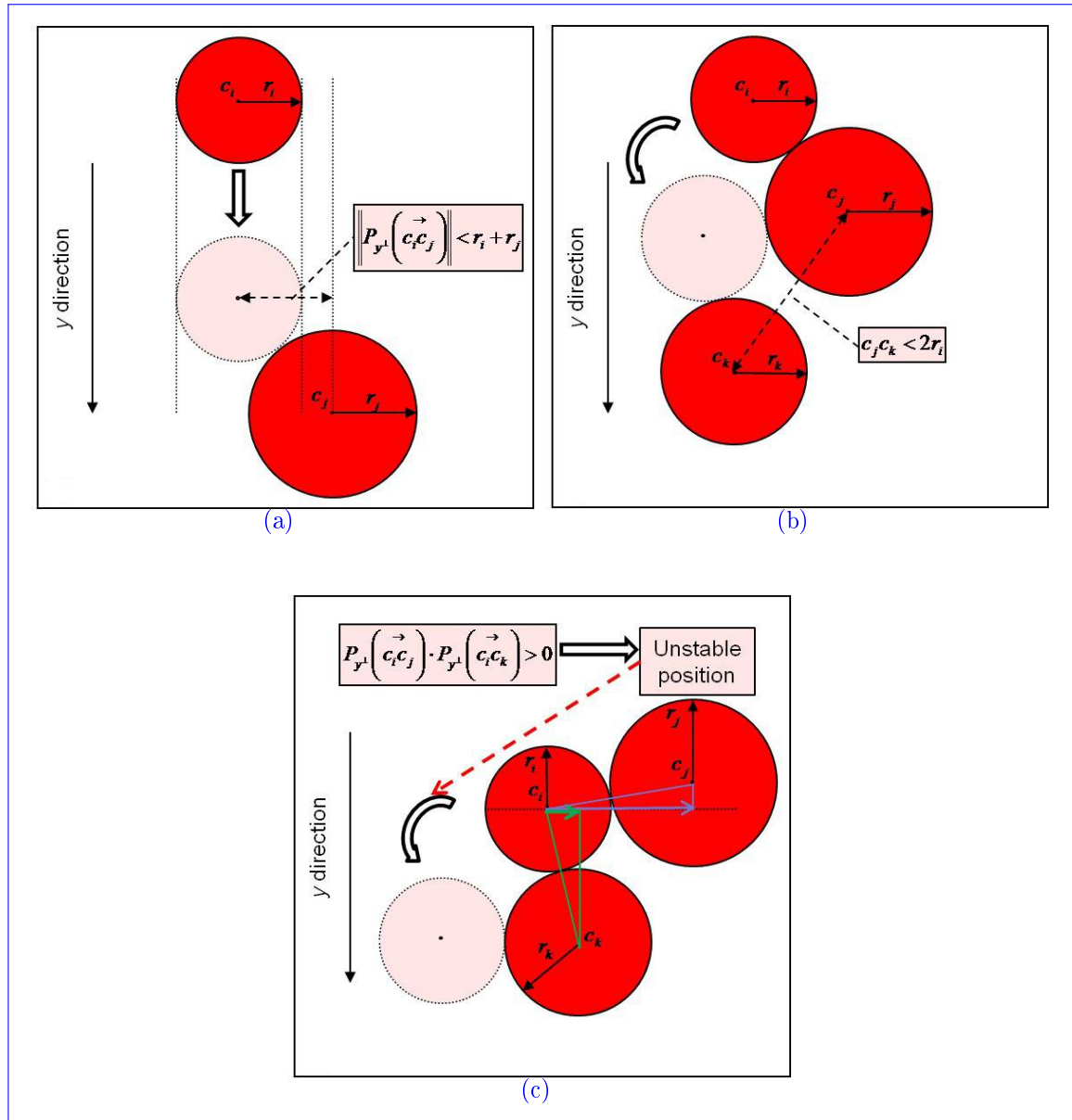
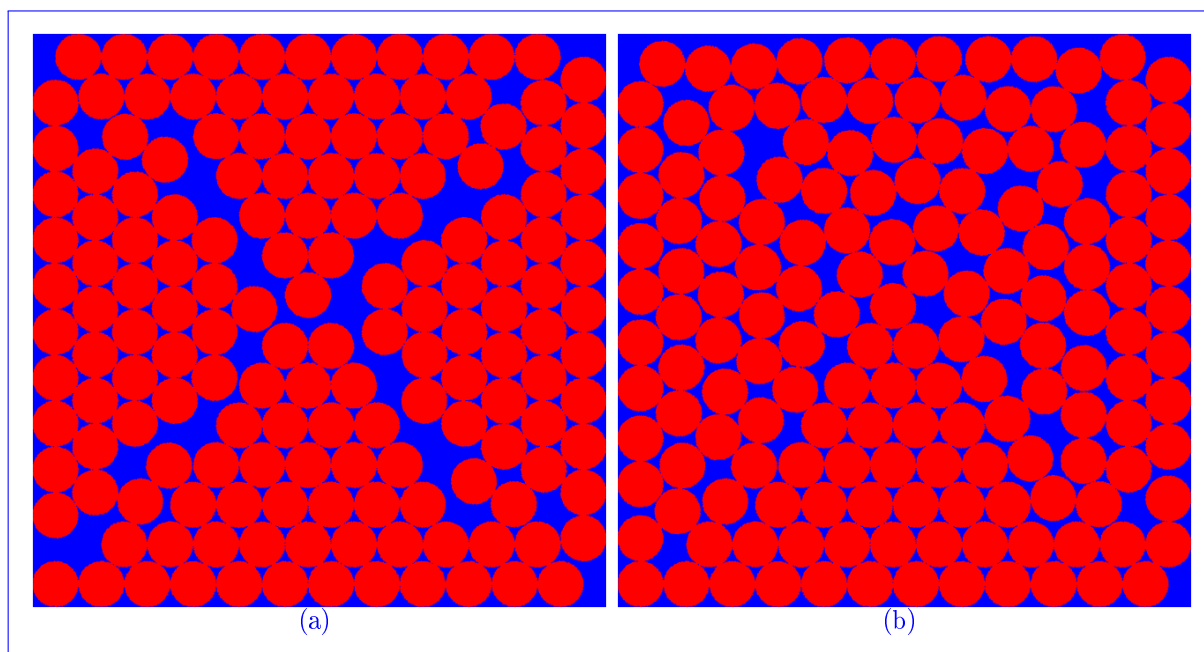


Figure 2.29: Illustration of the two-dimensional POA for a disc of center  $c_i$ : (a) dropping, (b) rolling and (c) unstable position

The interest of the coupled IPM-POA approach is to cumulate the advantages of the two methods: to respect a given radius statistical distribution and to achieve a high density thanks to the IPM and to correct the local un-physical disposition of the particles while improving the local density and without modifying the radius distribution thanks to the variant of the dropping and rolling method. Due to the action of "dropping", an empty space appears in the highest region of the computational domain. Two simple solutions to eliminate this empty space are either to truncate the domain in the y-direction (z-direction in 3D) by considering the  $\max_{1 \leq i \leq N_c}(y_{c_i} + r_i)$  as the new y-upper ( $\max_{1 \leq i \leq N_c}(z_{c_i} + r_i)$

as the new z-upper in 3D) bound of the domain or to generate the sphere packing in a larger domain in the y-direction (z-direction) than the considered computational domain (leading to obtain uncompleted spheres at the y-upper (z-upper) bound of the FE domain). Figures 2.30 and 2.31 illustrate the effect of the POA on mono-disperse and poly-disperse discs. It is noticed that the local voids vanish and are distributed in all the domain and also the particles are displaced to stable positions unlike the previous un-physical ones.



*Figure 2.30: Effects of the POA on mono-disperse discs: (a) before applying the POA and (b) after applying the POA.*

Figure 2.32 illustrates the effect of the POA on poly-disperse spheres. It is noticed that the local voids inside the domain vanish and also the particles are displaced to stable positions unlike the previous un-physical ones.

We note also that the proposed dropping and rolling algorithms can surely be used to generate the spherical particles directly without the use of the IPM. This technique will be compared to the coupled IPM-POA approach in the next chapter. Furthermore, the effects of the IPM-POA coupled algorithms on powder RVE generation and comparisons with other methods are also discussed in the next chapter.

## 2.3 Polyhedral microstructures

As we have already mentioned, the VTM is the most widely used method to model polyhedral microstructures. The Voronoï tessellation or diagram is fully described by a set of  $N$  seeds or Voronoï nuclei  $(S_i)_{i=1,\dots,N}$ . Each nucleus  $S_i$  defines a Voronoï cell  $V_i$ , which consists of all points closer to  $S_i$  than to any other nucleus (see Figure 2.33):

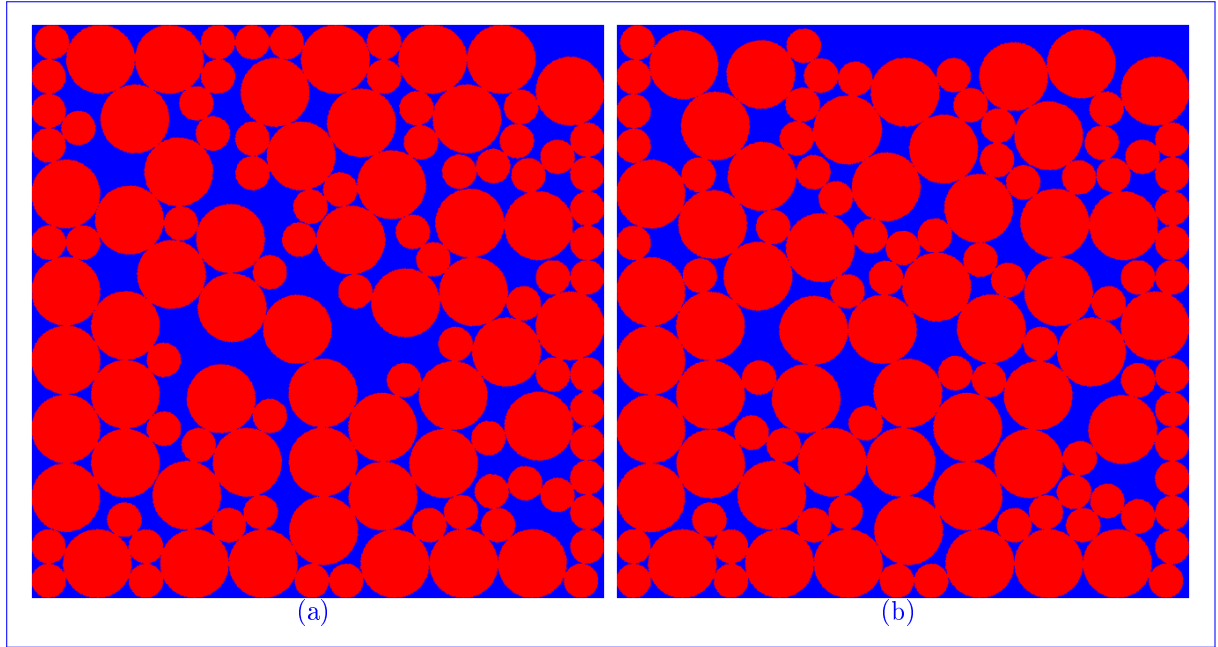


Figure 2.31: Effects of the POA on poly-disperse discs: (a) before applying the POA and (b) after applying the POA

$$V_i = \{x \in \mathbb{R}^d / d(x, S_i) = \min_{j \neq i} d(x, S_j)\}, \quad (2.46)$$

where  $d$  is the space dimension and  $d(., .)$  is the Euclidean distance.

Two techniques exist to generate a Voronoï diagram. A first direct method consists in constructing the perpendicular bisectors of the adjacent sites and their intersections will form the diagram. The second method consists in constructing the Delaunay triangulation (detailed in chapter 4, section 4.2.2), Voronoï's dual, and then drawing the perpendicular bisectors of its edges. Many commercial softwares, such as Qhull, MATLAB, Mathematica, etc, generate Voronoï tessellations and Delaunay triangulations. Figure 2.34 illustrates a Voronoï diagram constructed in Mathematica and a 3D Voronoï diagram with 200 cells.

A polyhedral structure with a mean cell size can be constructed using the VTM when a sufficiently large number of Voronoï nuclei is imposed. However, modelling equiaxed polyhedral structures which follow specific cell size distributions is not possible in the classical VTM.

### 2.3.1 Laguerre tessellations

Thus, polyhedral microstructures with a specific cell size distribution law are very difficult to generate. To obtain such microstructures, Xu and Li [107] developed what they called the Constrained Voronoï Tessellation (CVT) where the Voronoï nuclei are contin-

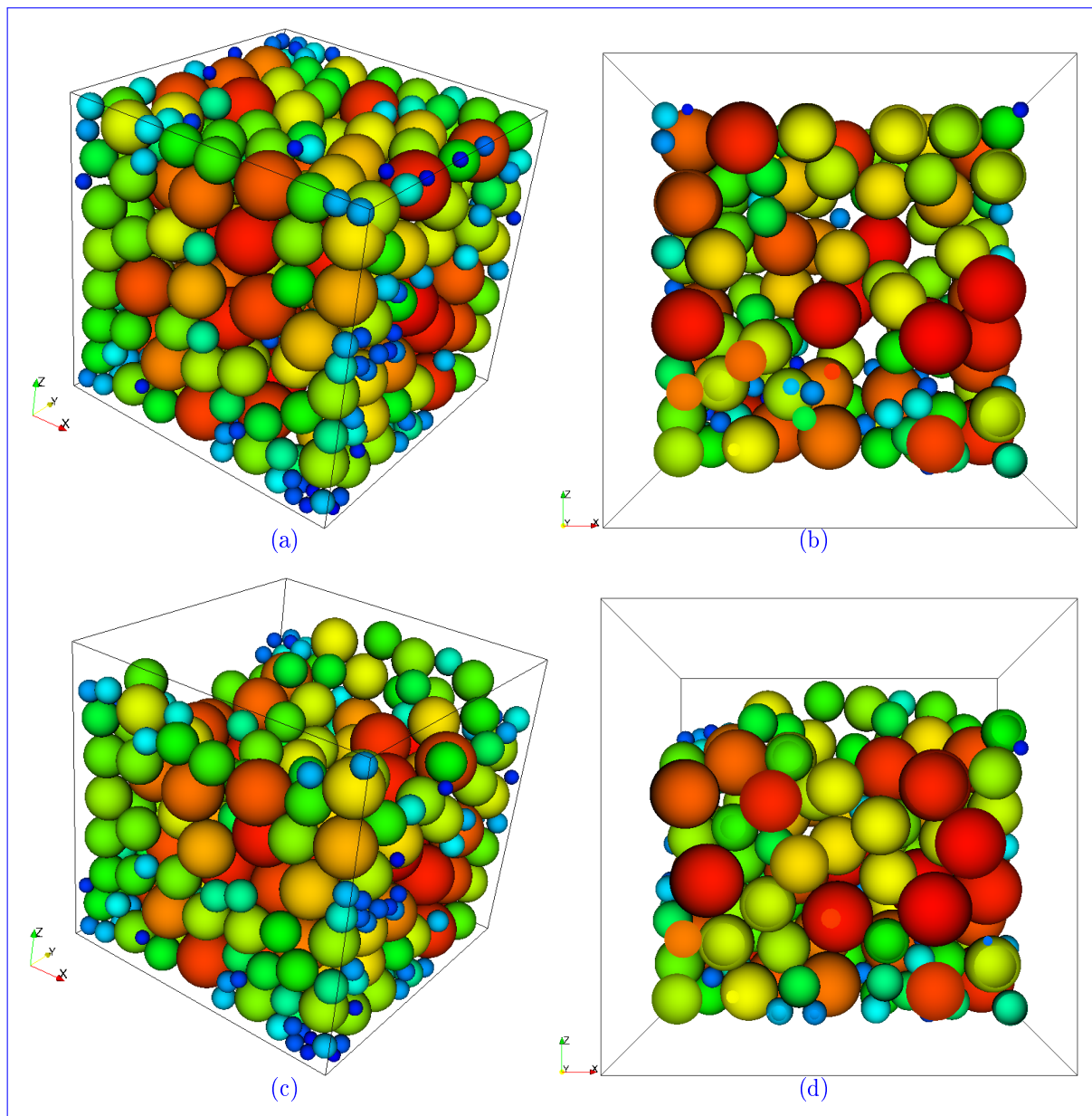


*Figure 2.32: Effects of the POA on poly-disperse spheres: (a) before applying the POA, (b) a cut in the domain showing the inner filling before applying the POA, (c) after applying the POA and (d) a cut in the domain showing the inner filling after applying the POA*

ously displaced in order to obtain the wanted cell size. The CVT proved its efficiency in respecting complex cell size distribution laws. Another efficient method is the Laguerre Tessellation Method (LTM) [95, 96]. It consists in using a distribution of non-intersecting spherical particles that serves as a basis for constructing the microstructure. This method was successfully used to model polycrystalline structures [108] and nanostructured mate-

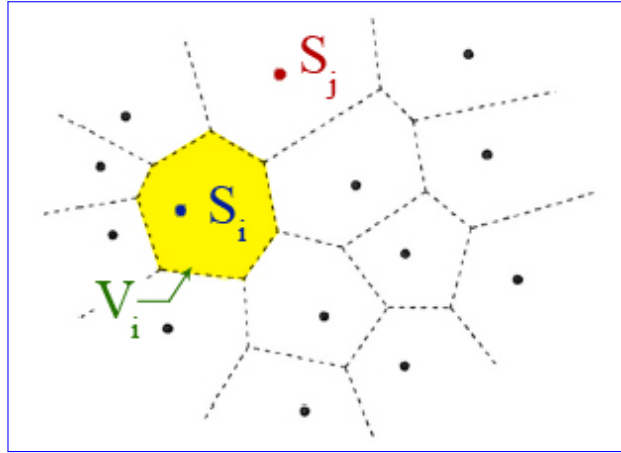


Figure 2.33: A Voronoi diagram in the two-dimensional space  $\mathbb{R}^2$

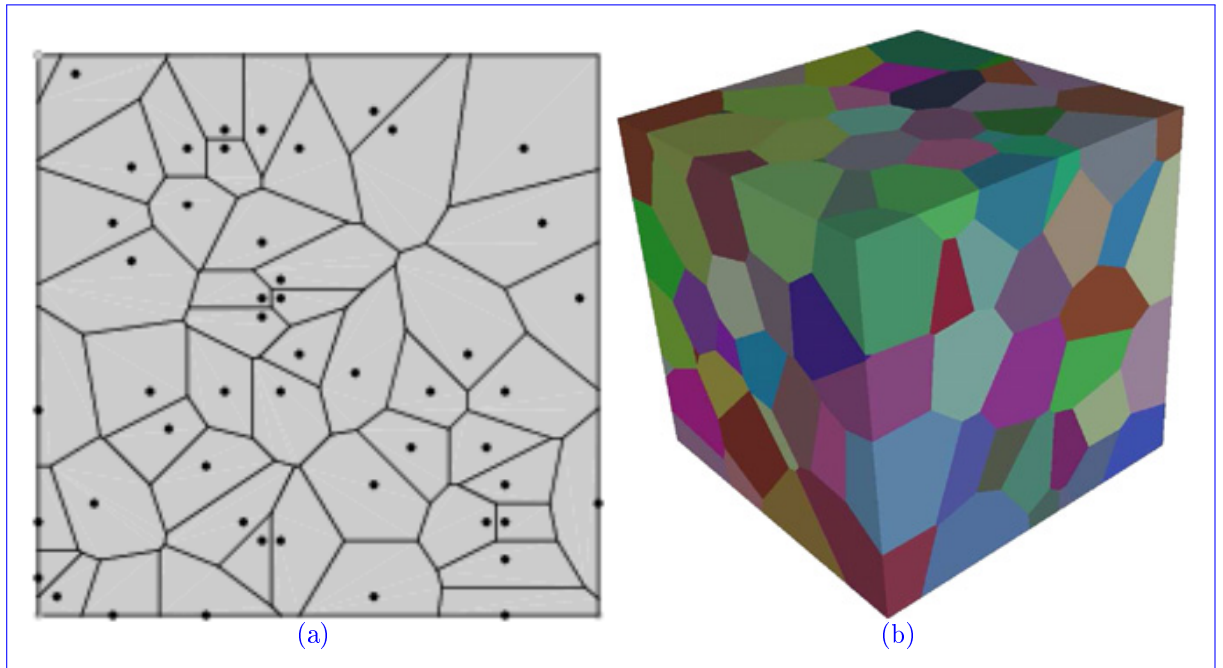


Figure 2.34: (a) A Voronoi diagram obtained in Mathematica and (b) a 3D Voronoi diagram with 200 Voronoi sites

rials [34] where, in addition, the corresponding weighted Delaunay triangulation (detailed in chapter 4, section 4.2.5.1), Laguerre's dual, was built. The Laguerre tessellation is described by a set of  $N$  seeds and weights  $(S_i, R_i)_{i=1, \dots, N}$ . Each nucleus and weight  $(S_i, R_i)$  defines a Laguerre cell  $L_i$ , which consists of all points closer to  $S_i$ , via the power distance defined below, than to any other nucleus:

$$L_i = \{x \in \mathbb{R}^d / \Pi(x, S_i) = \min_{j \neq i} \Pi(x, S_j)\}, \quad (2.47)$$

where  $\Pi(x, S_i) = d(x, S_i)^2 - R_i^2$  is the power of  $S_i$  to  $x$ . Figure 2.35 illustrates spherical particles generated by the IPM and the corresponding Laguerre cells in 3D.

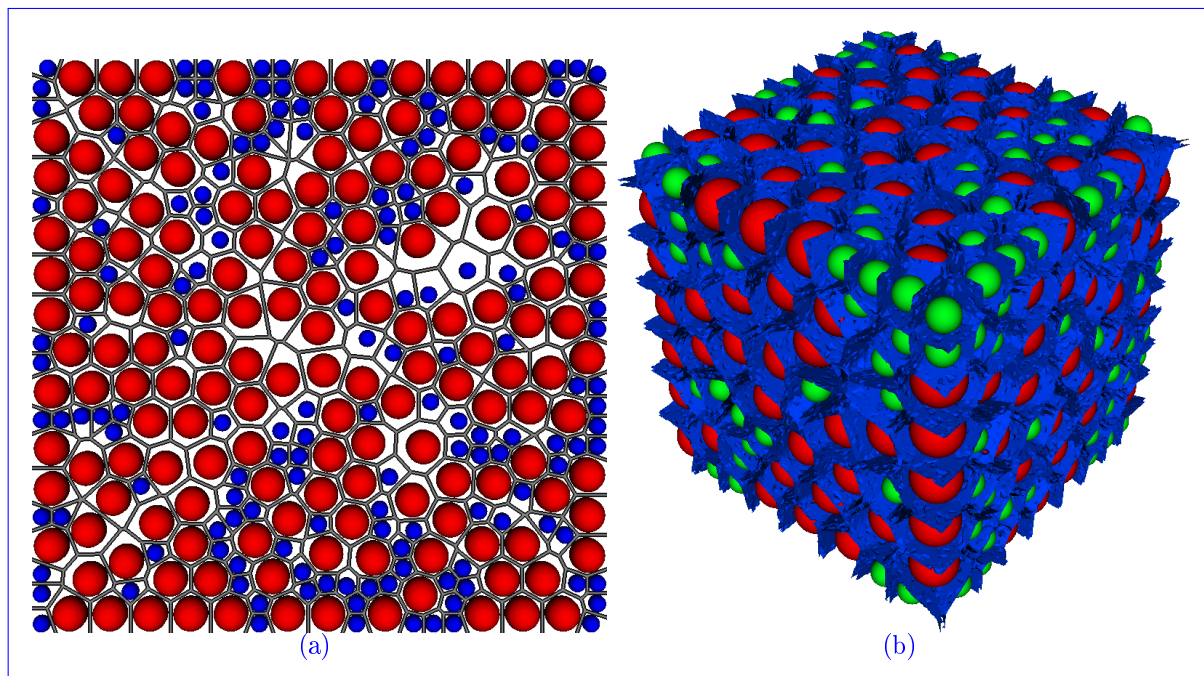


Figure 2.35: Generated spherical particles and the corresponding Laguerre tessellations: (a) the 2D case and (b) the 3D case

### 2.3.2 The Grain Optimization Algorithm (GOA)

As it was mentioned in the introduction, the GOA is a variant of the so-called "Laplacian Smoothing" (LS) algorithm and it is dedicated to equiaxial polyhedral RVEs. It consists, after the generation of the initial sphere packing by the IPM, in moving each sphere as close as possible to the barycenter of the spheres forming its graph (see section 4.2.2) while avoiding overlapping. The global idea of this procedure is to obtain, for all Laguerre cells, a ratio "volume of the corresponding sphere/volume of the cell" more uniformly distributed and so, nearer to the sphere packing density  $\rho$ . The final step corresponds then, to applying a scale factor equal to  $\rho^{1/d}$  at the obtained microstructure. The procedure, illustrated in Figure 2.36, is described below independently of the space dimension:

**GOA.1** The IPM is performed according to the imposed cell size distribution.

**GOA.2** The weighted Delaunay triangulation (see section 4.2.5.1) of the obtained sphere packing is constructed.

**GOA.3** For each sphere  $S_i(c_i, r_i)$  of center  $c_i$  and radius  $r_i$ , do:

- (a) The barycenter  $b_i$  of its graph is calculated by writing:

$$\overrightarrow{Ob_i} = \sum_{j \in \text{Graph}(S_i)} \frac{\overrightarrow{Oc_j}}{\#\text{Graph}(S_i)}, \quad (2.48)$$

where  $O$  is the center of the standard basis and  $\#\text{Graph}(S_i)$  is the number of spheres belonging to  $\text{Graph}(S_i)$ . If the displacement of  $S_i$  on the position  $b_i$  is not responsible of overlapping with the spheres of its graph, this new position of  $S_i$  is validated. Otherwise, a linear displacement of a fictitious sphere of center  $b_i$  and radius  $r_i$  toward  $S_i$  is realized step by step until obtaining a non-overlapping configuration and  $S_i$  is updated by the position obtained. The displacement of the center  $c_T$  of the fictitious sphere is performed by writing  $\overrightarrow{Oc_T} = \alpha \overrightarrow{Oc_i} + (1 - \alpha) \overrightarrow{Ob_i}$ , where  $\alpha$  is the step size.

- (b) If necessary, a new weighted Delaunay triangulation of  $c_i$  and its graph is performed. In this case, the graph of the centers belonging to  $\text{Graph}(S_i)$  is updated.

**GOA.4** End do.

**GOA.5** The scale factor  $\rho^{1/d}$  is applied to the obtained microstructure.

Figure 2.37 illustrates the effect of the GOA by a zoom on an equiaxial polyhedral structure.

The effects of the GOA on equiaxial polycrystal RVE generation are discussed in chapter 3.

## 2.4 Extension to other microstructures

Other, more complex microstructures, can be generated using the pre-explained methods by performing some additional steps. In this section we detail the generation of semi-solid granular structures, foams and disordered fiber arrays.

### 2.4.1 Semi-solid granular structures

Semi-solid granular structures are biphasic structures composed of a liquid and solid phases. Voronoï tessellations are used extensively to model this type of structures in order to compute their permeability [17] and to simulate their solidification [18, 19]. Furthermore, in order to create the liquid channels of a semi-solid granular structure, boundaries between adjacent cells are spread by shifting them in the direction of each center with random values. These values, referred to as  $\epsilon_i$ , can either be chosen between  $\epsilon_{min}$  and  $\epsilon_{max}$ , follow a size distribution law or be defined by a set of boundary shifts  $\{1, \dots, N\}$ . In this case the modified cells  $\tilde{V}_i$  are defined by:

$$\tilde{V}_i = \{x \in V_i / d(x, V_i) \geq \epsilon_i\}, \quad (2.49)$$

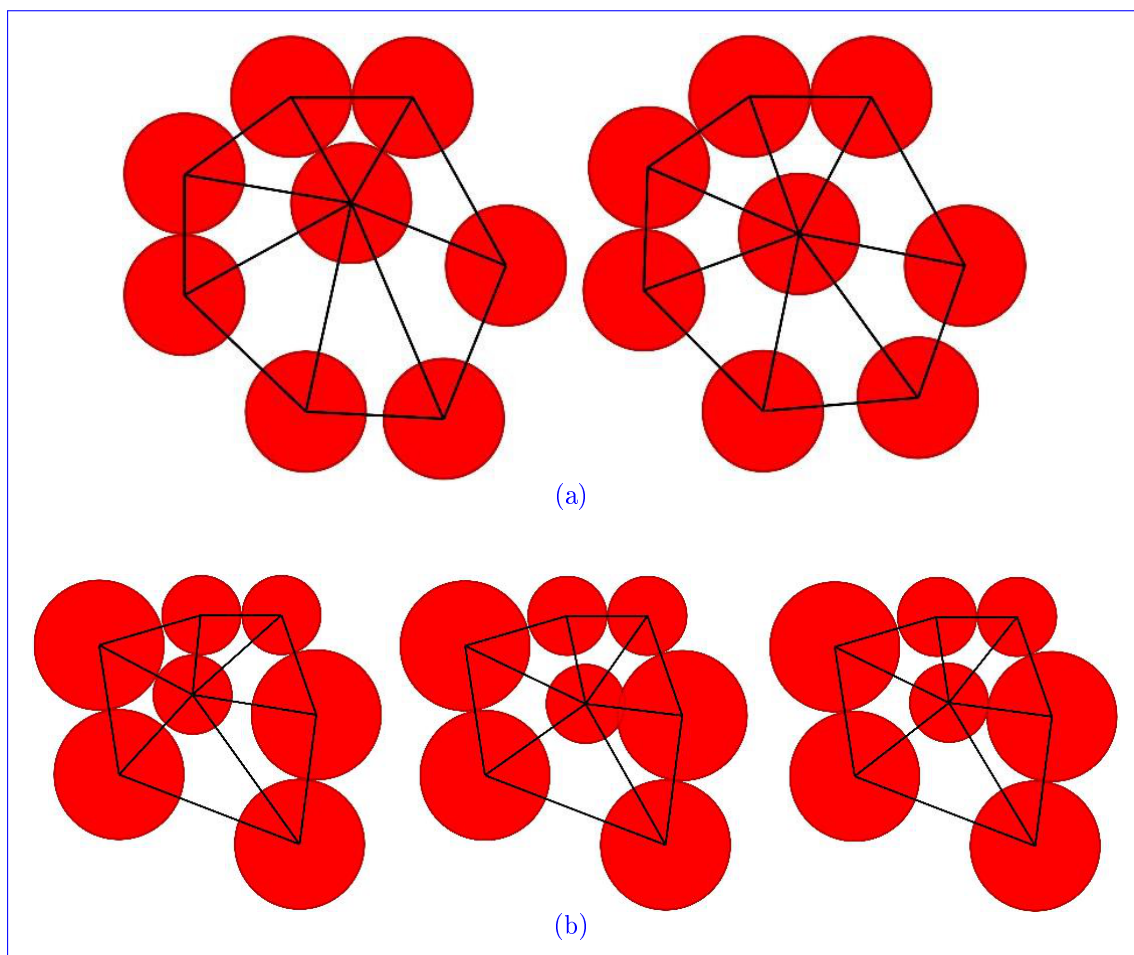


*Figure 2.36: Illustration of GOA.3: (a) a case where the displacement on the position of the barycenter is not responsible of overlapping so, this position is validated and (b) this displacement caused overlapping with another particle of the graph, hence, a linear displacement from the barycenter toward the initial position is realized step by step until a non-overlapping configuration is obtained.*

where  $V_i$  are the Voronoi cells given by Eq.(2.46). This procedure was used to create liquid channels between the solid grains modelling a semi-solid granular structure (see Figure 2.38). Most precisely, for two initially neighboring cells  $V_i$  and  $V_j$ , this procedure has for effect of creating a channel of thickness  $\epsilon_i + \epsilon_j$  between the two cells.

## 2.4.2 Foams

Traditionally, RVEs of foams are defined thanks to two important parameters, their relative density and their regularity. In this section we will explain the capability of our methods to generate Voronoi honeycombs and three-dimensional closed-cell with different relative densities and regularities. The open-cell foams will be discussed further on in this

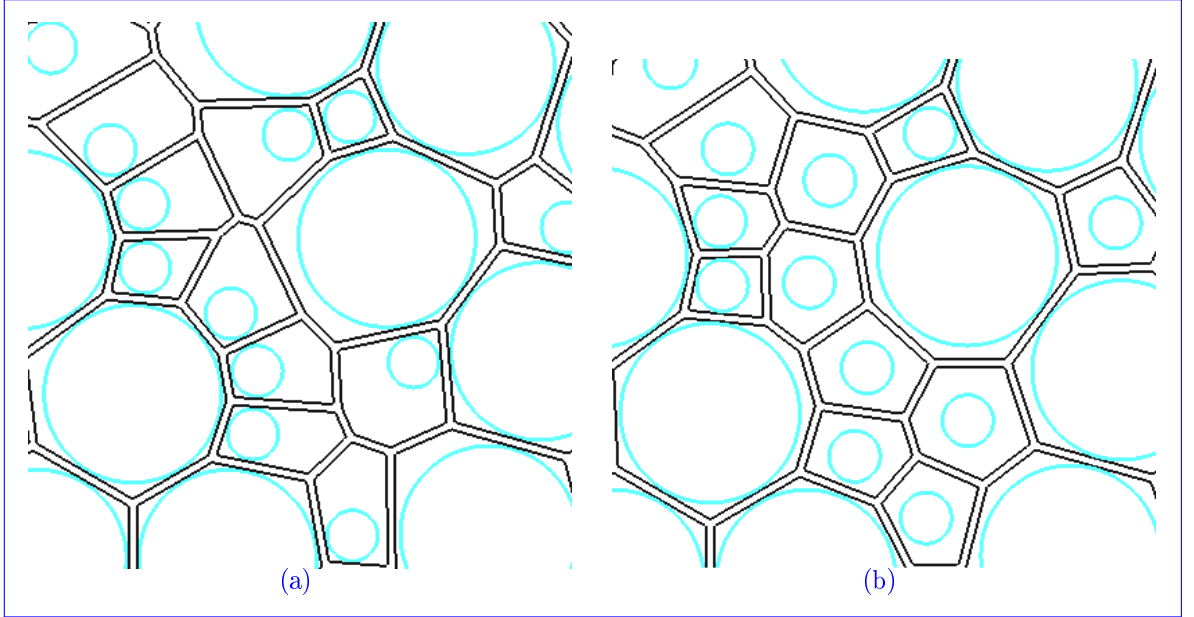


Figure 2.37: A zoom on an equiaxial polyhedral RVE illustrating the effects of the GOA: (a) before applying the GOA and (b) after applying the GOA.

manuscript.

The relative density of a foam is defined as the solid fraction's surface (volume in 3D) on the computing domain's surface (volume in 3D). In the case of honeycombs, this density is calculated in function of the solid skeleton's thickness which is manipulated using the cell-spreading technique used to create the liquid channels of the semi-solid granular structures. In three-dimensional foams, we add the surface of the cells' faces (if it's a closed-cell). In our method, the relative density is controlled using the cells spreading technique. Assuming that a density  $\rho_d$  is desired in the particular case of a constant solid skeleton (or liquid channels of a semi-solid granular structure) thickness that we denote  $2b$ . A simple procedure to determine the adequate  $b$  consists in using the approximation:

$$\rho_d \simeq \frac{\sum_{i=1}^{N_c} F_i b}{|\Omega|}, \quad (2.50)$$

with,  $F_i$  the fluid/solid interfacial area of cell (or grain)  $C_i$  and  $|\Omega|$  the domain's volume. And so,  $b$  is fixed using the equation:

$$b = \frac{\rho_d |\Omega|}{\sum_{i=1}^{N_c} F_i}. \quad (2.51)$$

Now, supposing that the desired density is always  $\rho_d$  but with a heterogeneous thickness of the solid skeleton (or the liquid channels). An astute approach consists in firstly generating the microstructure with  $\{\epsilon_1, \dots, \epsilon_N\}$  as the heterogeneous shifting parameters.

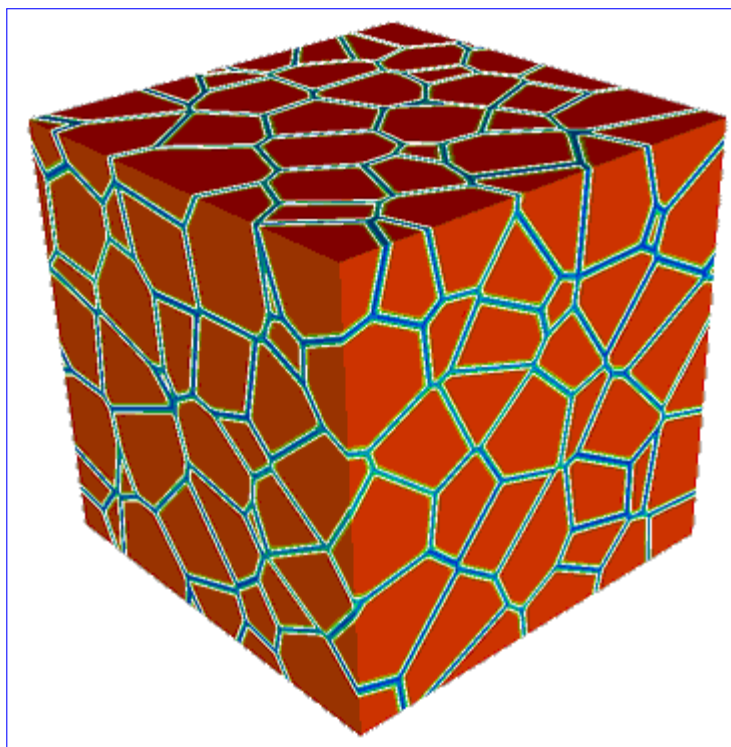


Figure 2.38: Spread Voronoï cells modelling a biphasic granular structure in a unit cube with  $\epsilon_{min} = 0.02$  and  $\epsilon_{max} = 0.05$  [23]

The initial density is then given by  $\rho_0 \simeq \frac{\sum_{i=1}^{N_c} F_i \epsilon_i}{|\Omega|}$ , with a channel size equal to  $\epsilon_i + \epsilon_j$  for two neighboring cells (or grains)  $C_i$  and  $C_j$  (see Figure 2.39).

Afterwards, it is enough to modify each  $\epsilon_i$  by a constant value  $\tilde{b}$  which allows reaching the desired density while conserving the heterogeneous thicknesses, by using:

$$\begin{aligned} \rho_d &= \frac{\sum_{i=1}^{N_c} F_i (\epsilon_i + \tilde{b})}{|\Omega|}, \\ \rho_d &= \rho_0 + \frac{\sum_{i=1}^{N_c} F_i \tilde{b}}{|\Omega|}, \\ \tilde{b} &= \frac{(\rho_d - \rho_0) |\Omega|}{\sum_{i=1}^{N_c} F_i}. \end{aligned} \tag{2.52}$$

Finally, Eq.(2.49) is modified as:

$$\tilde{V}_i = \{x \in V_i / d(x, V_i) \geq \epsilon_i + \tilde{b}\}. \tag{2.53}$$

Furthermore, the choices of the distribution  $\{\epsilon_1, \dots, \epsilon_N\}$  and of the desired density can play an important role on interesting characteristics for a semi-solid such as the creation

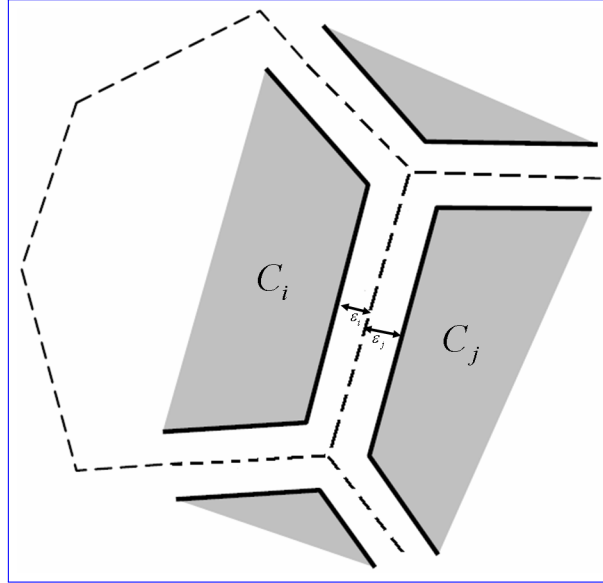


Figure 2.39: Two spread cell with a channel size equal to  $\epsilon_i + \epsilon_j$

of solid bridges. Indeed, assuming that  $\rho_d$  is smaller than  $\rho_0$  leading to a reduction of the initial channels ( $\tilde{b} < 0$ ). The minimum of the  $\epsilon_i$  can be chosen such as  $\epsilon_i + \tilde{b} < 0$  favoring the closure of certain channels and the creation of solid bridges while respecting the desired density.

Concerning foam regularity, a regular honeycomb (foam in 3D) is composed of identical hexagonal (tetrakaidecahedral in 3D) cells. In order to fit  $n$  hexagonal (tetrakaidecahedral) cells into an area (volume)  $a_0$ , the distance  $d_0$  between any two adjacent nuclei must be equal to  $\sqrt{\frac{2a_0}{n\sqrt{3}}} \left( \frac{\sqrt{6}}{2} \left( \frac{a_0}{\sqrt{2n}} \right)^{\frac{1}{3}} \right)$  in 3D. This is performed by placing the spherical particles, used as a basis for constructing the Laguerre cells, in an hexagonal lattice (body-centered cubic in 3D). To construct a random Voronoï honeycomb (foam) with  $n$  cells in the area  $a_0$ , and hence to randomly place  $n$  discs (spheres) in the area  $a_0$ , then the minimum exclusion distance,  $\delta$ , between the nuclei must be less than  $d_0$ . The value of  $d_0$  is therefore an upper limit on the diameter of the  $n$  discs (spheres) which may be accommodated. In order to quantify the regularity of the Voronoï honeycomb (foam), a parameter  $\gamma$  is defined as  $\frac{\delta}{d_0}$  [7, 13]. Then,  $\gamma = 1$  (i.e.  $d = d_0$ ) for a regular hexagonal honeycomb (tetrakaidecahedral foam). For a fully-random structure,  $\gamma = 0$  ( $d = 0$ ). By imposing a maximal and a minimal radius equal to  $d_0/2$  and  $\delta/2$  respectively, our Laguerre method can be used to generate honeycombs and foams with different degrees of regularity (see figures 2.40 and 2.41).

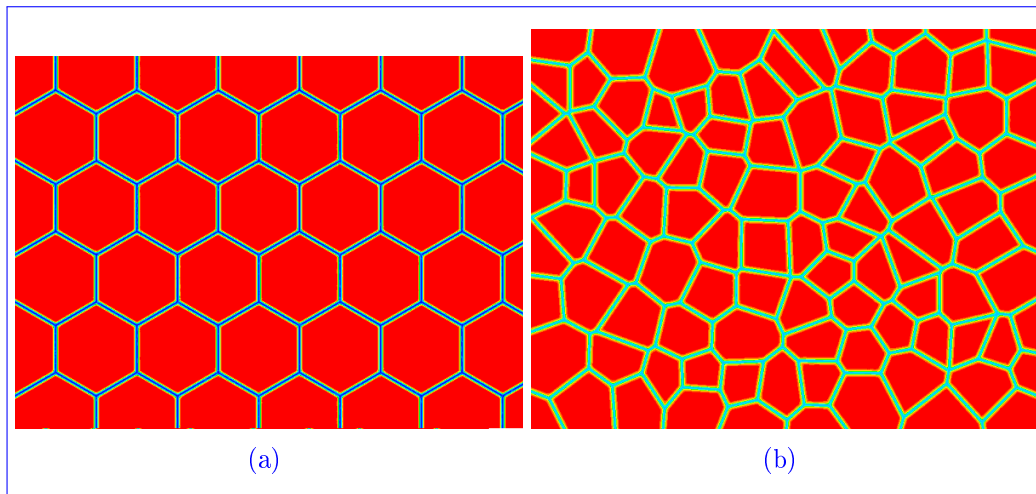


Figure 2.40: (a) A regular Voronoi honeycomb with relative density 0.075 and (b) a Voronoi honeycomb with a regularity degree of 0.5 and a relative density of 0.125

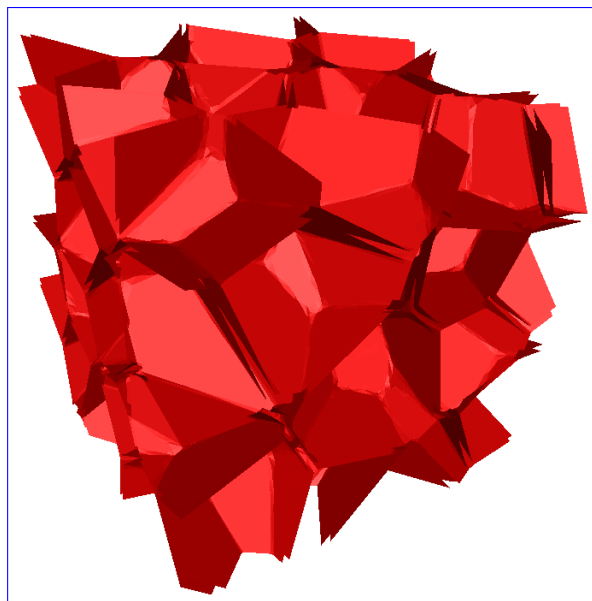


Figure 2.41: A three-dimensional closed-cell foam with a regularity degree of 0.5 and a relative density of 0.2

### 2.4.3 Disordered fiber arrays

In the two-dimensional space and at the microscopic scale, unidirectional fibers are represented by discs of the same size and defined by their porosity  $\phi$  and minimal inter-fiber distance  $\delta_{min}$  (see Figure 2.42). In the case of ordered fiber arrays, simple geometries, such as square or triangular packing of unidirectional arrays of cylinders are considered [80, 83]. In the case of disordered fiber arrays, disc packing coupled with a Monte Carlo

procedure [1] and sequential perturbation of the fibers' locations is used by Chen and Papathanasiou [8, 20] to generate these arrays governed by the choice of the porosity and the minimum allowable inter-fiber distance.

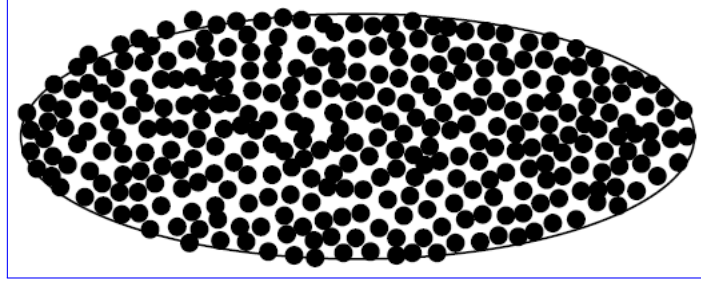


Figure 2.42: *The unidirectional disordered fibers at their microscopic scale*

In order to generate the disc packing modelling unidirectional disordered arrays of fibers with pre-chosen porosity, radius and inter-fiber spacing, we propose the use of the IPM coupled with the POA and a disc shrinking technique. At first, the tangent discs are generated with radii bigger than the wanted radius and equal to  $R + \delta_i/2$  where  $R$  is the wanted radius and  $\delta_i$  is the  $i^{th}$  inter-fiber spacing. And then, the radii are decreased by removing the  $\delta_i/2$  leaving for two fibers  $f_i$  and  $f_j$ , in contact after the IPM-POA algorithm, to obtain a  $\frac{\delta_i + \delta_j}{2}$  inter-fiber spacing. Furthermore, the choice of  $\delta_i$  has a great influence on the porosity and on the degree of disorder of the fiber arrays. Hence, we propose the use of a Gaussian distribution law for the choice of the inter-fiber spacings. The reason for choosing a Gaussian distribution law comes from the fact that, contrary to other classical probability distributions, the sum of independent Gaussian distributions  $N(\mu_i, \sigma_i^2)$  is the Gaussian distribution  $N(\sum_i \mu_i, \sum_i \sigma_i^2)$ . So when the inter-fiber distance is wanted according to  $N(\delta, \sigma^2)$ , it is actually generated following  $N(\frac{\delta}{2}, \frac{\sigma^2}{2})$  and added to the wanted radius then when subtracted, the inter-fiber distance between two fibers will follow a  $N(\delta, \sigma^2)$  distribution. Furthermore, a simple yet efficient choice of  $\delta_{mean}$ , which is the mean of the Gaussian distribution law, leads to obtaining the wanted porosity. This choice is influenced by the fact that the optimal density,  $\rho_{opt}$ , of equally spaced discs (i.e. the hexagonally packed) is given by (see Figure 2.43):

$$\rho_{opt} = \frac{2\pi R^2}{\sqrt{3}(2R + \delta)^2}. \quad (2.54)$$

But since the IPM does not reach the optimal density, this equation should be multiplied by  $\rho(R)$  which is the disc density obtained by the IPM using the radius  $R$ . Finally, the wanted porosity, equal to  $1 - \rho_{opt} \cdot \rho(R)$ , yields that:

$$\delta_{mean} = R \left( \sqrt{\frac{2\pi\rho(R)}{(1 - \phi)\sqrt{3}}} - 2 \right). \quad (2.55)$$

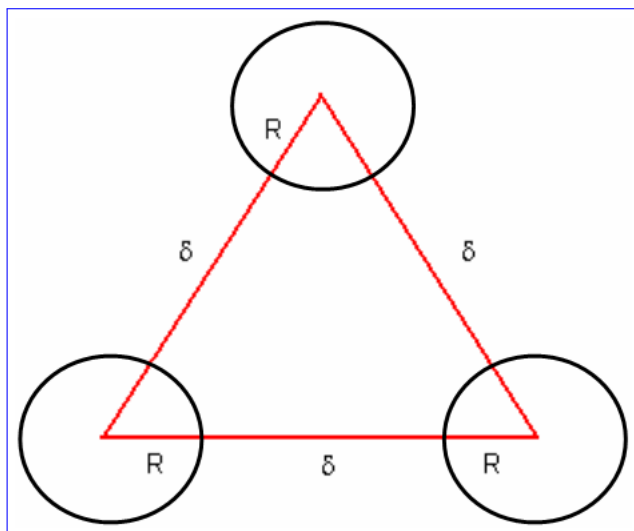


*Figure 2.43: Three equally spaced discs of radius  $R$  and their equilateral disposition*

The standard deviation of the Gaussian distribution is written  $\sigma = \frac{\delta_{mean} - \delta_{min}}{3}$ , where  $\delta_{min}$  is the minimal allowable inter-fiber spacing. Typical fiber distributions are shown in Figure 2.44 for different values of  $\phi$  and  $\sigma$ . Larger values of  $\sigma$  give fiber arrays with a higher degree of disorder.

It is noticed that  $\sigma$  has a greater effect on the fiber distribution when the porosity is large. Moreover, by varying  $\sigma$  a spectrum of fiber distributions can be generated at the same  $\phi$ . Moreover, Figure 2.45 illustrates a comparison between the wanted and obtained distributions of the inter-fiber distances  $\delta_i$  of the fiber array represented in Figure 2.44b. We notice that the difference between the distributions is negligible which means that the imposed inter-fiber spacing distribution is well respected.

## 2.5 Conclusion

This chapter represented the core of our virtual multi-physical microstructure builder where we detailed the IPM which is the sphere packing method used in this work, the Voronoï and Laguerre tessellation methods and the extension to other types of microstructures.

After a general overview of the existing sphere packing methods detailing their advantages and weaknesses, the IPM [25, 34], was chosen as the sphere packing method of this work. The algorithm of this method was detailed in 2D and 3D and some results were shown. This method is fast, generates high packing densities and respects size distribution laws but generates local voids coming from the fact that it is based on the frontal mesh generation method. Hence, an algorithm based on dropping and rolling techniques, that we called the POA, was developed to optimize these voids. The POA was detailed in 2D and 3D. Contrary to other classical dropping and rolling algorithms where small steps

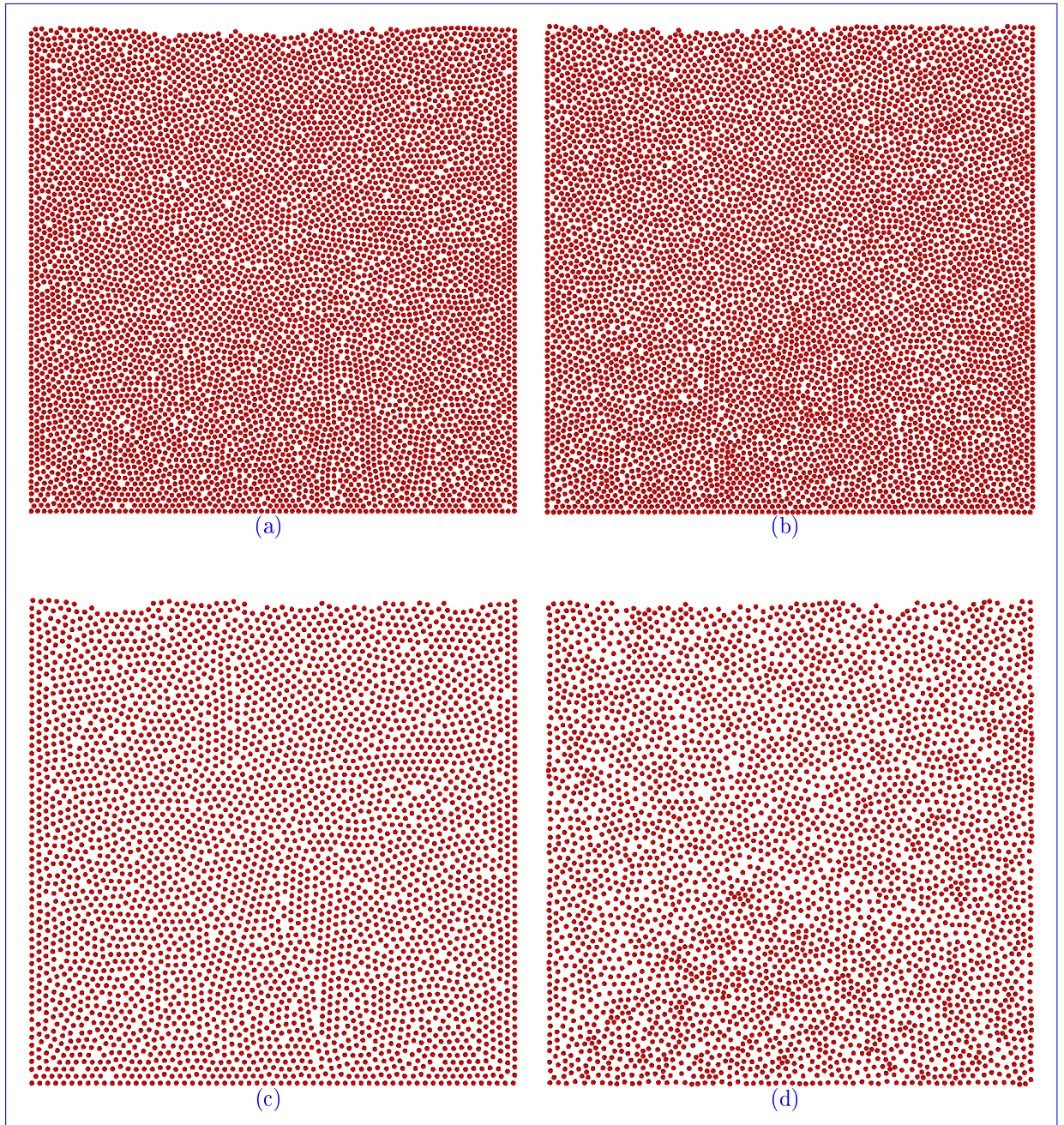


*Figure 2.44: Fiber distributions generated by our method in a  $10 \times 10$  square: (a) 6130 fibers with  $\phi = 0.51$  and  $\sigma = 0.06R$ , (b) 6111 fibers with  $\phi = 0.51$  and  $\sigma = 0.12R$ , (c) 3678 fibers with  $\phi = 0.7$  and  $\sigma = 0.03R$  and (d) 3634 fibers with  $\phi = 0.7$  and  $\sigma = 0.4R$*

are used to reach the stable positions, our POA uses analytical equations to perform the dropping and rolling phases.

In what concerns equiaxed polyhedral generation, the VTM, which is the most widely used method for generating this type of structures, was detailed. Since this method

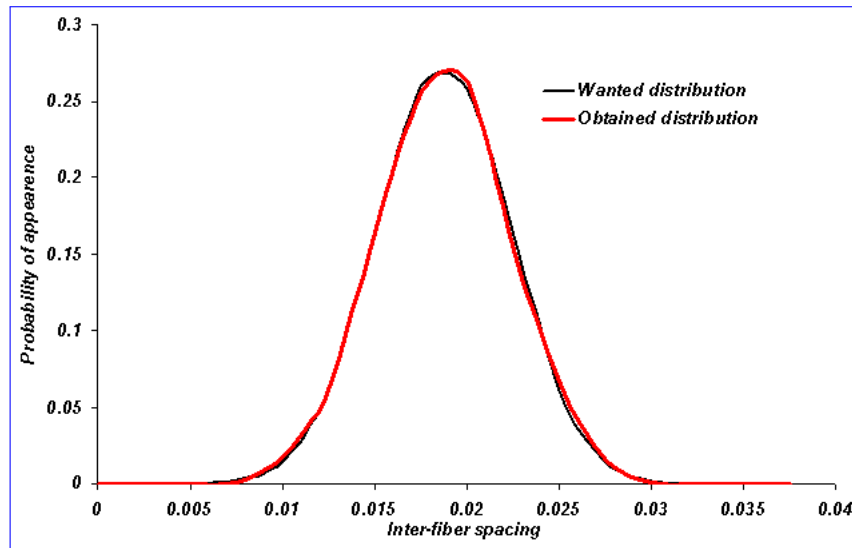


Figure 2.45: A comparison between the wanted and obtained distributions of the inter-fiber distances  $\delta_i$  of the fiber array represented in Figure 2.44b

presents some limitations towards cell size distributions, the LTM, where the location of the cells faces is constrained by a given non-intersecting spherical packing, was used. Nevertheless, local decorrelation between the size of the spherical particles and the size of the corresponding Laguerre cells may persist. For this reason, another optimization algorithm, called GOA, was developed. The GOA is based on the displacement of each sphere towards the barycenter of the spheres forming its graph while avoiding overlapping. The global idea of this procedure is to obtain, for all Laguerre cells, a ratio "volume of the corresponding sphere/volume of the cell" more uniformly distributed.

Afterwards, the Voronoï and Laguerre tessellation methods were extended to generate semi-solid granular structures and foams by using a cell-spreading technique. Also, the IPM coupled with the POA and a disc shrinking technique was used to generate disordered fiber arrays with a given porosity and inter-fiber spacing.

## 2.6 Résumé français

Ce chapitre s'est focalisé sur le générateur de microstructures virtuelles. La méthode frontale de remplissage qui est la méthode d'empilement de particules sphériques utilisée dans cette thèse, les méthodes de Voronoï et Laguerre pour la génération de cellules polyédriques et l'extension à d'autres types de microstructures ont été détaillées.

Dans la première section on s'est concentré sur les méthodes d'empilement de particules sphériques. Nous avons commencé par une étude bibliographique des méthodes de remplissage des domaines parallélépipédiques par des particules sphériques. Deux grandes familles existent, les techniques dynamiques et les techniques constructives. Après l'étude

des avantages et des inconvénients de ces deux grandes approches, une méthode frontale a été adoptée et utilisée dans le reste de cette thèse. Cette méthode présente les avantages d'être rapide, de donner la possibilité de respecter des statistiques de tailles et de générer des empilements de grande densité surtout en 2D. La méthode frontale consiste à construire initialement un front constitué de disques (sphères en 3D) tangents entre eux et à la frontière du domaine. Puis, des nouvelles particules sont générées en contrôlant les intersections avec les particules existantes et le front se propage vers l'intérieur du domaine tout en le remplissant. Des résultats sont détaillés pour des rayons qui respectent différentes lois de probabilité. Finalement, une méthode qui permet d'optimiser les vides locaux créés par la méthode frontale a été proposée. Cette méthode, adaptée aux VERs de poudres, est basée sur l'idée d'enrichir la méthode frontale par une variante de la technique de "Dropping and Rolling". Les résultats de ce couplage sont détaillés dans le chapitre suivant.

La deuxième section a été consacrée à la génération de microstructures polyédriques equiaxes. La méthode du diagramme de Voronoï, qui est souvent utilisée pour modéliser ce type de microstructures a été détaillée en premier lieu. Mais puisque cette méthode présente des limitations pour le respect de lois statistiques concernant la taille des cellules, la méthode de Laguerre qui consiste à utiliser des particules sphériques comme une base pour la génération des cellules polyédriques a été utilisée. Finalement, une méthode, qui limite la décorrélation entre la taille de la cellule polyédrique et la taille de la sphère qui la génère dans le formalisme de Laguerre, a été proposée. Cette méthode, adaptée aux polyèdres equiaxes est une variante d'une méthode appelée "Laplacien Smoothing" qui consiste à placer chaque particule génératrice au barycentre de son graphe. Les résultats de ce deuxième couplage sont détaillés dans le chapitre suivant.

Dans la troisième section, nous nous sommes intéressés à l'extension des outils développés pour la génération d'autres types de microstructures. Les méthodes de Voronoï et Laguerre couplée à une méthode d'écartement de cellules, nous a permis de générer des structures granulaires semi-solide respectant des fractions liquide précises ainsi que des mousses où la densité relative peut être contrôlée précisément. Enfin, il a été démontré que la méthode frontale développée, couplée avec la méthode de "Dropping and Rolling" et une méthode de rétrécissement de disques, permet également de générer des fibres monodirectionnelles hétérogènes tout en respectant une porosité et une distance inter-fibre imposées.





# Chapter 3

## Statistical microstructure modelling

### Contents

---

<b>3.1</b>	<b>Introduction</b>	<b>70</b>
<b>3.2</b>	<b>Modelling applications: Comparison with existing methods</b>	<b>70</b>
3.2.1	Powder RVE modelling	71
3.2.2	Equiaxial polycrystal RVE modelling	74
3.2.3	3D RVEs modelling	77
<b>3.3</b>	<b>Modelling applications: Experimental examples</b>	<b>81</b>
3.3.1	Powder RVE modelling	82
3.3.2	Equiaxial polycrystal RVE modelling	85
<b>3.4</b>	<b>Conclusion</b>	<b>87</b>
<b>3.5</b>	<b>Résumé français</b>	<b>89</b>

---

### 3.1 Introduction

This chapter is dedicated to the validation of the proposed generation algorithms by using experimental data and by comparing their efficiency with other suitable methods. Our focus is on powder and equiaxial grain RVEs. In both cases we compute the error between the given and obtained size distributions and in the case of powders we focus on the spherical particles' density and on the particles' dispositions as well. In the powder modelling applications, we first compare our POA to Bagi's densification method [24] where the voids of an advancing front method are filled with particles non-intersecting preexisting ones. Comparisons are also realized, with Cui and O'Sullivan's triangulation based and vertex filling method [103] where the initial discs are the incircles of the elements of a triangulation of the domain and where more discs are added on the vertices of the elements without intersecting preexisting ones. Then, a more complex granulometry given by a Gaussian distribution law is considered. And finally, experimental data given by laser granulometry performed on a stainless steel 316L are used [29]. In the equiaxial grain modelling applications, we first compare our GOA to the Laplacian Smoothing (LS) algorithm [38] where the grain size distribution is given by a Gaussian distribution law. And then experimental data of a stainless steel 304L, obtained by EBSD, are used [28]. Three-dimensional RVE modelling are also performed for both kinds of microstructure using the statistics of a pure iron [109]. We note that, when dealing with equiaxial grains, the size of the grains (surface or volume) is actually calculated and compared with the wanted size distribution and not the size of the generating particles. This kind of comparison is far more complex than the one where the size of the generating particles is only considered as in [25, 38]. It is important to mention and that all the size functions and domains are nondimensional but can be used also with precise measurements.

### 3.2 Modelling applications: Comparison with existing methods

In this section, six test cases are considered and discussed. The first test case corresponds to the generation of a 2D powder RVE with a granulometry given by a uniform distribution on the interval  $[6 \times 10^{-2}, 4.2 \times 10^{-1}]$ . In this case, the POA is compared with the densification method introduced in [24] where the same granulometry is considered. Bagi's densification method [24] consists in adding new particles to the assembly by testing their possible positions at both sides of every contact of the initial assembly. In other words, this methods tries to fill the voids of the initial disc packing by generating new particles. The second test case corresponds also to the generation of a 2D powder RVE with a granulometry given by a histogram distribution law. In this case, our POA is compared to the method introduced in [103] where this distribution law was obtained. The method of Cui and O'Sullivan [103] consists in constructing a triangulation of the domain with an imposed minimum angle and the initial discs are the incircles of the elements of this triangulation. Then, more discs are added on the vertices of the elements without

intersecting preexisting ones. It is important to mention that the size distribution used in this test case was not imposed in [103], only obtained. Most precisely, discussions around the respect of a given distribution are not described in [103]. The third one corresponds to the generation of a 2D powder RVE defined by a Gaussian distribution law for its granulometry, with mean  $\mu_p = 4 \times 10^{-2}$  and standard deviation  $\sigma_p = 10^{-2}$ . The fourth test case corresponds to a study of the GOA in a 2D equiaxial polycrystal context for a Gaussian distribution of the grain size with mean  $\mu_G = 2.5 \times 10^{-3}$  and standard deviation  $\sigma_G = 5 \times 10^{-4}$ . Results obtained by the GOA are compared with the results obtained without optimization (Laguerre tessellation of the sphere packing obtained without optimization) and the results obtained with the LS optimization [38]. In order to study the evolution of the  $L_2$  error (between the given distribution law and the ones obtained thanks to the POA or the GOA) as a function of the number of particles, the RVEs were generated for different domain sizes. Finally, the fifth and sixth test cases illustrate the capability of our methods to generate 3D powder and equiaxial grain RVEs. The size distribution corresponds to that of a pure iron structure [109]. To be more statistically representative, 20 random configurations were generated for each RVE and the data were collected for analysis.

### 3.2.1 Powder RVE modelling

For the first test case, as in [24], a uniform distribution law  $U[6 \times 10^{-2}, 4.2 \times 10^{-1}]$  is considered as the powder granulometry. Five different domains, denoted  $\{U_i, 0 \leq i \leq 4\}$ , which correspond, respectively, to a  $10 \times 10$ ,  $50 \times 50$ ,  $100 \times 100$ ,  $110 \times 110$  and  $120 \times 120$  square domain, are used. For the second test case, as in [103], a histogram distribution law is considered as the powder granulometry and a unit square denoted  $H_0$  is used. For the third test case, a Gaussian distribution law, with mean  $\mu_p = 4 \times 10^{-2}$  and standard deviation  $\sigma_p = 10^{-2}$  is considered for the radius distribution. Four different domains, denoted  $\{G_i, 0 \leq i \leq 3\}$ , are used. The initial domain  $G_0$  corresponds to a unit square and the three others correspond, respectively, to a  $4 \times 4$ ,  $8 \times 8$  and  $12 \times 12$  square domain. In this third case, a cut-off of  $7.5 \times 10^{-2}$  for the disc radius is realized to avoid large disc surface. The mean (in the sense of the mean of the 20 calculations realized for each case) numbers of discs, the mean densities without optimization, the mean densities using the POA after the domain truncation (as explained in section 2.2.5), the mean average radius and the mean  $L_2$  errors between the obtained and the desired distribution for the three test cases and for the different domains considered are summarized in Table 3.1. Figures 3.1 and 3.2 illustrate the results obtained in term of distribution law for the different configurations.

The different results allow putting forward the following conclusions:

- As illustrated by Figure 3.1a (in the U-cases), Figure 3.2 (the G-cases) and table 3.1, the used IPM-POA coupled algorithm allows converging towards the desired distribution when the number of particles increases. Moreover, the error decreasing is quite homogeneous on the considered distribution ranges.

Domain	number of discs	density without optimization	density with optimization	average radius	$L_2$ error in %
$U_0$	403	0.785	0.817	0.226	10.48
$U_1$	9300	0.788	0.817	0.23	6.15
$U_2$	37400	0.796	0.833	0.231	3.5
$U_3$	44735	0.795	0.831	0.232	3
$U_4$	53687	0.796	0.83	0.232	2.72
$H_0$	2762	0.767	0.816	0.0089	4.94
$G_0$	150	0.759	0.796	0.0392	9.02
$G_1$	2405	0.788	0.813	0.0396	3.54
$G_2$	9708	0.796	0.816	0.0396	3.15
$G_3$	21904	0.8	0.821	0.0397	2.79

Table 3.1: Statistics (mean for 20 calculations) of the 2D powder modelling cases

- The density values when the POA is not used illustrate also that the used advancing front method, in addition to provide unrealistic powder, does not enable to achieve a very high density and to improve it significantly when the number of particles increases. This fact is noticeable in the U-cases and the G-cases.
- The improvement of the density combined to the convergence toward the desired distribution law when the POA is used proves the ability of the proposed approach to answer to the three primordial criteria to model very precisely a powder: to achieve very high densities, to respect precisely a given granulometry and to be realistic for the particles arrangement. This result is not trivial. Indeed, in the most sphere packing methods, one of these objectives can be performed in the detriment of the others. Typically, the optimization results described in [24], concerning the uniform law used in our first test case (the U-cases), describe an increase of the density when the number of the particles considered increases (achieving 0.858 for 56213 particles) but with a regular increasing of the error concerning the average radius of the packing obtained (achieving 7.91% for 56213 particles). In our case, the improvement of the density (achieving 0.83 on the  $U_4$  domain for 53687 particles) is correlated to the decreasing of the error concerning the mean radius (achieving 3.33% on the  $U_4$  domain). This difference can be explained by the fact that when Bagi's densification method [24] is used, small particles have a much higher probability to be accepted than large ones; whereas, when the POA is used, all the particles in suspension, which are un-physically positioned, are displaced eliminating the voids created by the IPM, which makes the microstructure locally denser (but less than Bagi's method) without modifying the radius distribution obtained thanks to the IPM.

As for the method described in [103], the void ratio, equal to  $1 - \text{density}$ , was

### 3.2. MODELLING APPLICATIONS: COMPARISON WITH EXISTING METHODS73

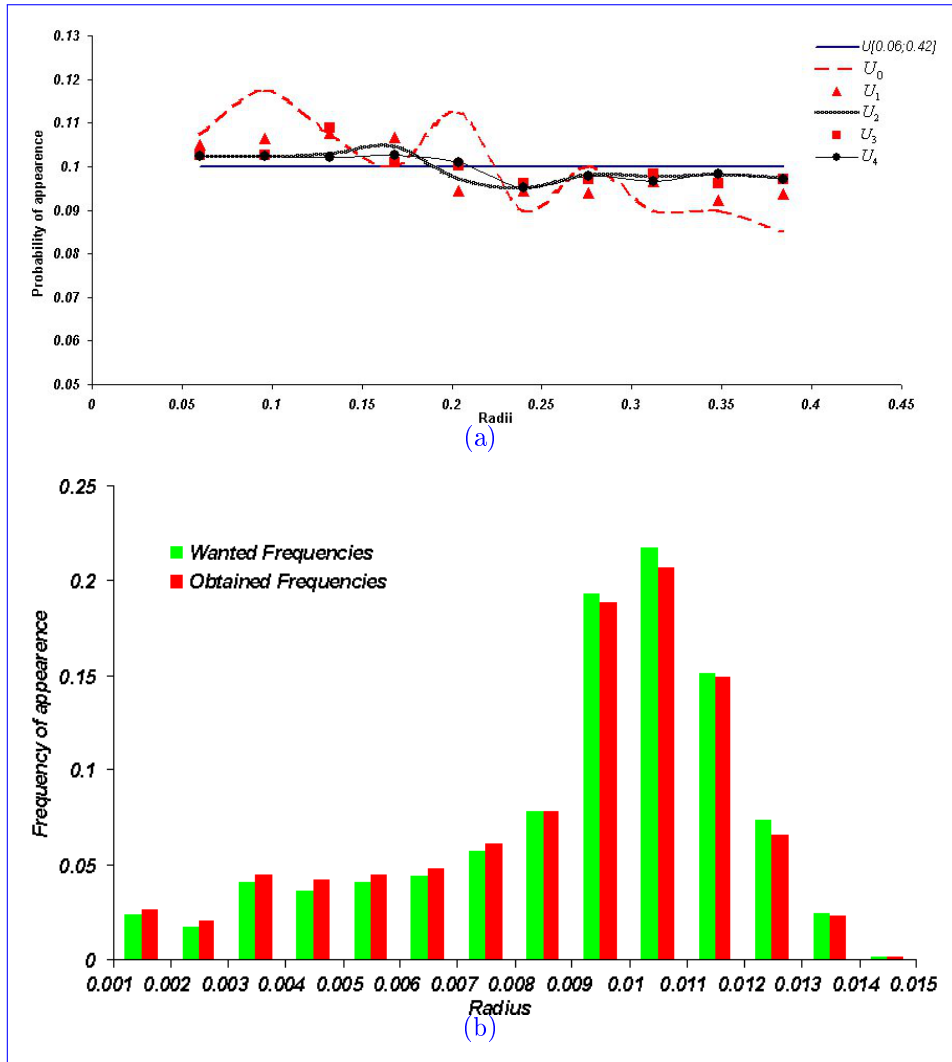


Figure 3.1: (a) The probability density functions obtained in each domain of the first test case compared with the density function of  $U[6 \times 10^{-2}, 4.2 \times 10^{-1}]$  and (b) the obtained frequencies compared with the wanted ones for the second test case in  $H_0$

calculated. Their minimal void ratio obtained was 0.2968 which corresponds to the maximal density of 0.7032. Also, the number of generated discs in [103] was approximately 2283 and, as it was mentioned earlier, the size distributions in their case were not imposed only obtained. Our POA generated an average number of discs of 2762 with an average density of 0.816 which is much higher than the one in [103] and also it respected the wanted statistical law obtained in [103].

Concerning the third test case (the G-cases), our POA proved its ability to answer to the three primordial criteria of powder modelling even for a complex powder granulometry (a Gaussian distribution law).

Figure 3.3 illustrates one of the calculations performed in  $U_4$  (made of 53805 discs)

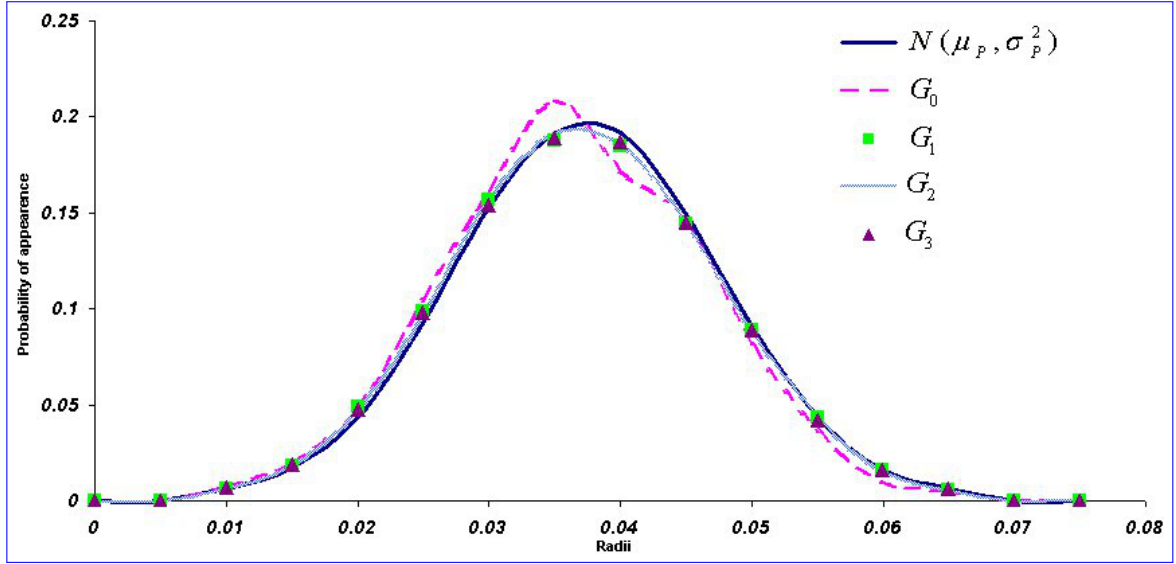


Figure 3.2: The probability density functions obtained in each domain of the third test case compared with the density function of  $N(\mu_p, \sigma_p^2)$

when the POA is applied and a zoom at the center of the microstructure, Figure 3.4 illustrates one of the calculations realized in  $G_2$  (made of 9703 discs) before and after applying the POA. In these Figures, the used coloration describes the size of the particles.

### 3.2.2 Equiaxial polycrystal RVE modelling

As mentioned earlier, the size of an equiaxial grain is approximated by the size of the spherical particle included within. In fact, we start from a given statistical law for an equiaxial polycrystal. This law is then applied to the spherical particles included inside the grains and serving as a basis for the size of the cells. Moreover, the mean ratio of particle volume and grain volume is equal to  $\rho$ , the density of the sphere packing. Hence, a scale factor equal to  $\rho^{1/d}$  is then applied (see section 2.3.2). In 2D, a Gaussian distribution law, with mean  $\mu_G = 2.5 \times 10^{-3}$  and standard deviation  $\sigma_G = 5 \times 10^{-4}$  is considered for the cell surface distribution. The three domains  $G_0$ ,  $G_1$  and  $G_2$  are used (see section 3.2.1). To avoid unphysical results or large cell surface dispersal, we chose a cut-off of  $5 \times 10^{-3}$  for the cell surface. Furthermore, the GOA is compared to the LS optimization technique [38] which attempts to position each particles at the barycenter of its weighted graph by performing small step by step displacements. The mean numbers of grains and the mean  $L_2$  errors between the obtained and the desired distribution for the three cases are illustrated in Table 3.2.

As for the three previous test cases, by considering the results described in Figure 3.5 (comparison between the density functions obtained in each domain and for each method with the desired  $N(\mu_G, \sigma_G^2)$  distribution) and the  $L_2$  errors given in table 3.2, we can conclude that the results were improved when the number of grains increases and also

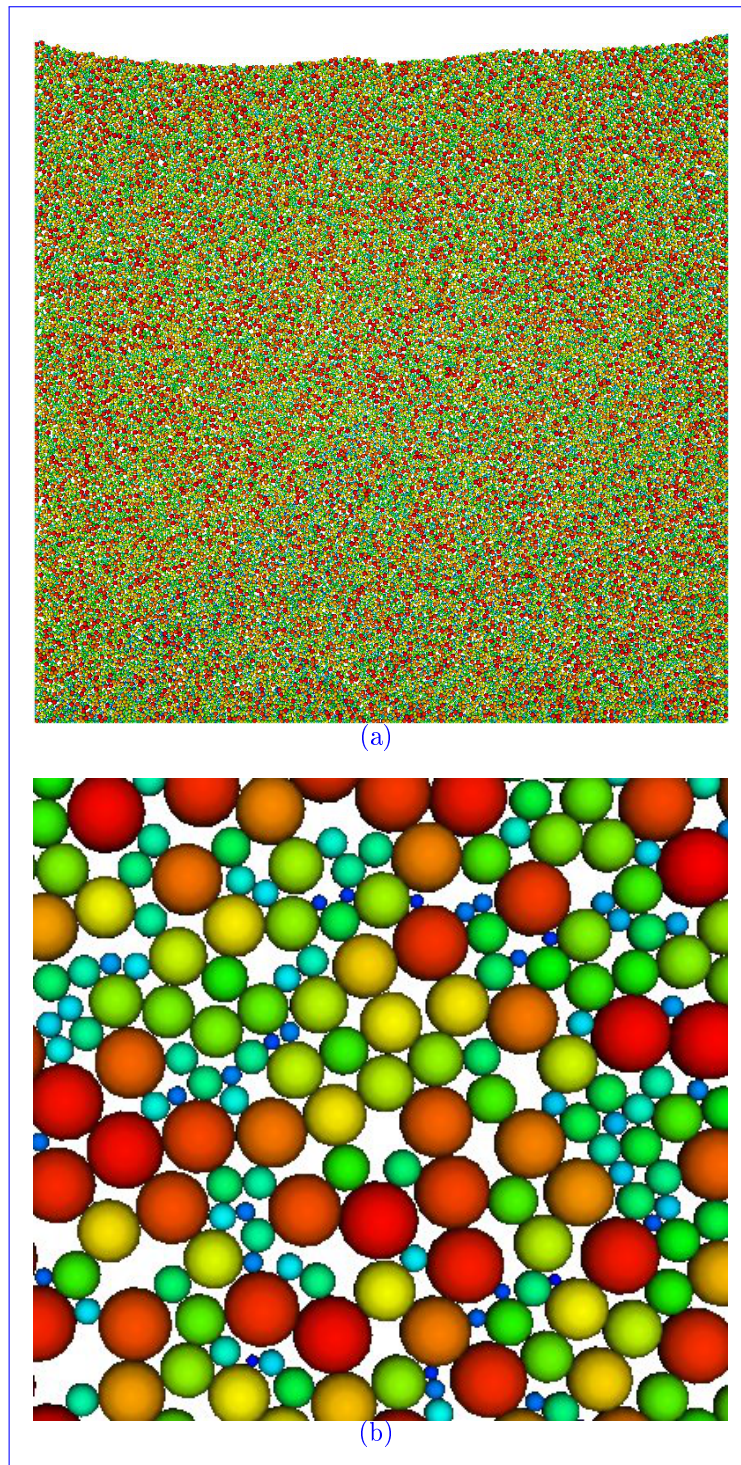


Figure 3.3: (a) The powder RVE obtained using the POA in  $U_4$  made of 53805 discs and (b) a zoom at the center of the microstructure

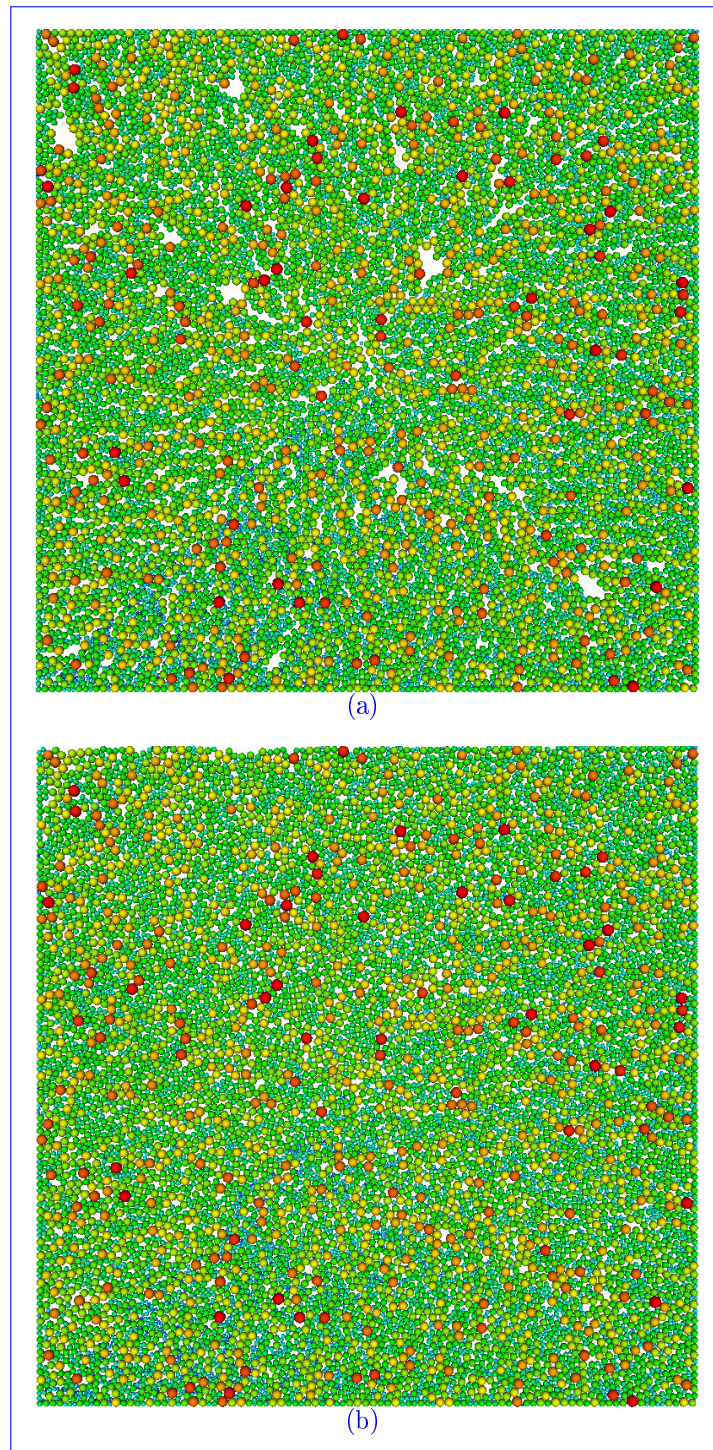


Figure 3.4: (a) The powder RVE obtained without using the POA in  $G_2$  and (b) the same powder RVE when the POA is applied

Domain	number of grains	method used	$L_2$ error in %
$G_0$	300	without optimization	14.7
		GOA	10.74
		LS	12.97
$G_1$	4849	without optimization	9.56
		GOA	8.63
		LS	8.73
$G_2$	19468	without optimization	9.24
		GOA	7.85
		LS	8.16

Table 3.2: Statistics (mean for 20 calculations) of the 2D polycrystal modelling cases

when an optimization method is used. Moreover, the GOA and the LS optimization technique [38] act in the same manner by attempting to place the grain center, or the spherical particle used as a basis for the grain, at the barycenter of its weighted graph which has for effect of homogenizing the surface difference between each Laguerre cell and its corresponding disc in the sphere packing and finally to improve the respect of the distribution law when the scale factor  $\rho^{1/d}$  is applied. The slight improvement between the GOA and the LS method when the number of grains increases can be explained by the fact that the closest position to the barycenter of the weighted graph is systematically chosen in the GOA contrary to the LS method. The errors obtained remain acceptable since we are comparing the cell surface distributions, but the fact that the  $L_2$  error, when GOA is used, only decreases to 7.85% implies that this method may be improved.

Figure 3.6 illustrates one of the calculations realized in  $G_1$  (made of 4810 equiaxial grains) generated using the GOA.

### 3.2.3 3D RVEs modelling

This section contains the test cases dedicated to 3D RVEs modelling. The size distribution in both cases corresponds to that of a pure iron structure [109]. This distribution corresponded originally to size of the grains but was used also as a radius distribution for modelling a nanostructured material in [34]. These cases illustrate the ability of our methodology to deal with 2D or 3D configurations for both powder and equiaxial grain RVEs. 20 calculations were performed as well for each method and in each domain.

In the 3D powder modelling case, the size distribution is considered as the powder's granulometry. The calculations, performed in a unit cube denoted  $C_0$ , lead to obtain an error of 1.24% between the wanted and obtained granulometries hence calculations in a bigger domain were not necessary. Figure 3.7 illustrates the comparison between the size distributions.

Furthermore, the mean number of spheres obtained was 1969 with a mean density of 0.472 before applying the POA, 0.588 after applying the POA. Figure 3.8 illustrates one

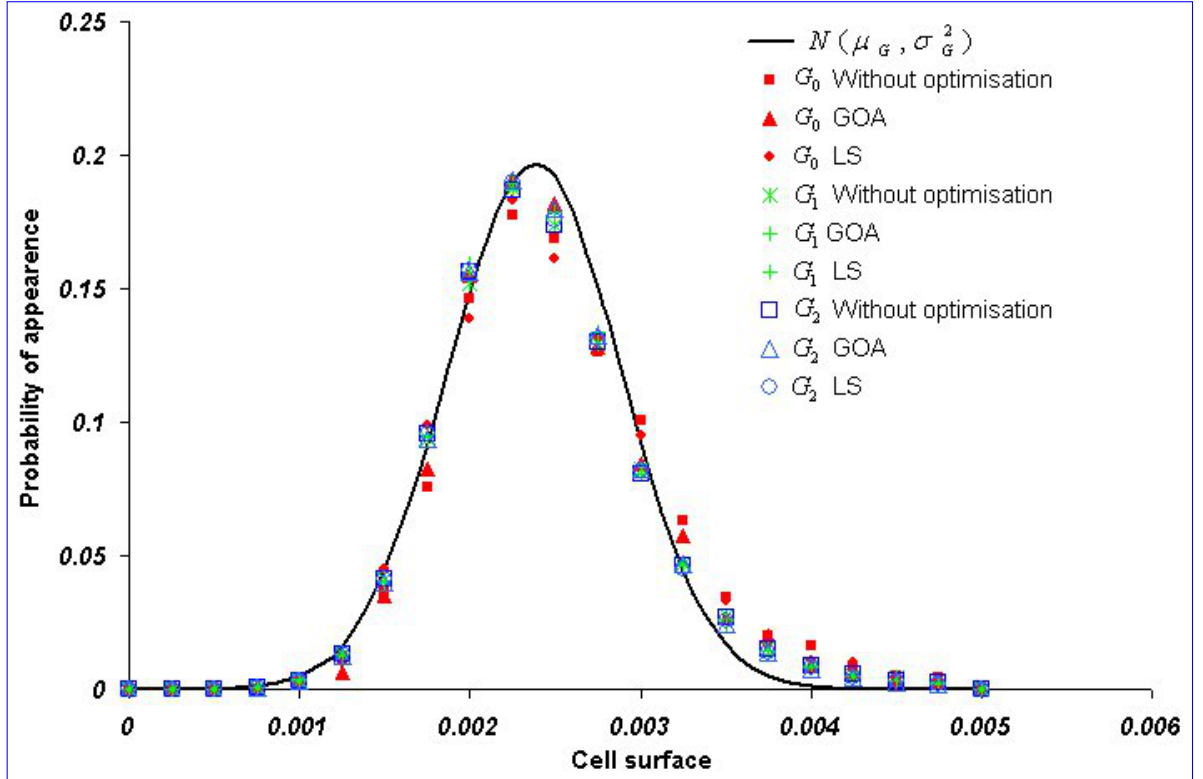


Figure 3.5: The probability density functions obtained without optimization, using the GOA and using the LS method in each domain compared with the density function of  $N(\mu_G, \sigma_G^2)$

of the runs, containing 2031 spheres before and after applying the POA along with cuts at the middle of the domain to show the inner filling. In this run, when the POA was not applied the sphere density was 0.484 and local voids were encountered at the inner part of the domain. After applying the POA and truncating the domain, the density increased to 0.602 and the local voids vanished.

The sphere density values for the IPM were reported in [25, 34, 38]. These densities are moderate when it comes to sphere packing which will enhance the void space in 3D, especially at the middle of the domain. Furthermore, since the size of a Laguerre cell is approximated by the one of a spherical particle, the 3D void will result in having cells much bigger than the corresponding sphere making the respect of a cell volume distribution in the 3D cases more complicated as illustrated in the next test case.

In the 3D grain modelling case, the size distribution is considered as the cell volume distribution. The calculations were performed in  $C_0$  and in a  $2 \times 2 \times 2$  cube denoted  $C_1$  in order to study the evolution of the  $L_2$  error. Also, they were performed without optimization and using the GOA. The mean numbers of grains and the mean  $L_2$  errors between the obtained and the desired frequencies for all cases are illustrated in Table 3.3. Figure 3.9 shows the comparison between the size distributions obtained for each method

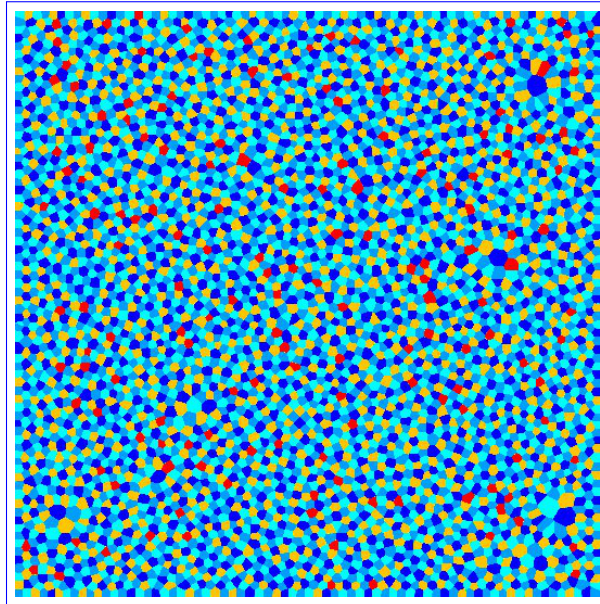


Figure 3.6: 4810 equiaxial grains generated in  $G_1$  using the GOA

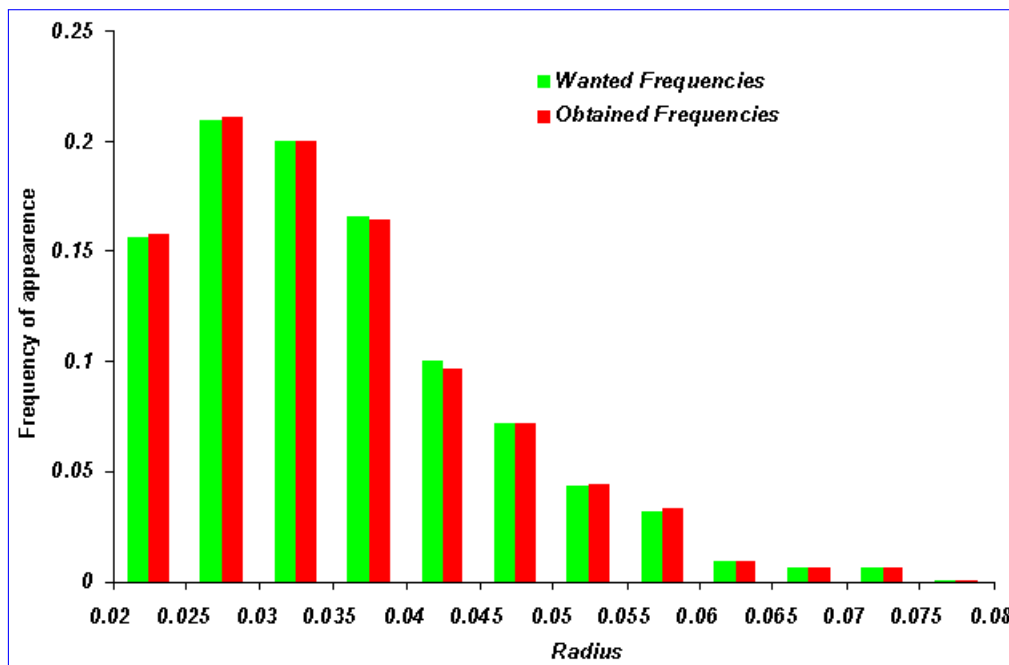
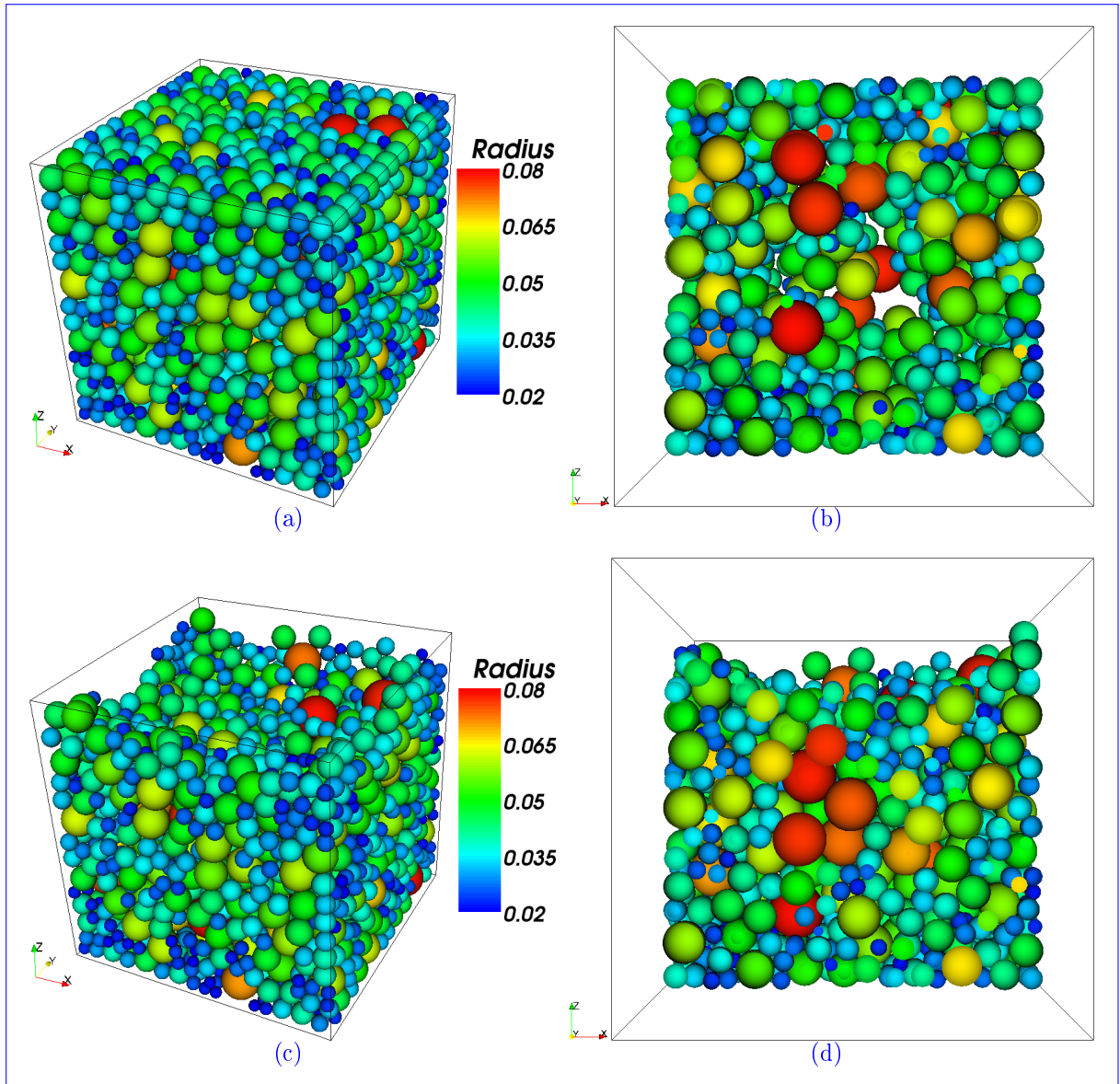


Figure 3.7: The obtained size distributions in the 3D powder modelling case

used and in each domain and Figure 3.10 shows one of the calculations in  $C_0$  performed using GOA and containing 1748 grains.

We can notice from Table 3.3 and Figure 3.9 that, similarly to the 2D case, the error is



*Figure 3.8: 2031 spheres in a unit cube modelling a 3D powder RVE: (a) the whole domain before applying the POA, (b) a cut in the domain showing the inner filling before applying the POA, (c) the whole domain after applying the POA and (d) a cut in the domain showing the inner filling after applying the POA*

inversely proportional to the number of grains and decreases when the GOA is used. But, this error remains bigger than the 2D polycrystal modelling case even when the GOA is used. This is due to the voids encountered when the IPM is used (which are amplified from 2D to 3D configurations) and result in generating grains larger than the basis spheres especially in the middle of the domain. This weakness is illustrated in Figure 3.9. Indeed, we can notice that we obtain quite good results for the small cells. But, in the last four

Domain	number of grains	method used	$L_2$ error in %
$C_0$	1730	without optimization	25.26
		GOA	20.35
$C_1$	11926	without optimization	18.18
		GOA	13.7

Table 3.3: Statistics (mean for 20 calculations) of the 3D polycrystal modelling cases

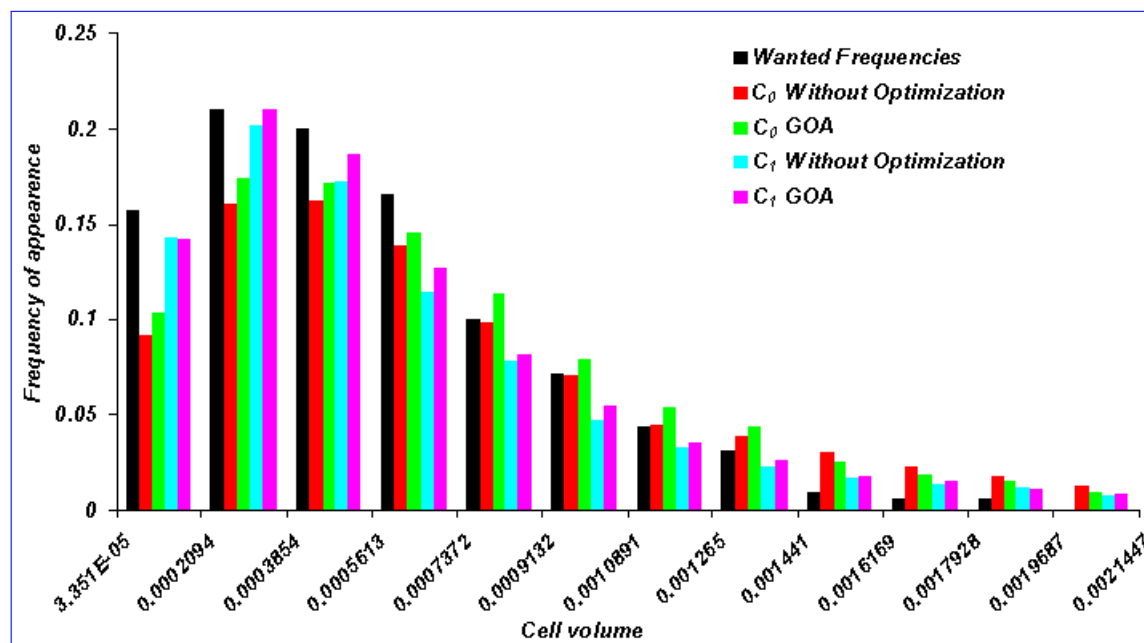
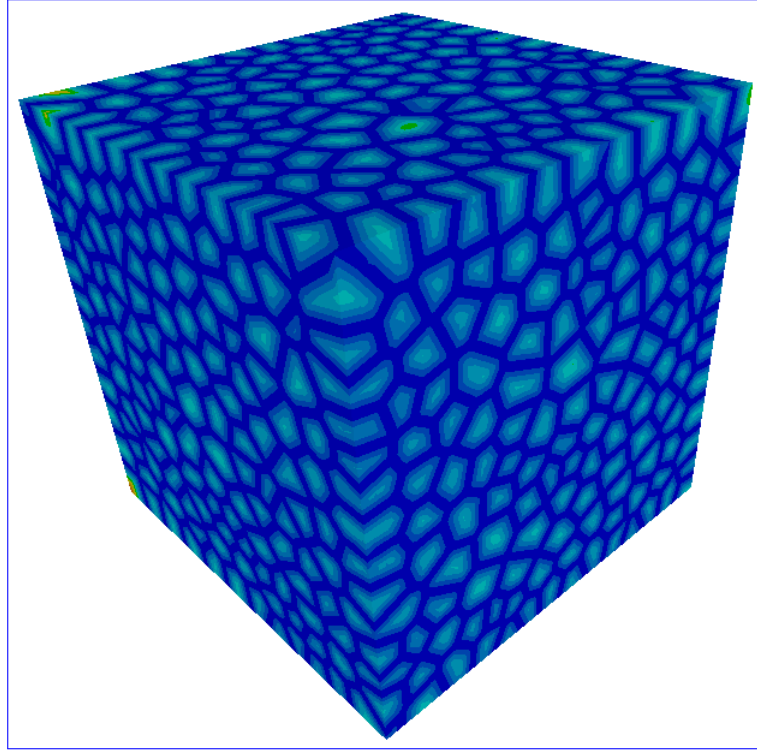


Figure 3.9: The obtained size distributions in the 3D equiaxial grain modelling case

intervals of the histogram distribution, we notice that the cell sizes are bigger than the wanted ones. This is due to the fact that when a sphere is generated at the middle of the domain, the corresponding Laguerre cell would be much larger.

### 3.3 Modelling applications: Experimental examples

In the previous section, some academic test cases were performed in order to validate and compare our methods to other preexisting methods. In this section, the statistics of powders and grains are issued from experimental data. In these cases, seven different domains, denoted  $\{S_i, 0 \leq i \leq 6\}$ , which correspond, respectively, to a  $1 \times 1$ ,  $2 \times 2$ ,  $3 \times 3$ ,  $8 \times 8$ ,  $12 \times 12$ ,  $16 \times 16$ , and  $20 \times 20$ , square domain, are used in 2D. In 3D, a  $0.5 \times 0.5 \times 0.5$  cube denoted  $E_0$  and a  $0.5 \times 0.5 \times 0.3$  parallelepiped denoted  $E_1$  are used.



*Figure 3.10: A 3D equiaxial grain RVE containing 1748 grains and generated using the GOA*

### 3.3.1 Powder RVE modelling

A laser granulometry was performed on a stainless steel 316L in order to get the statistics of its powder [30]. The radius distribution was found to follow a discrete probability law where each radius has a specific frequency of appearance. In 3D, this statistic was used in  $E_0$  and  $E_1$ . For the 2D calculations, performed in  $S_0$ ,  $S_1$  and  $S_2$ , the 3D statistics was converted thanks to the Saltykov technique [110]. It is important to underline that the considered granulometry, issued of experimental data, is clearly more complex than the classical granulometry reported in the literature. Indeed, as illustrated in Figure 3.11, the main difficulty comes from the important size ratio between the smaller and bigger spheres which must be considered. A comparison is performed between three different generation methods, the IPM, the POA and the dropping and rolling technique. The results obtained, in the two-dimensional case, are summarized in Table 3.4 and in Figure 3.11.

Figures 3.12a and 3.12b represent one of the calculations performed, using the IPM, in  $S_0$  containing 3595 discs before and after using the POA and Figure 3.12c represents one of the calculations performed, using the dropping and rolling algorithm, in  $S_0$  containing 3760 discs.

From these results, we can draw the following conclusions. When the POA or the

Domain	method used	mean number of discs	density	$L_2$ error in %
$S_0$	IPM	3427	0.776	2.54
	POA	3427	0.84	2.54
	Dropping Rolling	4085	0.8154	5.08
$S_1$	IPM	13939	0.779	1.25
	POA	13939	0.839	1.25
	Dropping Rolling	14978	0.818	1.5
$S_2$	IPM	29869	0.778	1.12
	POA	29869	0.84	1.12
	Dropping Rolling	33650	0.8197	1.31

Table 3.4: Statistics (mean for 20 calculations) of the 2D experimental powder modelling case

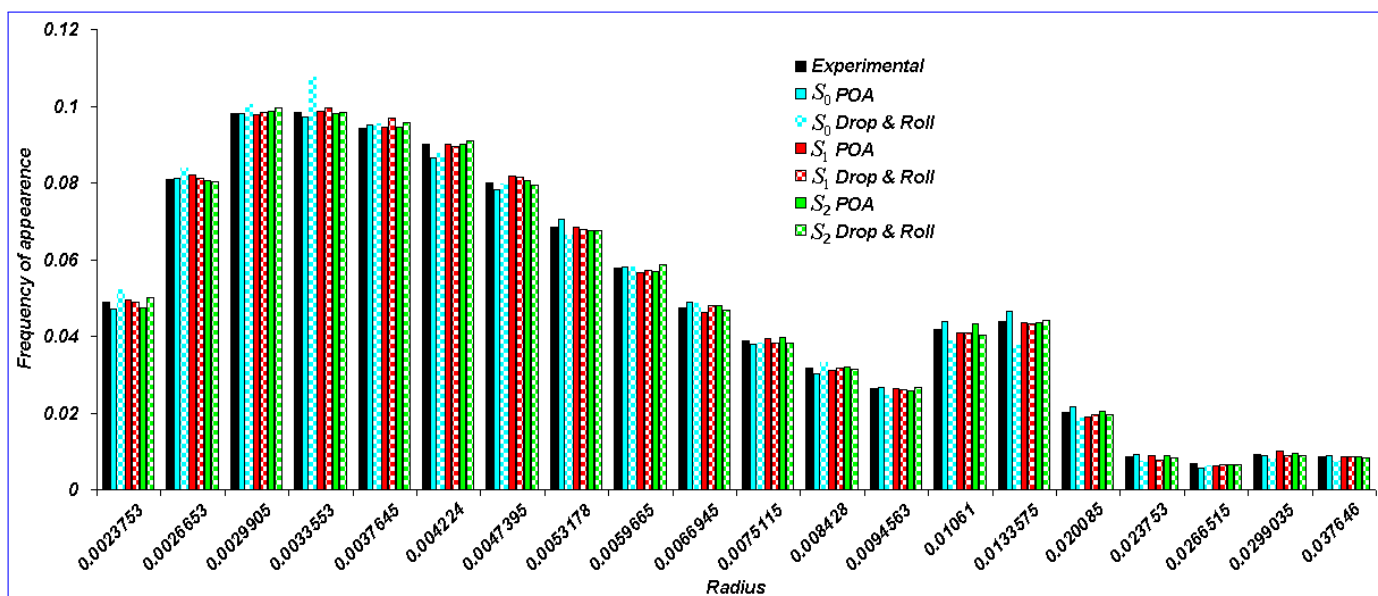
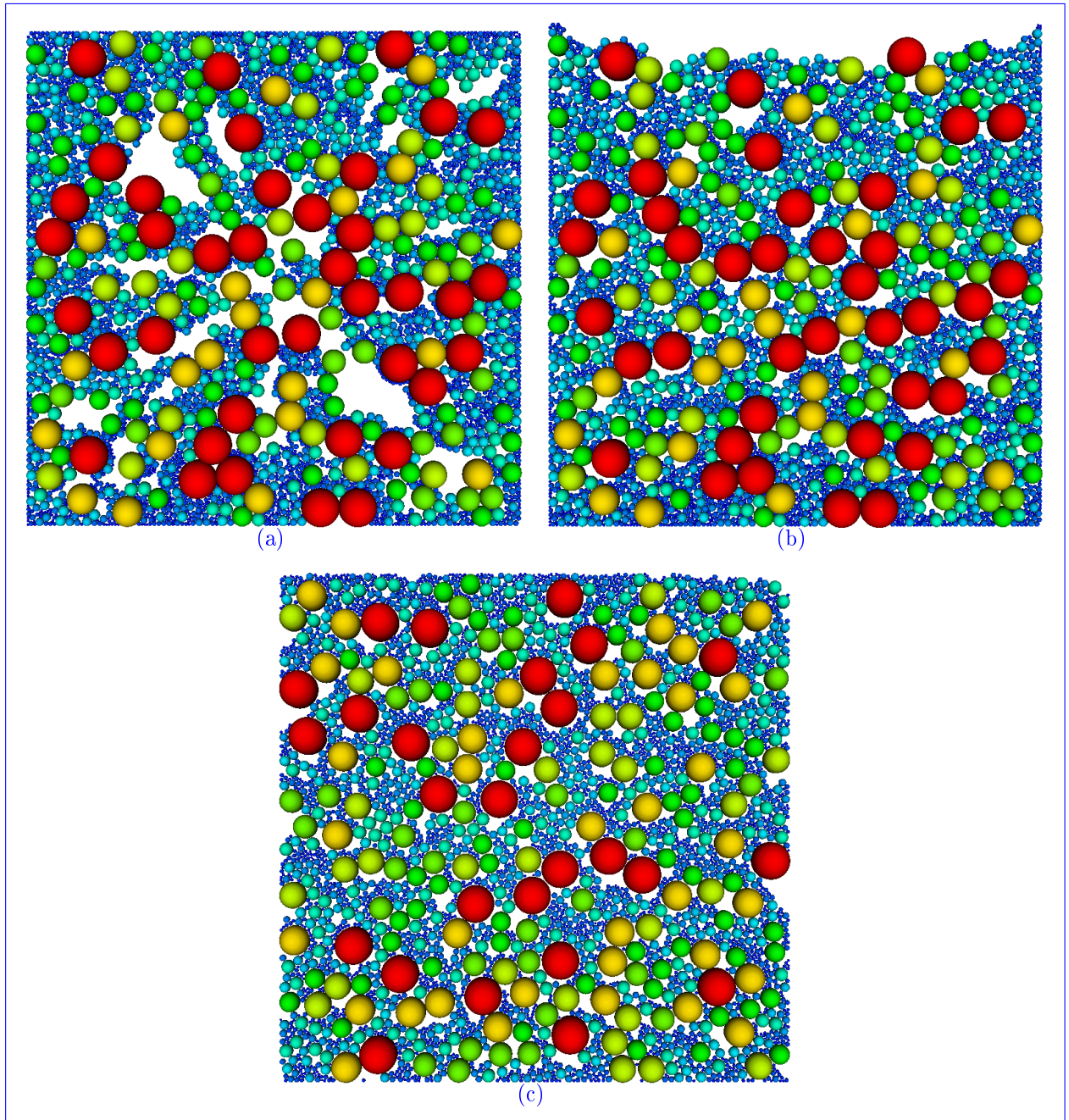


Figure 3.11: The frequencies obtained in  $S_0$ ,  $S_1$  and  $S_2$  for each generation method compared with the experimental frequencies

dropping and rolling algorithm are used, high densities representative of a powder RVE are obtained but higher values are achieved with the POA. And also, we converge towards the exact experimental statistics, using both methods, as the number of discs increases but with a slight improvement when the POA is used. This is due to the fact that the smaller particles have a higher probability than bigger ones to be generated at the highest region of the domain when the dropping and rolling technique is used. This fact is illustrated in the first four obtained frequencies in Figure 3.11 and in Figure 3.12c.

In 3D, 7750 was the mean number of spheres obtained in  $E_0$  with a mean  $L_2$  error



*Figure 3.12: (a) The powder RVE obtained using the IPM without the POA in  $S_0$ , (b) the same powder RVE when the POA is applied and (c) the powder RVE obtained using the dropping and rolling technique*

of 3.1% between the wanted and obtained distributions when the IPM was used. In this case, the mean sphere packing density obtained without using the POA was 0.358 which increased to 0.62 when the POA was used which resulted also in having a void region in

the domain bounded by the plane  $z = 0.3$  and  $z = 0.5$  (where  $z$  is the dropping and rolling direction). Hence, the dropping and rolling algorithm was performed in  $E_1$  in order to compare it to the POA using the same dimensions. It resulted in having a mean number of spheres of 9602 with a mean density of 0.578 and a mean  $L_2$  error of 4.26%. As for the two-dimensional cases, the POA generated powder RVEs with higher densities and lower  $L_2$  errors than the dropping and rolling technique. Once again, our IPM-POA coupled approach proved its efficiency in modelling 2D and 3D powder RVEs.

Figure 3.13 illustrates one of the runs, containing 7777 spheres generated using the IPM before and after applying the POA along with cuts at the middle of the domain to show the inner filling. In this run, when the POA was not applied, the sphere density was 0.365 and local voids were encountered at the inner part of the domain. After applying the POA and truncating the domain, the density increased to 0.64 and the local voids vanished. Figure 3.14 illustrates one of the runs, containing 9495 spheres generated using the dropping and rolling technique with a sphere density of 0.578 along with a cut at the middle of the domain to show the inner filling.

It is important to mention that in all the figures of this section, the ratio of the maximal and minimal radius is 15.85 while the maximal ratio used in previous works using an AFM was 7 [24, 25, 34, 38]. Our illustrations (see Figures 3.12a and 3.13b) show that the voids created using an AFM, or most precisely the IPM, are enhanced when this ratio is large. But it also shows that our optimization method (i.e. the POA) reduced greatly this void making the microstructure representative of a powder RVE (see Figures 3.12b and 3.13d).

### 3.3.2 Equiaxial polycrystal RVE modelling

A 2D pixelated image of a stainless steel 304L, containing 1387 grains, was obtained by EBSD [28]. A part of this image is illustrated in Figure 3.15 where the grain joints were identified and drawn in white lines. In this figure the twin boundaries, which occur when two or more crystals intergrow and have elongated or deformed shapes, were not taken into account.

Afterwards, the surface of each grain is calculated using the software Visilog 6.3. This surface is considered as the one of the equivalent generating spherical particle and hence, a statistic of the equivalent radius is obtained and used for generating the virtual, statistically equivalent, microstructure. The statistic of the equivalent radii was approached by a histogram distribution law. We performed our 2D calculations in  $S_3$ ,  $S_4$ ,  $S_5$  and  $S_6$  using the GOA. The results obtained are summarized in Table 3.5 and in Figure 3.16. In this test case, we added the mean number of neighboring grains to Table 3.5. This number is usually very close to 6 in an equiaxial polycrystalline material.

The results show that the  $L_2$  error decreases when the number of grains increases. Although, this error remains higher than 11%, the results remain acceptable considering the complexity of the size distribution. In what concerns the mean number of neighbors, the results show that we are close to 6 in all the considered domains. One of the calculations performed in  $S_3$  containing 3680 equiaxed grains is illustrated in Figure 3.17.

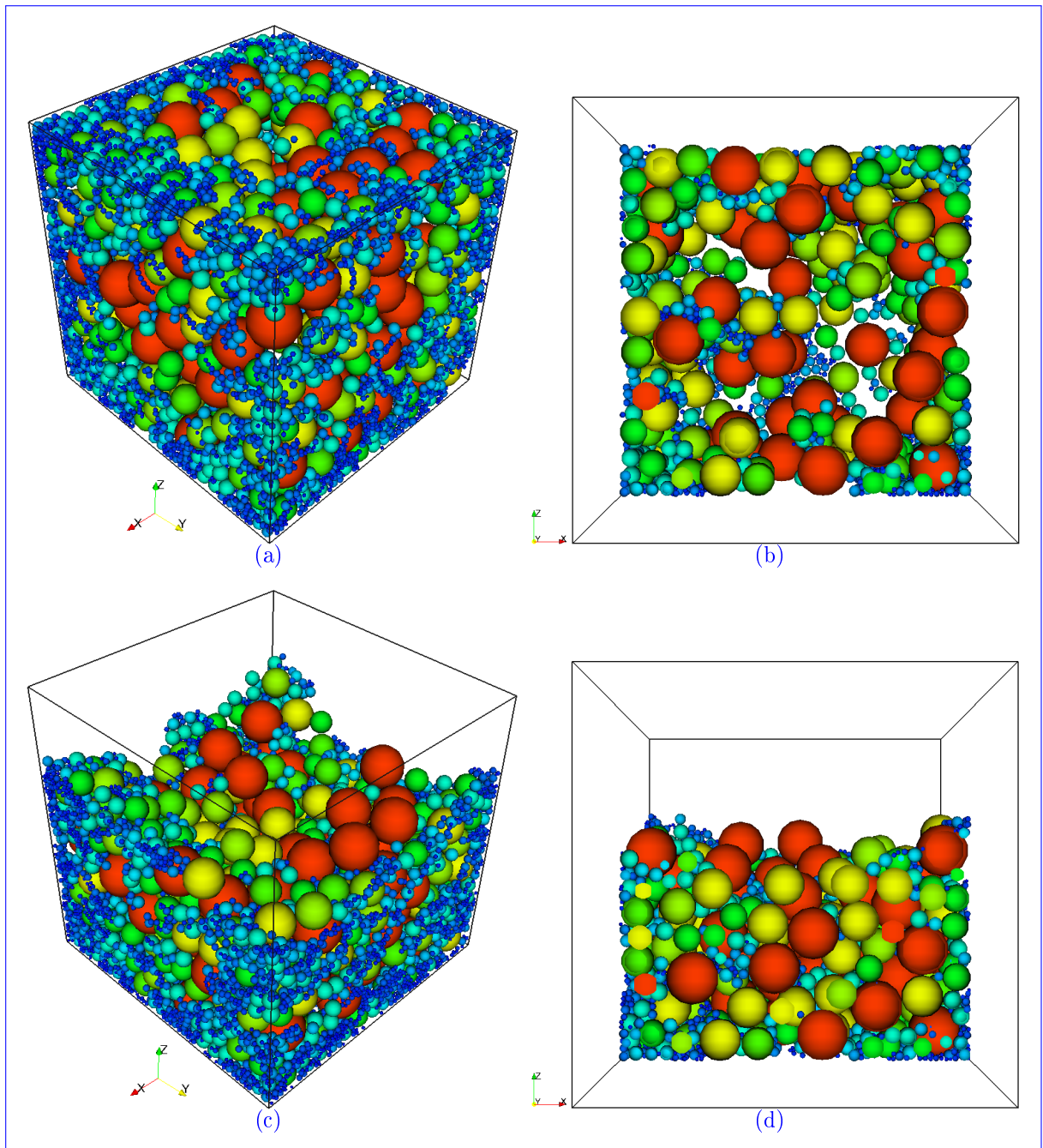
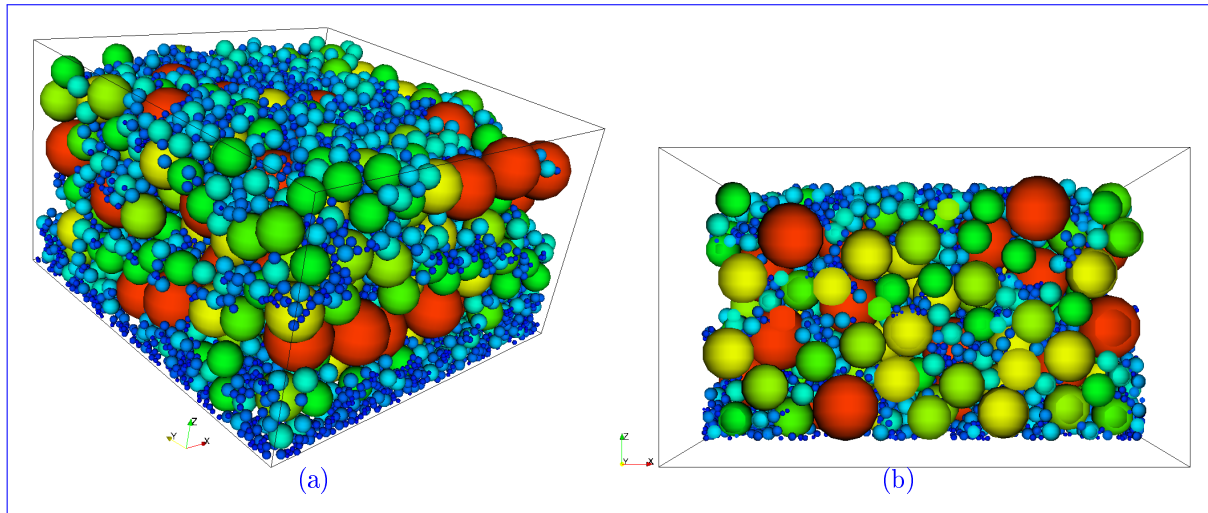
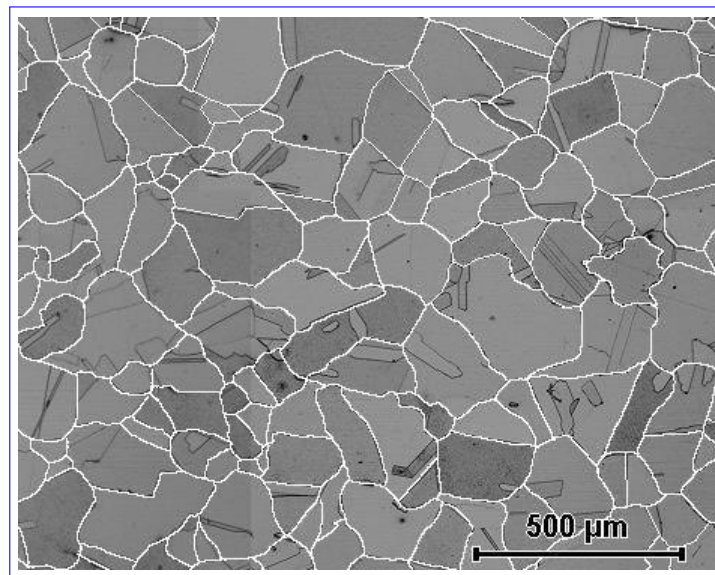


Figure 3.13: 7777 spheres in  $E_0$ , generated using the IPM, modelling a 3D powder RVE:  
 (a) the whole domain before applying the POA, (b) a cut at middle of the domain showing the inner filling before applying the POA, (c) the whole domain after applying the POA and (d) a cut at middle of the domain showing the inner filling after applying the POA



*Figure 3.14: 9495 spheres in  $E_1$ , generated using the dropping and rolling technique, modelling a 3D powder RVE: (a) the whole domain and (b) a cut at middle of the domain showing the inner filling*



*Figure 3.15: A microscopic illustration of a stainless steel 304L with grain joints drawn in white lines*

## 3.4 Conclusion

In this chapter, the ability of the POA, dedicated to powder modelling, to respect statistical data while achieving high density and the ability of the GOA, dedicated to equiaxial polycrystal modelling, to improve classical Laguerre tessellation technique were

Domain	mean number of grains	mean number of neighbors	$L_2$ error in %
$S_3$	3647	5.996	14.24
$S_4$	8296	6.024	13.27
$S_5$	15198	6.048	12.2
$S_6$	23628	6.06	11.67

Table 3.5: Statistics (mean for 20 calculations) of the 2D experimental grain modelling case

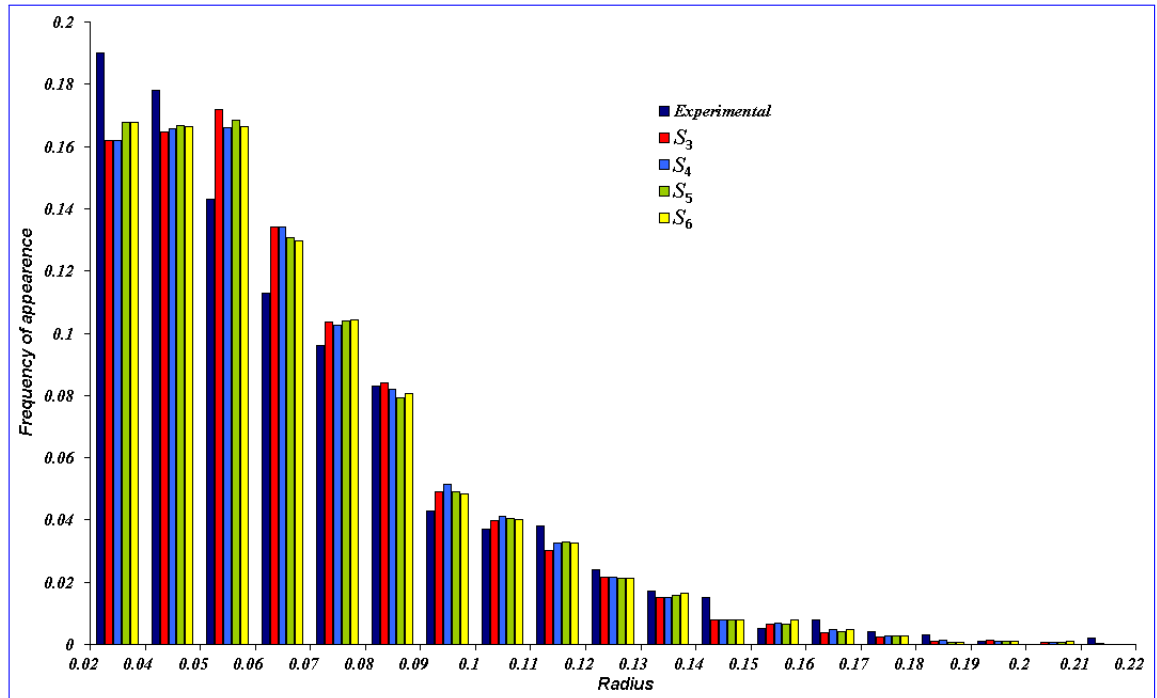
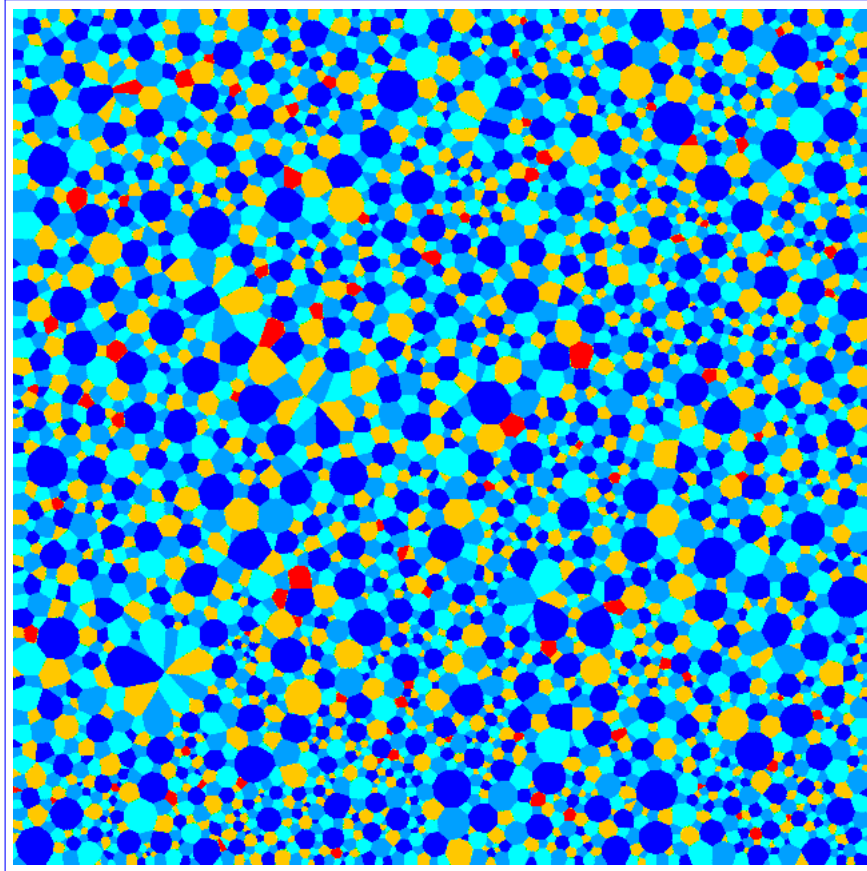


Figure 3.16: The frequencies obtained in all the domains compared with the experimental frequencies in the 2D case

illustrated.

Firstly, we compared our methods to other preexisting techniques. In the 2D powder modelling cases, the POA was compared to Bagi's densification method [24] and to Cui and O'Sullivan's triangulation method [103]. Our POA proved that it is more efficient than the two pre-cited methods in the sense that it answered to the three primordial criteria to model very precisely a powder: to achieve very high density, to respect precisely a given granulometry and to be realistic for the particles arrangement. In the 2D equiaxial polycrystal RVE modelling case, our GOA was compared to the Laplacian smoothing algorithm [38]. The results showed that the  $L_2$  error, between the wanted and obtained cell size distribution, was smaller when our algorithm was used. Furthermore, three-dimensional modelling cases were performed for both kinds of RVEs. A histogram



*Figure 3.17: An equiaxial polycrystal RVE containing 3680 grains obtained using the GOA in  $S_3$*

distribution law was used in both cases. As for the 2D cases, the POA proved its efficiency in modelling 3D powder RVEs and the GOA resulted in having acceptable  $L_2$  errors in the 3D equiaxial polycrystal RVE modelling.

Secondly, statistics issued from experimental data, more complex than the previous distributions, were used. In the 2D and 3D powder modelling cases, the POA was compared to the dropping and rolling technique. The results illustrated that the POA is slightly better than the dropping and rolling technique in terms of  $L_2$  errors and sphere packing densities. In the equiaxial polycrystal modelling case, the GOA resulted in having acceptable  $L_2$  errors considering the complex size distribution used.

### 3.5 Résumé français

Dans ce chapitre, la capacité du POA (consacrée à la modélisation de VERs de poudre), à respecter des données statistiques en obtenant des hautes densités et la capacité du GOA (consacrée à la modélisation de VERs de polycristaux equiaxes), à améliorer la

méthode classique du diagramme de Laguerre ont été illustrées. Les deux techniques ont été comparées avec d'autres méthodes d'optimisation afin de prouver leur efficacité.





# Chapter 4

## Level-Set Approach and Meshing Adaptation

### Contents

---

<b>4.1</b>	<b>Introduction</b>	<b>94</b>
<b>4.2</b>	<b>The Level-Set approach</b>	<b>95</b>
4.2.1	Voronoi tessellations	95
4.2.2	The Delaunay triangulation	96
4.2.2.1	Comparison of numerical costs	100
4.2.3	Cell spreading	102
4.2.4	Spherical particles	102
4.2.5	Laguerre tessellations and Open-cell foams	102
4.2.5.1	The weighted Delaunay triangulation	103
4.2.5.2	Laguerre tessellations	105
4.2.5.3	Three-dimensional open-cell foams	105
<b>4.3</b>	<b>Meshing adaptation</b>	<b>105</b>
<b>4.4</b>	<b>Conclusion</b>	<b>111</b>
<b>4.5</b>	<b>Résumé français</b>	<b>112</b>

---

## 4.1 Introduction

Explicit methods are often used to represent the microstructure's interface in a FE mesh. In [34, 38], this type of methods was used to represent the interfaces of granular structures defined by cells or by spherical particles. Most precisely, in a 2D context, a discretization of the boundary (microstructure's interface and domain boundary) according to a metric field, specified basing on the geometry and the proximity of grains, and the generation of a mesh of the points of the discretized boundary are firstly performed. Then, an adaptive scheme is proposed in order to generate quality meshes. These meshes are generated using a combined advancing front-Delaunay approach [51]. In the 3D context, the boundary is considered as a 2D surface and a surface mesh is built at first then a volume mesh is constructed. In these cases, the mesh generation is a long procedure combining steps of discretization, mesh construction and quality improvement. This method can be very costly for structures having a large number of grains especially in 3D. In [36, 52] a mesh was constructed for a 3D grain-based microstructure. First, a Voronoï tessellation is constructed by taking the centroids of the grains and additional points as the only seed points. Then, an initial mesh is generated by triangulating each face of each Voronoï cell. After triangulating each face, each corner of a triangle is connected to the seed point that generated the Voronoï cell to which the face belongs. This process produces a number of tetrahedral elements and ensures a conformal mesh because every face belongs to two Voronoï cells and thus the nodes on a face are the same for the two cells. After generating the initial mesh, the quality of the mesh is improved by performing additional steps. This method necessitates the construction of a Voronoï tessellation included inside the microstructure's grains and involves complex quality improvement techniques. Moreover, a regular rectangular FE mesh was used to perform mechanical loading on a 3D granular microstructure [111]. This technique uses the initial voxel-based image to construct the mesh but leads to some loss of fidelity of grain boundary morphology and to lower-resolution model.

In this work, we are going to use and detail an implicit method to capture the interfaces, the Immersed Volume Method (IVM) [55]. This method is based on the level-set approach to define the different interfaces, on mixing laws for physical properties and on meshing adaptation. The use of level-set functions to model equiaxed polycrystals made of Voronoï cells was introduced by Bernacki [15]. This approach was applied successfully for the generation of 2D or 3D polycrystals but for a moderate number of grains (less than 2000 in 3D). Indeed, one difficulty of this method is the numerical cost, which depends on the number of grains, as well as on the FE mesh used to describe the polycrystal. In this chapter, we describe the methodology to build Voronoï tessellations in a FE mesh using a level-set approach. An improvement in the computational time of the method described in [15] is also proposed. Also, the use of level-set functions to define Laguerre tessellations is introduced and the definition of spread cells to immerse foams or granular semi-solids is explained.

Furthermore, description of statistical RVEs in a monolithic context using a level-set framework undermines the necessity to work with a fine mesh at the interfaces of the

RVE not only to describe properly the considered microstructure but also to take into account possible discontinuities of physical properties when mechanical testing must be performed on this microstructure. Hence, section 4.3 is dedicated to a general overview of the existing mesh adaptation methods in CimLib. These methods are usually based on the level-set functions which are used to define the metric field used in remeshing [112]. We propose a new method for constructing this metric field. In our context, this method is based on a graph coloration algorithm [113] that limits the number of level-set functions used in remeshing.

## 4.2 The Level-Set approach

The location of the microstructures' interfaces are defined implicitly using a level-set framework. A level-set function  $\phi$ , defined over a domain  $\Omega$ , is called distance function of an interface  $\Gamma$  if, at any point  $x$  of  $\Omega$ , it corresponds to the distance from  $\Gamma$ . In turn, the interface  $\Gamma$  is then given by the iso-zero of the function  $\phi$  :

$$\begin{cases} \phi(x) = \pm d(x, \Gamma), x \in \Omega \\ \Gamma = \{x \in \Omega, \phi(x) = 0\} \end{cases} \quad (4.1)$$

In this document, a sign convention is used:  $\phi \geq 0$  inside the domain defined by the interface  $\Gamma$  and  $\phi \leq 0$  outside this domain. Figure 4.1 illustrates a level-set function of a square domain. The values of this function are positive inside the domain, negative outside and null at the interface.

In the following sections of this chapter we will explain how the level-set functions defining each type of microstructure are calculated.

### 4.2.1 Voronoï tessellations

For a node  $X$  of coordinates  $x$  of the FE mesh and two Voronoï nuclei  $S_i$  and  $S_j$ , the function [15]:

$$\alpha_{ij}(x) = \frac{1}{2} \left\| \overrightarrow{S_i S_j} \right\| - \frac{\overrightarrow{S_i S_j} \cdot \overrightarrow{S_i X}}{\left\| \overrightarrow{S_i S_j} \right\|} \quad for \quad 1 \leq i, j \leq N, \quad j \neq i, \quad (4.2)$$

with  $N$  the number of Voronoï nuclei, corresponds to the signed distance of  $X$  to the perpendicular bisector of  $[S_i S_j]$ . The level-set function  $\phi_i(x)$ , defining the Voronoï cell of the nucleus  $S_i$ , is then given by:

$$\phi_i(x) = \min_{\substack{1 \leq j \leq N \\ j \neq i}} (\alpha_{ij}(x)). \quad (4.3)$$

Figure 4.2 illustrates, in a 2D context, four level-set functions defining the cells of four different Voronoï nuclei.

A global unsigned distance function can also be defined as:

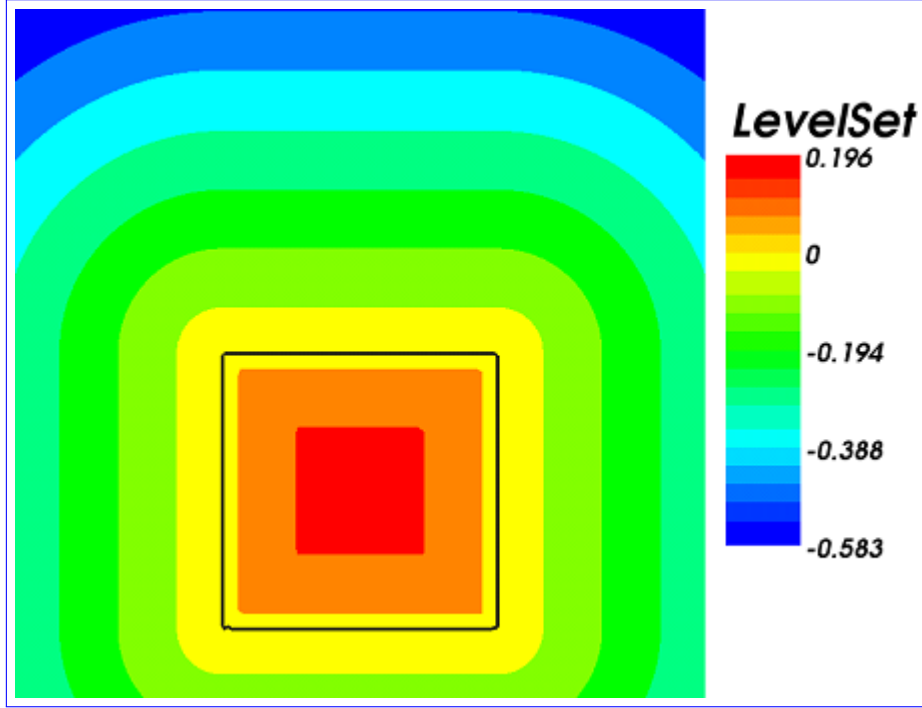


Figure 4.1: The level-set function of a square domain. The interface of the square is in black

$$\phi_{glob}(x) = \max\{\phi_i(x), 1 \leq i \leq N\}. \quad (4.4)$$

This function is positive everywhere and tends to zero on the cell boundary network. This function is shown in Figure 4.3 defining the Voronoï tessellation of the 4 nuclei in Figure 4.2. Also, Figure 4.4 illustrates the global distance function of 300 Voronoï cells in a three-dimensional case.

### 4.2.2 The Delaunay triangulation

The Voronoï tessellation can also be defined by constructing its dual, the Delaunay triangulation [51]. The Delaunay triangulation gives us the graph of each nucleus  $S_i$ , which is the set of the nuclei  $\{S_j, j \neq i\}$  that share the same edge of the Delaunay triangulation with  $S_i$ . In this section, we will explain the method used to construct the Delaunay triangulation and its importance on the calculation, in a FE mesh, of the level-set functions defining the Voronoï cells.

Let us begin by reminding about the 2D Delaunay's criteria (see Figure 4.5):

*A triangle net is a Delaunay triangulation if all the circumcircles of all the triangles in the net are empty, that is, if no vertices lie in the circles' interiors (Vertices may lie*

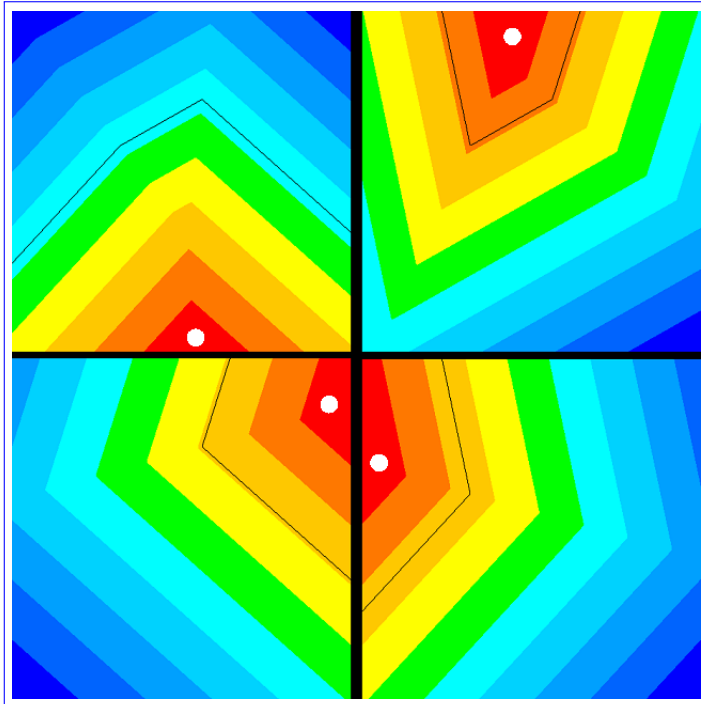


Figure 4.2: Four level-set functions defining four Voronoi cells. The Voronoi nuclei are the white dots and the cells' interfaces are in black

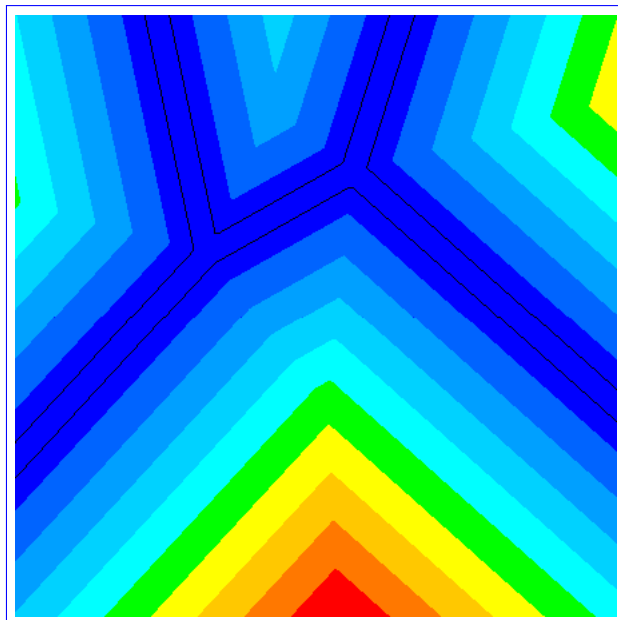


Figure 4.3: The  $\phi_{\text{glob}}(x)$  function corresponding to 4 Voronoi cells

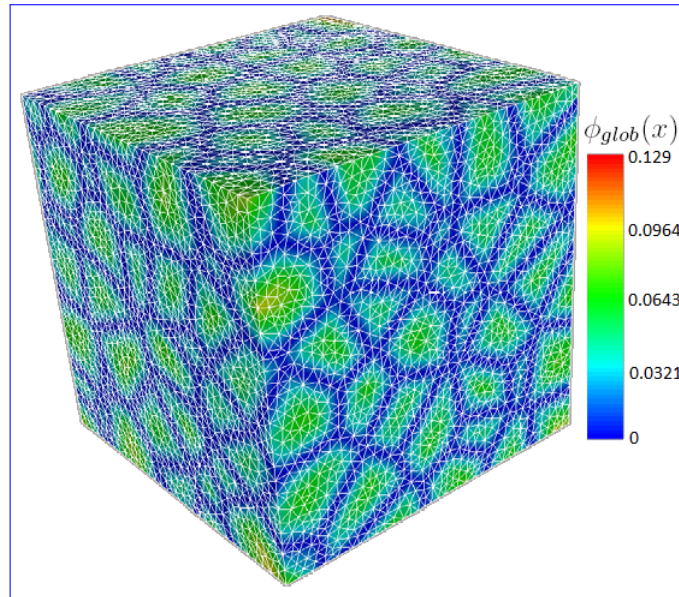


Figure 4.4: The  $\phi_{glob}(x)$  function corresponding to 300 Voronoï cells [17]. FE mesh in white

on the perimeter of any circumcircle.)

This is the original definition for two-dimensional spaces. It is possible to use it in three-dimensional spaces by using a circumscribed spheres in place of the circumscribed circles.

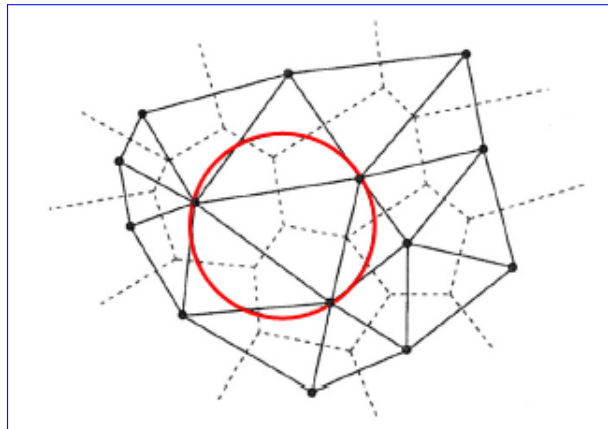


Figure 4.5: The Delaunay triangulation (full lines) and the corresponding Voronoï tessellation (dashed lines) [51]

For the construction of the Delaunay triangulation, the classical incremental method is used [51]. The first step consists in building an initial triangulation  $T_0$ . This triangulation

is given by what is called the "*supertriangle*" (or "*supertetrahedron*" in 3D) [114], which is one big triangle (tetrahedron) that would contain the union of the circles (spheres) of the final triangulation (see Figure 4.6).

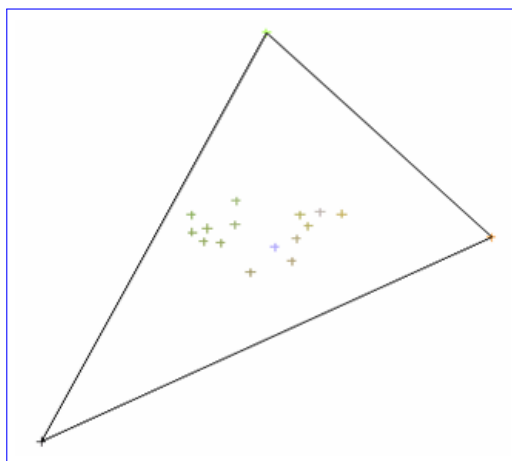


Figure 4.6: The supertriangle containing all the nuclei

Then, we suppose that  $T_i$ , the Delaunay triangulation of the first  $i$  nuclei, exists. Afterwards, we let the point  $P$  be the  $(i + 1)^{th}$  nucleus. The purpose is to build  $T_{i+1}$  such as it corresponds also to a Delaunay triangulation of the first  $(i + 1)$  nuclei. To this end, the Delaunay's kernel procedure is used. Since  $T_i$  contains the *supertriangle*,  $P$  is included in the triangulated domain  $T_i$ , then we define:

- $C_i^P$ , the cavity of  $P$ , which corresponds to the union of the elements of  $T_i$  which their circumscribed circle (circumscribed sphere) contains the point  $P$  (see Figure 4.7a)
- $B_i^P$ , the ball of  $P$ , which is the group of elements formed by joining  $P$  to the external edges of the cavity  $C_i^P$  (see Figure 4.7b)

And  $T_{i+1}$  is constructed as  $T_{i+1} = T_i - C_i^P + B_i^P$ . Since all the elements of  $T_i$  which their circumscribed circle (circumscribed sphere) contains the point  $P$  were removed and since the circumscribed circles (circumscribed spheres) of the new elements will not contain the point  $P$  because  $P$  is a vertex of all these new elements,  $T_{i+1}$  is a Delaunay triangulation.

At the end of the procedure, all the elements having a common vertex with the *supertriangle* (*supertetrahedron*) are removed.

Having constructed the Delaunay triangulation, the graph of each nucleus is at hand. The graph's information is important to calculate the level-set functions that define the Voronoï cells since the nucleus  $S_j$  giving the minimal value of  $\alpha_{ij}(x)$  (see Eq.(4.2)) is surely contained in  $Graph(S_i)$ . Indeed, the calculation of the level-set function  $\phi_i(x)$  can be simplified as follows:

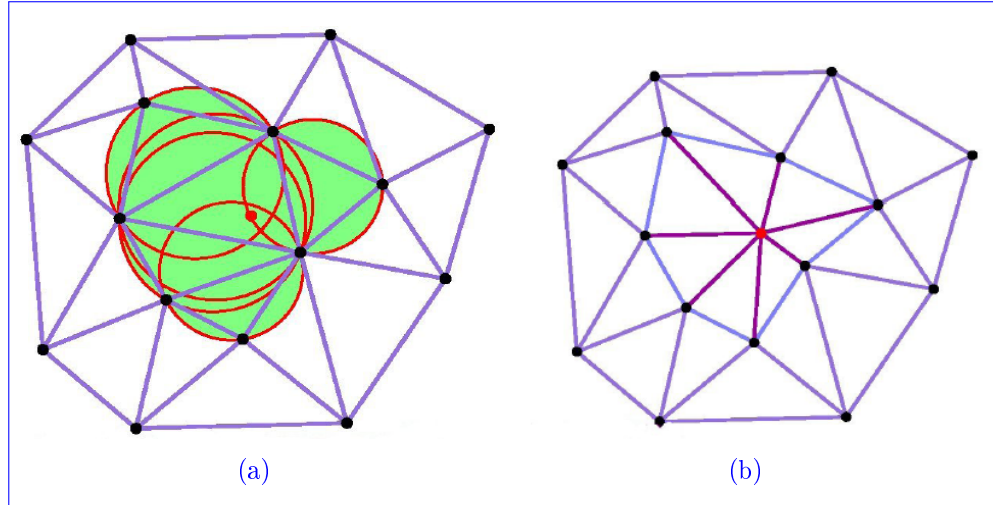


Figure 4.7:  $P$  is the red point: (a) The cavity of  $P$  and (b) the ball of  $P$

$$\phi_i(x) = \min_{S_j \in \text{Graph}(S_i)} (\alpha_{ij}(x)). \quad (4.5)$$

Figure 4.8 illustrates how useful the Delaunay triangulation is for calculating level-set functions. Without it, to calculate the level-set defining the Voronoï cell of a nucleus  $S_i$ , all the nuclei  $S_j$  ( $j \neq i$ ) must be taken into consideration in the algorithm. Thanks to the Delaunay triangulation, only the points  $S_j$  belonging to  $\text{Graph}(S_i)$  are considered.

#### 4.2.2.1 Comparison of numerical costs

Concerning the numerical cost, the new proposed algorithm undermines a supplementary step which is the Delaunay triangulation. The methodology used, which is the classical incremental technique [51], is an  $N^2$  algorithm; however this calculation is realized only once whereas the  $N^2$  algorithm realized for each node of the finite element mesh in Eq.(4.3) is replaced by an  $N \cdot \log N$  algorithm thanks to Eq.(4.5). The gain realized is illustrated by the following examples where we have compared the computing times of both algorithms described in a 2D and a 3D case. In 2D, the calculations were done in a unit square with two different finite element meshes. The first mesh, referred to as "Mesh 1" is made of 9901 nodes and 19456 elements and the second mesh, referred to as "Mesh 2" is made of 49457 nodes and 98161 elements. In 3D, the calculations were done in a unit cube with two different finite element meshes also. The first mesh in 3D, "Mesh 3", is made of 16192 nodes and 86518 elements and the second mesh in 3D, "Mesh 4" is made of 77669 nodes and 448586 elements. In "Mesh 1" and "Mesh 3" 300 and 1500 cells were generated whereas in the finest meshes "Mesh2" and "Mesh 4", 300, 1500 and 4500 cells were considered. All the calculations were performed using one processor. The results are given in Table 4.1. The algorithm made without using the Delaunay triangulation is referred to as "Algorithm 1" and the new one as "Algorithm 2".

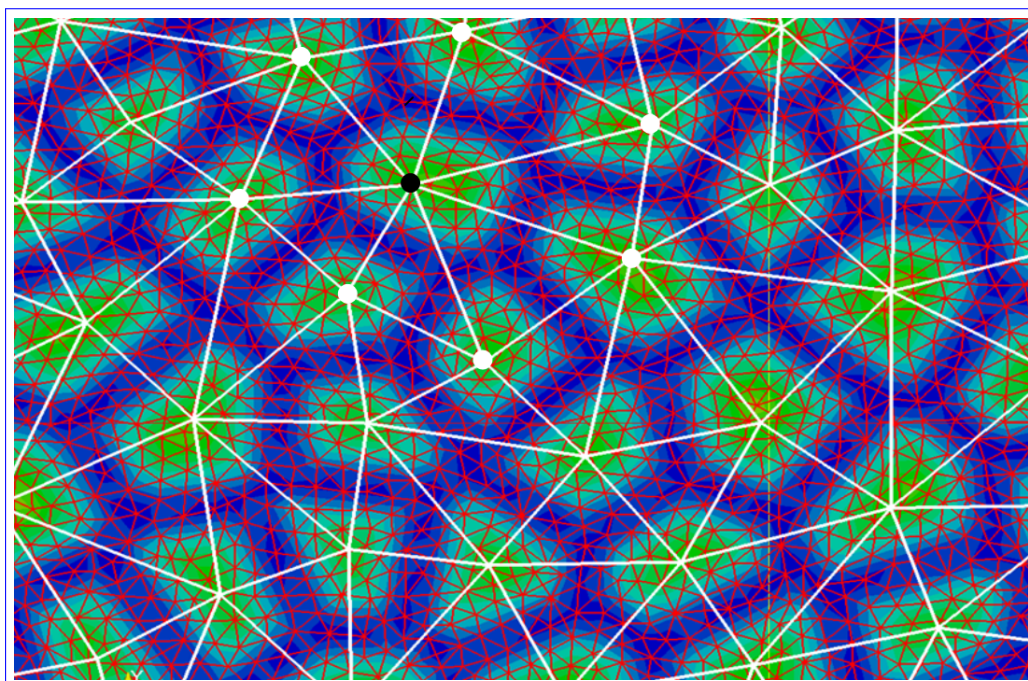


Figure 4.8: FE mesh (red), Delaunay triangulation (white), the nucleus  $S_i$  (black), its graph (white points) and the global level-set function defining the Voronoï tessellation

Number of sites	Algorithm	2D		3D	
		Mesh 1	Mesh 2	Mesh 3	Mesh 4
300	Algorithm 1	5min 28s	27min 8s	10min 9s	50min 40s
	Algorithm 2	4s	20s	19s	1min 38s
1500	Algorithm 1	2h 23min 40s	11h 22min 30s	4h 13min 43s	20h 12min 14s
	Algorithm 2	19s	1min 26s	1min 40s	6min 54s
4500	Algorithm 1		More than 2 days		More than 2 days
	Algorithm 2		4min 25s		21min 25s

Table 4.1: Comparison of the two algorithms

The calculations for 4500 cells in "Mesh1" and "Mesh3" were not performed because both meshes are very coarse in the sense that each level-set function defining a Voronoï cell will be calculated on approximately 2 nodes in "Mesh1" and 4 nodes in "Mesh3" which can not be representative of a Voronoï cell. These results show clearly the importance of the Delaunay triangulation on the computing times for the calculation of the level-

set functions defining the Voronoï tessellations. And they illustrate as well that the calculation times of both algorithms are a linear function of the number of nodes of the FE mesh considered, and also the  $N^2$  complexity of Algorithm 1 and the  $N.\log N$  complexity of Algorithm 2 [57].

### 4.2.3 Cell spreading

The geometrical procedure to perform cell spreading was described in section 2.4.1. We are going to describe how this procedure is easily realized in our level-set context. Boundaries between adjacent cells can be spread by shifting them in the direction of each center with random values. These values, referred to as  $\epsilon_i$  can either follow a specific probability law or be defined by a set of boundary shifts  $\{\epsilon_1, \dots, \epsilon_N\}$  (see Figure 2.38). The new level-set functions are then written:

$$\phi_i(x) = \min_{S_j \in \text{Graph}(S_i)} (\alpha_{ij}(x)) - \epsilon_i, \quad (4.6)$$

In this case the global level-set function, given by Eq.(4.4), reaches zero at the interface of the spread-cell structure and has also negative values outside the cells (i.e. in the new formed area). Figure 4.9a shows the function  $\phi_{glob}(x)$  defining a 3D semi-solid granular structure with a solid fraction of 0.9 and Figure 4.9b illustrates the iso-zero of the global level-set function defining a 3D closed-cell foam made of 105 cells with a cell irregularity of 0.5 and a relative density of 0.215.

### 4.2.4 Spherical particles

In the same way, level-set functions defining the spherical particles, of center  $S_i$  and radius  $r_i$ , can be calculated by writing:

$$\phi_i(x) = r_i - \|\overrightarrow{S_i X}\|. \quad (4.7)$$

Figure 4.10 illustrate the global distance function of 243 discs generated by the POA and the iso-zero of this function.

### 4.2.5 Laguerre tessellations and Open-cell foams

In the case of Laguerre tessellations, the graph's information is given by the weighted Delaunay triangulation [115], dual of the Laguerre tessellation. In this section, we begin by explaining the construction of a weighted Delaunay triangulation then we detail the calculation of the level-set functions defining Laguerre cells and finally we explain the method used to generate three-dimensional open-cell foams.

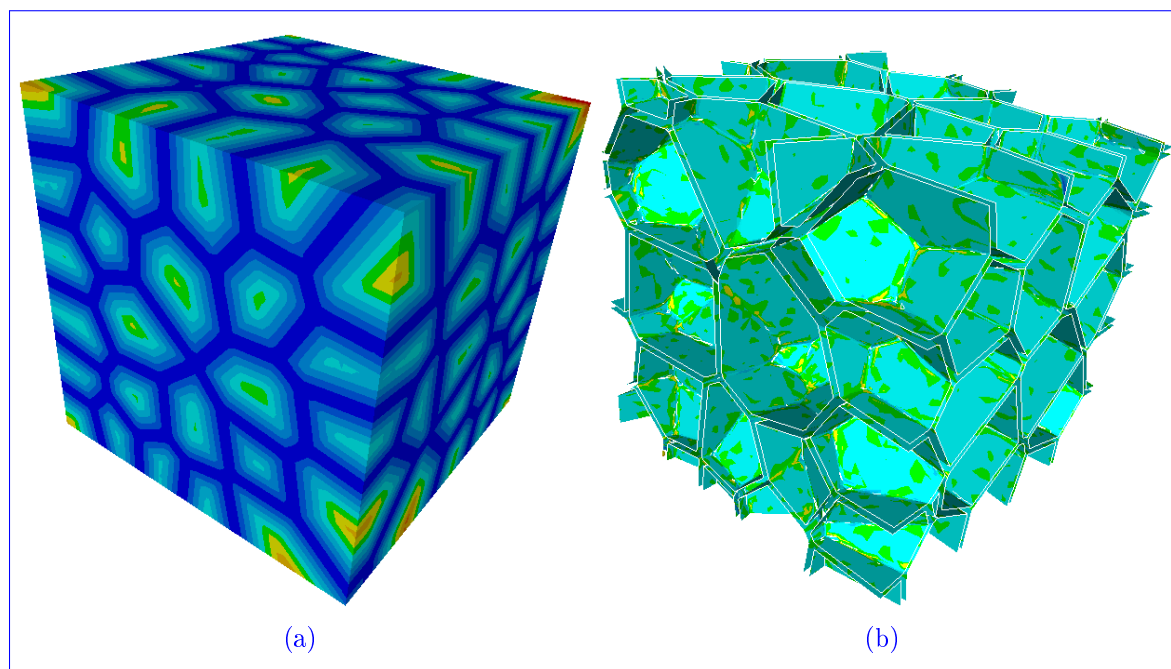


Figure 4.9: (a) The global level-set function  $\phi_{glob}(x)$  defining a 3D semi-solid granular structure with a solid fraction of 0.9 generated using the LTM and the cell spreading technique and (b) the global interface of a 3D closed-cell foam given by the iso-zero of  $\phi_{glob}(x)$

#### 4.2.5.1 The weighted Delaunay triangulation

The construction of the weighted Delaunay triangulation differs from that of the Delaunay triangulation only in the calculations of the circumscribed spheres (circumscribed circles in 2D). Here, we recall this calculation in 3D (the 2D case is similar). Let  $\mathcal{S}$  be a set of Voronoï nuclei and  $\mathbf{W}$  a set of positive scalars associated to  $\mathcal{S}$ . By definition, the circumscribed sphere of the tetrahedron whose vertices are the weighted points  $P_1$ ,  $P_2$ ,  $P_3$  and  $P_4$ , associated with the weights  $w_1$ ,  $w_2$ ,  $w_3$  and  $w_4$  is the sphere of center  $C$  and radius  $R$  satisfying:

$$R^2 = \|\overrightarrow{P_1C}\|^2 - w_1^2 = \|\overrightarrow{P_2C}\|^2 - w_2^2 = \|\overrightarrow{P_3C}\|^2 - w_3^2 = \|\overrightarrow{P_4C}\|^2 - w_4^2, \quad (4.8)$$

where  $\|\overrightarrow{P_iC}\|^2$  is the Euclidean distance between the point  $P_i$  and the center  $C$ . The square of the radius  $R$  of the circumscribed sphere is called the power of the center  $C$  to the points  $P_1$ ,  $P_2$ ,  $P_3$  and  $P_4$ . The expression above means that the point  $C$  has the same power to the vertices of the tetrahedron, and the circumscribed sphere is said empty if the power of  $C$  to all the other weighted points of  $\mathcal{S}$  is greater than or equal to  $R^2$ . Thus, among all the points of the space, the center  $C$  is the nearest point, in a weighted measure, to the vertices  $P_i$  of the tetrahedron.

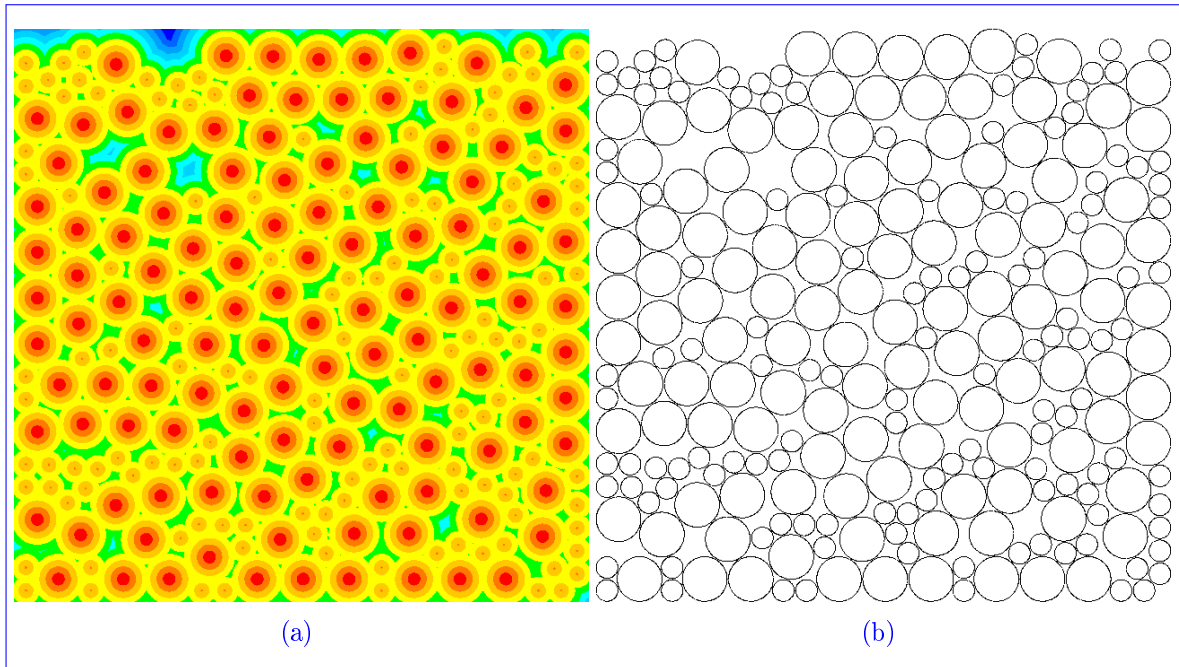


Figure 4.10: (a) The global level-set function  $\phi_{\text{glob}}(x)$  defining 243 discs and (b) the global interface of the discs given by the iso-zero of  $\phi_{\text{glob}}(x)$

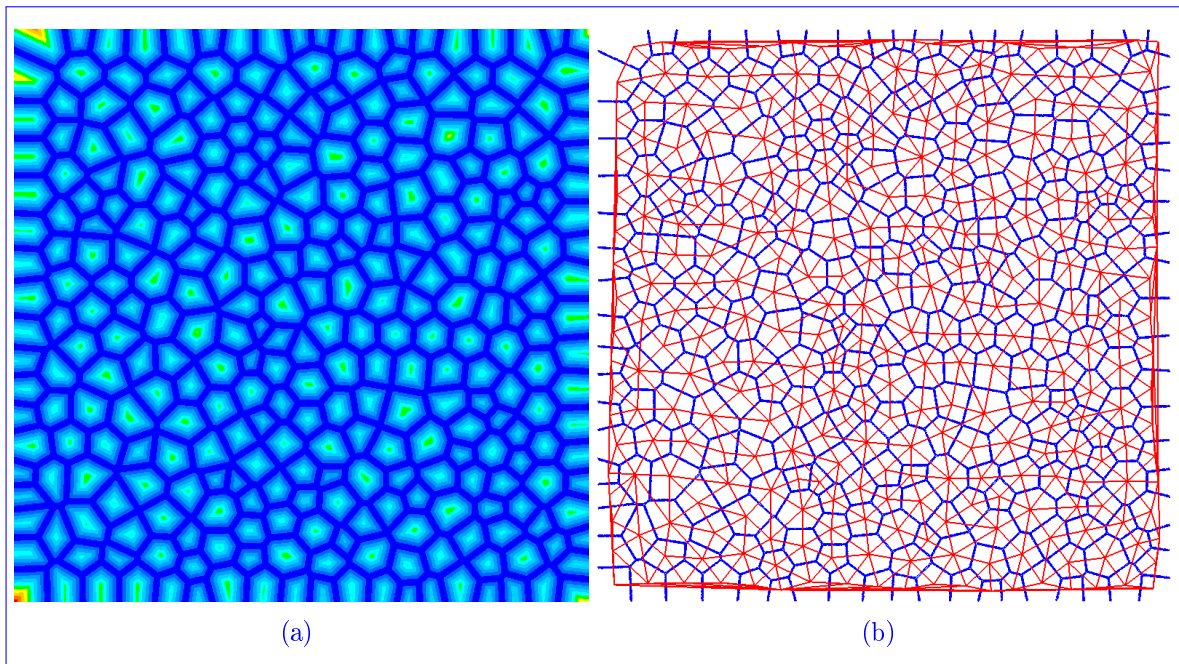


Figure 4.11: (a) The global level-set function  $\phi_{\text{glob}}(x)$  defining 306 Laguerre cells and (b) the global interface of the cells given by the iso-zero of  $\phi_{\text{glob}}(x)$  (in blue) and the weighted Delaunay triangulation (in red)

### 4.2.5.2 Laguerre tessellations

The level-set functions defining Laguerre cells are also given by Eq.(4.5) (with  $Graph(S_i)$  given by the weighted Delaunay triangulation) but the functions  $\alpha_{ij}$  (see Eq.(4.2)) are modified as follows:

$$\alpha_{ij}(x) = \frac{1}{2} \left( \frac{\|\overrightarrow{S_i S_j}\|}{\|\overrightarrow{S_i S_j}\|} + \frac{r_i^2 - r_j^2}{\|\overrightarrow{S_i S_j}\|} \right) - \frac{\overrightarrow{S_i S_j} \cdot \overrightarrow{S_i X}}{\|\overrightarrow{S_i S_j}\|^2}, \quad 1 \leq i, j \leq N, \quad j \neq i, \quad (4.9)$$

where  $r_i$  and  $r_j$  are respectively the radii of  $S_i$  and  $S_j$  (see Figure 4.11).

### 4.2.5.3 Three-dimensional open-cell foams

The three-dimensional closed-cell foams are generated using the Laguerre method coupled with cell spreading. The difficulty lies in removing the faces of the cells (or some cells) to model open-cell foams. To this end, a level-set function that defines an open-cell foam was developed. The idea is to force intersections between the spheres included in the Laguerre cells and then computing the level-set function of these cells without the intersection zone. Figure 4.12 represents a 2D case (for sake of clarity) where we forced intersections between five discs.

The goal is to compute the level-set function of the blue domain  $\Omega_b$ . This domain corresponds to the intersection between the complement of the union of the cells and the complement of the union of the discs:

$$OC = \overline{\bigcup_{i=1,\dots,5} C_i} \cap \overline{\bigcup_{i=1,\dots,5} S_i}. \quad (4.10)$$

Furthermore, if  $\phi_{closed-cell}$  and  $\phi_{spheres}$  are the level-set functions of the Laguerre cells and the spheres respectively, then  $-\phi_{closed-cell}$  and  $-\phi_{spheres}$  are the level-set functions of  $\overline{\bigcup C_i}$  and  $\overline{\bigcup S_i}$  respectively. Finally, the level-set function of the open-cell foam can be written as:

$$\phi_{open-cell} = \min\{-\phi_{closed-cell}, -\phi_{spheres}\} = -\max\{\phi_{closed-cell}, \phi_{spheres}\}. \quad (4.11)$$

Figure 4.13 shows the same foam with closed-cells and open-cells where intersections between the spheres included in the cells were generated. The technique of creating open-cell foams is a step forward in modelling this type of microstructure but in the framework of this thesis, we did not deal with the FE modelling concerning three-dimensional open-cell foams.

## 4.3 Meshing adaptation

Until now, we have only discussed the immersing procedure of the considered microstructures in a FE mesh without dealing with the problem of mesh precision necessary for obtaining microstructures such as the ones illustrated in Figures 4.9, 4.10 and 4.13.

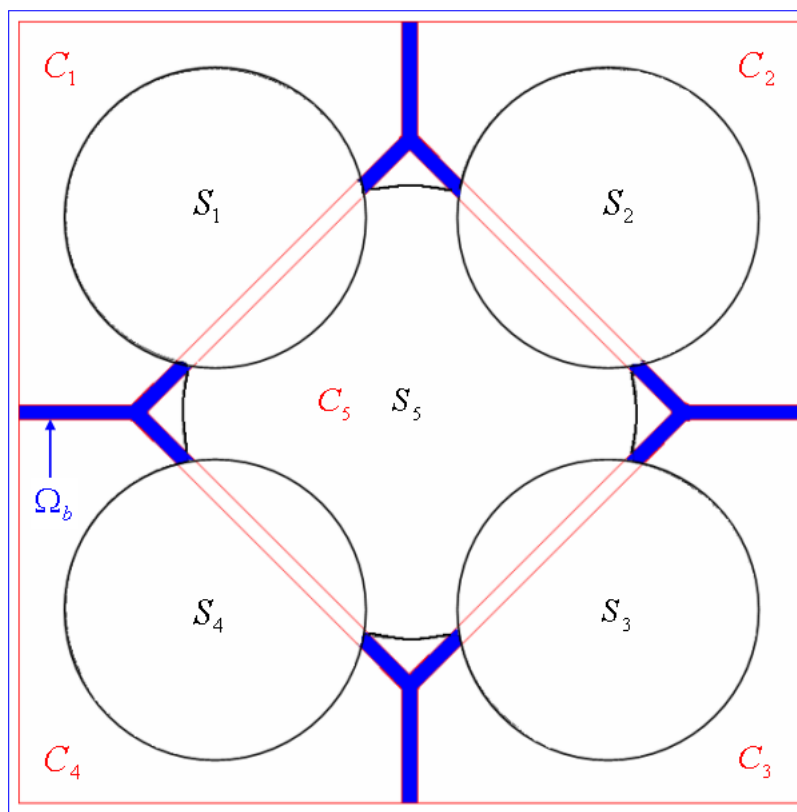


Figure 4.12: Representation of an open-cell foam in 2D where intersections between the Laguerre cell generating discs were forced

Isotropic refinement of the mesh can be used to reach a desired accuracy in the interface description. However, this strategy leads to a significant increase of computation resources. Therefore, an adaptive anisotropic remeshing technique is preferred. Different ways exist to generate adapted anisotropic meshes. A common approach consists in using an *a posteriori* error analysis in order to obtain an optimal mesh for a given physical field and number of elements [116, 117]. However this approach could be inappropriate in our case when an important number of level-set functions must be considered. Most precisely, when some strictly disjoint objects are described by level-set functions, a simple solution consists to adapt the mesh thanks to an *a posteriori* error estimator to the corresponding  $\phi_{glob}$  function [117]. However, such an approach is not straightforward when the different objects considered are not strictly disjoint as for some microstructure considered in this work (polycrystal, powder). These remarks explain why we preferred to deal with an automatic geometrical method for the generation of anisotropic mesh. The following method was initially developed for the multiscale modelling of microstructure evolutions in polycrystalline materials [15, 16, 56] and most recently adapted to the generation of granular semi-solid RVEs [17]. A brief recall of this method is described and an optimization procedure is proposed.

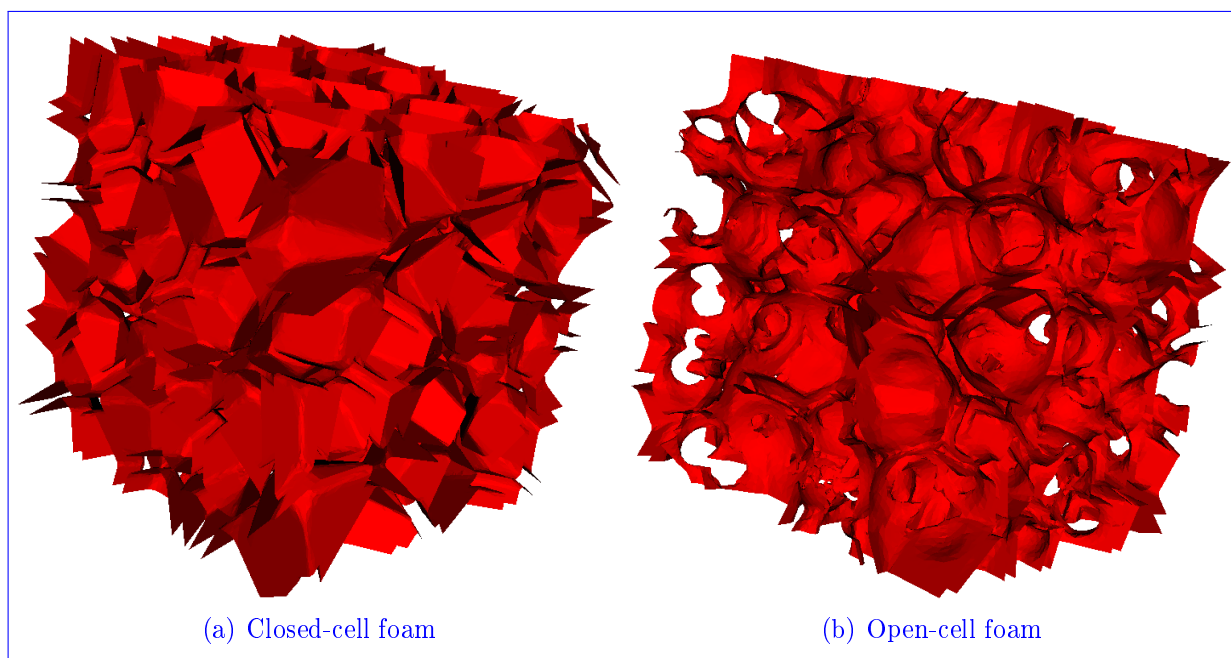


Figure 4.13: A three-dimensional foam

The idea of this method consists in fixing mesh refinement in a narrow zone surrounding the different interfaces. Besides, the refinement operates only in the direction perpendicular to the interface, which leads to anisotropic meshes. This anisotropic (re-)meshing method leads to a very high accuracy near the interfaces without increasing dramatically the computation resources [118].

The generation of such meshes requires the definition of a metric field and the use of a topological mesher. Anisotropic meshes are built using the MTC mesher-remesher developed by Coupez [118]. It is based on local mesh topology optimizations and works for all meshing applications from adaptive remeshing to mesh generation by using a minimal volume principle. MTC improves the mesh topology by considering the quality of the elements. The quality of an element is defined through a shape factor which takes into account the considered metric [112]. A metric is a symmetric positive definite tensor which represents a local base modifying the way to compute a distance, such that:

$$\|\vec{u}\|_{\mathbf{M}} = \sqrt{{}^t\vec{u}\mathbf{M}\vec{u}}, \quad \langle \vec{u}, \vec{v} \rangle_{\mathbf{M}} = {}^t\vec{u}\mathbf{M}\vec{v}. \quad (4.12)$$

If  $\mathbf{M}$  is the identity tensor, the distance corresponds to the usual one in the Euclidean space. As  $\mathbf{M}$  is a symmetric positive definite tensor, it is diagonalizable in an orthonormal basis of eigenvectors, and all the eigenvalues are strictly positive. The metric  $\mathbf{M}$  can be interpreted as a tensor whose eigenvalues are linked to the mesh sizes, and eigenvectors defining the directions in which these mesh sizes are applied. Let us consider the simple case of only one interface. The iso-zero of the level set function represents the boundary,  $\Gamma$ , and the gradient of the level set function defines the normal to the boundary which

corresponds to the direction of mesh refinement. To define the mesh size in that direction, and its distribution in space, a characteristic thickness  $E$  is introduced:

$$\begin{cases} |\phi(x)| \leq \frac{E}{2} & \text{near the interface} \\ |\phi(x)| > \frac{E}{2} & \text{far from the interface} \end{cases} \quad (4.13)$$

The mesh size takes a default value far from the interface, and is reduced in the perpendicular direction to the interface when  $|\phi(x)|$  is reduced. Let  $h_2$  be the desired refined mesh size in the direction of  $\nabla\phi$ , and  $h_1$  the desired mesh size in the perpendicular directions to  $\nabla\phi$ . Let us finally require an isotropic mesh size equal to  $h_0$  outside the anisotropic boundary layer. The corresponding metric  $\mathbf{M}$  is then expressed as follows:

$$\mathbf{M} = C(\nabla\phi \otimes \nabla\phi) + B\mathbf{I}, \quad (4.14)$$

with  $\mathbf{I}$  the identity matrix,  $B$  and  $C$  scalars given by:

$$B = \begin{cases} \frac{1}{h_0^2} & \text{if } |\phi(x)| > \frac{E}{2} \\ \frac{1}{h_1^2} & \text{if } |\phi(x)| \leq \frac{E}{2} \end{cases}, \quad C = \begin{cases} 0 & \text{if } |\phi(x)| > \frac{E}{2} \\ \frac{1}{h_2^2} - \frac{1}{h_1^2} & \text{if } |\phi(x)| \leq \frac{E}{2} \end{cases} \quad (4.15)$$

The eigenvalues of the metric near the boundary ( $|\phi(x)| \leq \frac{E}{2}$ ) are  $\lambda_2 = (1/h_2^2 - 1/h_1^2)\|\nabla\phi\| + 1/h_1^2$ , and  $\lambda_1 = \lambda_3 = 1/h_1^2$ . The former is associated to the eigenvector  $\mathbf{v}_2 = \nabla\phi$ , and the latter to the basis vectors  $(\mathbf{v}_1, \mathbf{v}_3)$  of the plane tangent to the boundary. Moreover, this metric is well equal to  $\frac{1}{h_0^2}\mathbf{I}$  far from the boundary ( $|\phi(x)| > \frac{E}{2}$ ) which corresponds to imposing an isotropic mesh size equal to  $h_0$  in this zone. Clearly, if  $h_2$  is chosen much smaller than  $h_1$ , which is chosen equal to  $h_0$ ,  $\nabla\phi$  corresponds to the refinement direction and the elements are only stretched in the tangent plane near the interface.

It could be also underlined that working with less (resp. more) anisotropic mesh near the interface corresponds to taking a value of  $h_2$  less close (resp. closer) to  $h_1$ . Furthermore, defining  $h_2$  as a function of  $\phi$  and not as a constant enables to obtain a progressive anisotropic refinement rather than a rough anisotropic refinement. When dealing with strictly separated cells (for example solid grains in a semi-solid granular structure in [17]), the above technique can be used by considering the global following distance function  $\phi_{glob}(x)$ . However, when contacts exist between the different cells (as for a polycrystal RVE or a powder RVE), this technique can no longer be used. Indeed, the gradient of the function  $\phi_{glob}(x)$  then becomes locally discontinuous and the normal to the interfaces is not properly defined. To solve this difficulty, multiple level set functions are used (one for each cell) to characterize the appropriate refinement directions and the corresponding metric. Two cases can be considered:

(A)  $|\phi_i(x)| > \frac{E}{2}$  for  $1 \leq i \leq N_c$ , where  $N_c$  is the number of cells, which means that  $x$  lies far from any cell interface. These points correspond to the isotropic regions with mesh size  $h_0$ .

(B)  $|\phi_i(x)| \leq \frac{E}{2}$  for  $n$  cells,  $n \leq N_c$ . The  $n$  vectors  $\nabla\phi_i$  along which refinement is required define a vector space  $\mathbf{V}$  of dimension 1, 2, or 3.

In case (B), if  $\mathbf{V}$  is one-dimensional, there is only one direction of mesh refinement and the metric takes the form given by Eqs. (4.14) and (4.15). When  $\mathbf{V}$  is three-dimensional, an isotropic metric is chosen, this time with the reduced mesh size  $h_2$ . When  $\mathbf{V}$  is two-dimensional, the required refinement is obtained with the following metric:

$$\mathbf{M} = C(\nabla\phi_1 \otimes \nabla\phi_1) + C(\vec{w} \otimes \vec{w}) + B\mathbf{I}, \quad (4.16)$$

with  $\vec{w}$  such as  $(\nabla\phi_1, \vec{w})$  corresponds to an orthonormal basis of  $\mathbf{V}$ . The metric (4.16) prescribes, in the anisotropic zone, a mesh size  $h_2$  in the plane  $\mathbf{V}$ , and a mesh size  $h_1$  in the direction normal to  $\mathbf{V}$  (which implies an isotropic mesh of mesh size equal to  $h_2$  near the interface in 2D context). Figure 4.14 illustrates a result obtained for a 2D case in a unit square made of 64 Laguerre cells. The anisotropic mesh adaptation was realized at the cells interfaces with the following parameters:  $h_1 = h_0 = 0.01$ ,  $h_2 = 2.10^{-4}$  and  $E = 3.10^{-3}$ . The anisotropic mesh, made of 30687 elements, was obtained in 92 seconds in a four processors parallel calculation. The zoom in Figure 4.14b illustrates the good meshing adaptation obtained at a triple junction with fine isotropic elements as required by the number of independent refinement directions in this zone.

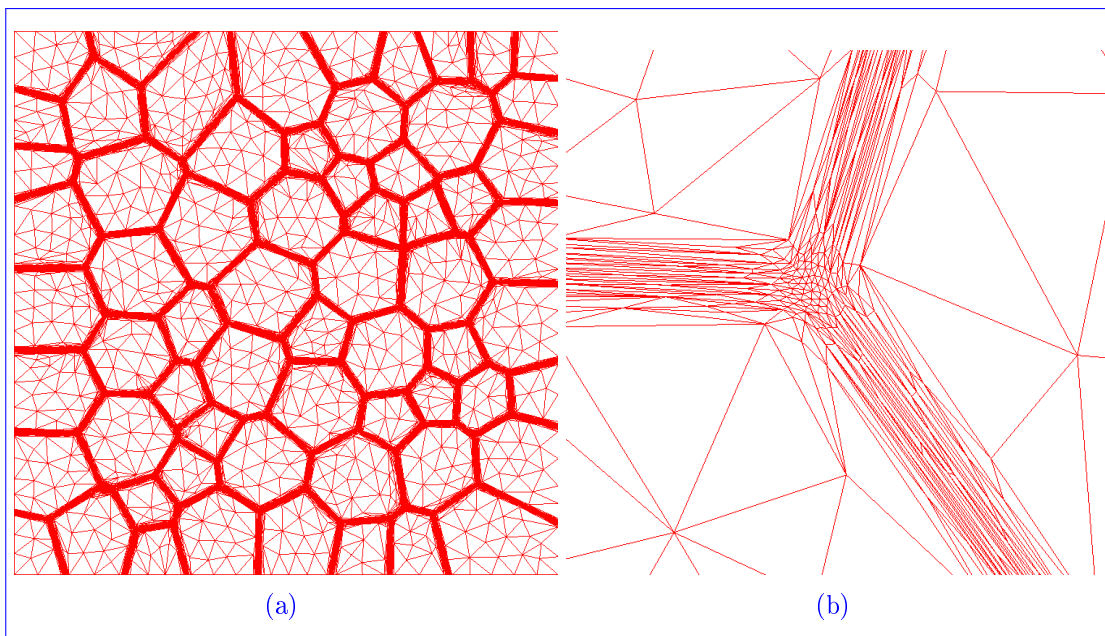


*Figure 4.14: (a) Anisotropic meshing adaptation for an equiaxial polycrystal and (b) zoom at a triple junction*

If this approach is efficient and allows obtaining easily appropriate meshing adaptation for complex RVEs, its principal weakness remains its numerical cost particularly in 3D. A first waste of computational resources can be identified in the fact to work with one level-set per cell. Indeed, on the majority of the RVEs considered, the microstructure is built to represent only two phases as for granular semi-solids, foams obtained by spreading Voronoï tessellation but also for powders. Even for the recrystallization modelling in polycrystal

RVEs, a global velocity depending of local characteristics can be defined without the knowledge of individual grains [15, 56]. Finally, in all these cases, knowing the individual level-set function of each cell is not a necessity to perform numerical modelling. Moreover, the important point for the meshing strategy proposed is not inevitably to know all the level-set functions but to deal with a set of level-set functions representing sets of strictly disjoint cells and which the gathering corresponds to the whole microstructure considered. The simple method proposed here, to limit the number of requisite level-set functions for meshing adaptation, is to use the classical technique of graph coloration [113]. The idea is to colour the vertices of a graph such that no two adjacent vertices share the same colour with a minimal number of colours. Graph colouring is a very active field of research and some results of this domain are famous such as the four colour theorem [119]. The idea developed in this work is to use a simple graph coloration algorithm of the Delaunay (or weighted Delaunay) triangulation calculated in our algorithm of generation of RVEs to gather all the level-set functions of the cells involved in few new level-set functions presenting the properties to correspond to a set of strictly disjoint cells and so, usable for the meshing strategy described previously.

Although quite old, the DSATUR coloration algorithm [120] remains an interesting choice of coloration method in term of ratio "computational cost/number of colours obtained". This algorithm, described below along with some examples, was added to our RVE builder:

**DSAT.1** Construct the graph of each site (Voronoi nucleus or spherical particle's center) using the Delaunay triangulation (or weighted Delaunay triangulation).

**DSAT.2** Initiate all the vertices of the triangulation as uncolored and their degree of saturation as the number of neighbors. The degree of saturation of a vertex  $v$ ,  $Dsat(v)$ , is the number of colored neighbors.

**DSAT.3** While uncolored vertices still exist, do:

- (a) Find the vertex  $v$  with the maximal  $Dsat(v)$ .
- (b) If none of the neighbors of  $v$  have been colored with a color  $c$  that already exists, assign  $c$  as the color of  $v$ . Else, define a new color and assign it to  $v$ .
- (c) Calculate the degree of saturation of the neighbors of  $v$ .

**DSAT.4** End while.

The DSATUR algorithm enabled us to decrease the number of level-set functions from  $N_c$ , the number of cells, to  $N_{co}$ , the number of colors, by computing the global level-set functions (i.e. the maximum) of all the cells associated to the same color instead of having one level-set per cell. A comparison of computational costs was done on a 2D equiaxial polycrystal made of 356 grains. When the DSATUR algorithm was used, five level-set

functions were used to construct an anisotropic mesh made of 302110 nodes and 602505 elements in 16 minutes and 43 seconds using 8 processors. When the DSATUR algorithm was not used, 356 level-set functions were used (one level-set for each grain) to construct an anisotropic mesh made of 306501 nodes and 611298 elements in 1 hour 3 minutes and 40 seconds using the same number of processors. Four figures illustrate the efficiency of our algorithm. The case of Figure 4.15a corresponds to a 2D equiaxial polycrystal made of 2000 grains, and represented using five level-set functions obtained with the DSATUR algorithm (one colour per level-set function). The zoom in Figure 4.15b, illustrates the anisotropic meshing adaptation obtained thanks to the metric defined by Eqs.(4.15) and (4.16) and calculated with the five level-set functions. The mesh is made of 919955 nodes and 1836561 elements and was generated in 26 minutes using eight processors. Figure 4.16 represents a powder RVE containing 554 discs generated using the POA represented by five colors (i.e. five level-set functions) and a zoom at the anisotropic mesh made of 905895 nodes and 1809190 elements and constructed in 55 minutes using 4 processors. Figure 4.17 illustrates the same strategy applied to a 3D powder RVE made of 585 spheres, described thanks to eight level-set functions. The mesh is made of 2594907 nodes and 15223519 elements and was generated in 4 hours and 26 minutes using 16 processors. And the final one, Figure 4.18, illustrates a three-dimensional tetrakaidecahedral closed-cell foam made of 250 cells, generated using the Laguerre tessellations method and represented by eight level-set functions. The anisotropic mesh in this case is made of 768326 nodes and 4331151 elements and generated in 2 hours and 37 minutes using 16 processors.

Another important discussion concerns the computation times required to generate, immerse and remesh the considered microstructures. In this section, the computation times, mentioned above, were reported for a number of cells or spherical particles which can be used when performing a specific mechanical application in 2D or 3D. Given the fact that the particle generation phases (IPM and POA or GOA) and the construction of the (weighted) Delaunay triangulation were not parallelized unlike the immersion and remeshing, the computation times are quite acceptable in 2D and 3D. Furthermore, the parallelization of the generation methods and also of the construction of the Delaunay triangulation are two important perspectives of this work.

## 4.4 Conclusion

All the microstructures generated in this work were defined using level-set functions. This chapter detailed the definition of these functions and the mesh adaptation methods.

We began by detailing the level-set approach used in [15] for defining Voronoï tessellations. Then, the computing time to calculate the level-set functions used to define Voronoï cells was reduced by introducing the Delaunay triangulation to the algorithm developed in [15]. Afterwards, this method was extended to generate Laguerre tessellations. The use of level-set functions for defining spread cells and spherical particles was also explained. Furthermore, level-set functions defining three-dimensional open-cell foams were developed.

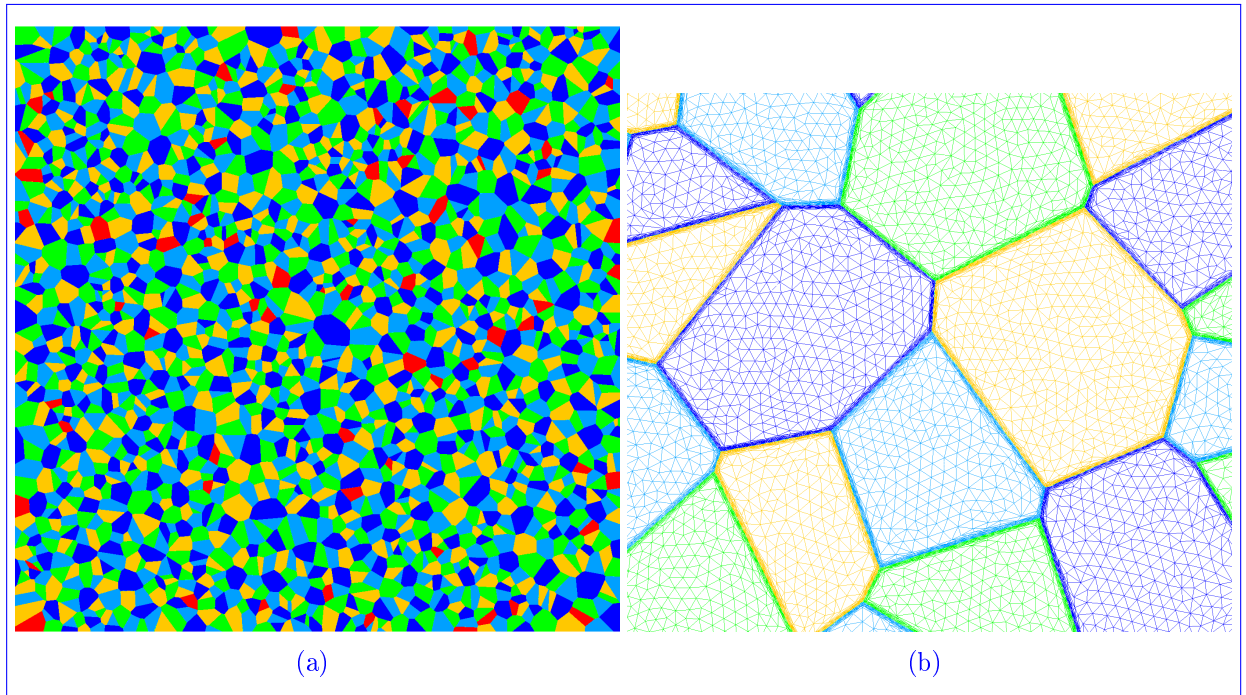


*Figure 4.15: (a) A 2000 equiaxial polycrystal RVE made of Laguerre cells, described using five level-set functions (one color per level-set function) and (b) a zoom illustrating anisotropic meshing at the interfaces of the Laguerre cells*

Concerning mesh adaptation and after a general overview of the existing methods in CimLib, the DSATUR, a graph coloring algorithm, was used to limit the number of requisite level-set functions used in remeshing. This algorithm reduced the remeshing computational times.

This chapter concluded the part of microstructure generation in this manuscript. All the algorithms and methods detailed to this point were added to CimLib but certain limitations still exist. The use of IPM should be parallelized in order to improve the spherical particles generation times. Also, fiber and ellipsoid packings should be added to this builder in order to pave the way for modelling elongated cells.

## 4.5 Résumé français

Ce chapitre a été consacré à la description de la méthode d’immersion des microstructures virtuelles, construites dans les chapitres précédents, dans un maillage éléments finis. Cette approche est basée sur un formalisme level-set, l’application de lois de mélanges et une technique d’adaptation de maillage.

Dans la première partie de ce chapitre, nous avons détaillé le calcul des fonctions level-set permettant de définir des cellules de Voronoï, méthode introduit par Bernacki [15]. Les temps de calcul de cette méthode ont été améliorés par l’introduction de la

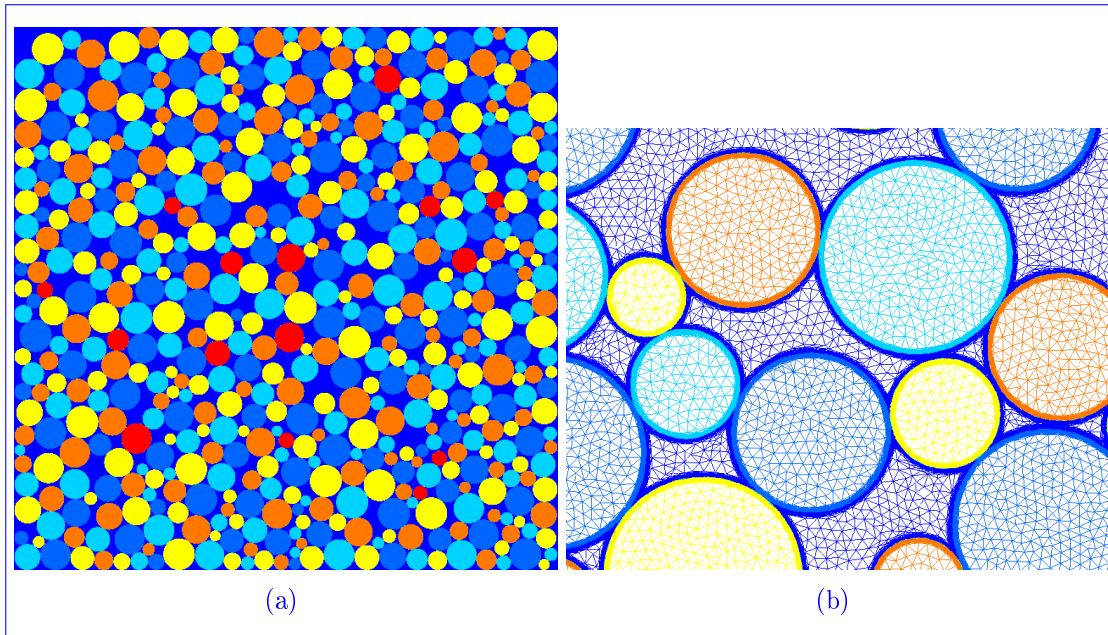


*Figure 4.16: (a) A powder RVE made of 554 discs obtained by the POA described by five level-set functions thanks to the graph coloration algorithm (one color per level-set function) and (b) the finite element mesh in a zoom of the microstructure*

triangulation de Delaunay, dual du diagramme de Voronoï. Cette triangulation fournit le graphe de chaque site de Voronoï  $S_i$  qui est l'ensemble des sites  $\{S_j, j \neq i\}$  qui partage une même arête de la triangulation de Delaunay avec  $S_i$ . L'information du graphe permet de simplifier la façon de calculer les fonctions level-set en réduisant donc les temps de calculs nécessaires. Ensuite, cette méthode a été étendue pour définir des cellules de Laguerre. Le calcul des fonctions level-set permettant également d'immerger des cellules polyédriques avec présence d'une seconde phase et des particules sphériques a été détaillé. Enfin une technique level-set permettant de définir des mousses à cellules ouvertes est également décrite.

Dans la deuxième partie, les différentes méthodes de remaillage existantes dans CimLib ont été détaillées. Toutes ces méthodes sont basées sur la notion de construction de métriques qui modifient la façon de calculer les longueurs dans l'espace. A leur tour ces métriques sont utilisées dans MTC, un mailleur topologique interfacée à CimLib. Ensuite, une nouvelle méthode de calcul de métriques, adaptée aux microstructures considérées dans ce travail de thèse, est détaillée, illustrée et validée.

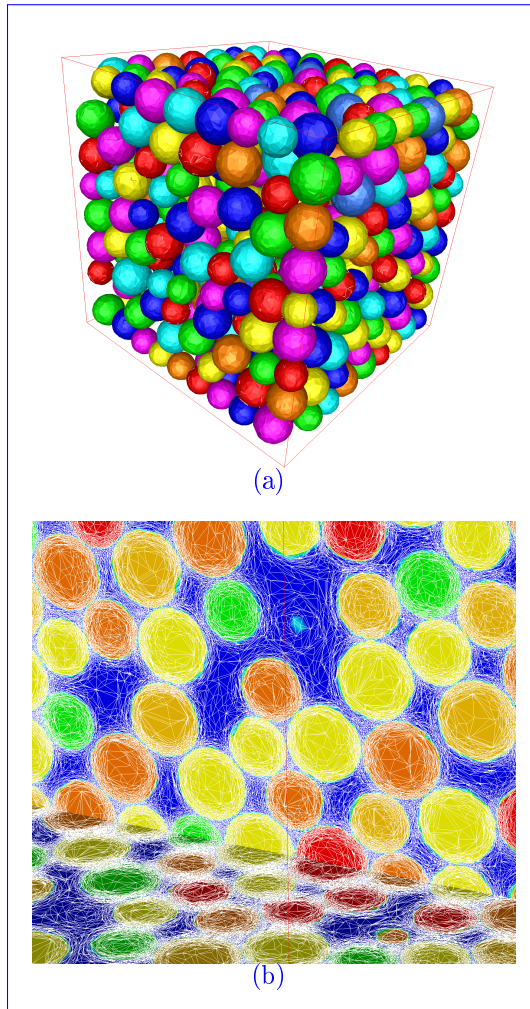


*Figure 4.17: (a) A poly-dispersed powder RVE made of 585 spheres, described using eight level-set functions and (b) a zoom on 2 cutting planes illustrating meshing at the interfaces of the spherical particles*

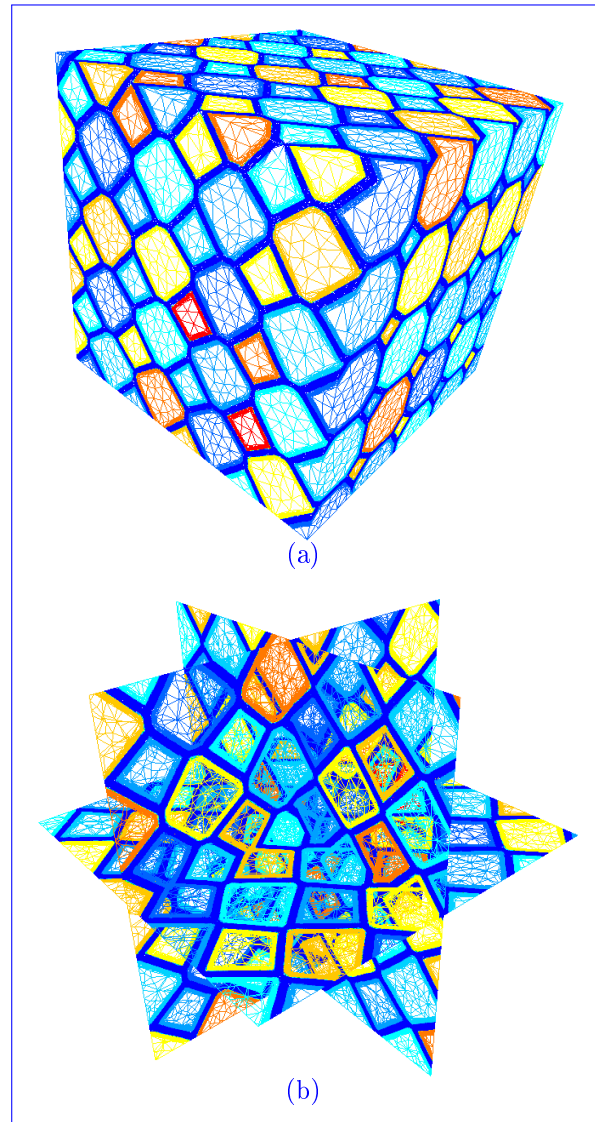


*Figure 4.18: (a) A 3D tetrakaidecahedral foam microstructure made of 250 cells, generated using the LTM and described by eight level-set functions and (b) the mesh on three orthogonal cross sections*



# Chapter 5

## Finite element calculations

### Contents

---

<b>5.1</b>	<b>Introduction</b>	<b>119</b>
<b>5.2</b>	<b>Elastic foam compression</b>	<b>121</b>
5.2.1	Governing equations	121
5.2.2	Numerical approach	124
5.2.3	The finite element formulation	125
5.2.3.1	Classical mixed formulation	126
5.2.3.2	Stable mixed formulation	127
5.2.3.3	Matrix formulation	129
5.2.4	Simulations and discussions	130
5.2.4.1	The RVE's size	130
5.2.4.2	The effect of the air	131
5.2.4.3	The effect of varying cell irregularity	133
5.2.4.4	Compression of a three-dimensional closed-cell foam	137
<b>5.3</b>	<b>Permeability computation of disordered fiber arrays</b>	<b>138</b>
5.3.1	Governing equations	138
5.3.2	Numerical approach	142
5.3.3	The FE formulation	142
5.3.4	The RVE	143
5.3.4.1	Ripley's $K_r$	144
5.3.5	Permeability computation	144
5.3.5.1	Computation of the transverse permeability tensor	145
5.3.5.2	Computation of longitudinal permeability	147
5.3.6	Numerical Results	147

5.3.6.1	The RVE's size . . . . .	147
5.3.6.2	Isotropic properties . . . . .	148
5.3.6.3	The effect of $\sigma$ on $\mathcal{K}$ . . . . .	148
<b>5.4</b>	<b>Conclusion . . . . .</b>	<b>151</b>
<b>5.5</b>	<b>Résumé français . . . . .</b>	<b>153</b>

---

## 5.1 Introduction

As it was mentioned, the mechanical applications or finite element calculations in this thesis are elastic foam compression and permeability computation of unidirectional disordered fiber arrays.

In what concerns foam properties and compression, analytical or numerical calculations have been performed on idealized microstructures constructed from a repeating unit cell. Structural mechanics have been applied to open-cell foams schematized either by a regular tetrahedral arrangement of beams [61, 62] or by a regular arrangement of tetrakaidecahedral cells [63, 64] or by the Kelvin cell model [121, 122]. In the case of closed-cell structures, finite element calculations on tetrakaidecahedral unit cell have also been derived [65, 123]. All these approaches lead to similar scaling laws for modulus or strength. They give quite fair estimations of modulus and strength though discrepancies are observed with experimental values. These discrepancies can be attributed to the fact that the perfectly ordered and symmetric microstructures are clearly an oversimplification to the actual perturbed architecture observed in the materials [121]. Modelling foams using X-ray computed tomography can be an answer to reproduce the real microstructure and use it in FE simulations as in [124, 125] where it was used to model polymeric open-cell foams. In these works, the reconstructed data was segmented and automatically converted into a tetrahedron based FE model and also 2D FE models were constructed by taking random slices of the 3D models. Uniaxial compression was performed on the constructed FE models and the typical deformation mechanisms such as bending and buckling were present in both experiments and FE results. Another possible solution, when real images are not used, is the introduction of different kinds of imperfections or defects to the constructed microstructure to try to explain the experimental discrepancies. In this context, Zhu and coworkers studied the effect of cell irregularity on the high strain compression and elastic properties of 2D Voronoï honeycombs [7, 12] and open-cell foams [11, 13]. They concluded that, for both kinds of foams, a more irregular foam has a higher tangential modulus at low strain but supports a lower compressive stress at higher strain when compared with a more regular one, and the more irregular the random foams, the larger will be their effective Young's modulus and shear modulus, and the smaller will be their bulk modulus. Li et al. studied the effects of cell shape and cell wall thickness variations on the elastic properties of two-dimensional cellular solids [32] and open-cell foams [9]. Their simulations indicate that the Young's and shear moduli increase as cell shapes become more irregular (as also described in [11, 12]), but decrease as cell wall thickness gets less uniform. The effects of cell irregularity, relative density and the shape of the strut cross section on the high strain compression of open-cell foams were studied in [126]. The cell irregularity was found to have a similar effect that the one described in [13] and the strut cross-section and relative density were found to have great effects on the compressive strength of open-cell foam.

In the above-cited cases the presence of the air inside the foam's cells was never taken into account though its presence may affect the foam's behavior. We intend to study the effect of cell irregularity on the strain compression of Voronoï honeycombs while

considering the existence of air inside the cells. By taking the air's presence into account, the foam compression becomes a Fluid Structure Interaction (FSI) problem between the air and the foam's solid skeleton. During the FSI, the pressure and the viscous stress of the fluid act on the solid boundary and lead to structural deformations, which in turn affect the fluid's behavior and consequently the velocity, pressure and viscous stress of the fluid. Thus the response of the system can only be determined if the coupled problem is solved. In the standard approach for simulating FSI problems, the solid's equations are solved for the displacement while the fluid's equations provide the velocity and pressure. We begin by writing the momentum and continuity equations and then, by using the behavior laws of both the fluid and solid and using specific mixture laws the final FSI system is obtained. This system is governed by the Stokes equations (when the gravity and inertia effects are neglected) with an extra stress tensor coming from the presence of the structure in the fluid. These equations are solved by a mixed finite element method with a P1+/P1 interpolation, and a Lagrangian framework is used in order to simulate foam compression. In this case, each node remains in coincidence with the same phase throughout the whole deformation process. In particular, the nodes located at the interface of the solid skeleton remains on its boundary during the whole simulation and hence, tracking a moving interface does not present major difficulties. Since the air's pressure increases rapidly during compression, reaching high compressive strains presents major difficulties because the cells tend to explode and their solid skeleton tends to fracture at high strain rates, especially for irregular foams, and we did not deal with such cases in this work.

In the case of ordered fiber arrays, several analytical relations have been established to predict the permeability of fibrous media [80, 82, 83]. All of these studies consider simple geometries, such as square or triangular packing of unidirectional arrays of cylinders and the analytical relations are only a function of the porosity,  $\phi$  which is the fluid's volume in the domain. However, in the case of disordered fiber arrays, the use of porosity alone cannot define their permeability. Other microstructural parameters should be taken into account. Chen and Papathanasiou [8, 20] studied the effect of the mean nearest inter-fiber spacing, denoted  $\bar{\delta}_1$ , on both the transverse and longitudinal permeabilities. They found that the latter decreases on all porosity levels and the former increases on porosity levels ranging from 0.45 to 0.7 and decreases above these levels when  $\bar{\delta}_1$  increases. Moreover,  $\bar{\delta}_1$  is related to the degree of disorder of the fiber arrays. This degree increases when  $\bar{\delta}_1$  decreases. In our case, when the inter-fiber spacing is chosen according to a Gaussian distribution law, the standard deviation of this law,  $\sigma$ , (see section 2.4.3) is proportional to the degree of disorder of the fiber array. We intend to study the effect of  $\sigma$  on the transverse and longitudinal permeabilities.

In our permeability computation application, the fibers are considered as rigid discs and the Stokes equations are solved on the RVE by an immersed domain method [55, 59]. This approach can rather be seen as an extension of the Stokes problem with two fluids, for which the solid behavior of one phase is imposed by using the viscosity as a penalty factor. The rigidity of the solid part is taken in account with a high viscosity value, which

acts as a penalty coefficient. Using this approach, a zero velocity boundary condition imposed on the solid's interface is propagated into the entire solid domain. Also, a mixed finite element method with a P1+/P1 interpolation is used to solve the Stokes equations. Afterwards, homogenization techniques, mainly volume averaging [86], are used to get Darcy's law.

After this introduction, this chapter contains two major sections. Section 5.2 details the foam compression application where we begin by writing the governing equations and finite element formulation. Afterwards, the effects of the air and the cell irregularity on the stress are studied and the compression of an irregular three-dimensional closed-cell foam is simulated. Section 5.3 details the permeability computation of disordered fiber arrays. Also, we begin by the governing equations and the finite element formulation till reaching Darcy's law. Furthermore, the capability of our microstructure generator to generate completely random fiber arrays is shown using Ripley's  $K_r$  function. Then, a study of the effect of disorder on the permeability is performed. Moreover, a search for the RVE's size is done for both applications before performing the pre-mentioned studies.

## 5.2 Elastic foam compression

Before detailing the simulations performed, we will explain the governing equations and the FE formulation of our FSI problem.

### 5.2.1 Governing equations

The mechanical problem is governed by the momentum equation, in which gravity and inertia effects are neglected, and by the continuity equation:

$$\nabla \cdot \sigma = 0, \quad (5.1)$$

$$\frac{\partial \rho}{\partial t} + \nabla \cdot (\rho \mathbf{v}) = 0, \quad (5.2)$$

where  $\sigma$  is the stress tensor,  $\rho$  is the density and  $\mathbf{v}$  is the velocity.

The aforementioned partial differential equations are valid for both solids and fluids. The difference lies in the constitutive relation for the stress tensor. In fluids, it is expressed in terms of the strain rate tensor (i.e. velocities) and pressure, while in solids it is a function of the strain tensor (i.e. displacements). More specifically, for a linear, viscous (or Newtonian) fluid, the stress tensor  $\sigma_f$  is given by:

$$\sigma_f = 2\eta_f \epsilon(\mathbf{v}) - \left( \frac{2}{3} \eta_f \nabla \cdot \mathbf{v} + p \right) I, \quad (5.3)$$

where  $\eta_f$  is the laminar viscosity of the fluid,  $p$  is the pressure,  $I$  is the identity matrix and  $\epsilon(\mathbf{v})$  is the strain rate tensor defined by:

$$\epsilon(\mathbf{v}) = \frac{1}{2} (\nabla \mathbf{v} + \nabla \mathbf{v}^T), \quad (5.4)$$

where  $\nabla \mathbf{v}^T$  is the transpose of the velocity's gradient  $\nabla \mathbf{v}$ . For an incompressible flow, which is not the case in this application because the air is a weakly compressible fluid,  $\nabla \cdot \mathbf{v} = 0$  and the second term on the right hand side of Eq.(5.3) will contain only the pressure. By writing Eq.(5.3) with a modified pressure  $p' = p + \frac{2}{3}\eta_f \nabla \cdot \mathbf{v}$  and replacing  $\sigma_f$  in Eq.(5.1), we get:

$$2\eta_f \nabla \cdot (\epsilon(\mathbf{v})) - \nabla p' = 0. \quad (5.5)$$

For a linear, elastic solid, the stress tensor  $\sigma_s$  is given by the generalized Hooke's law:

$$\sigma_s = 2\mu \epsilon(\mathbf{u}) + \lambda \text{tr}(\epsilon(\mathbf{u}))I, \quad (5.6)$$

where  $\mu$  and  $\lambda$  are the two Lamé coefficients,  $\mathbf{u}$  is the displacement,  $\epsilon(\mathbf{u})$  is the strain tensor and  $\text{tr}(\cdot)$  is the trace operator where  $\text{tr}(\epsilon(\mathbf{u})) = \nabla \cdot \mathbf{u}$ . The Lamé coefficients are related to the Young's modulus ( $E$ ) and the Poisson ratio ( $\nu$ ) by the following expressions:

$$\begin{aligned} \lambda &= \frac{\nu E}{(1+\nu)(1-2\nu)}, \\ \mu &= \frac{E}{2(1+\nu)}. \end{aligned} \quad (5.7)$$

Eq.(5.6) is not general as it cannot be used for incompressible solids for which  $\nu = 0.5$ . The reason is that the Lamé coefficient  $\lambda$  tends to infinity and  $\text{tr}(\epsilon(\mathbf{u}))$  is null so their product is indeterminable. Although, the foam's solid skeleton is compressible, writing a general form of this equation is preferred. Hence, the pressure is treated as a separate unknown variable. In solid mechanics, pressure is defined as

$$p = -\frac{\text{tr}(\sigma_s)}{3}, \quad (5.8)$$

where the sign convention corresponds to the positive stress in compression. The bulk modulus  $K$  is related to the Lamé coefficients by:

$$K = \frac{2}{3}\mu + \lambda. \quad (5.9)$$

Using the two previous relations, we can easily show that the pressure can be written as:

$$p = -K \text{tr}(\epsilon(\mathbf{u})). \quad (5.10)$$

Moreover, the bulk modulus is defined by [76],

$$K = -V \frac{dp}{dV} = \rho \frac{dp}{d\rho}, \quad (5.11)$$

where  $V$  is the fluid's volume. Using Eqs.(5.9) and (5.10) the following relation can be written:

$$\lambda \operatorname{tr}(\epsilon(\mathbf{u})) = - \left( p + \frac{2}{3} \mu \operatorname{tr}(\epsilon(\mathbf{u})) \right). \quad (5.12)$$

This relation is used in Eq.(5.6) which introduces the pressure to the solid's constitutive equation:

$$\sigma_s = 2\mu\epsilon(\mathbf{u}) - \left( \frac{2}{3}\mu\operatorname{tr}(\epsilon(\mathbf{u})) + p \right) I. \quad (5.13)$$

By writing Eq.(5.13) with a modified pressure  $p' = p + \frac{2}{3}\mu\nabla \cdot \mathbf{u}$  and replacing  $\sigma_s$  in Eq.(5.1), we get:

$$2\mu\nabla \cdot (\epsilon(\mathbf{u})) - \nabla p' = 0. \quad (5.14)$$

The additional unknown (pressure) is obtained by rearranging Eq.(5.10):

$$\nabla \cdot \mathbf{u} + \frac{1}{K} p = 0. \quad (5.15)$$

Eq.(5.14) is supplemented by Eq.(5.15) as well as the relationship between displacements and solid velocities and hence, a system of equations is obtained for the solid:

$$\begin{cases} 2\mu\nabla \cdot (\epsilon(\mathbf{u})) - \nabla p' = 0 & (a) \\ \frac{d\mathbf{u}}{dt} = \mathbf{v} & (b) \\ \nabla \cdot \mathbf{u} + \frac{1}{K} (p' - \frac{2}{3}\mu\nabla \cdot \mathbf{u}) = 0 & (c) \end{cases} \quad (5.16)$$

The corresponding system for a weakly compressible fluid is:

$$\begin{cases} 2\eta_f\nabla \cdot (\epsilon(\mathbf{v})) - \nabla p' = 0 & (a) \\ \nabla \cdot \mathbf{v} + \frac{1}{K} \frac{dp'}{dt} = 0 & (b) \end{cases} \quad (5.17)$$

where the definition of the bulk modulus of the fluid  $K$  (i.e. Eq.(5.11)) was used in Eq.(5.2) in order to write the second equation of the fluid's system.

Also by using the definition of the bulk modulus  $K$ , and the fact that the air is an ideal gas, which means that  $PV$  is a constant is isothermal conditions, Eq.(5.17(b)) can be written as:

$$\nabla \cdot \mathbf{v} + \frac{1}{p'} \frac{dp'}{dt} = 0. \quad (5.18)$$

A velocity-pressure formulation should be written for the solid in order to solve a coupled FSI problem. The displacement is linked to the velocity by Eq.(5.16(b)) and since a Lagrangian framework is used, this equation could be written as:

$$\mathbf{u}^t = \mathbf{u}^{t-\Delta t} + \mathbf{v}^t \Delta t. \quad (5.19)$$

Using this expression for the displacement in the solid's system of equations (5.16), this system could be written as:

$$\begin{cases} 2\mu\Delta t\nabla\cdot(\epsilon(\mathbf{v}^t)) - \nabla p^{tt} = -2\mu\nabla\cdot(\epsilon(\mathbf{u}^{t-\Delta t})) & (a) \\ \nabla\cdot\mathbf{v}^t + \frac{1}{K-\frac{2}{3}\mu}\frac{dp^{tt}}{dt} = 0 & (b) \end{cases} \quad (5.20)$$

The expression  $-2\mu\epsilon(\mathbf{u}^{t-\Delta t})$  of the right-hand side of Eq.(5.20(a)) is the extra-stress tensor in the governing Stokes equations. Eq.(5.20(b)) is obtained by rearranging Eq.(5.16(c)) to the form:

$$\nabla\cdot\mathbf{u} = -\frac{1}{K-\frac{2}{3}\mu}p' \quad (5.21)$$

Then replacing  $\nabla\cdot\mathbf{u}^t$  and  $\nabla\cdot\mathbf{u}^{t-\Delta t}$  by  $-\frac{1}{K-\frac{2}{3}\mu}p^{tt}$  and  $-\frac{1}{K-\frac{2}{3}\mu}p^{tt-\Delta t}$  respectively in:

$$\nabla\cdot\mathbf{u}^t = \nabla\cdot\mathbf{u}^{t-\Delta t} + \nabla\cdot\mathbf{v}^t\Delta t. \quad (5.22)$$

Moreover, using the expression of the bulk modulus  $K$  in Eq.(5.9), Eq.(5.20(b)) could be written as:

$$\nabla\cdot\mathbf{v}^t + \frac{1}{\lambda}\frac{dp^{tt}}{dt} = 0 \quad (5.23)$$

Finally, the governing equations for the FSI problem are:  
*for the fluid*

$$\begin{cases} 2\eta_f\nabla\cdot(\epsilon(\mathbf{v}^t)) - \nabla p^t = 0 \\ \nabla\cdot\mathbf{v}^t + \frac{1}{p^t}\frac{dp^t}{dt} = 0 \end{cases} \quad (5.24)$$

*for the solid*

$$\begin{cases} 2\mu\Delta t\nabla\cdot(\epsilon(\mathbf{v}^t)) - \nabla p^{tt} = -2\mu\nabla\cdot(\epsilon(\mathbf{u}^{t-\Delta t})) \\ \nabla\cdot\mathbf{v}^t + \frac{1}{\lambda}\frac{dp^{tt}}{dt} = 0 \end{cases} \quad (5.25)$$

### 5.2.2 Numerical approach

Since we have two phases, solid and fluid, the computational domain  $\Omega$  is decomposed into two subdomains,  $\Omega_f$  and  $\Omega_s$ , designating respectively the fluid domain and the solid domain which is described by a level-set function  $\alpha$ . The location of the air is given by the positive values of  $\alpha$  whereas  $\Omega_s$  corresponds to the negative values of  $\alpha$ . Once calculated, the level-set allows us to define a presence function of the subdomain  $\Omega_i$ . A smoothed Heaviside function  $H(\alpha)$  is used in this work, where a thickness  $e$  is fixed near the interface in order to prevent a discontinuous transition in this region. The value of  $e$  is chosen accordingly to the mesh size. The function  $H(\alpha)$  is defined as:

$$H(\alpha) = \begin{cases} 0 & \text{if } \alpha < -e \\ \frac{1}{2} \left(1 + \frac{\alpha}{2}\right) & \text{if } |\alpha| \leq e \\ 1 & \text{if } \alpha > e \end{cases} \quad (5.26)$$

Furthermore, the objective being to calculate the physical properties on the entire geometry  $\Omega$ , mixing laws [55] are introduced and anisotropic adaptive meshing is used. These laws are defined as functions of the level-set. For variables  $\Theta$ , such as the viscosity and the compressibility coefficient, a linear mixing rule is applied at the neighborhood of the interface between the two subdomains  $\Omega_s$  and  $\Omega_f$ :

$$\Theta = H(\alpha)\Theta_f + (1 - H(\alpha))\Theta_s. \quad (5.27)$$

We used the mixing rules to mix the physical properties of the solid and fluid (see Figure 5.1) by writing:

$$\Psi = H(\alpha)\eta_f + (1 - H(\alpha))\mu\Delta t, \quad (5.28)$$

$$\tau = H(\alpha)0 + (1 - H(\alpha))\mu, \quad (5.29)$$

and

$$\chi = H(\alpha)\frac{1}{p'} + (1 - H(\alpha))\frac{1}{\lambda}, \quad (5.30)$$

which gives us the final system of our FSI problem where, for sake of clarity,  $p^t$  is denoted  $p$  and  $\mathbf{v}^t$  is denoted  $\mathbf{v}$ :

$$\begin{cases} 2\Psi\nabla \cdot (\epsilon(\mathbf{v})) - \nabla p = -2\tau\nabla \cdot (\epsilon(\mathbf{u}^{t-\Delta t})) \\ \nabla \cdot \mathbf{v} + \chi \frac{dp}{dt} = 0 \end{cases} \quad (5.31)$$

This system of equations is solved using a mixed FEM that we are going to detail in the next section.

### 5.2.3 The finite element formulation

First, let us define the function spaces used in the remainder of this chapter. The scalar function space for the pressure  $Q = \mathcal{L}^2(\Omega)$ , the function space for the velocity  $V = (\mathcal{H}^1(\Omega))^d$  and the weighting function space  $V_0 = (\mathcal{H}_0^1(\Omega))^d$ , where  $d$  is the space dimension,  $\mathcal{L}^2(\Omega)$  is the Lebesgue space of square assumable functions on  $\Omega$  and  $\mathcal{H}^1(\Omega)$  is the Sobolev space included in  $\mathcal{L}^2(\Omega)$ , are respectively defined by:

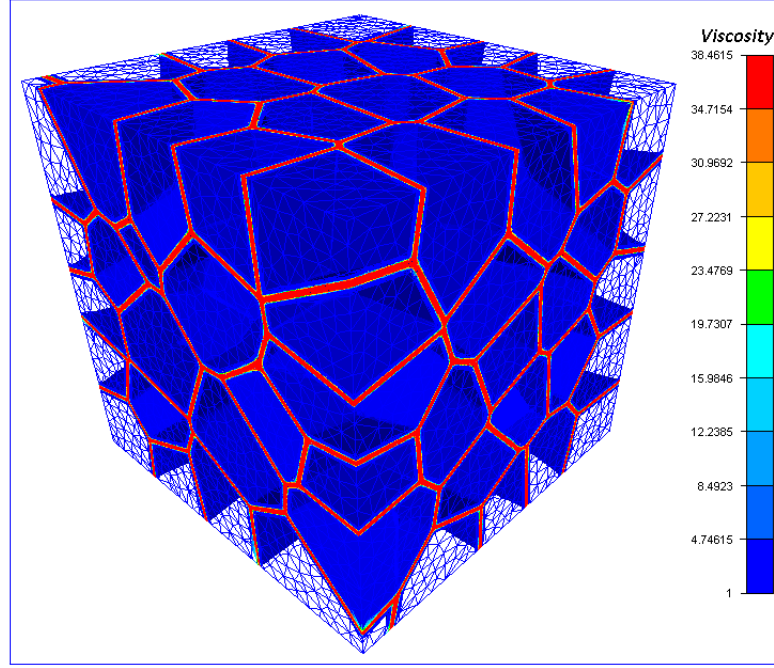


Figure 5.1: Mixing the air's viscosity  $\eta_f$  with  $\mu\Delta t$

$$\begin{cases} \mathcal{L}^2(\Omega) = \{q / \int_{\Omega} q^2 d\Omega < \infty\} \\ \mathcal{H}^1(\Omega) = \{u \in \mathcal{L}^2(\Omega) / \nabla u \in \mathcal{L}^2(\Omega)\} \\ \mathcal{H}_0^1(\Omega) = \{u \in \mathcal{H}^1(\Omega) / u = 0 \text{ on } \partial\Omega\} \end{cases}$$

Moreover, let  $(\cdot, \cdot)_{\Omega}$  denote the dot product in  $\mathcal{L}^2(\Omega)$  defined as:

$$(u, v)_{\Omega} = \int_{\Omega} u(x)v(x)d\Omega. \quad (5.32)$$

### 5.2.3.1 Classical mixed formulation

The finite element formulation begins by writing the weak form of the compressible Stokes equations (5.31). The problem consists in finding  $(\mathbf{v}, p) \in V \times Q$  such that  $\forall (\mathbf{w}, q) \in V_0 \times Q$ :

$$\begin{cases} 2\Psi(\epsilon(\mathbf{v}) : \epsilon(\mathbf{w}))_{\Omega} - (p, \nabla \cdot \mathbf{w})_{\Omega} = -2\tau(\epsilon(\mathbf{u}^{t-\Delta t}) : \epsilon(\mathbf{w}))_{\Omega} \\ -(\nabla \cdot \mathbf{v}, q)_{\Omega} - (\frac{\chi}{\Delta t} p^t, q)_{\Omega} = -(\frac{\chi}{\Delta t} p^{t-\Delta t}, q)_{\Omega} \end{cases} \quad (5.33)$$

The Galerkin approximation consists in decomposing our domain  $\Omega$  into  $N_{el}$  simplices  $T$  such that they cover the domain and they are either disjoint or share a complete edge.

The triangulation will be denoted  $\mathcal{T}_h$ . Using this partition, the above-defined functional spaces are approached by finite dimensional spaces, used in the remainder of this chapter, spanned by continuous piecewise polynomials such that:

$$\begin{cases} Q_h = \{q_h \in C^0(\Omega) / q_h|_T \in P^1(T), \forall T \in \mathcal{T}_h\} \\ V_h = \{\mathbf{v}_h \in (C^0(\Omega))^d / \mathbf{v}_h|_T \in (P^1(T))^d, \forall T \in \mathcal{T}_h\} \\ V_{h,0} = \{\mathbf{v}_h \in V_h / \mathbf{v}_h|_\Gamma = 0\} \end{cases}$$

where  $P^1(T)$  is the vector space of first degree polynomials defined on the simplex  $T$ .

The Galerkin discrete problem consists now in solving the mixed problem by finding the pair  $(\mathbf{v}_h, p_h) \in V_h \times Q_h$  such that  $\forall (\mathbf{w}_h, q_h) \in V_{h,0} \times Q_h$ :

$$\begin{cases} 2\Psi(\epsilon(\mathbf{v}_h) : \epsilon(\mathbf{w}_h))_\Omega - (p_h, \nabla \cdot \mathbf{w}_h)_\Omega = -2\tau(\epsilon(\mathbf{u}_h^{t-\Delta t}) : \epsilon(\mathbf{w}_h))_\Omega \\ -(\nabla \cdot \mathbf{v}_h, q_h)_\Omega - (\frac{\chi}{\Delta t} p_h^t, q_h)_\Omega = -(\frac{\chi}{\Delta t} p_h^{t-\Delta t}, q_h)_\Omega \end{cases} \quad (5.34)$$

It is known that the finite element approximation (5.34) may fail because of the inf-sup condition (Brezzi-Babuska) which requires an appropriate pair of function spaces for the velocity and the pressure [127]. In the present work, we aim to retain the advantages of using linear approximations ( $P1$  finite elements) regarding the accuracy and the computational cost. But it is well known that the combination of  $P1/P1$  approximation for the velocity and the pressure does not lead to a stable discretization of system (5.34) since it fails to satisfy the inf-sup condition:

$$\inf_{q_h \in Q_h} \sup_{\mathbf{v}_h \in V_h} \frac{(\nabla \cdot \mathbf{v}_h, q_h)_\Omega}{\|q_h\|_0 \|\mathbf{v}_h\|_1} \geq \beta \geq 0, \quad (5.35)$$

where  $\beta$  is a constant independent of  $h$ ,  $\|\cdot\|_0$  and  $\|\cdot\|_1$  are the norms of  $\mathcal{L}^2(\Omega)$  and  $\mathcal{H}^1(\Omega)$  respectively.

### 5.2.3.2 Stable mixed formulation

A very popular method was proposed by Arnold, Brezzi and Fortin [128] for the Stokes problem to respect the velocity-pressure compatibility condition. It was suggested to enrich  $V_h$  with the space of bubble functions known as Mini-element or  $P1 + /P1$  (see Figure 5.2) denoted  $V^b$ :

$$V^b = \{v^b/v^b|_{T_i} \in P^1(T_i) \cap \mathcal{H}_0^1(T_i), \forall T \in \mathcal{T}_h, i = 1, \dots, D\}, \quad (5.36)$$

where  $D$  is the topological dimension and  $T_i$  is a decomposition of  $T$  in  $D$  sub-simplices, that have as a common vertex the barycenter,  $G_T$ , of  $T$ . In other words, the choice of this bubble function is continuous inside the element, considered as linear on each sub-simplex and vanishes at the boundary of  $T$ .

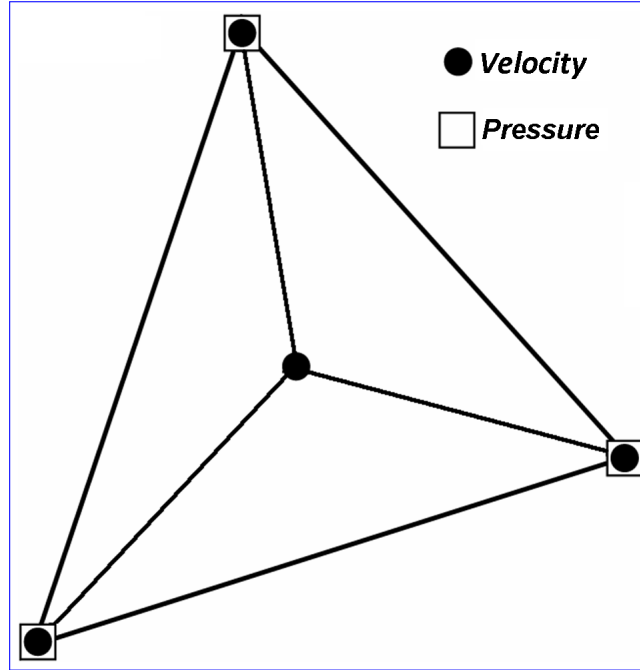


Figure 5.2: The MINI-element  $P1 + /P1$

The velocity field is now an element of the function space generated by the following direct sum:

$$\mathcal{V}_h = V_h \oplus V^b. \quad (5.37)$$

Hence, on each element  $T$ , the solution takes the form:

$$\mathbf{v}_h|_T = \sum_i^D v_T^i N_i + v_T^b b_T, \quad (5.38)$$

where  $N_i$  is the interpolation function associated with node  $i$ . The bubble function  $b_T$  is defined on each element  $T$  as follows:  $b_T = 0$  on  $\partial T$ ;  $b_T(G_T) = 1$ , Furthermore,  $b_T$  satisfies the orthogonality condition:

$$\int_T \partial_{x_k} N_i \partial_{x_l} b_T d\Omega = 0 \quad \forall (k, l, N_i) \in [0, d-1]^2 \times P^1(T). \quad (5.39)$$

The mixed-finite element approximation of problem (5.34) consists now in finding the pair  $(\mathbf{v}, p_h) \in \mathcal{V}_h \times Q_h$  such that  $\forall (\mathbf{w}, q_h) \in \mathcal{V}_{h,0} \times Q_h$ :

$$\begin{cases} 2\Psi(\epsilon(\mathbf{v}) : \epsilon(\mathbf{w}))_\Omega - (p_h, \nabla \cdot \mathbf{w})_\Omega = -2\tau(\epsilon(\mathbf{u}^{t-\Delta t}) : \epsilon(\mathbf{w}))_\Omega \\ -(\nabla \cdot \mathbf{v}, q_h)_\Omega - \left(\frac{\chi}{\Delta t} p_h^t, q_h\right)_\Omega = -\left(\frac{\chi}{\Delta t} p_h^{t-\Delta t}, q_h\right)_\Omega \end{cases} \quad (5.40)$$

Since the fine-scale problem is independent and uncoupled at the element level and vanishes on the element boundaries, the system (5.40) can be decomposed into:

$$\begin{cases} 2\Psi(\epsilon(\mathbf{v}_h) : \epsilon(\mathbf{w}_h))_\Omega - (p_h, \nabla \cdot \mathbf{w}_h)_\Omega = -2\tau(\epsilon(\mathbf{u}_h^{t-\Delta t}) : \epsilon(\mathbf{w}_h))_\Omega \\ 2\Psi(\epsilon(\mathbf{v}^b) : \epsilon(\mathbf{w}^b))_\Omega - (p_h, \nabla \cdot \mathbf{w}^b)_\Omega = -2\tau(\epsilon(\mathbf{u}^{b t-\Delta t}) : \epsilon(\mathbf{w}^b))_\Omega \\ -(\nabla \cdot \mathbf{v}_h, q_h)_\Omega - (\nabla \cdot \mathbf{v}^b, q_h)_\Omega - \left(\frac{\chi}{\Delta t} p_h^t, q_h\right)_\Omega = -\left(\frac{\chi}{\Delta t} p_h^{t-\Delta t}, q_h\right)_\Omega \end{cases} \quad (5.41)$$

As the fine-scale space is assumed to be orthogonal to the finite element space, the crossed viscous terms in the equations of (5.41) vanished [129].

### 5.2.3.3 Matrix formulation

The equations of system (5.41) give rise to the following global system to solve:

$$\begin{pmatrix} A_{ww} & 0 & A_{wq}^t \\ 0 & A_{bb} & A_{bq}^t \\ A_{wq} & A_{bq} & A_{qq} \end{pmatrix} \begin{pmatrix} \mathbf{v}_h \\ \mathbf{v}^b \\ p_h \end{pmatrix} = \begin{pmatrix} B_w \\ B_{wb} \\ B_q \end{pmatrix}, \quad (5.42)$$

where,

$$\begin{aligned} A_{ww}(\mathbf{v}_h) &= 2\Psi(\epsilon(\mathbf{v}_h) : \epsilon(\mathbf{w}_h))_\Omega, \quad A_{bb}(\mathbf{v}^b) = 2\Psi(\epsilon(\mathbf{v}^b) : \epsilon(\mathbf{w}^b))_\Omega, \\ A_{wq}(\mathbf{v}_h) &= -(\nabla \cdot \mathbf{v}_h, q_h)_\Omega, \quad A_{bq}(\mathbf{v}^b) = -(\nabla \cdot \mathbf{v}^b, q_h)_\Omega, \\ A_{wq}^t(p_h) &= -(p_h, \nabla \cdot \mathbf{w}_h)_\Omega, \quad A_{bq}^t(p_h) = -(p_h, \nabla \cdot \mathbf{w}^b)_\Omega, \\ A_{qq}(p_h) &= -\left(\frac{\chi}{\Delta t} p_h, q_h\right)_\Omega, \quad B_w = -2\tau(\epsilon(\mathbf{u}_h^{t-\Delta t}) : \epsilon(\mathbf{w}^b))_\Omega, \\ B_{wb} &= -2\tau(\epsilon(\mathbf{u}^{b t-\Delta t}) : \epsilon(\mathbf{w}_h))_\Omega, \quad B_q = -\left(\frac{\chi}{\Delta t} p_h^{t-\Delta t}, q_h\right)_\Omega. \end{aligned} \quad (5.43)$$

The static condensation process consists in solving the second line for the bubble function  $v^b$  and inserting the result into the third line of (5.42) which yields the condensed matrix scheme for large-scale unknowns  $\mathbf{v}_h$  and  $p_h$ :

$$\begin{pmatrix} A_{ww} & A_{wq}^t \\ A_{wq} & \tilde{A}_{qq} \end{pmatrix} \begin{pmatrix} \mathbf{v}_h \\ p_h \end{pmatrix} = \begin{pmatrix} B_w \\ \tilde{B}_q \end{pmatrix}, \quad (5.44)$$

where,

$$\begin{aligned} \tilde{A}_{qq} &= A_{qq} - A_{bq} \cdot A_{bb}^{-1} \cdot A_{bq}^t, \\ \tilde{B}_q &= B_q - A_{bq} \cdot A_{bb}^{-1} \cdot B_{wb}. \end{aligned} \quad (5.45)$$

It is clear that taking into account locally the influence of fine scales (bubble functions) upon the resolved large scales has introduced new stabilizing terms and has modified the components of the global matrix. The new operator  $\tilde{A}_{qq}$  provides a so-called pressure stabilization while the new right hand side  $\tilde{B}_q$  ensures consistency [55].

It is important to underline that the formalism and the simulations presented in this thesis correspond to a first prospective work and that some simplifications have been taken into account mainly concerning the foam behaviour. Indeed, in the considered Lagrangian framework, the elastic behaviour assumption concerning the foam remains acceptable only when a very little time step is used. Current work, to overcome this difficulty, consists to extend our approach in an Eulerian framework.

### 5.2.4 Simulations and discussions

The solid skeleton was prescribed to be of equal and uniform thickness. This thickness, manipulated using the cell spreading technique (see section 2.4.1), controls the foam's relative density,  $\rho$ , which was maintained at approximately 0.1 in this work. The Young's modulus of the solid,  $E$ , was set to 100 *MPa* and its Poisson's ratio was set to 0.3.

In order to be symmetric, biaxial compression was simulated for all cases by imposing displacements on the domain's upper and lower boundaries. Symmetrical boundary conditions were imposed on the domain's left and right boundaries by writing  $\mathbf{v} \cdot \mathbf{n} = 0$ , where  $\mathbf{n}$  is the outwards normal vector of each boundary. Depending on the foam's irregularity  $\gamma$  (see section 2.4.2), strains ranging from 0.15 to 0.3 were achieved using our approach. Furthermore, the following reduced stress [7, 13] was used:

$$\bar{\sigma} = \frac{\sigma}{E\rho^3}. \quad (5.46)$$

The stress, in the compression direction, is calculated as the mean of the values on the simplices of an elementary volume. Because the solid material is assumed to be elastic throughout the deformation, the adoption of Eq.(5.46) can eliminate the effect of the foam's relative density and the solid's Young's modulus and make the results more useful.

#### 5.2.4.1 The RVE's size

The sensitivity of the results to the RVE's size or also the number of cells,  $n$ , was examined by comparing the predicted reduced stress/strain results. In order to be statistically representative 20 random Voronoï honeycombs with the same relative density of 0.1 and with  $\gamma = 0.5$  were generated and elementary volumes with a mean number of cells  $n = 19, 28, 46, 65$  and 100 were used to compute the reduced stress. Initially, the generated honeycombs contained, on average, 200 cells and elementary volumes were extracted (see Figure 5.3).

The results for the reduced stress are plotted against the strain for each value of  $n$  in Figure 5.4. The deviations between the results are reasonably small and hence, the size of the RVE was fixed to a minimum of 19 cells.

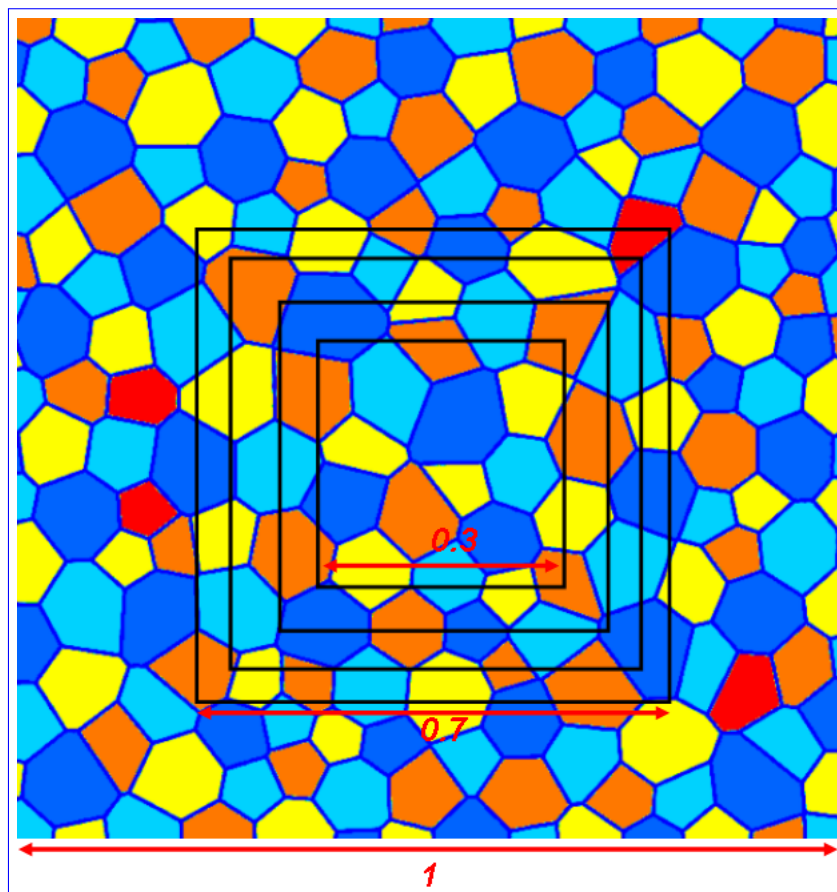


*Figure 5.3: Elementary volumes extracted from an irregular Voronoi honeycomb containing 198 cells in order to determine the size of the RVE*

Furthermore, we simulated the biaxial compression of a regular Voronoi honeycomb made of 135 cells generated in a unit square (see Figure 5.5a) and representing a periodic RVE. The compression was simulated up to 25% deformation (see Figure 5.5b).

Figure 5.6 illustrates the reduced stress/strain curve and the honeycomb's mass variation in function of the deformation.

It is noticed by Figure 5.6a that the foam presents a linearly elastic behavior before reaching a plateau region at about 17% of deformation, this is due to the beginning of the elastic buckling of the cells. Furthermore, the mass variation, shown in Figure 5.6b, does not exceed 0.15% which is a negligible variation. This yields that the foam's mass was conserved during the whole process.

#### 5.2.4.2 The effect of the air

In the simulations illustrated above, the honeycombs' cells contained air. In order to eliminate the presence of the air inside the cells and leave only the foam's solid skeleton, all the elements of the FE mesh (i.e. triangles) containing only air were killed (removed).

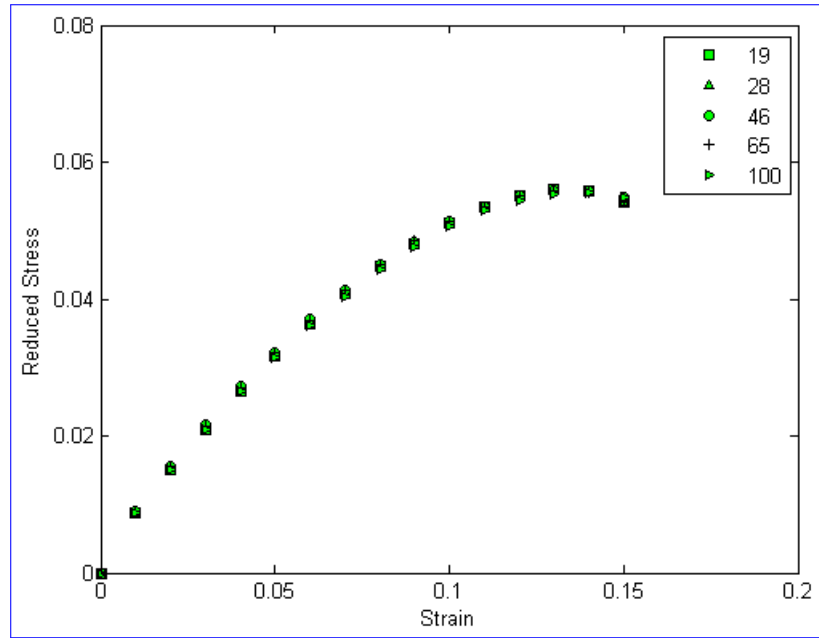


Figure 5.4: The influence of the number of cells in the honeycomb elementary volumes on the reduced stress/strain predictions

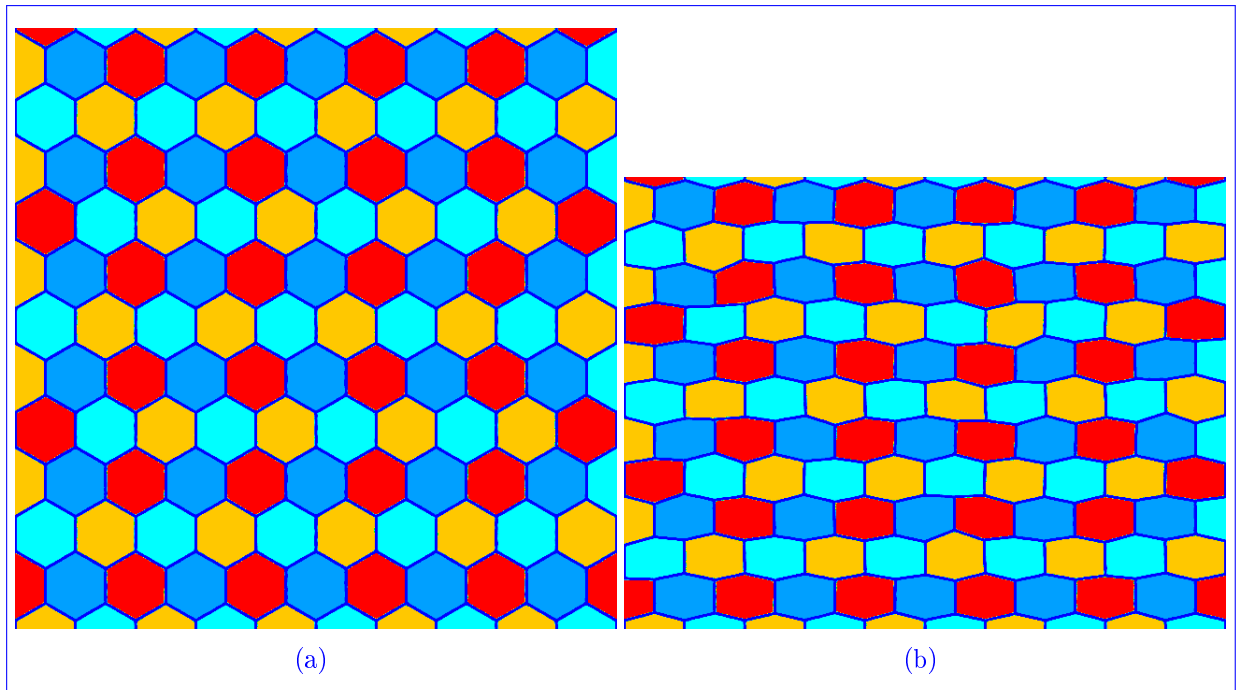


Figure 5.5: (a) The initial regular Voronoï honeycomb made of 135 cells and (b) the same honeycomb after 25% deformation

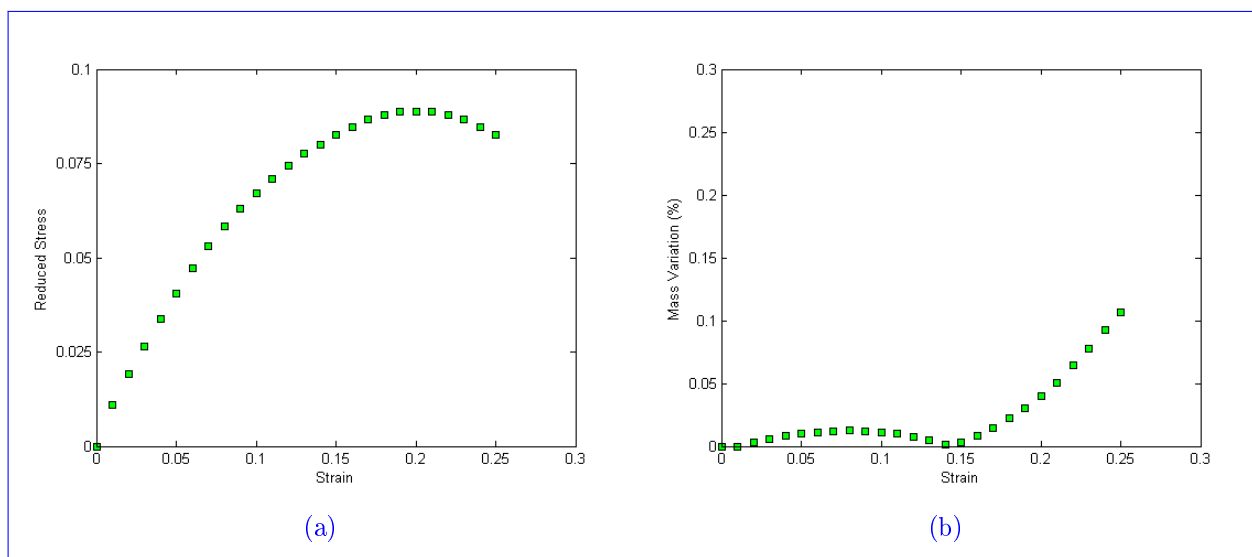


Figure 5.6: (a) The reduced stress/strain curve of the regular Voronoï honeycomb and (b) the mass variation of the whole structure (solid and air)

The killing process is simply performed by the means of the air's presence function; the element in which this function is equal to one is removed (see Figures 5.7a and b).

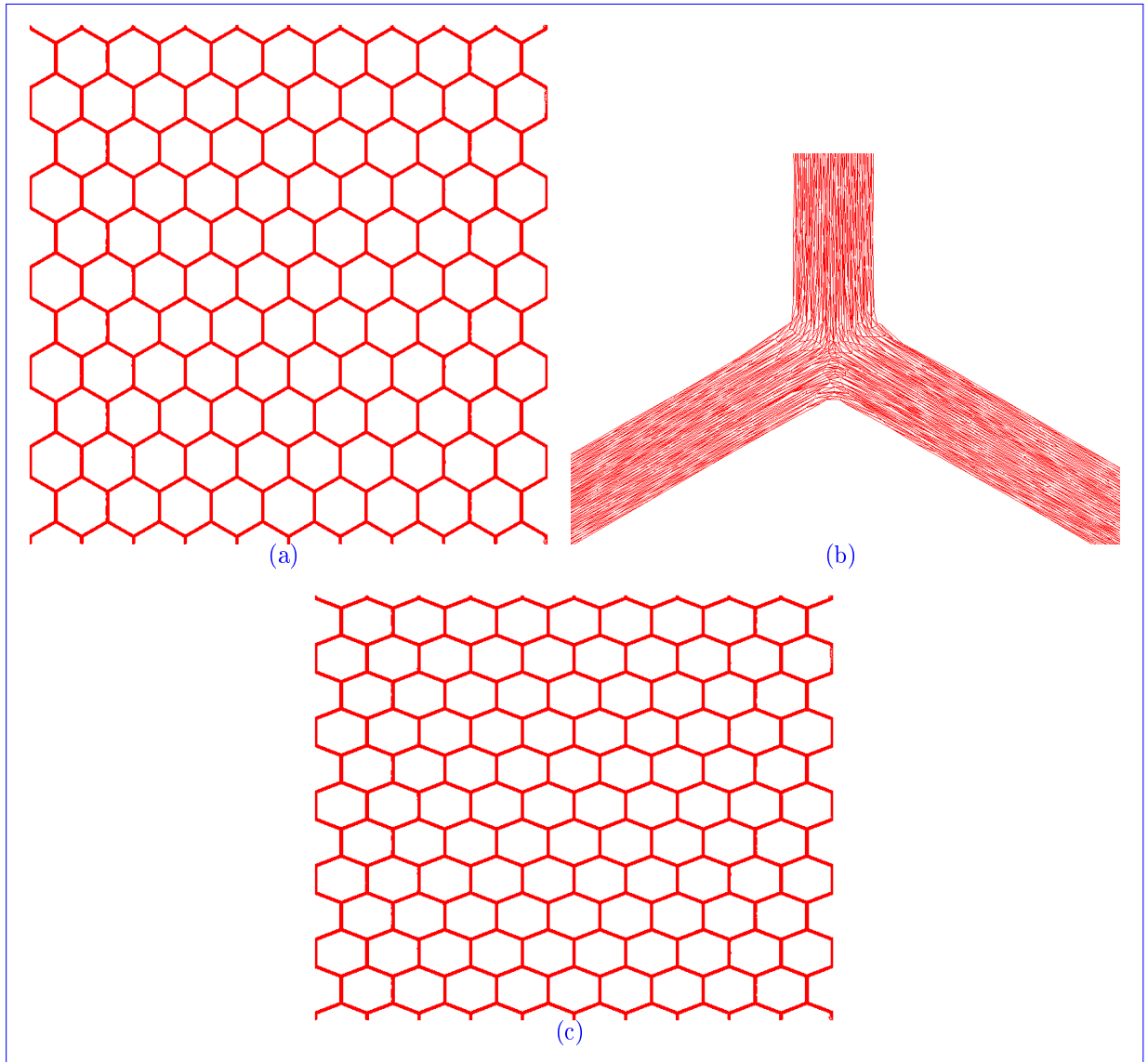
Considering only the elastic solid skeleton, our problem is now governed by equations (5.25). A simulation up to 20% deformation of a regular Voronoï honeycomb was carried out and illustrated in Figure 5.7c.

Figure 5.8 shows the norm of the velocity and the pressure of the Voronoï honeycomb at a strain of 0.2. We notice that the velocity is linear and symmetric in regards to the honeycomb's median plane which is normal since the honeycomb is periodic and since we considered frictionless contacts. The results show as well that the pressure is the highest on the solid edges that are parallel to the loading directions.

Moreover, we compared the reduced stress/strain curves of this Voronoï honeycomb (i.e. solid skeleton without air) and of the elastic solid skeleton of a Voronoï honeycomb with the same relative density but with air inside its cells (see Figure 5.9). We notice that the two skeletons have approximately the same reduced stress values at strains lower than 0.12. Then, the one with air reaches its plateau region and the one without air continues its linearly elastic behavior. This yields that the air, or most precisely the air's pressure, encourages the elastic buckling of the solid skeleton and hence, the plateau region is reached earlier during the compression.

### 5.2.4.3 The effect of varying cell irregularity

First of all, we send the reader to section 2.4.2 in chapter 2 where the cell irregularity  $\gamma$  is defined. Zhu et al. [7, 13] studied the effect of  $\gamma$  on the high strain compression of 2D Voronoï honeycombs and of open-cell foams. In their studies, where the air was not taken into consideration, they found that the compressive strength of a foam, defined as



*Figure 5.7: (a) The elastic solid skeleton of a regular Voronoï honeycomb in its stable position, (b) a zoom at a triple junction showing the nonexistence of mesh elements inside the cells and (c) the same honeycomb after 20% deformation*

the maximum value of stress achieved during the simulated compression, decreases as the irregularity increases. We intend to use our FSI approach to also study the effect of the cell irregularity on the compression of Voronoï honeycombs. For this purpose, three Voronoï honeycombs with  $\gamma$  values of 0.3, 0.5 and 0.7 were generated and biaxial compressions were carried out up to 25% deformation. In Figure 5.10 the results are compared along with the corresponding result for a regular hexagonal honeycomb ( $\gamma = 1$ ).

Though the air is present inside the cells, our results also show that the foam's stress is reduced as the irregularity increases. This can be explained by the fact that the air's frac-

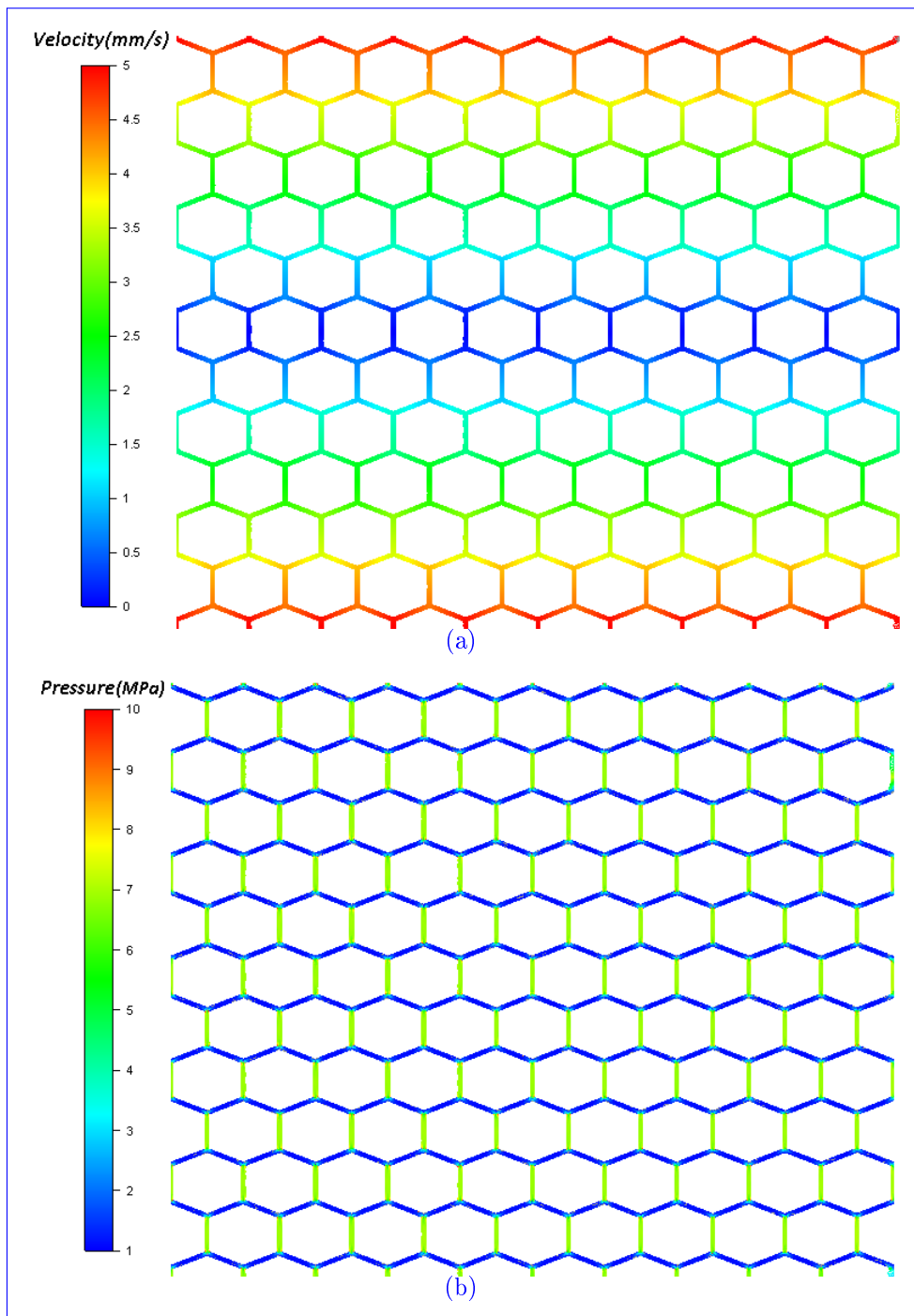


Figure 5.8: (a) The velocity of the solid skeleton at 20% deformation and (b) the pressure of the solid skeleton at 20% deformation

tion is the same for all the considered honeycombs, hence, the effect of the cell irregularity on the reduced stress remains the same.

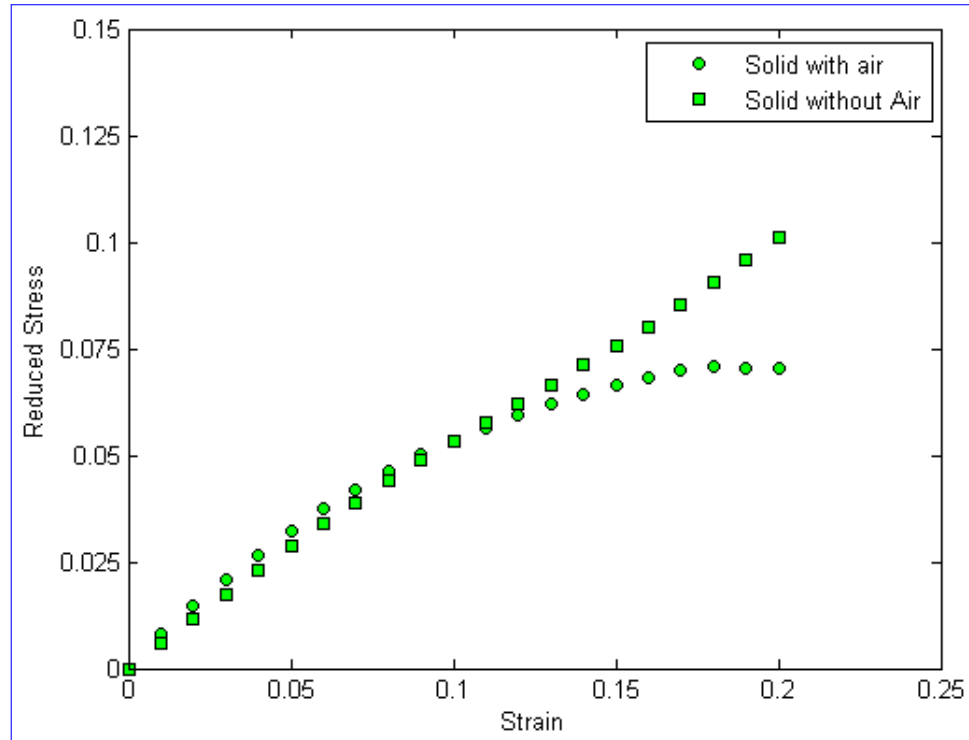


Figure 5.9: Comparison between the response of a solid skeleton with air inside the honeycomb's cells and without air

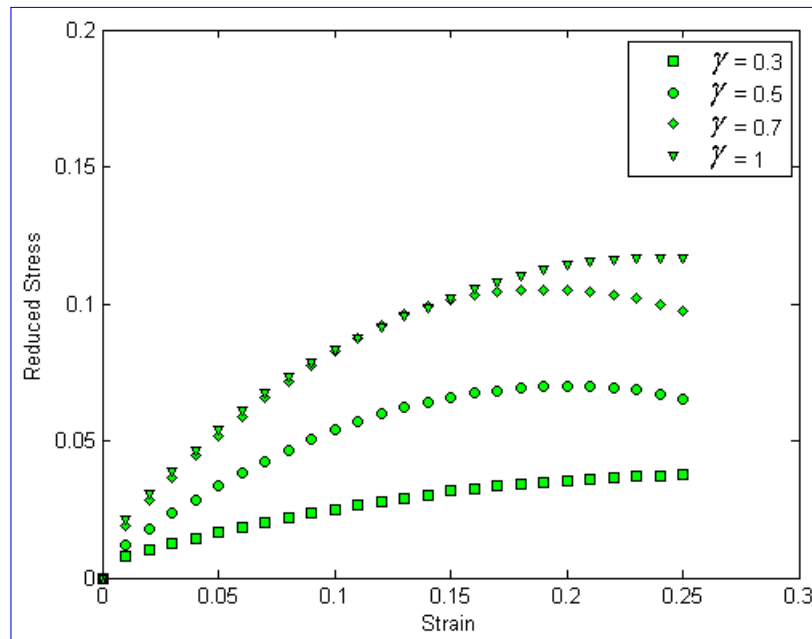


Figure 5.10: The influence of cell irregularity on the reduced stress/strain predictions

Figure 5.11 illustrates an irregular Voronoï honeycomb with  $\gamma = 0.7$  at its initial state and after 25% deformation. The velocity at 25% deformation is shown in Figure 5.12. In this case, the velocity is not symmetric which is logical since the honeycomb is not hexagonal.

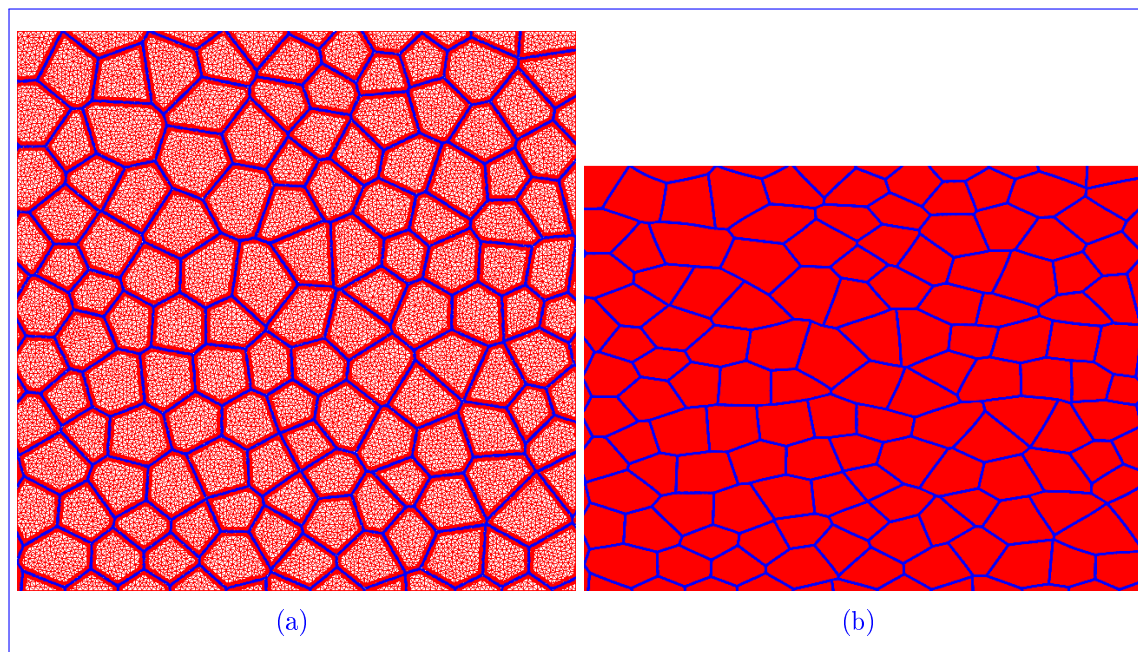


Figure 5.11: (a) The Voronoï honeycomb with  $\gamma = 0.7$  in its undeformed state and the anisotropic meshing at the interfaces (b) after 25% of biaxial compression

#### 5.2.4.4 Compression of a three-dimensional closed-cell foam

A three-dimensional closed-cell foam, made of 107 cells, with a cell irregularity of 0.5 and a relative density of 0.1 was generated in a unit cube. Anisotropic mesh adaptation was performed in order to properly describe the foam. The resulting FE mesh is made of 349659 nodes and 1957422 elements. Figure 5.13a illustrates the foam at its initial state defined by the iso-zero of its level-set function where the anisotropic mesh is shown. A biaxial compression up to 30% was performed by imposing velocities on the upper and lower boundaries of the domain (see Figure 5.13b).

The simulation was performed on 96 processors in 1 hour and 12 minutes after the construction of the initial mesh. Figure 5.14 illustrates the velocity's norm and pressure on the interface of the foam (i.e. the iso-zero of the level-set function) at 30% deformation.

Figure 5.15 shows the reduced stress/strain curve of the closed-cell foam and its mass variation. The foam presents a linearly elastic behavior before reaching a plateau region at about 23% of deformation, this is due to the beginning of the elastic buckling of the cells. This type of behavior for elastic closed-cell foams was already observed in [123, 130].

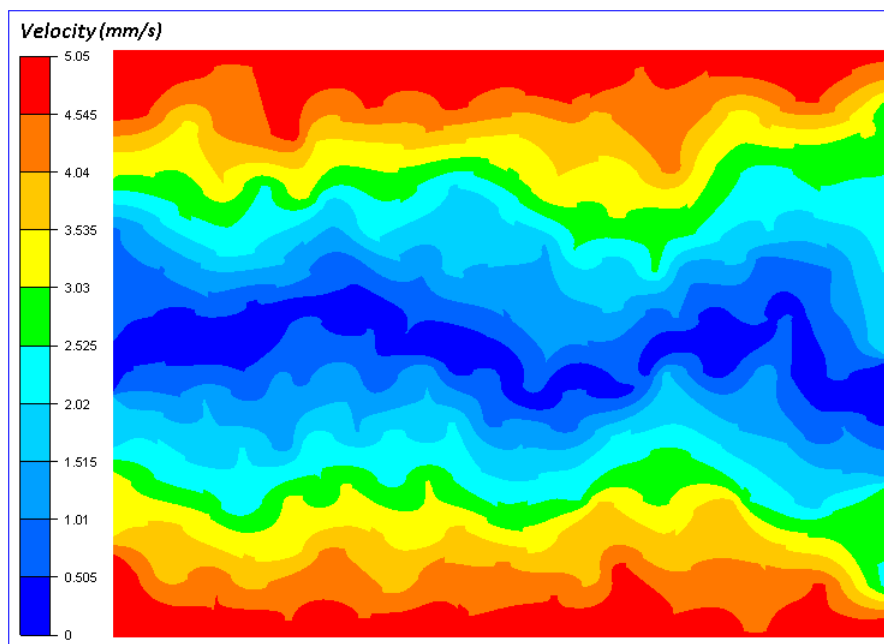


Figure 5.12: The velocity's norm of the Voronoi honeycomb with  $\gamma = 0.7$  after 25% of biaxial compression

Furthermore, the mass variation, does not exceed 0.6% which is a very reasonable loss and proves that the foam's mass is conserved during the whole process.

## 5.3 Permeability computation of disordered fiber arrays

Before illustrating the simulations performed, we begin by detailing the governing equations and FE formulation of our problem.

### 5.3.1 Governing equations

A resin is injected in the disordered fibrous media in order to compute its permeability. The injected resin is considered as a Newtonian incompressible fluid. Because of the low pressure imposed for the injection and its high viscosity, inertia and gravity terms can be neglected. Consequently, Stokes equations describe the fluid flow:

$$\begin{cases} \eta_f \Delta \mathbf{v} - \nabla p = 0 \\ \nabla \cdot \mathbf{v} = 0 \end{cases} \quad (5.47)$$

with  $\mathbf{v}$  the fluid velocity,  $p$  the pressure and  $\eta_f$  the dynamic viscosity.

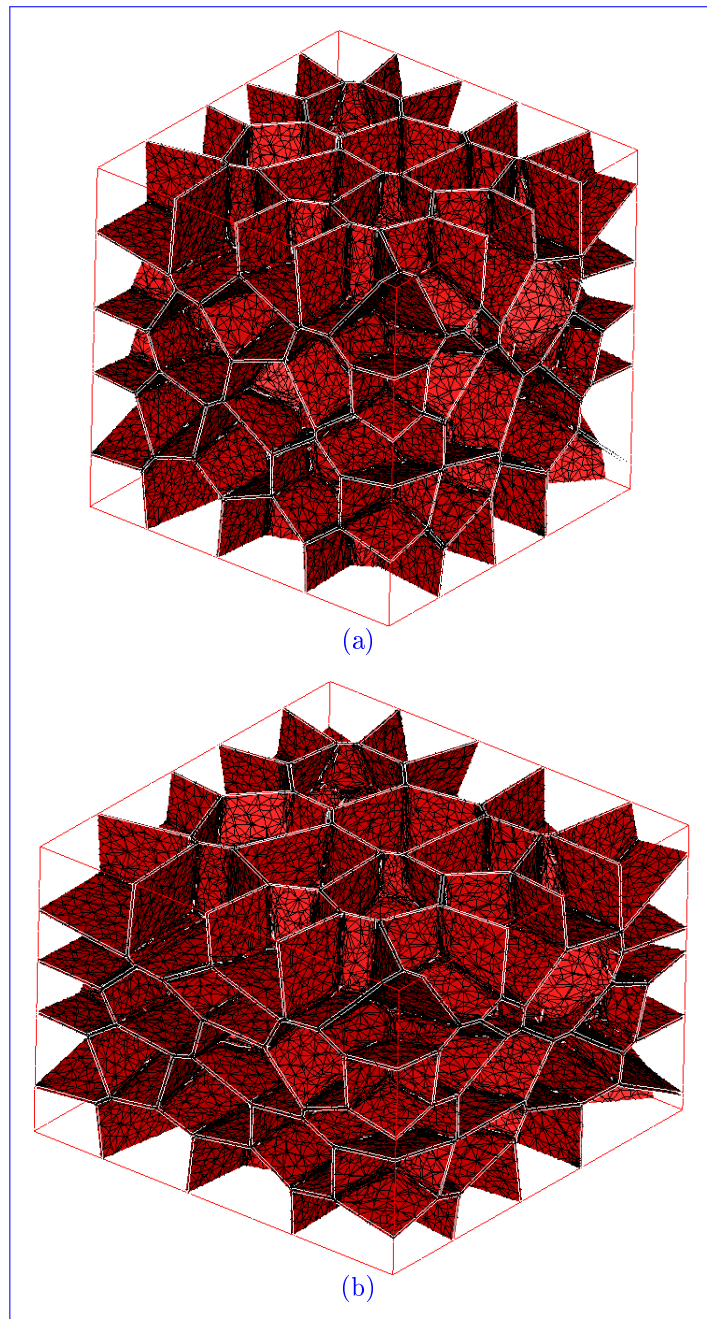


*Figure 5.13: (a) The iso-zero of the level-set function defining a three-dimensional closed-cell foam made of 107 cells with a cell irregularity of 0.5 and a relative density of 0.1 at its initial state with the anisotropic remeshing and (b) the same foam after 30% deformation*

Darcy's law is traditionally used to model flow motion in porous media at the macroscopic scale. These macroscopic equations are obtained from a volume average of the Navier-Stokes ones [86, 131, 132], describing the flow motion at the microscopic scale.

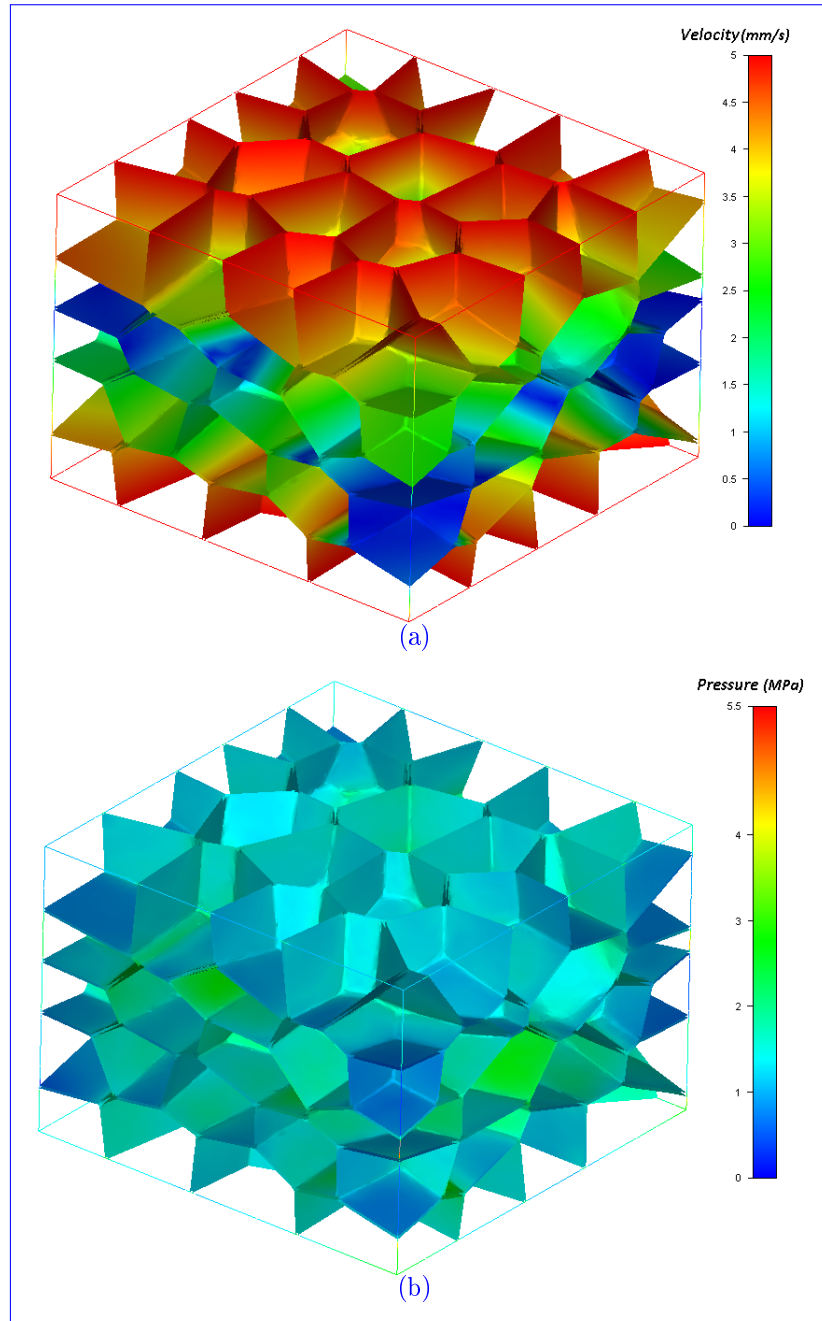


*Figure 5.14: (a) The velocity's norm at 30% deformation of the closed-cell foam shown at the foam's interface and (b) the pressure at 30% deformation also shown at the foam's interface*

We will use the definitions of the averages given in [86], where the spatial average of

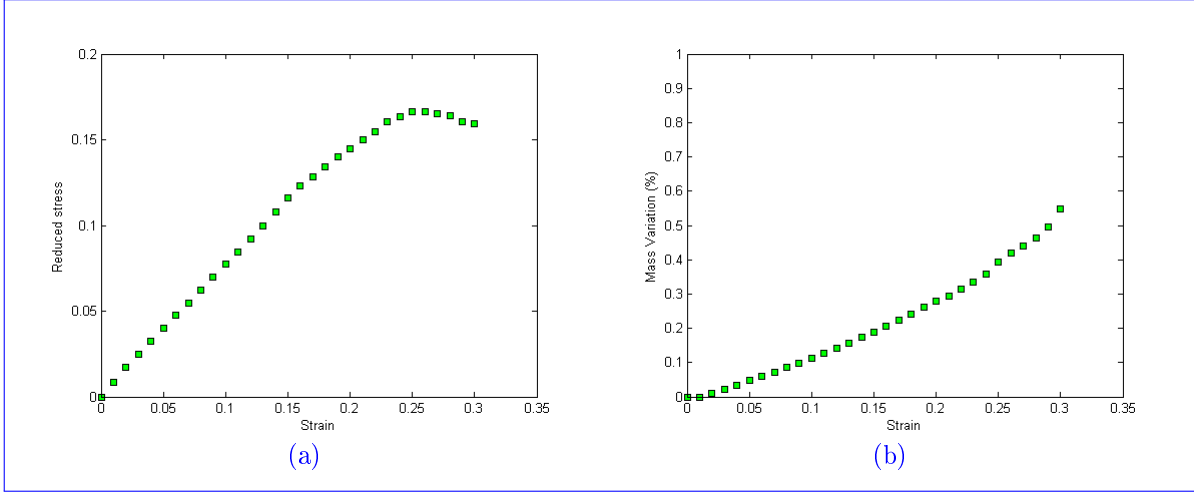


Figure 5.15: (a) The reduced stress/strain curve of the irregular closed-cell foam and (b) the variation of its mass

a quantity  $B$  is defined in the whole volume:

$$\langle B \rangle = \frac{1}{V} \int_{\Omega} B \, d\Omega. \quad (5.48)$$

The intrinsic phase average of a quantity  $B_f$  is defined in the fluid phase:

$$\langle B_f \rangle^f = \frac{1}{V_f} \int_{\Omega_f} B_f \, d\Omega, \quad (5.49)$$

with  $\Omega_f$  the fluid domain. The porosity  $\phi$ :

$$\phi = \frac{V_f}{V}, \quad (5.50)$$

is defined as the ratio of the volume occupied by the fluid  $V_f$  and the total volume  $V$ .

We suppose that the solid skeleton is static and non-deformable, and that the porous media is saturated. Neglecting effects of viscosity on the flow with respect to the resistance of the skeleton, Darcy's equation is obtained:

$$\langle v \rangle = -\frac{1}{\eta_f} \mathcal{K} \cdot \langle \nabla p \rangle^f, \quad (5.51)$$

where the permeability  $\mathcal{K}$  is a tensor for anisotropic porous media, like fibrous media for example. In the case of unidirectional fiber packings, if the  $z$  axis of the coordinate system is taken in the same direction as the axis of the fibers, the permeability tensor can be then written as follows:

$$\mathcal{K} = \begin{pmatrix} K_{\perp} & 0 \\ 0 & K_{\parallel} \end{pmatrix}, \quad (5.52)$$

with  $K_{\perp}$  a transverse permeability tensor and  $K_{\parallel}$  the permeability along the fiber axis. For regular packings (rectangular, triangular or hexagonal) the matrix  $K_{\perp}$  is proportional to the unit matrix and then only a scalar  $K_{\perp}$  has to be computed. However for disordered arrays, we need to look for a more suitable form:

$$K_{\perp} = \begin{pmatrix} K_{xx} & K_{xy} \\ K_{xy} & K_{yy} \end{pmatrix} \quad \text{or} \quad K_{\perp} = \begin{pmatrix} K_{xx} & 0 \\ 0 & K_{yy} \end{pmatrix} \quad (5.53)$$

### 5.3.2 Numerical approach

All the phases of the multidomain problem are implicitly represented by a level-set function,  $\alpha$ . To obtain an accurate description of the interface and small errors concerning the computed flow, efficient anisotropic adaptive meshing is used. The viscosity  $\eta(\alpha)$  is defined on the whole computational domain using a mixture law as for the foam compression problem (see Figure 5.16). The rigidity of the solid part is taken into account with a high value of the viscosity (namely  $\eta_s = 10^3 \eta_f$  [21])

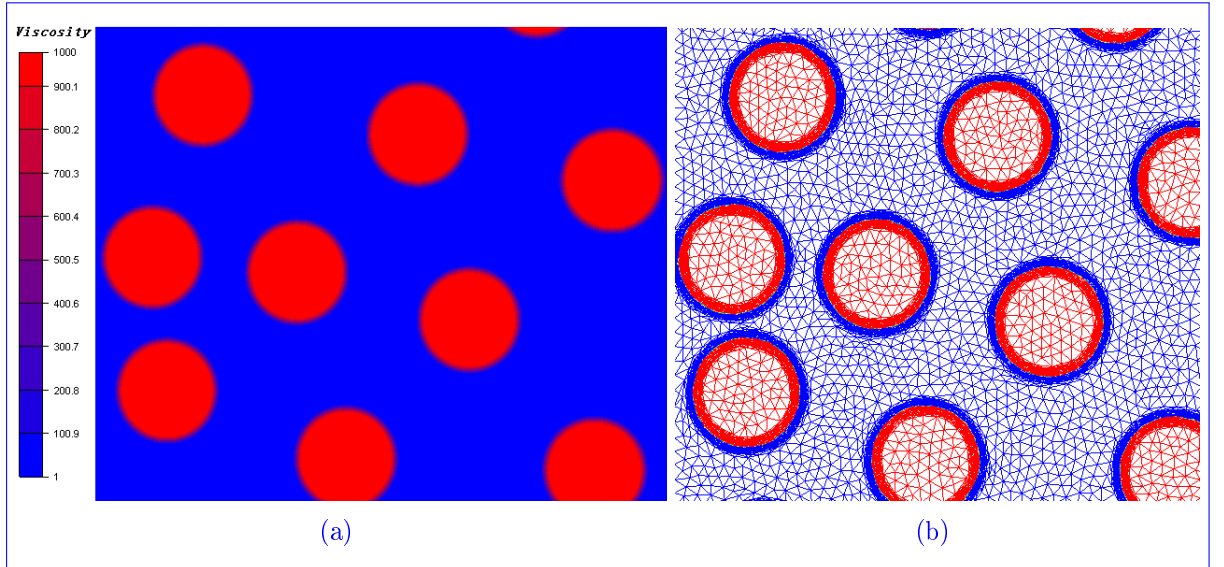


Figure 5.16: (a)  $\eta(\alpha)$  defined on the whole computational domain using a mixture law and (b) anisotropic remeshing at the solid-fluid interface

### 5.3.3 The FE formulation

The FE formulation begins by writing the weak form of the Stokes equations (5.47). The problem consists in finding  $(\mathbf{v}, p) \in V \times Q$  such that:

$$\begin{cases} 2\eta(\alpha) (\varepsilon(\mathbf{v}) : \varepsilon(\mathbf{w}))_{\Omega} - (p, \nabla \cdot \mathbf{w})_{\Omega} = 0 \\ (q, \nabla \cdot \mathbf{v})_{\Omega} = 0 \end{cases} \quad (5.54)$$

where the trial function  $q$  for the pressure is defined in  $Q$  and the trial function  $\mathbf{w}$  for the velocity is defined in  $V_0$ .

As for the FE formulation of the foam compression, the Mini-element was used, hence the discrete Stokes formulation is then written: find  $(\mathbf{v}, p_h) \in \mathcal{V}_h \times Q_h$  such that

$$\begin{cases} 2\eta(\alpha) (\varepsilon(\mathbf{v}_h) : \varepsilon(\mathbf{w}_h))_\Omega - (p_h, \nabla \cdot \mathbf{w}_h)_\Omega = 0 \\ 2\eta(\alpha) (\varepsilon(\mathbf{v}^b) : \varepsilon(\mathbf{w}^b))_\Omega - (p_h, \nabla \cdot \mathbf{w}^b)_\Omega = 0 \\ (q_h, \nabla \cdot (\mathbf{v}_h + \mathbf{v}^b))_\Omega = 0 \end{cases} \quad (5.55)$$

This system can be put naturally under the following matrix form:

$$\begin{pmatrix} A_{vv} & 0 & A_{vp}^t \\ 0 & A_{bb} & A_{bp}^t \\ A_{vp} & A_{bp} & 0 \end{pmatrix} \begin{pmatrix} \mathbf{v}_h \\ \mathbf{v}^b \\ p_h \end{pmatrix} = \begin{pmatrix} 0 \\ 0 \\ 0 \end{pmatrix}, \quad (5.56)$$

where:

$$\begin{aligned} A_{vv} &= 2\eta(\alpha) (\varepsilon(\mathbf{v}_h) : \varepsilon(\mathbf{w}_h))_\Omega, \\ A_{bb} &= 2\eta(\alpha) (\varepsilon(\mathbf{v}^b) : \varepsilon(\mathbf{w}^b))_\Omega, \\ A_{vp} &= (p_h, \nabla \cdot \mathbf{w}_h)_\Omega, \\ A_{bp} &= (p_h, \nabla \cdot \mathbf{v}^b)_\Omega. \end{aligned} \quad (5.57)$$

Finally, the static condensation process consisting in solving the second line for the bubble function  $\mathbf{v}^b$ , which by inserting into the third line of (5.56), results the condensed matrix scheme for large-scale unknowns  $\mathbf{v}_h$  and  $p_h$  reading:

$$\begin{pmatrix} A_{vv} & A_{vp}^t \\ A_{vp} & C \end{pmatrix} \begin{pmatrix} \mathbf{v}_h \\ p_h \end{pmatrix} = \begin{pmatrix} 0 \\ 0 \end{pmatrix}, \quad (5.58)$$

with  $C = -A_{bp}A_{bb}^{-1}A_{vp}^t$ .

### 5.3.4 The RVE

In order to get suitable averaged quantities describing the macroscopic behavior of the material, it is necessary to perform computations on an RVE. The RVE is a two dimensional rectangle of width,  $L$  and height  $H$  on which three different boundary conditions are applied:

1. the pressure gradient is in the horizontal direction  $x$ ,  $v_y$  is null on the external boundary and

$$\partial_y v_x(x, 0) = \partial_y v_x(x, H) = 0 ; v_z(x, y) = 0, \partial_z p(x, y) = 0 ; p(0, y) = P, p(L, y) = 0. \quad (5.59)$$

2. the pressure gradient is in the vertical direction  $y$ ,  $v_x$  is null on the external boundary and

$$\partial_y v_x(0, y) = \partial_y v_x(L, y) = 0 ; v_z(x, y) = 0, \partial_z p(x, y) = 0 ; p(x, 0) = P, p(x, H) = 0. \quad (5.60)$$

3. the pressure gradient is in the longitudinal direction  $z$ ,  $v_x$  and  $v_y$  are null,

$$\partial_x v_z(0, y) = \partial_x v_z(L, y) = 0 ; \partial_y v_z(x, 0) = \partial_y v_z(x, H) = 0 ; \partial_z p(x, y) = P/L \quad (5.61)$$

In what concerns disordered fiber RVE generation, we send the reader to section 2.4.3 in the chapter 2 where we detailed the method used to generate this type of RVEs.

#### 5.3.4.1 Ripley's $K_r$

As we want to compute the permeability of different *random* fiber arrangements as a function of other parameters beyond porosity, the microstructure needs to be properly quantified. The Ripley's  $K_r$  function [133, 134] can be used to differentiate between regular arrangements, Completely Spatially Random (CSR) arrangements, and clustered point patterns. This function is defined as:

$$K_r(r) = \frac{A}{N^2} \sum_{k=1}^N \frac{I_k(r)}{w_k(r)}, \quad (5.62)$$

where  $I_k(r)$  is the number of points found within a distance  $r$  of the point  $k$ ,  $N$  is the total number of points in the area of interest  $A$ , and  $w_k(r)$  is a correction factor taking into account the fact that it is possible that only a part of the observation area  $\pi r^2$  falls within the area of interest  $A$ . This correction factor is computed as the proportion of the perimeter of the circle centered in  $k$  with radius  $r$  which is inside the area of interest [135].  $K_r(r)$  describes characteristics of point patterns at many length scales. The  $K_r$ -function of a Poisson distribution is  $\pi r^2$  and draws a dividing line between a regular and a clustered pattern. Estimates of  $K_r(r)$  are expected to be smaller than  $\pi r^2$  if the points form a regular pattern, and to be larger than  $\pi r^2$  in the presence of clustering [136]. Furthermore, the extent of the deviation of  $K_r(r)$  from  $\pi r^2$  and the length scale at which such deviations occur give some additional insight into a microstructure. The  $L$ -plot, a linearized plot of  $K_r(r)$  defined as:  $L(r) = \sqrt{K_r(r)/\pi}$ , is frequently used to show these deviations and the length scales at which they occur. The  $L$ -plot of a Poisson distribution is simply a straight line of 45-degree slope through the origin. Figure 5.17 shows the resulting  $L(r)$ -function applied to the fiber distributions in Figure 2.44. It is evident that at large distances all fiber distributions approach the CSR pattern. This concludes that our method can generate random distributions usable in this type of studies.

#### 5.3.5 Permeability computation

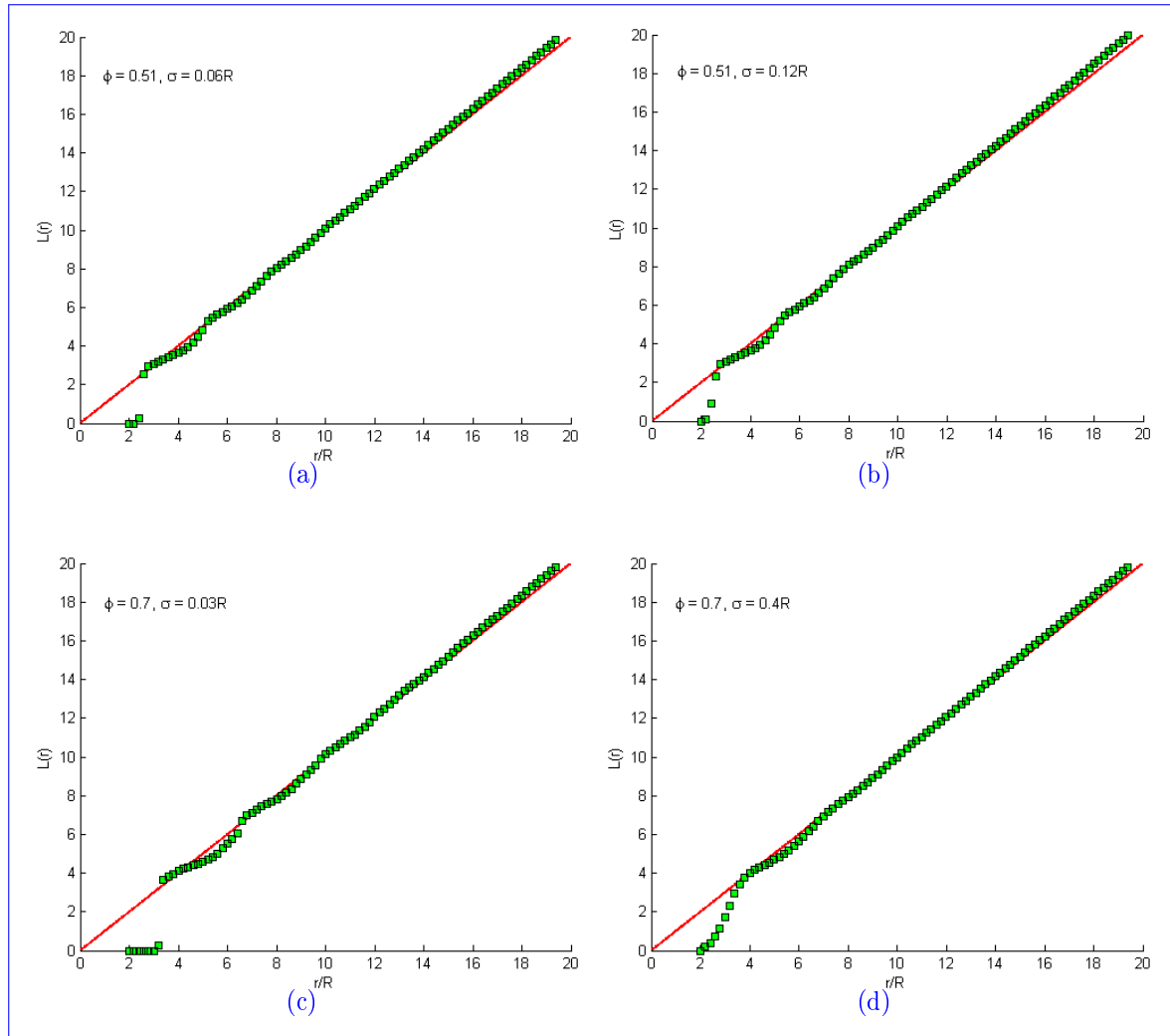


Figure 5.17: The  $L(r)$  functions of the fiber distributions described in Figure 2.44

### 5.3.5.1 Computation of the transverse permeability tensor

The transverse permeability is computed with a least square method. The computations are performed with the first two sets of boundary conditions for 2D Stokes equations (5.47).

First assuming that the permeability tensor  $K_{\perp}$  has the form

$$K_{\perp} = \begin{pmatrix} K_{xx} & K_{xy} \\ K_{xy} & K_{yy} \end{pmatrix}. \quad (5.63)$$

And second, that  $k$  computations were performed which gives  $\langle \mathbf{v}_i \rangle$  and  $\langle \nabla p_i \rangle^f$  with  $i = 1, \dots, k$ .

The least square method consists in minimizing the function  $J$

$$J(K_{xx}, K_{yy}, K_{xy}) = \sum_{i=1}^k \left( K_{xx} \langle \partial_x p_i \rangle^f + K_{xy} \langle \partial_y p_i \rangle^f + \eta_f \langle v_{x,i} \rangle \right)^2 + \left( K_{xy} \langle \partial_x p_i \rangle^f + K_{yy} \langle \partial_y p_i \rangle^f + \eta_f \langle v_{y,i} \rangle \right)^2. \quad (5.64)$$

The minimum of Eq.(5.64) is reached when the partial derivatives of the function  $J$  with respect to the permeability components are zero i.e.

$$\begin{aligned} \frac{\partial J}{\partial K_{xx}} &= 0, \\ \frac{\partial J}{\partial K_{yy}} &= 0, \\ \frac{\partial J}{\partial K_{xy}} &= 0. \end{aligned} \quad (5.65)$$

This leads to the following system of equations:

$$\begin{aligned} AK_{xx} + CK_{xy} &= E, \\ BK_{yy} + CK_{xy} &= F, \\ CK_{xx} + CK_{yy} + (A+B)K_{xy} &= G, \end{aligned} \quad (5.66)$$

with

$$\begin{aligned} A &= \sum_{i=1}^k \left( \langle \partial_x p_i \rangle^f \right)^2, \\ B &= \sum_{i=1}^k \left( \langle \partial_y p_i \rangle^f \right)^2, \\ C &= \sum_{i=1}^k \langle \partial_x p_i \rangle^f \langle \partial_y p_i \rangle^f, \\ E &= -\eta_f \sum_{i=1}^k \langle \partial_x p_i \rangle^f \langle v_{x,i} \rangle, \\ F &= -\eta_f \sum_{i=1}^k \langle \partial_y p_i \rangle^f \langle v_{y,i} \rangle, \\ G &= -\eta_f \sum_{i=1}^k \left( \langle \partial_y p_i \rangle^f \langle v_{x,i} \rangle + \langle \partial_x p_i \rangle^f \langle v_{y,i} \rangle \right), \end{aligned}$$

and so,

$$\begin{aligned} K_{xx} &= \frac{-BCG + C^2F - C^2E + EAB + EB^2}{d}, \\ K_{yy} &= \frac{A^2F - CAG + C^2E - C^2F + ABF}{d}, \\ K_{xy} &= \frac{BAG - BCE - FAC}{d}, \end{aligned}$$

with  $d = (A + B)(AB - C^2)$ .

If  $K_{xy}$  is assumed to be zero, then,

$$\begin{aligned} K_{xx} &= \frac{E}{A}, \\ K_{yy} &= \frac{F}{B}. \end{aligned}$$

If  $K_{xy} = 0$  and  $K_{xx} = K_{yy}$ , a scalar transverse permeability  $K$  can be computed as

$$\begin{aligned} K &= \frac{E + F}{A + B} = -\eta_f \frac{\sum_{i=1}^k \langle \partial_x p_i \rangle^f \langle v_{x,i} \rangle + \langle \partial_y p_i \rangle^f \langle v_{y,i} \rangle}{\sum_{i=1}^k \left( \langle \partial_x p_i \rangle^f \right)^2 + \left( \langle \partial_y p_i \rangle^f \right)^2} \\ &= -\eta_f \frac{\sum_{i=1}^k \langle \mathbf{v}_i \rangle \cdot \langle \nabla p_i \rangle^f}{\sum_{i=1}^k \langle \nabla p_i \rangle^f \cdot \langle \nabla p_i \rangle^f}. \end{aligned} \quad (5.67)$$

### 5.3.5.2 Computation of longitudinal permeability

The longitudinal permeability is obtained by computing the scalar  $v_z$  solution of the reduced Stokes equation

$$\eta_f \left( \frac{\partial^2 v_z}{\partial y^2} + \frac{\partial^2 v_z}{\partial x^2} \right) = \frac{\partial p}{\partial z} \quad \text{on } \Omega_f, \quad (5.68)$$

and

$$K_{\parallel} = -\eta_f \frac{\langle v_{z,i} \rangle}{\partial_z p}. \quad (5.69)$$

## 5.3.6 Numerical Results

### 5.3.6.1 The RVE's size

The randomness of the generated fiber distributions leads to a scatter in the computed permeability. Hence, an average permeability should be calculated along with a data variation in order to be statistically representative. In this work, 20 random microstructures were generated for each class of fiber distributions characterized by the same  $\phi$  and  $\sigma$  (see section 2.4.3). The average permeability and its standard deviation,  $\sigma_p$ , are given by:

$$\langle K \rangle = \frac{1}{20} \sum_{i=1}^{20} K_i, \quad (5.70)$$

$$\sigma_p = \frac{1}{19} \sqrt{\sum_{i=1}^{20} (K_i - \langle K \rangle)^2}. \quad (5.71)$$

Moreover, the permeability of fiber distributions is not only a function of microstructural parameters but also a function of the RVE's size or also the number of fibers  $N_f$  in the domain. An extremely large computational domain is surely representative of the fiber array but this will cause a drastic increase in the computational cost which makes this type of studies quasi-impossible. A similar approach for determining the RVE's size of the Voronoï honeycombs is performed for finding the size of the fiber arrays' RVE. In this case a study of the size effect on  $\langle K \rangle$ ,  $\langle K_{\parallel} \rangle$  and  $\phi$  was performed and computations were carried out on elementary volumes of different size extracted from microstructures generated with  $\sigma = 0.06R$  and  $\phi = 0.5$  as illustrated in Figure 5.18.

The results for the permeability values are shown in Figure 5.19 where they are adimensionalised and in Figure 5.20 for the porosity.

Fluctuations are observed in the values of  $\langle K \rangle/R^2$ ,  $\langle K_{\parallel} \rangle/R^2$  and  $\langle \phi \rangle$  when a relatively small number of fibers is considered then the values reach a plateau after  $N_f > 385$ . Also, after  $N_f > 555$  the associated standard deviations are reduced. As a conclusion, an RVE's size of  $N_f > 555$  is used in the remainder of this chapter.

### 5.3.6.2 Isotropic properties

We computed the values of the components of the transverse permeability tensor  $K_{\perp}$ ,  $K_{xx}$ ,  $K_{yy}$  and  $K_{xy}$ , in order to see if the scalar transverse permeability  $K$  can be computed. In Figure 5.21 the averaged components are computed at different porosity levels and plotted against  $\sigma/R$ . The values at different porosities are illustrated in different figures for the sake of clarity.

Figure 5.21 shows that  $K_{xx}$  is equal to  $K_{yy}$  and  $K_{xy}$  is negligible on all porosity levels and at all values of  $\sigma$ . This means that the transverse permeability is independent of the flow direction and that the fiber arrays are isotropic. In this case, a scalar transverse permeability is computed by Eq.(5.67).

### 5.3.6.3 The effect of $\sigma$ on $\mathcal{K}$

Figure 5.22 shows two representative flow paths computed on RVEs at  $\phi = 0.7$  and Figure 5.23 illustrates the velocity computed for the boundary conditions of type 3 (Eq.(5.61)) on the same previous RVEs. The difference between the two microstructures lies in the choice of  $\sigma$  ( $\sigma = 0.03R$  in Figures 5.22(a) and 5.23(a) and  $\sigma = 0.4R$  in Figures 5.22(b) and 5.23(b)).

We notice from these two figures that the microstructure has a great effect on the flow distribution in the interstitial space. In what concerns transverse flows (boundary

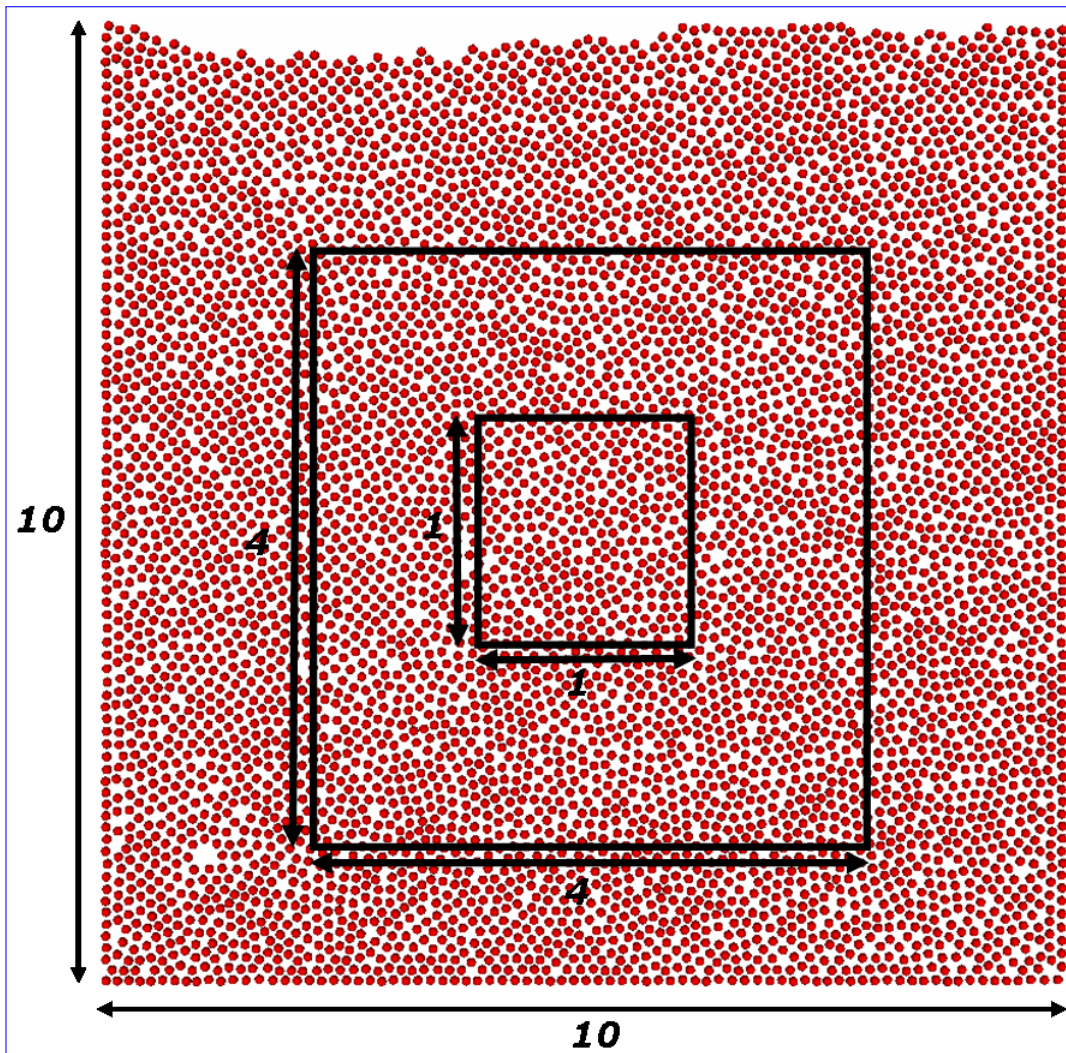


Figure 5.18: Elementary volumes extracted from a  $10 \times 10$  microstructure in order to determine the size of the RVE

conditions 2 and Figure 5.22), a larger degree of local heterogeneity caused by an increase of  $\sigma$  results in a wider range of flow paths. In this case, a few major flow paths exist while in the case of  $\sigma = 0.03R$  a large number of small paths exist giving a uniform flow through the fiber array. In what concerns longitudinal flows (boundary conditions 3 and Figure 5.23), a larger degree of local heterogeneity results in the formation of pockets of high-speed fluid against a more uniform speed for small values of  $\sigma$ . From these figures, it is evident that fibers at the same porosity can exhibit drastically different patterns of fluid flows. It follows that the use of porosity alone cannot define properly their permeability. In Figure 5.24, the numerically computed  $\langle K \rangle$  and  $\langle K_{\parallel} \rangle$  at each porosity level are plotted against  $\sigma/R$ .

In Figures 5.24(a) and 5.24(b), the ending point is the permeability of the hexagonal array

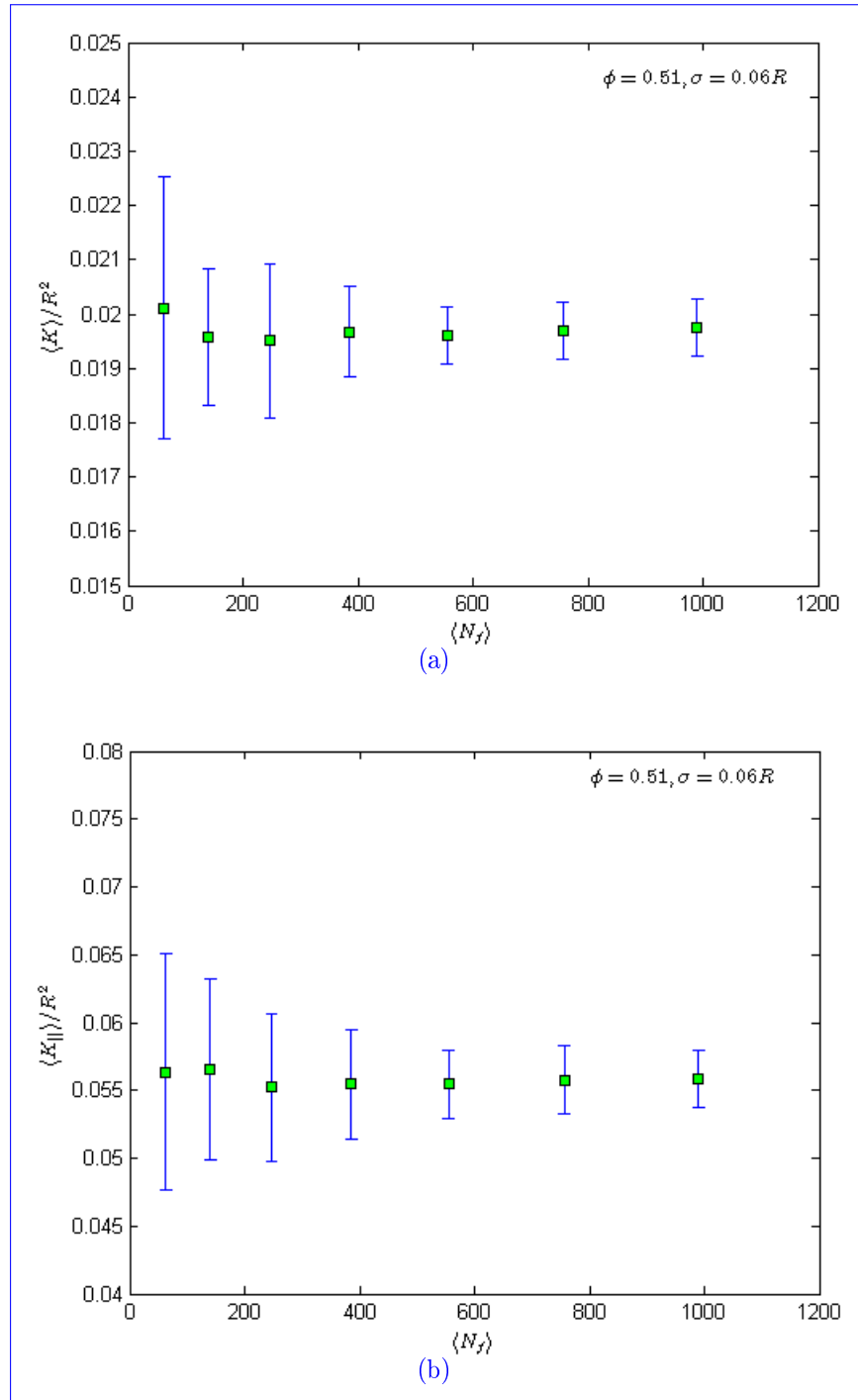


Figure 5.19: The size effect on  $\langle K \rangle / R^2$ . The fiber distributions were generated with  $\sigma = 0.06R$  and  $\phi = 0.51$ . The error bars represent the standard deviations  $\pm \sigma_p$

(filled star), for which the inter-fiber spacing is only linked to the porosity [80]. From the plot in these figures, the effect of  $\sigma/R$  on  $\langle K \rangle / R^2$  and  $\langle K_{\parallel} \rangle / R^2$  is evident. An increasing

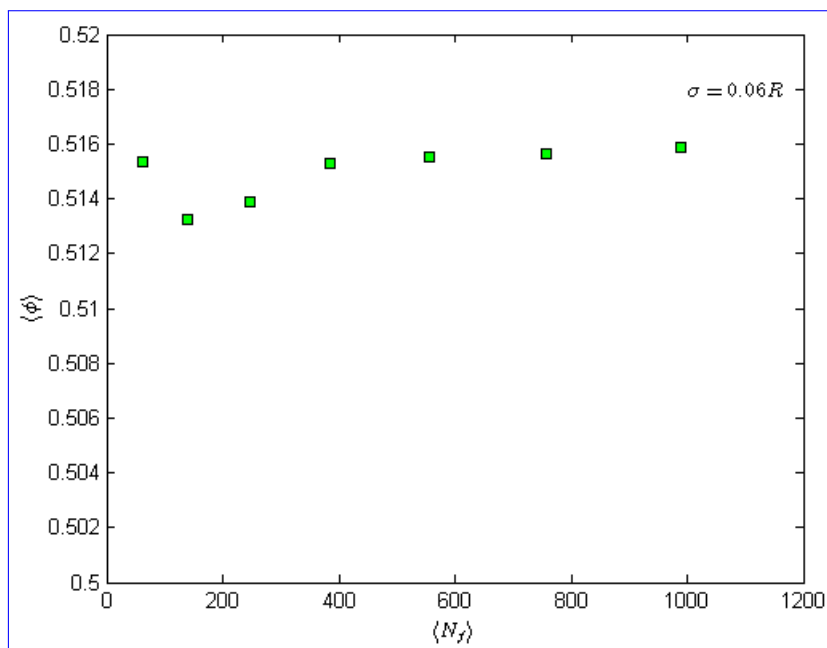


Figure 5.20: The size effect on the porosity

$\sigma$  or also moving from a uniform array to an array showing higher degrees of disorder results in an increase of both permeability values, the transverse and the longitudinal. The results of  $\langle K_{\parallel} \rangle$  are in agreement with those of Chen and Papathanasiou [20] who found also that an increase of the microstructure heterogeneity or a decrease in the mean nearest inter-fiber spacing,  $\bar{\delta}_1$ , enhances  $\langle K_{\parallel} \rangle$ . This is due to the formation of large flow paths. On the other hand, our results concerning  $\langle K \rangle$  are opposite to those of Chen and Papathanasiou [8] except for  $\phi > 0.7$ . They explain that the decrease in  $\langle K \rangle$  in the range  $0.45 < \phi < 0.7$  comes from the presence of narrow gaps which reduce the permeability and that the increase of  $\langle K \rangle$  in the range  $\phi > 0.7$  comes from the formation of flow paths whose size is comparable to the size of fiber aggregates. In our case, we explain this increase by the simple fact that large gaps enhance  $\langle K \rangle$  as they enhance  $\langle K_{\parallel} \rangle$ .

## 5.4 Conclusion

This chapter presented the mechanical applications performed in this work.

First, a finite element analysis has been presented to simulate the biaxial compression of elastic foams. By taking the presence of air inside the foams' cells into account, the simulations were considered as an FSI problem, between a compressible elastic solid (i.e. the foam's skeleton) and a compressible fluid (i.e. the air), that was solved by a monolithic formulation in a Lagrangian framework. This kind of approach enabled us to study the air's effect on the foam's behavior. Also, the effect of cell irregularity was studied and a compression of a three-dimensional closed-cell foam was performed. The results yielded

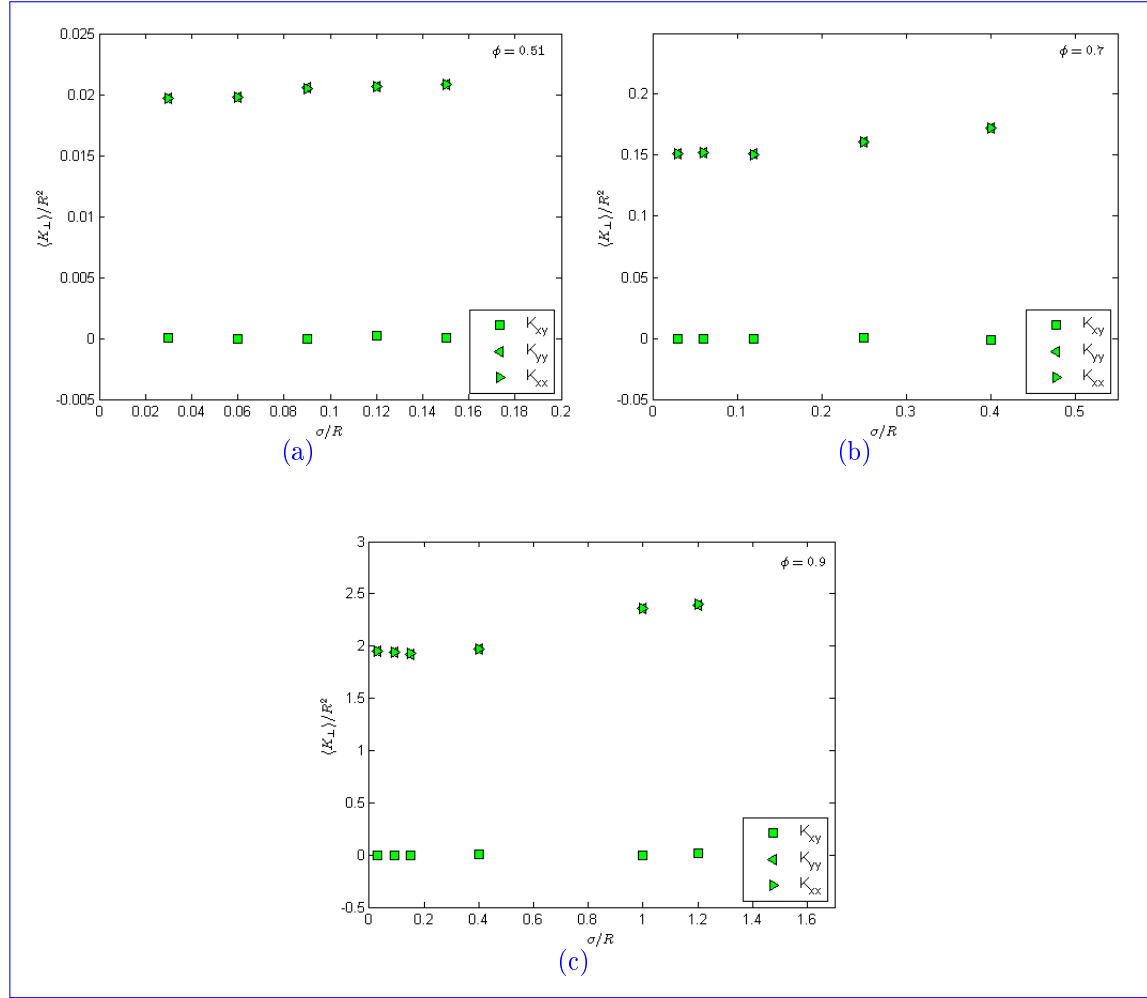


Figure 5.21: The averaged permeability components at different values of  $\sigma$ : (a)  $\phi = 0.51$ , (b)  $\phi = 0.7$  and (c)  $\phi = 0.9$

that the honeycomb's stress reaches a plateau region earlier when the air is present inside the foam's cells and that it is reduced as the irregularity increases. Furthermore the closed-cell foam presented a typical behavior of elastic foams during compression and the mass of the whole structure was conserved.

Second, permeability computations of disordered unidirectional fiber arrays were performed. The flow through the fibers, which were considered as rigid discs, is governed by the Stokes equations that, when averaged, lead to Darcy's law. Hence, the permeability of a fiber array can be computed. The RVE's size or number of fibers was determined by studying its influence on the transverse and longitudinal permeabilities. Afterwards, we have shown that the fiber arrays are isotropic and that the transverse permeability is independent of the flow direction. Furthermore, the influence of the degree of disorder of fiber arrays on transverse and longitudinal permeabilities was studied and the results have shown that both permeabilities increase on all porosity levels as the disorder increases.

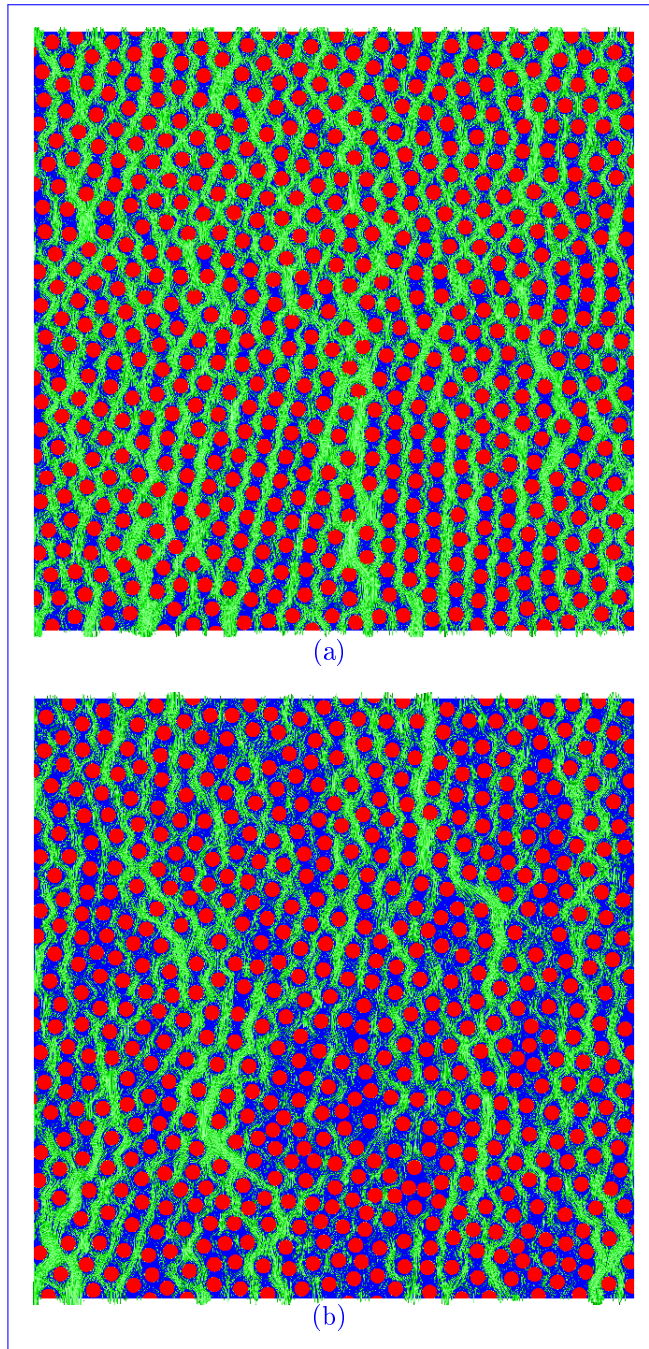


Figure 5.22: Flow paths for boundary conditions 2 across unidirectional fiber array: (a)  $\phi = 0.7$  ,  $\sigma = 0.03R$  and (b)  $\phi = 0.7$  ,  $\sigma = 0.4R$

## 5.5 Résumé français

Ce chapitre a permis de présenter les applications mécaniques étudiées dans cette thèse. Premièrement, une analyse éléments finis a été présentée pour simuler la compression

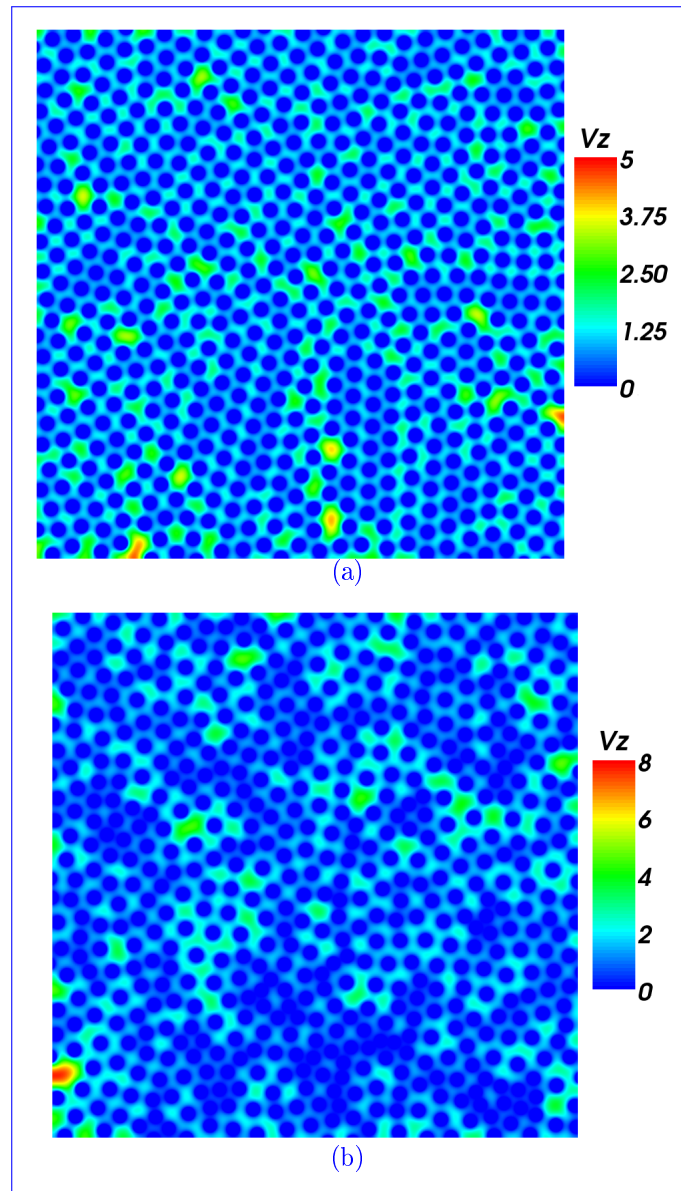


Figure 5.23: Contours of fluid velocity for longitudinal flows across unidirectional fiber array: (a)  $\phi = 0.7$  ,  $\sigma = 0.03R$  and (b)  $\phi = 0.7$  ,  $\sigma = 0.4R$

biaxiale de mousses élastiques. En prenant en compte la présence de l'air à l'intérieur des cellules des mousses, le problème physique doit être considéré sous l'angle d'un problème d'interaction fluide structure, entre un solide élastique compressible (le squelette de la mousse) et un fluide compressible (l'air). Ce problème a été résolu par une approche monolithique dans un contexte Lagrangien. Ce type d'approche nous a permis d'étudier l'effet de l'air sur le comportement de la mousse. De plus, l'effet de l'irrégularité de la forme des cellules a été étudié et une compression d'une mousse tridimensionnelle à cellules fermées a été réalisée. Les résultats ont montré que la contrainte pour une mousse

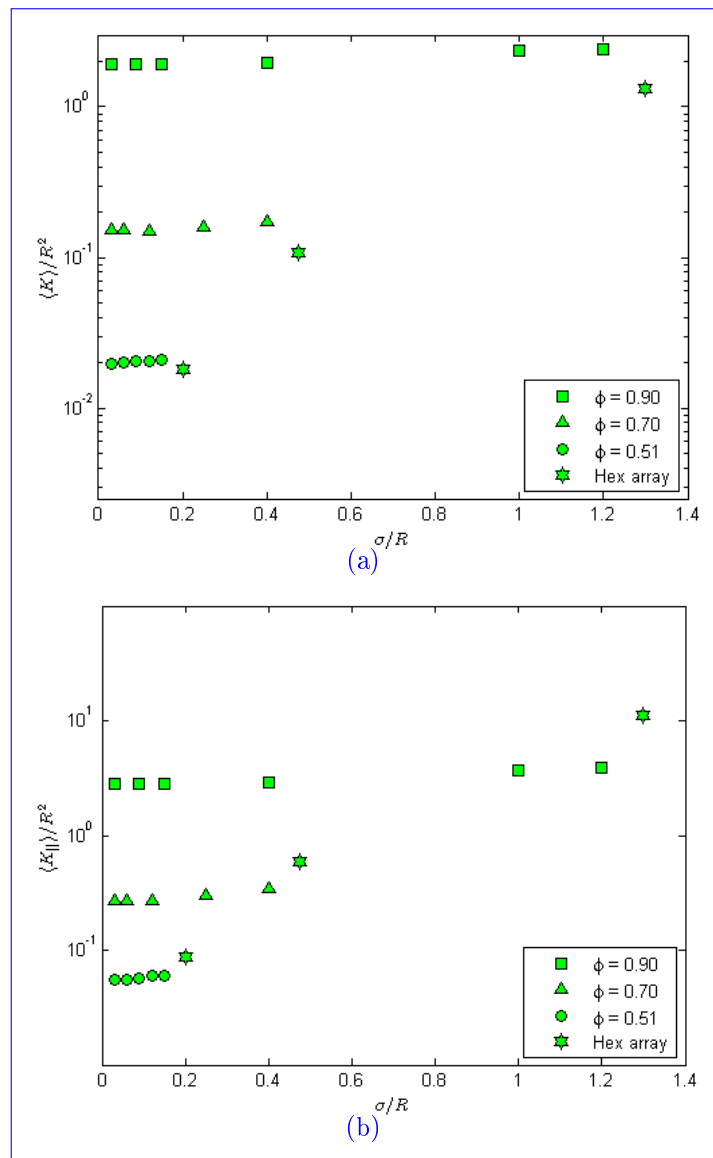


Figure 5.24: The effect of averaged standard deviation of the inter-fiber spacing on the normalized averaged transverse (a) and longitudinal (b) permeability. Also shown are permeability values for hexagonal arrays [80]

régulière atteint un plateau plus tôt lorsque l'air à l'intérieur des cellules de la mousse est pris en compte et que la valeur de ce plateau est réduite lorsque l'irrégularité augmente.

Deuxièmement, des calculs de perméabilité sur des milieux fibreux monodirectionnels désordonnés ont été effectués. L'écoulement entre les fibres est gouverné par les équations de Stokes. Ces équations mènent à la loi de Darcy lorsqu'elles sont moyennées. De là, le tenseur de perméabilité du milieu fibreux peut être calculé. La taille idéale du VER a été déterminée en étudiant son influence sur les perméabilités transversale et longitudinale. Ensuite, nous avons montré que l'écoulement à travers les fibres est isotrope

et que la perméabilité transversale est indépendante de la direction de l'écoulement. De plus, l'influence du degré de désordre des milieux fibreux considérés sur les perméabilités transversales et longitudinales a été étudiée et les résultats obtenus ont montré que les deux perméabilités augmentent, quelque soit le niveau de porosité, lorsque le désordre s'accroît.





## Chapter 6

### General conclusion and perspectives

"The influence of microstructural heterogeneities on material processing is of great importance" and "the response of a Representative Volume Element (RVE) when it is subject to a given macroscopic loading path is of the main interest". These two phrases are behind the motivations of this Ph.D. thesis which is dedicated to two main objectives: (i) the creation of a multi-physical virtual microstructure builder for generating various types of RVEs (chapters 2, 3 and 4); (ii) the calculations performed on RVEs of elastic foams and disordered fibrous media generated by this microstructure builder (chapter 5).

In chapter 2, the core of our microstructure generator, which is the simultaneous generation of polyhedra and spherical particles, is detailed. The Voronoï Tessellation Method (VTM) and the Laguerre Tessellation Method (LTM) are used for the polyhedral generation part. The polyhedra can model random metallurgical grains when the VTM is used and the same microstructures with specific cell size distributions when the LTM is used. Boundaries between adjacent cells can also be spread by shifting them in the direction of each center with random values. This cell spreading technique enables our generator to model semi-solid granular structures and foams as well while respecting a given solid fraction. Furthermore, the LTM is based on the generation of spherical particles which are used as a basis for approximating the cells' sizes. These particles are also used to model powder RVEs most importantly. However, for the both kinds of microstructure considered, powders and polycrystals, the spherical particles should be densely packed to be realistic in the case of powder RVEs and to optimize the size difference between them and the resulting Laguerre cells for polycrystal RVEs. This fact explains the use of the Inwards Packing Method (IPM) as our sphere packing method. The IPM has the advantages of being fast, relatively easy to implement, has the capability of respecting size distributions and generates high packing densities. On the other hand, the resulting sphere packing can present heterogeneities for the local density (local voids can be seen especially when mono-sized discs are generated). Hence, the use of this method without any void optimization technique can not model realistic powders and can lead to local decorrelation between the size of the spherical particles and the size of the corresponding Laguerre cells. Two optimization techniques were developed. The first, adapted to equiaxed cell RVEs and referred to as the Grain Optimization Algorithm (GOA), consists in moving each sphere as close as possible to the barycenter of the spheres forming its graph while avoiding overlapping. The global idea of this procedure is to obtain, for all Laguerre cells, a ratio "volume of the corresponding sphere/volume of the cell" more uniformly distributed and so, nearer to the sphere packing density. The second, adapted to powder RVEs and referred to as the Powder Optimization Algorithm (POA), is based on the techniques of dropping and rolling. Each particles is dropped then rolled till reaching its stable position eliminating the voids of the IPM as well as any un-physical positioning of the particles. This method, unlike other classical dropping and rolling techniques where small dropping and rolling steps are used, uses analytical equations in order to displace the particles. Also, the IPM coupled with the POA and a radius reduction technique generates disordered fiber arrays with specific porosities and inter-fiber spacing. The abilities of the GOA and the POA to model equiaxial grain and powder RVEs are presented in chapter 3. We first compare our

POA to a densification method, used in the generation of granular structures, where the voids of an advancing front method are filled with particles non-intersecting preexisting ones. Then, experimental data given by laser granulometry, performed on a stainless steel 316L, are used. In the equiaxial grain modelling applications, we first compare our GOA to the Laplacian Smoothing (LS) algorithm where the grain size distribution is given by a Gaussian distribution law. And then, experimental data of a stainless steel 304L, obtained by EBSD, are used. Three dimensional powder and equiaxial grain RVE modelling are also performed using the statistics of a pure iron. In all the above-mentioned cases, our algorithms proved their efficiency, ability to respect complex and experimental size distribution laws and most importantly their capability to model equiaxial grain, powder, foam and 2D disordered fiber RVEs. Chapter 4 was dedicated to the level-set approach and meshing adaptation. In our case, the mesh is not conform to the microstructure's boundaries and level-set functions are used to implicitly locate these boundaries. This type of definition is an innovative approach in microstructure generation and is combined with an unstructured monolithic meshing strategy. Anisotropic (re-)meshing is essential for guaranteeing geometric accuracy, avoiding prohibitive calculation times and taking into account discontinuities of physical properties. The meshing adaptation is based on the level-set functions and can be performed if the appropriate metric field is constructed. To this end we developed a new strategy, based on the DSATUR graph coloring algorithm, which decreases the number of requisite level-set functions for remeshing by limiting them to a small number of functions representing sets of strictly disjoint cells and which the gathering corresponds to the whole microstructure considered.

The mechanical applications performed in this thesis were detailed in chapter 5. The first application was the compression of elastic foams. The foam RVEs, with different cell irregularities and relative densities, were generated using the LTM coupled with cell spreading and anisotropic remeshing was performed to capture properly the cells' interfaces. The compression itself is a Fluid Structure Interaction (FSI) problem between a compressible fluid (i.e. the air inside the foam's cells) and an elastic compressible solid (i.e. the foam's solid skeleton). In order to solve this problem, a monolithic formulation is used. Such strategy gives rise to an extra stress tensor in the Stokes equations, which are solved by a mixed Finite Element Method (FEM) with a P1+/P1 interpolation, coming from the presence of the structure in the fluid. A Lagrangian framework was used to simulate foam compression. After finding the appropriate RVE size by studying the deviations of the reduced stress on different elementary volumes, several simulations were performed. A first simulation was dedicated for understanding the effect of the air inside the cells. For this reason two regular Voronoï honeycombs with the same relative density were generated, one where we have air inside the cells and another where all the elements containing air were removed. By comparing the reduced stress/strain curves, we observed that the one with air reaches a plateau region while the other continues its linearly elastic behavior. A second simulation studied the effect of cell irregularity on the honeycomb's stress. The compressions of three Voronoï honeycombs with different irregularity degrees were performed. The comparison between the respective stress/strain

curves revealed that the foam's stress is reduced as the irregularity increases. A third simulation was dedicated to the compression of an irregular three-dimensional closed-cell foam. Its stress/strain curve had the same behavior as the one of a Voronoï honeycomb; a linearly elastic phase then a plateau region is reached.

The second application was the permeability computation of unidirectional disordered fiber arrays. The fibers are considered as rigid discs and the RVEs, with different porosities and degrees of disorder, were generated using the POA coupled with radius reduction. The randomness of the generated fiber arrangements was proven using the Ripley's  $K_r$  function. The flow of the Newtonian fluid is governed by the Stokes equations which are solved on the RVE by an immersed domain method. This approach can rather be seen as an extension of the Stokes problem with two fluids, for which the solid behavior of one phase is imposed by using the viscosity as a penalty factor. The rigidity of the solid part is taken into account with a high viscosity value, which acts as a penalty coefficient. Using this approach, a zero velocity boundary condition imposed in a part of the solid domain is propagated into the entire solid domain. Also, a mixed FEM with a P1+/P1 interpolation is used to solve the Stokes equations. Afterwards, homogenization techniques are used to get Darcy's law and so, the permeability is computed. The RVE's size was found by studying the deviations of the permeability tensor and the porosity on different elementary volumes. Furthermore, we computed the values of the components of the transverse permeability tensor on various porosity levels and for different degrees of disorder. The results showed that the transverse permeability is independent of the flow direction and that the fiber arrays are isotropic. In this case, a scalar transverse permeability was computed. The effect of the disorder on both the transverse and longitudinal permeabilities was studied and it was found that both permeability values increase when moving from a uniform array to an array showing higher degrees of disorder.

Given the fact that our virtual microstructure generator can only model equiaxed cell based or spherical particle based microstructures, generating other types of microstructural heterogeneities like fibers or elongated cells can pave the way for modelling more various types of microstructures. Hence, the permeability computations can be extended to 3D multidirectional fiber arrays. Although, the errors in the equiaxial grain RVE modelling cases were acceptable, they remain large. In this context, the GOA should be perfected in order to respect more precisely the given size distribution laws. Moreover, checking the intersections between different particles when using the IPM is time consuming especially when a large number of particles is generated. A solution of this drawback could be the parallelization of the IPM. Also, it is important to compare the computation times of our dropping and rolling algorithm with other algorithms of the same type using small dropping and rolling steps in order to prove the rapidity of our new proposed technique. Furthermore, developing the strategy for generating three-dimensional open-cell foams is crucial for performing simulations on this type of foams. One other important perspective is comparing the FE results of foam compression with experimental results and reaching higher strain values which may be achieved by performing adaptive mesh refinement and automatic remeshing.

# References

- [1] S. Torquato, *Random Heterogeneous Materials: Microstructure and Macroscopic Properties*. Springer-Verlag, 2002.
- [2] P. R. Dawson, “Computational crystal plasticity,” *International Journal of Solids and Structures*, vol. 37, no. 1-2, pp. 115 – 130, 2000.
- [3] R. E. Logé, M. Bernacki, H. Resk, L. Delannay, H. Dignonnet, Y. Chastel, and T. Coupez, “Linking plastic deformation to recrystallization in metals, using digital microstructures,” *Philosophical magazine*, vol. 88, pp. 3691–3712, 2008.
- [4] J. Fish, A. Suvorov, and V. Belsky, “Automated adaptive multilevel solver,” *Computer Methods in Applied Mechanics and Engineering*, vol. 149, no. 1-4, pp. 267 – 287, 1997. Containing papers presented at the Symposium on Advances in Computational Mechanics.
- [5] V. Kouznetsova, M. G. D. Geers, and W. A. M. Brekelmans, “Multi-scale constitutive modelling of heterogeneous materials with a gradient-enhanced computational homogenization scheme,” *International Journal for Numerical Methods in Engineering*, vol. 54, no. 8, pp. 1235–1260, 2002.
- [6] K. Matsui, K. Terada, and K. Yuge, “Two-scale finite element analysis of heterogeneous solids with periodic microstructures,” *Computers and Structures*, vol. 82, no. 7-8, pp. 593–606, 2004.
- [7] H. X. Zhu, S. M. Thorpe, and A. H. Windle, “The effect of cell irregularity on the high strain compression of 2D Voronoi honeycombs,” *International Journal of Solids and Structures*, vol. 43, pp. 1061–1078, 2006.
- [8] X. Chen and T. Papathanasiou, “The transverse permeability of disordered fiber arrays: a statistical correlation in terms of the mean nearest interfiber spacing,” *Transport in Porous Media*, vol. 71, pp. 233–251, 2008.
- [9] K. Li, X.-L. Gao, and G. Subhash, “Effects of cell shape and strut cross-sectional area variations on the elastic properties of three-dimensional open-cell foams,” *Journal of the Mechanics and Physics of Solids*, vol. 54, no. 4, pp. 783 – 806, 2006.

- [10] A. P. Roberts and E. J. Garboczi, “Elastic moduli of model random three-dimensional closed-cell cellular solids,” *Acta materialia*, vol. 49, pp. 189–197, 2001.
- [11] H. X. Zhu, J. R. Hobdell, and A. H. Windle, “Effects of cell irregularity on the elastic properties of open-cell foams,” *Acta Materialia*, vol. 48, no. 20, pp. 4893 – 4900, 2000.
- [12] H. X. Zhu, J. R. Hobdell, and A. H. Windle, “Effects of cell irregularity on the elastic properties of 2D Voronoi honeycombs,” *Journal of the Mechanics and Physics of Solids*, vol. 49, no. 4, pp. 857 – 870, 2001.
- [13] H. X. Zhu and A. H. Windle, “Effects of cell irregularity on the high strain compression of open-cell foams,” *Acta Materialia*, vol. 50, no. 5, pp. 1041 – 1052, 2002.
- [14] M. Bernacki, Y. Chastel, H. Dignonet, H. Resk, T. Coupez, and R. E. Logé, “Development of numerical tools for the multiscale modelling of recrystallisation in metals, based on a digital material framework,” *Computer Methods in Materials Science*, vol. 7, pp. 142–149, 2007.
- [15] M. Bernacki, H. Resk, T. Coupez, and R. E. Logé, “Finite element model of primary recrystallization in polycrystalline aggregates using a level set framework,” *Modelling and Simulation in Materials Science and Engineering*, vol. 17, p. 064006, 2009.
- [16] H. Resk, L. Delannay, M. Bernacki, T. Coupez, and R. E. Logé, “Adaptive mesh refinement and automatic remeshing in crystal plasticity finite element simulations,” *Modelling and Simulation in Materials Science and Engineering*, vol. 17, p. 7:075012, 2009.
- [17] Z. Sun, R. Logé, and M. Bernacki, “3d finite element model of semi-solid permeability in an equiaxed granular structure,” *Computational Materials Science*, vol. 49, no. 1, pp. 158 – 170, 2010.
- [18] S. Vernède, P. Jarry, and M. Rappaz, “A granular model of equiaxed mushy zones: Formation of a coherent solid and localization of feeding,” *Acta Materialia*, vol. 54, no. 15, pp. 4023 – 4034, 2006.
- [19] S. Vernède and M. Rappaz, “A simple and efficient model for mesoscale solidification simulation of globular grain structures,” *Acta Materialia*, vol. 55, no. 5, pp. 1703 – 1710, 2007.
- [20] X. Chen and T. Papathanasiou, “Micro-scale modeling of axial flow through unidirectional disordered fiber arrays,” *Composites Science and Technology*, vol. 67, no. 7-8, pp. 1286 – 1293, 2007.

- [21] P. Laure, G. Beaume, O. Basset, L. Silva, and T. Coupez, “Numerical methods for solid particles in particulate flow simulations,” *European Journal of Computational Mechanics*, vol. 16, pp. 365–383, 2007.
- [22] Y. Shi and Y. Zhang, “Simulation of random packing of spherical particles with different size distributions,” *Applied Physics A*, vol. 92, pp. 621–626, 2008.
- [23] J. Zhou, Y. Zhang, and J. K. Chen, “Numerical simulation of random packing of spherical particles for powder-based additive manufacturing,” *Journal of Manufacturing Science and Engineering*, vol. 131, no. 3, p. 031004, 2009.
- [24] K. Bagi, “An algorithm to generate random dense arrangements for discrete element simulations of granular assemblies,” *Granular Matter*, vol. 7, pp. 31–43, 2005.
- [25] A. Benabbou, H. Borouchaki, P. Laug, and J. Lu, “Geometrical modeling of granular structures in two and three dimensions. application to nanostructures,” *International Journal for Numerical Methods in Engineering*, vol. 80, pp. 425–454, 2009.
- [26] H. Digonnet, L. Silva, and T. Coupez, “Cimlib: a fully parallel application for numerical simulations based on components assembly,” in *Materials Processing and Design; Modeling, Simulation and Applications; NUMIFORM '07; Proceedings of the 9th International Conference on Numerical Methods in Industrial*, 2007.
- [27] A. Agnoli, “Understanding and prediction of inhomogeneous grain growth in Inconel 718 forgings,” tech. rep., CEMEF, 2011.
- [28] A. L. Cruz-Fabiano, “Modélisation de la plasticité cristalline et de la croissance de grains dans un cadre éléments finis,” tech. rep., CEMEF, 2011.
- [29] A. Zouaghi, “Modélisation numérique multi-échelle de la compaction à chaud de poudres métalliques,” tech. rep., CEMEF, 2010.
- [30] A. Zouaghi, M. Bellet, Y. Bienvenu, G. Perrin, D. Cedat, and M. Bernacki, “Modélisation de la phase de compaction du procédé CIC à l’échelle mésoscopique,” in *20ème Congrès Français de Mécanique*, 2011.
- [31] G. Beaume, *Modélisation et simulation numérique directe de l’écoulement d’un fluide complexe*. PhD thesis, Ecole Nationale Supérieure des Mines de Paris, 2008.
- [32] K. Li, X. L. Gao, and G. Subhash, “Effects of cell shape and cell wall thickness variations on the elastic properties of two-dimensional cellular solids,” *International Journal of Solids and Structures*, vol. 42, pp. 1777–1795, 2005.
- [33] A. P. Roberts and E. J. Garboczi, “Elastic properties of model random three-dimensional open-cell solids,” *Journal of the Mechanics and Physics of Solids*, vol. 50, pp. 33–55, 2002.

- [34] A. Benabbou, H. Borouchaki, P. Laug, and J. Lu, “Numerical modeling of nanostructured materials,” *Finite Elements in Analysis and Design*, vol. 46, no. 1-2, pp. 165 – 180, 2010.
- [35] A. Brahme, M. H. Alvi, D. Saylor, J. Fridy, and A. D. Rollett, “3d reconstruction of microstructure in a commercial purity aluminum,” *Scripta Materialia*, vol. 55, pp. 75–80, 2006.
- [36] A. D. Rollett, D. Saylor, J. Frid, B. S. El-Dasher, A. Barhme, S.-B. Lee, C. Cornwell, and R. Noack, “Modelling polycrystalline microstructures in 3d,” in *Proc. Conf. Numiform*, ed. Ghosh, S., Castro, J.C., Lee, J.K., Columbus, pp. 71–77, 2004.
- [37] K. Bagi, “A quasi-static numerical model for micro-level analysis of granular assemblies,” *Mechanics of Materials*, vol. 16, no. 1-2, pp. 101 – 110, 1993. Special Issue on Mechanics of Granular Materials.
- [38] A. Benabbou, *Modélisation géométrique et maillage des structure granulaires. Application aux matériaux nanostructurés*. PhD thesis, INRIA, 2008.
- [39] W. M. Visscher and M. Bolsterli, “Random Packing of Equal and Unequal Spheres in Two and Three Dimensions,” *Nature*, vol. 239, no. 5374, pp. 504–507, 1972.
- [40] L. Xuefeng, S. Jianmeng, and W. Haitao, “Reconstruction of 3-D digital cores using a hybrid method,” *Applied Geophysics*, vol. 6, pp. 105–112, 2009.
- [41] A. Donev, F. H. Stillinger, P. M. Chaikin, and S. Torquato, “Unusually dense crystal packings of ellipsoids,” *Physical Review Letters*, vol. 92, no. 25, p. 255506, 2004.
- [42] C. Y. Wang and V.-C. Liang, “A packing generation scheme for the granular assemblies with planar elliptical particles,” *International Journal for Numerical and Analytical Methods in Geomechanics*, vol. 21, pp. 347–358, 1997.
- [43] C. Y. Wang, C.-F. Wang, and J. Sheng, “A packing generation scheme for the granular assemblies with 3d ellipsoidal particles,” *International Journal for Numerical and Analytical Methods in Geomechanics*, vol. 23, pp. 815–828, 1999.
- [44] Y. Lee, C. Fang, Y.-R. Tsou, L.-S. Lu, and C.-T. Yang, “A packing algorithm for three-dimensional convex particles,” *Granular Matter*, vol. 11, pp. 307–315, 2009.
- [45] F. Jin, H. Xin, C. Zhang, and Q. Sun, “Probability-based contact algorithm for non-spherical particles in dem,” *Powder Technology*, vol. In Press, Corrected Proof, pp. –, 2011.
- [46] M. L. Hunt, R. C. Weathers, A. T. Lee, C. E. Brennen, and C. R. Wassgren, “Effects of horizontal vibration on hopper flows of granular materials,” *Physics of Fluids*, vol. 11, no. 1, 1999.

- [47] O. Skrinjar and P.-L. Larsson, "On discrete element modelling of compaction of powders with size ratio," *Computational Materials Science*, vol. 31, no. 1-2, pp. 131 – 146, 2004.
- [48] R. Bouix, *Caractérisation mécanique et modélisation numérique du comportement des mousse polymériques sous sollicitations statiques et dynamiques*. PhD thesis, Ecole Nationale Supérieure d'Arts et Métiers, 2008.
- [49] Y. Chen, D. Imbault, and P. Dorémus, "Numerical simulation of cold compaction of 3d granular packings," *Materials Science Forum*, vol. 534-536, pp. 301–304, 2007.
- [50] B. Harthong, J.-F. Jérier, P. Dorémus, D. Imbault, and F.-V. Donzé, "Modeling of high-density compaction of granular materials by the discrete element method," *International Journal of Solids and Structures*, vol. 46, no. 18-19, pp. 3357 – 3364, 2009.
- [51] P. J. Frey and P.-L. George, *Maillages: applications aux éléments finis*. HERMES Science Publications, 1999.
- [52] M. A. Groeber, M. D. Uchic, D. M. Dimiduk, Y. Bhandari, and S. Ghosh, "A framework for automated 3d microstructure analysis & representation," *Journal of Computer-Aided Material Design*, vol. 14, pp. 63 – 74, 2008.
- [53] S. J. Osher and J. A. Sethian, "Fronts propagating with curvature dependent speed. algorithms based on hamilton-jacobi formulations," *Journal of Computational Physics*, vol. 79, pp. 12–49, 1988.
- [54] J. A. Sethian, *Level Set Methods and Fast Marching Methods: Evolving Interfaces in Computational Geometry, Fluid Mechanics, Computer Vision, and Material Science*. Cambridge University Press, Cambridge, UK, 1996.
- [55] E. Hachem, *Stabilized finite element method for heat transfer and turbulent flows inside industrial furnaces*. PhD thesis, Ecole Nationale Supérieure des Mines de Paris, 2009.
- [56] M. Bernacki, Y. Chastel, T. Coupez, and R. Logé, "Level set framework for the numerical modelling of primary recrystallization in polycrystalline materials," *Scripta Materialia*, vol. 58, no. 12, pp. 1129 – 1132, 2008.
- [57] K. Hitti, P. Laure, T. Coupez, L. Silva, and M. Bernacki, "Fast generation of complex statistical Representative Elementary Volumes (REVs) in a finite element context," *submitted to Journal of Computational Physics*, 2011.
- [58] K. Hitti, T. Coupez, L. Silva, and M. Bernacki, "Generation of cellular Representative Volume Elements (RVEs) in a finite element (FE) context - application to foam compression," in *20ème Congrès Français de Mécanique*, 2011.

- [59] G. Puaux, L. Silva, P. Laure, M. Vincent, and T. Coupez, “An immersed finite element method for permeability determination of a porous media,” *International Journal For Numerical Methods in Fluids*, p. submitted, 2010.
- [60] L. J. Gibson and M. F. Ashby, *Cellular Solids: Structure and Properties, second ed.* Cambridge University Press, Cambridge, UK, 1997.
- [61] C. S. Marchi and A. Mortensen, “Deformation of open-cell aluminum foam,” *Acta Materialia*, vol. 49, no. 19, pp. 3959 – 3969, 2001.
- [62] W. E. Warren and A. M. Kraynik, “The linear elastic properties of open-cell foams,” *Journal of Applied Mechanics*, vol. 55, no. 2, pp. 341–346, 1988.
- [63] W. E. Warren and A. M. Kraynik, “Linear elastic behavior of a low-density Kelvin foam with open cells,” *Journal of Applied Mechanics*, vol. 64, no. 4, pp. 787–794, 1997.
- [64] H. X. Zhu, N. J. Mills, and J. F. Knott, “Analysis of the high strain compression of open-cell foams,” *Journal of the Mechanics and Physics of Solids*, vol. 45, no. 11-12, pp. 1875 – 1899, 1997.
- [65] A. Simone and L. Gibson, “Effects of solid distribution on the stiffness and strength of metallic foams,” *Acta Materialia*, vol. 46, no. 6, pp. 2139 – 2150, 1998.
- [66] C. W. Hirt, A. A. Amsden, and J. L. Cook, “An arbitrary lagrangian-eulerian computing method for all flow speeds,” *Journal of Computational Physics*, vol. 14, no. 3, pp. 227 – 253, 1974.
- [67] T. J. R. Hughes, W. K. Liu, and T. K. Zimmermann, “Lagrangian-eulerian finite element formulation for incompressible viscous flows,” *Computer Methods in Applied Mechanics and Engineering*, vol. 29, no. 3, pp. 329 – 349, 1981.
- [68] D. J. Benson, “An efficient, accurate, simple ALE method for nonlinear finite element programs,” *Computer Methods in Applied Mechanics and Engineering*, vol. 72, pp. 305–350, 1989.
- [69] M. Souli, A. Ouahsine, and L. Lewin, “Ale formulation for fluid-structure interaction problems,” *Computer Methods in Applied Mechanics and Engineering*, vol. 190, no. 5-7, pp. 659 – 675, 2000.
- [70] R. van Loon, P. D. Anderson, F. N. van de Vosse, and S. J. Sherwin, “Comparison of various fluid-structure interaction methods for deformable bodies,” *Comput. Struct.*, vol. 85, pp. 833–843, 2007.
- [71] J. F. Gerbeau and M. Vidrascu, “A quasi-newton algorithm based on a reduced model for fluid-structure interaction problems in blood flows,” *ESAIM: Mathematical Modelling and Numerical Analysis*, vol. 37, no. 04, pp. 631–647, 2003.

- [72] C. Michler, E. H. van Brummelen, and R. de Borst, “An interface newton-krylov solver for fluid-structure interaction,” *International Journal for Numerical Methods in Fluids*, vol. 47, no. 10-11, pp. 1189–1195, 2005.
- [73] M. Ángel Fernández and M. Moubachir, “A newton method using exact jacobians for solving fluid-structure coupling,” *Computers and Structures*, vol. 83, no. 2-3, pp. 127 – 142, 2005. Advances in Analysis of Fluid Structure Interaction.
- [74] P. Causin, J. Gerbeau, and F. Nobile, “Added-mass effect in the design of partitioned algorithms for fluid-structure problems,” *Computer Methods in Applied Mechanics and Engineering*, vol. 194, no. 42-44, pp. 4506 – 4527, 2005.
- [75] C. S. Peskin, “The immersed boundary method,” *Acta Numerica*, vol. 11, pp. 479–517, 2002.
- [76] G. Papadakis, “A novel pressure-velocity formulation and solution method for fluid-structure interaction problems,” *Journal of Computational Physics*, vol. 227, no. 6, pp. 3383 – 3404, 2008.
- [77] J. Bear, *Dynamics of fluids in porous media*. Elsevier, 1972.
- [78] H. Darcy, *Les fontaines publiques de la ville de Dijon*. Dalmont, Victor, 1856.
- [79] P. C. Carman, *L’écoulement des gaz à travers les milieux poreux*. Institut National des Sciences et Techniques Nuléaires, 1961.
- [80] B. R. Gebart, “Permeability of unidirectional reinforcements for RTM,” *Journal of Composite Materials*, vol. 26, no. 8, pp. 1100–1133, 1992.
- [81] C. Hoareau, *Injection sur renfort : Etude du remplissage de moule et détermination théorique de la perméabilité des tissus*. PhD thesis, Ecole Nationale Supérieure des Mines de Paris, 1994.
- [82] J. B. Keller, “Viscous flow through a grating or lattice of cylinders,” *Journal of Fluid Mechanics*, vol. 18, pp. 94–96, 1964.
- [83] A. Tamayol and M. Bahrami, “Analytical determination of viscous permeability of fibrous porous media,” *International Journal of Heat and Mass Transfer*, vol. 52, pp. 2407–2414, 2009.
- [84] M. Nordlund and T. S. Lundström, “Numerical study of the local permeability of noncrimp fabrics,” *Journal of Composite Materials*, vol. 39, no. 10, pp. 929–947, 2005.
- [85] Y. Song and J. R. Youn, “Asymptotic expansion homogenization of permeability tensor for plain woven fabrics,” *Composites: Part A*, vol. 37, pp. 2080–2087, 2006.

- [86] C. L. Tucker III and R. B. Dessenberger, *Flow and Rheology in Polymer Composites Manufacturing*, ch. Governing Equations for Flow and Heat Transfer in Stationary Fiber Beds (Chapter 8). Elsevier Science Publisher, 1992.
- [87] T. Coupez, “Génération de maillage et adaptation de maillage par optimisation locale,” *Revue européenne des éléments finis*, vol. 9, pp. 403–423, 2000.
- [88] C. Voivret, F. Radjaï, J-Y, Delenne, and M. S. E. Youssoufi, “Space-filling properties of polydisperse granular media,” *Physical Review E*, vol. 76, p. 021301, 2007.
- [89] W. R. Hwang and M. A. Hulsen, “Direct numerical simulations of hard particle suspensions in planar elongational flow,” *Journal of Non-Newtonian Fluid Mechanics*, vol. 136, pp. 167–178, 2006.
- [90] H. L. Liu and W. R. Hwang, “Transient filling simulations in unidirectional fibrous porous media,” *Korea-Australia Rheology Journal*, vol. 21, pp. 71 – 79, 2009.
- [91] R. Al-Raoush and M. Alsaleh, “Simulation of random packing of polydisperse particles,” *Powder Technology*, vol. 176, no. 1, pp. 47 – 55, 2007.
- [92] D. He and N. N. Ekere, “Computer simulation of powder compaction of spherical particles,” *Journal of Materials Science Letters*, vol. 17, pp. 1723–1725, 1998.
- [93] J. L. Finney, “Volume occupation, environment, and accessibility in proteins. environment and molecular area of rna-s,” *Journal of Molecular Biology*, vol. 119, no. 3, pp. 415 – 430, 1978.
- [94] F. F. Mallory and B. N. Boots, “Spatial distribution of lemming mats in the canadian high arctic,” *Canadian Journal of Zoology*, vol. 61, pp. 99 – 107, 1983.
- [95] F. Aurenhammer, “Power diagrams: properties, algorithms and applications,” *SIAM J. Comput.*, vol. 16, pp. 78–96, 1987.
- [96] H. Imai, M. Iri, and K. Murota, “Voronoi diagram in the Laguerre geometry and its applications,” *SIAM Journal on Computing*, vol. 14, no. 1, pp. 93–105, 1985.
- [97] S. P. Ferguson, *Sphere Packings, V*. PhD thesis, University of Michigan, 1997.
- [98] T. C. Hales, “A proof of the kepler conjecture,” *Annals of Mathematics*, vol. 162, pp. 1065–1185, 2005.
- [99] R. D. Kamien and A. J. Liu, “Why is Random Close Packing Reproducible?,” *Physical Review Letters*, vol. 99, no. 15, p. 155501, 2007.
- [100] X. Lin and T. T. Ng, “A three-dimensional discrete element model using arrays of ellipsoids,” *Geotechnique*, vol. 47, pp. 319–329, 1997.

- [101] C. O'Sullivan, *The Application of Discrete Element Modelling to Finite Deformation Problems in Geomechanics*. PhD thesis, University of California, Berkeley, 2002.
- [102] J. W. Evans, "Random and cooperative sequential adsorption," *Rev.Mod.Phys*, vol. 65, pp. 1281–1304, 1993.
- [103] L. Cui and C. O'Sullivan, "Analysis of a triangulation based approach for specimen generation for discrete element simulations," *Granular Matter*, vol. 5, pp. 135–145, 2003.
- [104] O. Häggström and R. Meester, "Nearest neighbour and hard sphere models in continuum percolation," *Random Structures and Algorithms*, vol. 9, pp. 295–315, 1996.
- [105] D. Stoyan, "Models of random systems of non-intersecting spheres," in *Stochastics' 98, JCMF, Prague*, pp. 543–547, 1998.
- [106] G. E. P. Box and M. E. Muller, "A note on the generation of random normal deviates," *The Annals of Mathematical Statistics*, vol. 29(2), pp. 610–611, 1958.
- [107] T. Xu and M. Li, "Topological and statistical properties of a constrained Voronoi tessellation," *Philosophical Magazine*, vol. 89: 4, pp. 349–374, 2009.
- [108] Z. Fan, Y. Wu, X. Zhao, and Y. Lu, "Simulation of polycrystalline structure with Voronoi diagram in Laguerre geometry based on random closed packing of spheres," *Computational Materials Science*, vol. 29, no. 3, pp. 301 – 308, 2004.
- [109] N. R. Tao, Z. B. Wang, W. P. Tong, M. L. Sui, J. Lu, and K. Lu, "An investigation of surface nanocrystallization mechanism in fe induced by surface mechanical attrition treatment," *Acta Materialia*, vol. 50, no. 18, pp. 4603–4616, 2002.
- [110] E. Underwood, *Quantative Stereology*. Addison-Wesley Publishing Company, 1970.
- [111] A. Lewis and A. Geltmacher, "Image-based modeling of the response of experimental 3D microstructures to mechanical loading," *Scripta Materialia*, vol. 55, no. 1, pp. 81 – 85, 2006.
- [112] C. Gruau, *Génération de métriques pour adaptation anisotrope de maillages, applications à la mise en forme des matériaux*. PhD thesis, Ecole Nationale Supérieure des Mines de Paris, 2004.
- [113] M. Kubale, *Graph Colorings*. American Mathematical Society, Providence, Rhode Island, 2004.
- [114] P. Schneider and D. Eberly, *Geometric tools for computer graphics*. New York: Morgan Kaufman, 2003.
- [115] D. Glickenstein, "A monotonicity property for weighted Delaunay triangulations," *Discrete and Computational Geometry*, vol. 38, pp. 651–664, 2007.

- [116] R. Almeida, R. Feijoo, A. Galeao, C. Padra, and R. Silva, “Adaptive finite element computational fluid dynamics using an anisotropic error estimator,” *Computer Methods in Applied Mechanics and Engineering*, vol. 182, pp. 379–400, 2000.
- [117] Y. Mesri, W. Zerguine, H. Digonnet, L. Silva, and T. Coupez, “Dynamic parallel adaption for three dimensional unstructured meshes: Application to interface tracking,” in *Proceedings of the 17th International Meshing Roundtable*, pp. 195–212, 2008.
- [118] T. Coupez, H. Digonnet, and R. Ducloux, “Parallel meshing and remeshing,” *Applied Mathematical Modelling*, vol. 25, no. 2, pp. 153 – 175, 2000. Dynamic load balancing of mesh-based applications on parallel.
- [119] K. Appel and W. Haken, “Every planar map is four colorable,” *Bulletin of the American Mathematical Society*, vol. 82, no. 5, pp. 711–712, 1976.
- [120] D. Brélaz, “New methods to color the vertices of a graph,” *Communications of the ACM*, vol. 22, pp. 251–256, 1979.
- [121] W.-Y. Jang, A. M. Kraynik, and S. Kyriakides, “On the microstructure of open-cell foams and its effect on elastic properties,” *International Journal of Solids and Structures*, vol. 45, pp. 1845 – 1875, 2008.
- [122] N. Mills, “The high strain mechanical response of the wet Kelvin model for open-cell foams,” *International Journal of Solids and Structures*, vol. 44, no. 1, pp. 51 – 65, 2007.
- [123] N. J. Mills and H. X. Zhu, “The high strain compression of closed-cell polymer foams,” *Journal of the Mechanics and Physics of Solids*, vol. 47, pp. 669–695, 1999.
- [124] J. Wismans, J. van Dommelen, L. Govaert, and H. Meijer, “X-ray computed tomography based modelling of polymer foams,” *Materials Science Forum*, vol. 638-642, pp. 2761–2765, 2010.
- [125] J. G. F. Wismans, L. E. Govaert, and J. A. W. van Dommelen, “X-ray computed tomography-based modeling of polymeric foams: The effect of finite element model size on the large strain response,” *Journal of Polymer Science Part B: Polymer Physics*, vol. 48, no. 13, pp. 1526–1534, 2010.
- [126] J. L. Zhang and Z. X. Lu, “Numerical modeling of the compression process of elastic open-cell foams,” *Chinese Journal of Aeronautics*, vol. 20, pp. 215–222, 2007.
- [127] L. Franca, A. Neslitrk, and M. Stynes, “On the stability of residual-free bubbles for convection diffusion problems and their approximation by a two-level finite element method,” *Computer Methods in Applied Mechanics and Engineering*, vol. 166, pp. 35–49, 1998.

- [128] D. Arnold, F. Brezzi, and M. Fortin, “A stable finite element for the stokes equations,” *Calcolo*, vol. 21, pp. 337–344, 1984.
- [129] T. Coupez, “Stable-stabilized finite element for 3d forming calculation,” *Technical Report, CEMEF*, 1996.
- [130] N. Mills, R. Stämpfli, F. Marone, and P. Brühwiler, “Finite element micromechanics model of impact compression of closed-cell polymer foams,” *International Journal of Solids and Structures*, vol. 46, no. 3-4, pp. 677 – 697, 2009.
- [131] K. M. Pillai, “Governing equations for unsaturated flow through woven fiber mats. Part 1. Isothermal flows,” *Composites Part A: Applied Science and Manufacturing*, vol. 33, no. 7, pp. 1007–1019, 2002.
- [132] S. Whitaker, *The Method of Volume Averaging*, vol. 13 of *Theory and Applications of Transport in Porous Media*. Kluwer Academic Publishers, 1999.
- [133] B. Ripley, “Modelling spatial patterns,” *Journal of the Royal Statistical Society. Series B*, vol. 39(2), pp. 172–212, 1977.
- [134] B. Ripley, *Spatial Statistics*. Wiley, New York, 1981.
- [135] F. Goreaud and R. Pélissier, “On explicit formulas of edge effect correction for Ripley’s K-function,” *Journal of Vegetation Science*, vol. 10, pp. 433–438, 1999.
- [136] P. J. Diggle, *Statistical Analysis of Spatial Point Patterns, 2nd edn.* Oxford University Press, Oxford, 2003.

## Simulation numérique de Volumes Élémentaires Représentatifs (VERs) complexes : Génération, Résolution et Homogénéisation

**RESUME :** L'influence des hétérogénéités microstructurales sur le comportement d'un matériau est devenue une problématique industrielle de première importance, cet état de fait explique l'engouement actuel pour la prise en compte de ces hétérogénéités dans le cadre de la modélisation numérique. Ainsi, de nombreuses méthodes pour représenter de manière digitale un matériau virtuel statistiquement équivalent à la microstructure réelle et pour connecter cette représentation à des calculs éléments finis se sont développés ces dernières années. Les travaux réalisés durant cette thèse s'inscrivent en grande partie dans cette thématique. En effet, un générateur de microstructures virtuelles permettant de générer à la fois des microstructures polyédriques ou sphériques a été développé. Ce générateur est basé sur les diagrammes de Laguerre et une méthode frontale de remplissage, une approche level-set pour l'immersion de ces microstructures dans un maillage éléments finis et une technique d'adaptation anisotrope de maillage pour assurer une grande précision lors de cette immersion mais également lors de la réalisation de simulations éléments finis sur ces microstructures. La capacité de ces outils à respecter des données statistiques concernant les microstructures considérées est assurée par le couplage d'une méthode frontale à une méthode d'optimisation des défauts locaux selon la nature de la microstructure considérée. Une technique de coloration de graphe est également appliquée afin de limiter le nombre de fonctions level-set nécessaires à l'adaptation de maillage.

En outre, le coût élevé d'une simulation micro-macro entièrement couplée peut-être significativement réduite en limitant les calculs à une analyse entièrement découplée. Dans ce contexte, la réponse d'un Volume Élémentaire Représentatif (VER) soumis à des conditions aux limites représentatives de ce que subit la matière en un point précis d'un calcul macroscopique reste l'approche la plus complète à l'heure actuelle. Dans le cadre de ce travail, nous nous sommes intéressés à deux types de VER pour deux applications différentes : la déformation de VERs de mousses polyédriques élastiques et le calcul du tenseur de perméabilité pour des VERs composés de fibres cylindriques hétérogènes mais monodirectionnelles.

Plus précisément, pour la première de ces applications, des cas de compression biaxiale de mousses élastiques à cellules fermées en nids d'abeille ou irrégulières sont modélisés comme un problème d'interaction fluide structure (IFS) entre un fluide compressible (l'air à l'intérieur des cellules) et un solide élastique compressible (le squelette de la mousse). Une formulation monolithique est utilisée pour résoudre ce problème en regroupant les équations d'états régissant le solide et le fluide en un seul jeu d'équations résolu sur un maillage unique discrétisant les deux phases. Une telle stratégie donne lieu, pour la partie solide, à l'apparition d'un tenseur d'extra-contrainte dans les équations de Navier-Stokes. Ces équations sont ensuite résolues par une méthode éléments finis mixte avec une interpolation de type  $P1+/P1$ .

Concernant la deuxième application, des écoulements dans des milieux fibreux sont simulés en considérant les fibres comme rigides. Ici encore, une formulation monolithique est adoptée. Ainsi, les équations de Stokes sont résolues sur l'ensemble du domaine de calcul en utilisant une méthode de pénalisation. Par homogénéisation, la loi de Darcy est utilisée pour obtenir le tenseur de perméabilité.

**Mots clés :** VER, Diagramme de Voronoï, Particules sphériques, Compression de mousses, Perméabilité, méthodes des éléments finis



## Direct numerical simulation of complex Representative Volume Elements (RVEs): Generation, Resolution and Homogenization

**ABSTRACT :** The influence of microstructural heterogeneities on material processing is an issue of prime importance, which explains the need to generate a digital material, statistically equivalent to the considered microstructure, and to connect this digital description to finite element (FE) calculations. For this reason, a multi-physical virtual microstructure generator which can simultaneously generate cells and spherical particles is created. This generator is based on Laguerre tessellations and advancing front method, level-set description of interfaces and anisotropic meshing adaptation. The capability of its tools to respect statistical data could be insured by the advancing front method coupled with an optimization procedure depending on the nature of the considered microstructure. Moreover, a graph coloration technique is applied in order to reduce the number of level-set functions used in anisotropic mesh adaptation.

Furthermore, the high cost of a fully coupled micro-macro simulation can be significantly reduced when restricting the attention to a fully uncoupled analysis. In this context, the response of the Representative Volume Element (RVE) when subject to a given macroscopic loading path is of the main interest. RVEs of elastic Voronoï honeycombs and fiber arrays are considered in the manuscript.

The first is used to simulate the compression of an elastic foam subject to a biaxial load. In this case, a fluid structure interaction (FSI) problem occurs between a compressible fluid, the air inside the foam's cells, and an elastic compressible solid, the foam's skeleton. A monolithic formulation is used for solving this problem where a single grid is considered and one set of equations with different material properties is solved. Such strategy gives rise to an extra stress tensor in the Navier-Stokes equations, which are solved by a mixed finite element method with a P1+/P1 interpolation, coming from the presence of the structure in the fluid.

The second RVE is used to compute the permeability of disordered fiber arrays. In this case, flows through unidirectional fibrous media are simulated and the fibers are considered as rigid discs. Also, a monolithic formulation is used for solving this problem. Therefore the Stokes equations are solved in the whole domain using a penalization method. After using volume average techniques, Darcy's law is obtained giving the possibility to compute the permeability tensor.

**Keywords :** RVE, Voronoï tessellations, Spherical particles, foam compression, permeability computation, finite element method